

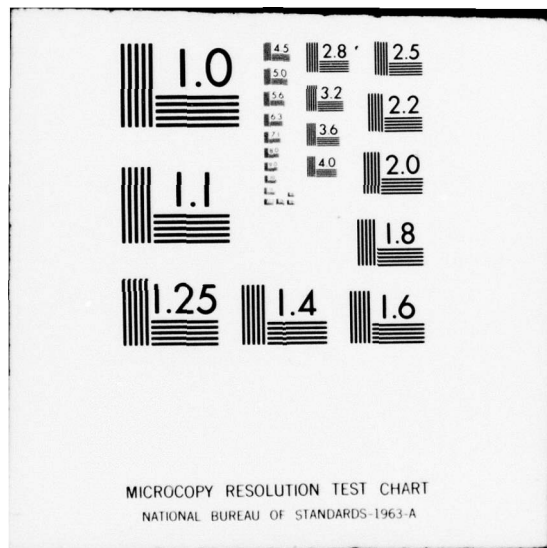
AD-A067 364

CASE WESTERN RESERVE UNIV CLEVELAND OHIO DEPT OF CHEMISTRY F/G 11/6
PASSIVATION STUDIES OF IRON, NICKEL AND THEIR ALLOYS BY 'IN SIT--ETC(U)
FEB 79 C T CHEN, B D CAHAN, E YEAGER N00014-75-C-0953
TR-48 NL

UNCLASSIFIED

of 3
AD
A057364





LEVEL ~~11~~

(12)

ADA067364

ELECTROCHEMISTRY RESEARCH LABORATORIES

DEPARTMENT OF CHEMISTRY

JOHN SCOFF MILLIS SCIENCE CENTER ← 31dg

CASE WESTERN RESERVE UNIVERSITY

CLEVELAND, OHIO 44106

DDC
APR 16 1979
C

TECHNICAL REPORT NO. 48

**PASSIVATION STUDIES OF IRON, NICKEL AND THEIR
ALLOYS BY IN SITU ELLIPSONOMETRY AND EX SITU ESCA TECHNIQUES**

by

C. T. Chen, B. D. Cahan and E. Yeager

DDC FILE COPY

February 15 1979

OFFICE OF NAVAL RESEARCH

Contract N00014-75-C-0953

Project NR 359-451 5

This document has been approved
for public release and sale; its
distribution is unlimited.

79 04 13 006

OFFICE OF NAVAL RESEARCH

Contract N00014-75C-0953

12

Task No. NR 359-451

9 TECHNICAL REPORT NO. 48

6 PASSIVATION STUDIES OF IRON, NICKEL AND THEIR ALLOYS BY 'IN SITU' ELLIPSOMETRY AND 'EX SITU' ESCA TECHNIQUES.

10 by C. T. Chen, B. D. Cahan and E. Yeager

Prepared as part of the Ph.D. thesis of C. T. Chen in Chemistry at Case Western Reserve University June, 1979

15 N00014-75-C-0953

11 15 Feb 79

Case Laboratories for Electrochemical Studies

12 224 p and The Chemistry Department Case Western Reserve University

14 TR-48 Cleveland, Ohio 44106

D D C REPORT APR 16 1979 RECEIVED

use 1473 source. A Dept. of Chem.

February 15, 1979

Reproduction in whole or in part is permitted for any purpose of the United States Government

*This document has been approved for public release and sale; its distribution is unlimited

This document has been approved for public release and sale; its distribution is unlimited.

404 239 79 04 13 006 xlt

REPORT DOCUMENTATION PAGE		READ INSTRUCTIONS BEFORE COMPLETING FORM
1. REPORT NUMBER 48	2. GOVT ACCESSION NO.	3. RECIPIENT'S CATALOG NUMBER
4. TITLE (and Subtitle) Passivation Studies of Iron, Nickel and Their Alloys by In Situ Ellipsometry and Ex Situ ESCA Techniques		5. TYPE OF REPORT & PERIOD COVERED Technical Report #48
7. AUTHOR(s) C. T. Chen, B. D. Cahan and E. Yeager		6. PERFORMING ORG. REPORT NUMBER
9. PERFORMING ORGANIZATION NAME AND ADDRESS Dept. of Chemistry Case Western Reserve University Cleveland, Ohio 44106		8. CONTRACT OR GRANT NUMBER(s) N00014-75-C-0953
11. CONTROLLING OFFICE NAME AND ADDRESS Office of Naval Research Chemistry Program - Chemistry Code 472 Arlington, Virginia 22217		10. PROGRAM ELEMENT, PROJECT, TASK AREA & WORK UNIT NUMBERS NR-359-451
14. MONITORING AGENCY NAME & ADDRESS (if different from Controlling Office)		12. REPORT DATE 15 February 1979
		13. NUMBER OF PAGES 210
		15. SECURITY CLASS. (of this report) Unclassified
16. DISTRIBUTION STATEMENT (of this Report) This document has been approved for public release and sale; its distribution unlimited.		15a. DECLASSIFICATION/DOWNGRADING SCHEDULE
17. DISTRIBUTION STATEMENT (of the abstract entered in Block 20, if different from Report)		
18. SUPPLEMENTARY NOTES		
19. KEY WORDS (Continue on reverse side if necessary and identify by block number) passivation, iron, nickel, corrosion, ellipsometry, ESCA, electrochemical interfaces		
20. ABSTRACT (Continue on reverse side if necessary and identify by block number) The passivation film on iron has been examined in situ using automatic ellipsometry to obtain the spectral properties. Both structural and mechanistic information has been obtained concerning this film. This represents the first time such spectroscopic information is available. ESCA has been used as a ex situ complementary tool to examine iron and also nickel and their alloys.		

TABLE OF CONTENTS

	page
REPORT DOCUMENTATION PAGE	ii
LIST OF FIGURES	iv
LIST OF TABLES	viii
CHAPTER I INTRODUCTION	1
I. General View of Passivation	1
II. Mechanism of Anodic Oxide Growth	5
III. Characterization of Passive Film on Iron	27
A. Chemical Composition and Structure of the Passive Films on Iron	27
B. General Electronic Properties	35
C. <u>In situ</u> Ellipsometric Studies of Passive Films on Iron	49
CHAPTER II EXPERIMENTAL	56
I. Electrode and Cell	56
II. Optical Alignment	59
Principles of Alignment by an Auto-collimator (Telescope)	62
1. Principles of Operation of an Auto-collimator	62
2. Alignment of Ellipsometer System by the Autocollimator	66
3. Initial Alignment Procedures	66
4. Light Source Alignment	68
5. Alignment of Rotating Analyzer Prism	69

write Section	<input checked="" type="checkbox"/>
half Section	<input type="checkbox"/>
Investigation	<input type="checkbox"/>
BY	
DISTRIBUTION/AVAILABILITY CODES	
Dist.	AVAIL. and/or SPECIAL
A	

	page
6. Alignment of the Prisms (Polarizer and Rotating Analyzer)	72
7. Alignment of the Cylindrical Optics for Electrochemical Studies	75
III. <u>In situ</u> Automatic Ellipsometric Measurements	81
IV. Spectroscopic Ellipsometry of Poly- and Single-Crystal $\alpha\text{-Fe}_2\text{O}_3$	88
V. <u>Ex situ</u> ESCA Measurements	88
CHAPTER III. RESULTS AND DISCUSSION	91
I. Three-Parameter (3-P) Solutions: n_2 , k_2 , d (Thickness of the Passive Film)	91
A. Model and Basic Equations	91
B. Computer Iteration Procedure	96
II. Critique on Present Status of Ellipsometric Data	99
III. Optical Spectrum of Bare Iron	102
IV. Optical Spectra of Poly- and Single Crystalline Hematite ($\alpha\text{-Fe}_2\text{O}_3$)	104
V. Optical Spectra of Passive Film on Iron	111
VI. Potentiostatic Anodic Oxidation	118
A. Single Potential Step Oxidation	118
B. Progressive Step Oxidation	133
VII. Potentiostatic Oxide Reduction	136
A. Single Step Reduction	136
A-1. Interpretation and Comments on Reduction Process	142

	page
B. Potential Dependence of the Film Properties Grown at More Anodic Potentials	146
VIII. Cyclic Sweep Experimental Results	149
IX. <u>Ex situ</u> ESCA Studies on Passive Films	157
CHAPTER IV. CONCLUSIONS AND REMARKS	164
I. Applicability of Automatic Ellipsometry to Passivation Studies	164
II. The Growth of Passive Films on Iron	166
III. The Reduction of the Passive Films on Iron	168
IV. Applicability of Ellipsometry to Study Transition Metal Oxides	170
V. Applicability of ESCA to Passivation Studies	172
VI. Optical Properties of the Passive Film Grown in Borate Buffer	173
VII. The Nature of the Passive Film Grown in Borate Buffer	175
VIII. Remarks	178
REFERENCES	180
APPENDIX A	188
DISTRIBUTION LIST	211

LIST OF FIGURES

FIGURE		page
I-1.	Typical current-potential curve for an iron electrode in borate buffer solution (pH = 8.4)	1
I-2.	Schematical representation of the pH-electrode potential diagram of iron	2
I-3.	Potential energy of mobile ions vs distance with and without an applied field	7
I-4.	Model of the place exchange process	11
I-5.	Phase scheme of the electrode and the inner potential level	12
I-6.	A structural representation for the passive film on iron in borate buffer (pH = 6.8) at 300 mV vs NHE	34
I-7.	A band structure of passive films on iron under different anodic bias potentials	47
II-1.	Taflon cell top and electrode	58
II-2.	Cylindrical optical cell	58
II-3.	Configuration of cylindrical cell for optical and electrochemical studies	60
II-4.	Block diagram of ellipsometer and electrochemical instrumentation	61
II-5.	Telescope lens system	63
II-6.	Cut-away view of telescope autocollimator	65
II-7.	The geometries to show the relationship of the light beam from autocollimator and the reflected beams through a sample surface with and without tilt back to autocollimator	74
II-8.	Schematic representation of cell mount on ellipsometer table	76
II-9.	The optical geometry of the sample surface inside a cylindrical cell and lens system	78

FIGURE	page
II-10. The optical geometry for a system set for reflection at an angle of incidence ϕ to show the necessary adjustment of the cell and lenses if the sample is displaced from center of the cell by a distance D	82
II-11. Flow chart of data gathering (real-time) and data processing	84
II-12. Schematic of various waveforms	86
III-1. Graphical representation of 3-P solution for a film of 15 Å thick with $\lambda = 350$ nm and $\phi = 68^\circ$	98
III-2. Complex refractive index ($\hat{n}_3 = n_3 - ik_3$) of iron	103
III-3. Complex dielectric constant $\hat{\epsilon} = \epsilon_1 - i\epsilon_2$ of two polycrystalline specimens of α -Fe ₂ O ₃ powder-pressed pellet, followed by sintering at high temperature	105
III-4. Complex dielectric constants of single crystal α -Fe ₂ O ₃	106
III-5. Complex dielectric constant spectrum for the Lorentz oscillator model	107
III-6. Complex dielectric constant ($\epsilon_1 - i\epsilon_2$) of passive film on iron grown in borate buffer at pH 8.4 at 1.35 V and measured at 1.25 V, $\phi = 68^\circ$	112
III-7. Complex dielectric constant ($\epsilon_1 - i\epsilon_2$) of passive film on iron grown in borate buffer at pH 8.4 at 1.15 V and measured at 1.05 V, $\phi = 65^\circ$	115
III-8. Complex dielectric constant ($\epsilon_1 - i\epsilon_2$) of passive film on iron grown in borate buffer at pH 8.4 at 1.15 V and measured at 1.05 V, $\phi = 70^\circ$	116
III-9. Log i vs log t and Q (charge after current integration) vs log t plots during single potential steps experiments	119

FIGURE	page
III-10. Q, Δ , Ψ , and $\Delta R/R\%$ vs log t plots for simple potential step experiments	120
III-11. The ellipsometric parameters (Δ , Ψ) vs log t plots for single potential step experiments with differences in final anodic potentials	121
III-12. The ellipsometric parameter $\Delta R/R\%$ vs log t plots for single potential step experiments with differences in final anodic potentials	123
III-13. The k_2 vs log t plots for a single potential step oxidation at $\phi = 68^\circ$ and different wavelengths	125
III-14. The range of thickness (d) vs log t plots for the corresponding experiments shown in Fig. III-13	126
III-15. The k_2 vs Q plots for the corresponding experiments shown in Fig. III-13	128
III-16. The range of thickness (d) vs Q plots for the corresponding experiments shown in Fig. III-13	129
III-17. Time dependence of refractive index and thickness of passivation layer on iron during growth at different potentials	130-1
III-18. i vs log t plots for progressive step oxidation	134
III-19. i , Q, Δ , Ψ vs log t for a progressive step oxidation	135
III-20. Typical Δ vs Q_r and Ψ vs Q_r plots during one-step reduction for the oxides formed at different potentials for 5 min	137
III-21. K_2 vs Q_r and d vs Q_r during one-step reduction for passive films formed at different anodic potentials for 5 min in borate buffer solution	138-9

FIGURE	page
III-22. The k_2 spectrum vs Q_r and d vs Q_r for a film grown at 1.15 V for 5 min and subsequently reduced potentiostatically back to -0.25 V at different wavelengths	140-1
III-23. The Ψ vs $\log t$ and i vs $\log t$ plots during a single potential step reduction for a film grown at 1.15 V for 5 min	144
III-24. n_2 , k_2 vs $\log t$ for progressive reduction of a film on iron grown in borate buffer	147
III-25. Typical sweep experimental data	150
III-26. The Ψ -E curves for different wavelengths during sweep experiments	154
III-27. Two typical sweep experimental results obtained by combinations of various voltage waveforms with the regular sweep	156
III-28. Fe 2P photo-electron spectra for passive films on iron grown in borate buffer (pH 8.4) at different potentials: 1. 0.35 V; 2. 0.65 V, 3. 1.35 V; 4. 1.55 V vs RHE	159
III-29. O 1s photo-electron spectra for passive films on iron grown in borate buffer (pH 8.4) at different potentials: 1) 0.35 V; 2) 0.65 V; 3) 1.35 V; 4) 1.55 V vs RHE	161
III-30. X-ray photo-electron spectra of valence band of passive films on iron grown in borate buffer (pH 8.4) at different potentials: 1) 0.35 V; 2) 0.65 V; 3) 1.35 V vs RHE	163

LIST OF TABLES

TABLE	page
I. Analysis of Pure Iron	57
II. Electrode Materials for ESCA Measurements and Their Sources	89
III. The n_2 , k_2 , and d (thickness) Evaluated from Ellipsometric Data by 3-P Method for Passive Film on Iron Grown in Borate Buffer at 1.35 V and Measured at 1.25 V at $\phi = 68^\circ$	113

CHAPTER I

INTRODUCTION

I. General View of Passivation

Passivation can be described as a general phenomenon such that the activity of the metal surface is much reduced compared with that of its bare metal surface. In the extreme case, the metal surface can become completely inert towards the environment. This phenomenon was already observed in 1836 by Faraday with iron in concentrated nitric acid. Since then there have been numerous investigations on this subject because of its apparent complexity and its practical significance to the corrosion resistance of metal and alloys.

Electrochemically, the current-potential curve of a metal electrode has been most often used to demonstrate the passivation

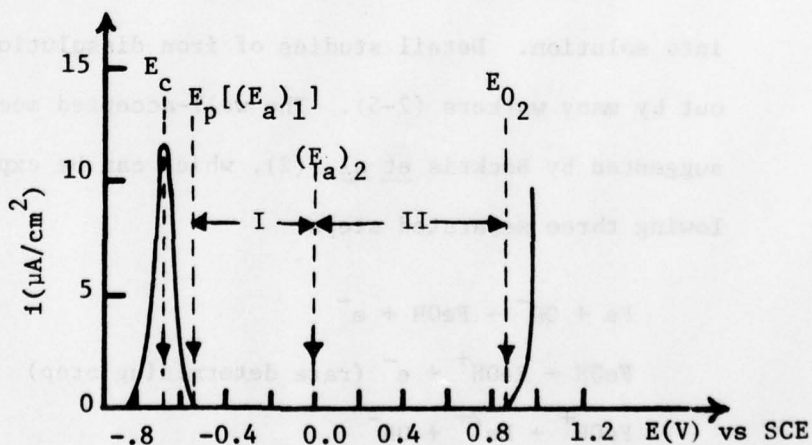
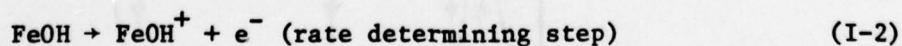


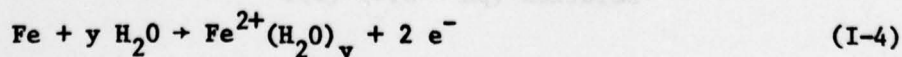
Fig. I-1 Typical current-potential curve for an iron electrode in solution (pH = 8.4) (1).

phenomena. Figure I-1 shows a typical current-potential curve of an iron electrode in an equi-volume mixture of 0.15 N $\text{Na}_2\text{B}_4\text{O}_7$ and 0.15 N H_3BO_3 solution (pH = 8.4). From the far cathodic side of the curve, the current increases drastically to a maximum value, then decreases steeply until the applied potential reaches E_p , at which the current becomes very small. As the electrode potential is scanned to more anodic values, the current falls further and approaches to a limiting value. As the electrode potential reaches E_{O_2} , however, oxygen evolution sets in, and consequently the current increases. The portion of the curve before E_c is called the active (or dissolution) region, the portion between E_c and E_p is called the active-passive transition region, the portion between E_p and E_{O_2} is the passive region, and finally the region beyond E_{O_2} is the transpassive region.

In the active corrosion region, the iron electrode dissolves into solution. Detail studies of iron dissolution have been carried out by many workers (2-5). The well-accepted mechanism is the one suggested by Bockris et al. (2), which can be expressed by the following three separated steps:



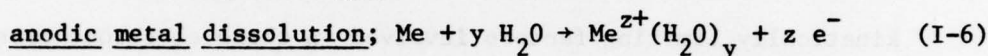
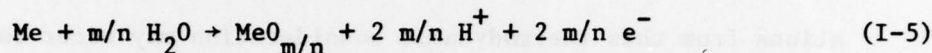
The overall reaction equivalent to this mechanism is



where y is the number of water molecules coordinated with Fe^{2+} ion.

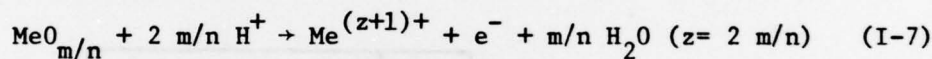
The transition from active to passive is generally believed to be resulted from the following several concurrent and competing reactions at the metal-solution interface:

oxide film formation;

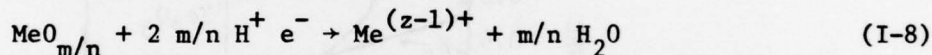


In some cases, the following two reactions must also be considered:

oxidative dissolution of oxide;



reductive dissolution of oxide;



Theoretical modeling and computer simulations for the i-E curves, based on detailed mechanistic steps including parallel and consecutive reactions for the kinetic equations to describe the complete anodic behavior of iron electrode, have been reported by several workers (3,4). Miligy et al. (3) concluded that the active dissolution region is characterized by the consecutive [Bockris et al. (2)] mechanism including the adsorbed species $(FeOH)_{ads}$ and that the transition range involves the formation of the adsorbed intermediate $[Fe(OH)_2]_{ads}$ which partially covers the surface and acts as an inhibitor on the active dissolution. The pre-passive range can be described by further electrochemical parallel steps starting from $[Fe(OH)_2]_{ads}$, and final passivation is due to non-porous oxide layers involving Fe_2O_3 and Fe_3O_4 and originating from $[Fe(OH)_3]$ oxide

and $[\text{Fe}(\text{OH})_2]_{\text{ads}}$.

Thermodynamically, the equilibrium pH-potential diagram (Fig. I-2) indicates the range of pH values and potentials where the reactants and products involved in the Eqs. I-1, I-2, and I-3 are the most stable components for iron electrode systems. However, deviations from this thermodynamic consideration may occur because of kinetically limiting factors involved in these electrode processes and result in producing some less stable oxide species coexisting with the most stable ones.

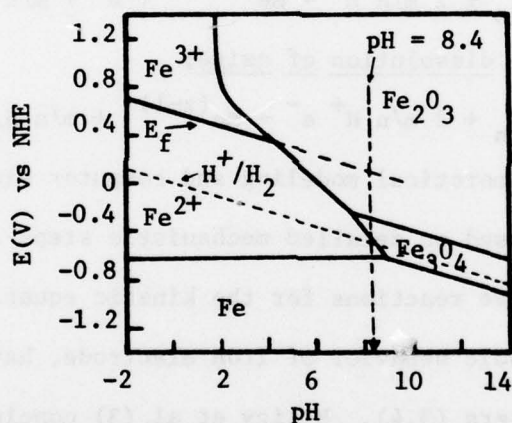


Fig. I-2 Schematic representation of the pH-electrode potential diagram of iron (6). The dotted lines correspond to: pH 8.4, the value used in this study; E_f , the Flade potential according to Eq. I-9; H^+/H_2 electrode potential.

The pH dependent lowest potential of film formation is called the Flade potential (E_f). It has been experimentally (7,8) established that this potential^a in the pH range less than 6 at 25°C can be expressed as:

^aHowever, less anodic values of Flade potential than expected from the below equation in the higher pH range have been reported by many workers (12-14).

$$E_f = 0.58 - 0.059 \text{ pH} \quad (\text{V vs SHE}) \quad (\text{I-9})$$

The rate of dissolution in the metal-electrolyte system under consideration drops drastically when the electrode potential approaches anodically to the Flade potential. Above it, the rate of dissolution of the metal is governed by the dissolution rate of the passivating film which is compensated in the steady state by the growth processes of the oxide film. Several interpretations have been suggested for the Flade potential and the associated phenomena. Uhlig et al. (9) attributed the Flade potential to the formation of a monolayer of adsorbed oxygen or hydroxyl ions which cover the metal surface and thus prevent the dissolution of metal ions. Gohr and Lange (10) and Vetter (11) offered an interpretation based on the thermodynamic argument that the Flade potential is caused by the transition from a rapidly dissolving oxide of Fe_3O_4 to the metal-passive film of $\gamma\text{-Fe}_2\text{O}_3$ which exhibits a very slow rate of dissolution in acid media. Wagner (15) interpreted the Flade potential of iron as the potential at which the composition of the oxide approaches the formula $\text{Fe}_{2.83}\text{O}_4$ halfway between the limiting compositions of Fe_3O_4 and Fe_2O_3 (or $\text{Fe}_{2.67}\text{O}_4$).

II. Mechanism of Anodic Oxide Growth

The most common behavior observed for the growth of anodic oxide films by electrochemical methods is that of a limiting thickness. The rate of film growth initially is extremely rapid, but after a few minutes or hours drops to very small or negligible values. A

protective film of a few tens of an Angstrom up to about 100 Angstroms thick is formed on the metal electrode surface. The rate of film growth, except in the very early stage, is usually logarithmic with time. This observed logarithmic growth behavior of the anodic oxide films has usually been interpreted either by the high-field mechanism (16-19) or place-exchange mechanism (12,20-21).

The high-field mechanism was originally proposed by Cabrera and Mott (16) to derive and account for the logarithmic growth behavior of air-formed oxide films produced at sufficiently low temperature and of anodic oxide film. It includes the following major assumptions: first, growth is by cation migration only; second, oxygen molecules dissociate on the oxide surface, creating traps with an energy ($e \cdot \Delta V$) below the Fermi level of the metal; third, the density of such traps is sufficient to provide enough electron levels to give a potential drop ΔV across the film and thus a field ϵ such that $\epsilon = \Delta V/x$, with x as the thickness of the oxide film, and fourth, the activation energy W for the movement of the cation in the oxide drops to $W - qa\Delta V$, where q is the charge on the ion and $2a$ the jump distance from an interstitial site to another. An alternative assumption is that this is the activation energy for bringing an ion from the metal into the oxide. Figure I-3 is a schematic diagram of an interstitial ion in the high-field oxide formation process.

The growth rate^b thus derived is of the form

$$dx/dt = 16N \cdot a^4 \nu \cdot \exp[-(W - (qa\Delta V/x))/k_B T] \quad (I-10)$$

where N is the number of mobile ions per unit volume in the oxide, and ν a phonon frequency for the normal optical mode corresponding to the transmission over the barrier in Fig. I-3. A similar model

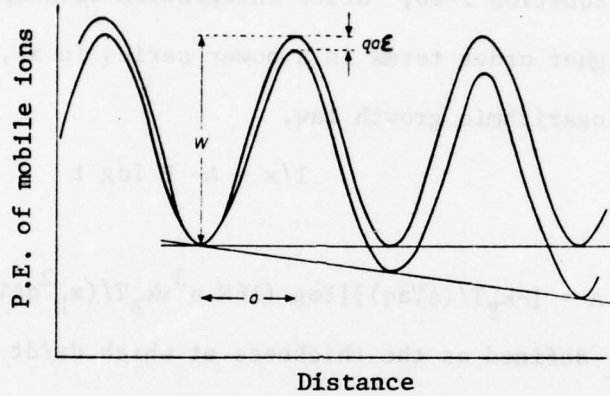


Fig. I-3 Potential energy (P.E.) of mobile ions vs distance with and without an applied field. a is the activation distance which is one half of the jump distance (17).

but where the rate-controlling step is the transport of cations between the interstitial sites in the oxide layer has been proposed by Verwey (18). Dewald (19) extended Verwey's idea in combination with the Cabrera and Mott (16) high-field mechanism to derive a logarithmic growth law. Dewald further took into account the space charge field introduced during the oxide film growth process. The

^bThe general form of growth rate according to Mott-Cabrera model for high-field case without approximation is expressed as

$$dx/dt = 16Na^4 \nu \{ \exp[-(W - (qa\Delta V/x))/k_B T] - \exp[-(W + (qa\Delta V/x))/k_B T] \} \quad (I-10a)$$

$$\text{or } dx/dt = 32Na^4 \nu \exp(-W/k_B T) \cdot \sinh[(qa\Delta V/x)/k_B T] \quad (I-10b)$$

$$\text{or } dx/dt = 2u \cdot \sinh(X_1/x) \quad (I-10c)$$

with

$$u = 16Na^4 \nu \cdot \exp(-W/k_B T)$$

$$\text{and } X_1 = qa\Delta V/k_B T$$

space charge within the oxide layer then significantly reduces the entrance (metal-oxide) barrier and the transport of the cation between interstitial sites in the oxide becomes the rate determining step for growth.

Equation I-10,^c after integration with approximation (dropping higher order terms in a power series in x), leads to the inverse logarithmic growth law,

$$1/x = A - B \log t \quad (I-11)$$

where

$$A = [-k_B T / (\Delta V a q)] [\log (16 N \cdot a^3 v k_B T / (x_L^2 q \Delta V)) - W / k_B T]$$

with x_L defined as the thickness at which $dx/dt \approx 1 \text{ \AA}$ per day and

$B = k_B T / q a \Delta V$, k_B = Boltzmann constant.

The total charge per unit surface area of electrode during the oxide film growth can be correlated with the thickness of the oxide film by

$$x = QM / (zeF\rho\sigma) \quad (I-12)$$

where M is the molecular weight of the oxide, z is the valency state

^cGhez (101) examined the general form (Eq. I-10c) of Mott-Cabrera for the high-field case and derived numerically an equation of the following form for thin film growth

$$X_1/x = -\log[(t+\tau)/x^2] - \log(X_1 u) \quad (I-11a)$$

A plot of $1/x$ vs $\log[(t+\tau)/x^2]$ should thus yield a straight line with slope $-X_1^{-1}$ and intercept $-X_1^{-1} \cdot \log(X_1 u)$. The physical parameters of the theory u and X_1 can be easily evaluated from Eq. I-11a for a negligible τ (offset time) with respect to the smallest experimental time t . If τ is not negligible, then a distinct upward bending of the $1/x$ vs $\log(t/x^2)$ plot for the smaller oxidation times should be apparent. The data can be linearized by proper choice of τ .

of the cation in the oxide, F is Faraday constant, ρ is the density of the oxide film, and σ is a roughness factor.

The differentiated form of Eq. I-12 gives the current density i as

$$i = (zeF\rho\sigma/M) \cdot dx/dt \quad (I-13)$$

The rate of the anodic oxide film growth, thus, can be related to the current density.

The current density as a function of potential and thickness for the growth of the passive film on iron has been studied both potentiostatically and galvanostatically by many workers (1,13,35). An equation with empirical constants for the current density (26) can be expressed as

$$i = i_o \exp(\beta_1 \cdot \epsilon) = i_o \exp(\beta_1 \cdot \Delta V/x) = i_o \exp(\beta_2 \cdot \Delta V/Q) \quad (I-14)$$

where ϵ is the field strength, $\Delta V = \psi_o - \psi$ is the potential difference in the oxide film, ψ_o is the equilibrium potential of the oxide and Q the charge density corresponding to a film thickness x , and β_1 , β_2 , i_o can be correlated as

$$\beta_1 = qa/k_B T, \quad \beta_2 = qazeF\rho\sigma/Mk_B T, \quad \text{and} \quad i_o = i_o^* \exp(-w/k_B T)$$

with $i_o^* = i_o Na^4 vzeF\rho\sigma/M$.

The temperature dependence of the growth of the passive film on iron in acidic or neutral solutions has been investigated by several workers (12,13,103) in an attempt to determine the activation energy and the activation distance (half jump distance) as well as the equilibrium potential for the passive layer on iron. The experi-

mental results showed quite a range of scatter depending on the value assumed for the valence of the migrating species and the value of the density which, in turn, is determined by the lattice parameter of the bulk iron oxide. The most reasonable value obtained for the mean half-jump distance was 2.5 \AA by Moshtev (13), who assumed that the migrating ion is ferric in a passive film with a $\gamma\text{-Fe}_2\text{O}_3$ structure formed in pH 8.4 borate buffer solution.

Calvert and Kruger (22), however, from their ellipsometric results calculated the activation distance and the activation energy by assuming ferrous ion as the migrating species and further assuming the potential drop to be mainly across the non-conducting outer $\gamma\text{-Fe}_2\text{O}_3$ layer of the passive film. They obtained reasonable values for the activation distance (3 \AA) and an activation energy of 41-46 kcal/mole. The lack of experimental data on the nature of the migrating species, and other effects such as the space charge, with its distribution of the potential drops, and the probability of a concentration gradient across the passive layer made the calculation for the activation distance and the height of the energy barrier for the high-field oxide growth mechanism highly uncertain.

The place-exchange mechanism was proposed by Lanyon and Trapnell (20) to account for the logarithmic growth in a study involving O_2 adsorption on clean metal surfaces including iron. This mechanism involves the simultaneous interchange of the adsorbed oxygen with the underlying metal atoms and requires three necessary steps to account for the direct logarithmic behavior of the oxygen uptake of the metal

surfaces: first, the physisorbed O_2 assists interchange through the liberation of the heat of chemisorption; second, the presence of O_2 in the gas phase is necessary; third, the activation energy increases linearly with the amount of O_2 uptake (indicated by the exponential dependence of the rate on adsorbed volume). A schematic of this mechanism is shown in Fig. I-4. Lanyon and Trapnell (20) and later Eley and Wikinson (21) suggested that this mechanism operated only in the regime of no more than two monolayers or else modifications of the mechanism were required. Furthermore, Lanyon and Trapnell (20) did not apply this mechanism to the interpretation of their experimental results for O_2 interaction with a clean iron surface because their experimental results fitted better with the growth law according to high-field mechanism of Cabrera and Mott (16).

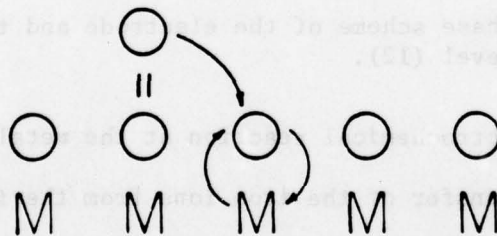


Fig. I-4 Model of the place exchange process (23).

Sato and Cohen (12) further developed the place-exchange mechanism to account for the steady-state growth of the passive film on iron in borate buffer (pH 8.4). Their mathematical manipulations are based on the concept of independent probability being applicable to the simultaneous interchange of iron-oxygen ions in the passive film without any influence by its nearest neighbors. In their development,

they divided the whole system into three separate regions: metal-oxide interface; the passive layer; and the oxide-solution interface (as shown in Fig. I-5). Each region has an electrochemical reaction associated with it. The activation energy associated with each electrochemical reaction then determines the probability of the interchange of iron and oxygen ions.

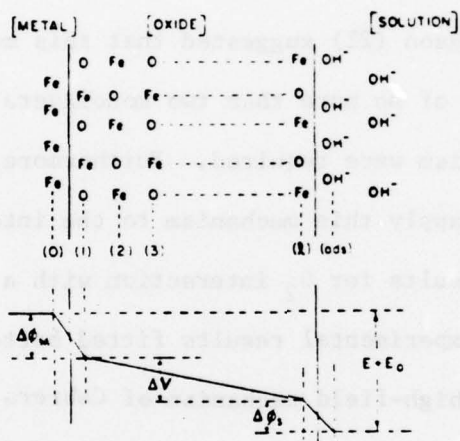
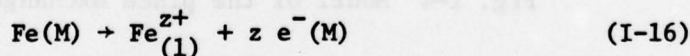


Fig. I-5 Phase scheme of the electrode and the inner potential level (12).

The electrochemical reaction at the metal-oxide interface involving the transfer of the iron ions from the iron metal to the first lattice layer of the passive film is given by



The activation energy of this reaction is

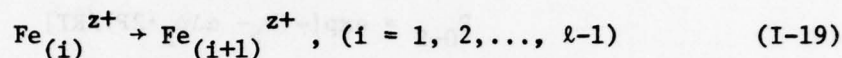
$$W_{\text{M-O}} = W_{\text{M}} - \alpha \Delta \psi_{\text{M}} z F \quad (\text{I-17})$$

where W_{M} is the chemical potential difference of the iron ion in the activated state and the metallic state, α the transfer coefficient, and F the Faraday. Thus the probability of an iron atom in the metal

surmounting this activation energy is given by

$$P_{M-0} = \exp[-(W_M - \alpha \Delta \psi_M z F) / RT] \quad (I-18)$$

A series of reactions involving exchange between the lattice layer of the oxide can be represented as



The activation energy associated with each of these reactions is

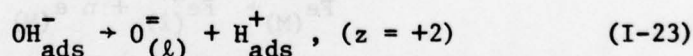
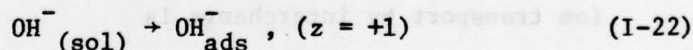
$$W_{Ox}^i = W_o - \alpha \Delta \epsilon_i a z F, \quad (i = 2, 3, \dots, \ell) \quad (I-20)$$

where W_o is the chemical potential difference between an iron ion in the activated state and the normal state in any lattice layer, ϵ_i is the gradient of the potential difference at the i^{th} layer of the oxide, and a the distance between two adjacent layers of the oxide.

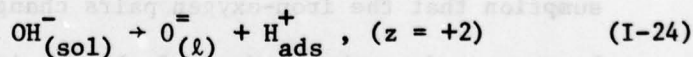
The corresponding probability of an iron ion in each layer being involved in the exchange process is given by

$$P_i = \exp[-(W_o - \alpha \epsilon_i a z F) / RT], \quad (i = 2, 3, \dots, \ell) \quad (I-21)$$

The reaction of the oxide-solution interface involves the transfer of oxygen from the solution to the outermost layer of the passive film. It can be expressed as the following two steps:



The overall reaction can be given as



The rate of the oxygen uptake is controlled by the reaction step described by Eq. I-23, a conclusion reached from their pH dependence studies. Thus the activation energy involved in the incorporation

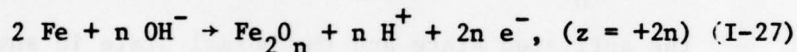
process at the solid-solution interface can be given as

$$W_{O-S} = W_S - \alpha \Delta \psi_S \cdot 2F \quad (I-25)$$

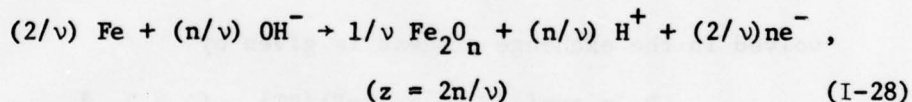
The probability of an oxygen ion involved in the incorporation process at the solid-solution interface thus can be given as

$$P_{O-S} = \exp[-(W_S - \alpha \Delta \psi_S \cdot 2F)/RT] \quad (I-26)$$

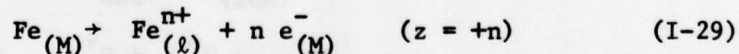
Since the oxygen uptake reaction (expressed by Eq. I-24) takes place n/v times when the rate determining step of the following overall reaction occurs once,



while the rate-determining step occurs v times. This in turn approximates reasonably well the overall reaction for the anodic formation of the passive film on iron,



In the steady state growth region equivalent number of iron ions and oxygen ions are transferred from the metal phase and solution phase into the oxide. The overall chemical reaction for the iron ion transport by interchange is



The probability corresponding to this overall reaction under the assumption that the iron-oxygen pairs change place simultaneously can be expressed as the product of all the individual probabilities involved in the iron ion transfer, expressed as

$$P_{M-\ell} = P_{M-O} \cdot \prod_1^{\ell} P_i, \quad i = 2, 3, \dots, \ell \quad (I-30)$$

The total probability for the interchange of ℓ ion pairs in the oxide thus becomes

$$P_{M-S} = P_{M-O} \cdot P_{O-S} \cdot \prod_{i=2}^{\ell} P_i = P_{M-O} \cdot P_{O-S} \cdot \exp\{(-\ell W_o - \alpha \sum_{i=2}^{\ell} \epsilon_i nF)/RT\}$$

$$= P_{M-O} \cdot P_{O-S} \cdot \exp\{[-(\ell-1)W_o - \alpha \Delta V nF]/RT\} \quad (I-31)$$

A linear increase of the activation energy with the growth of a passive film can easily be seen from this equation. By applying absolute rate theory, the rate of the anodic oxidation can be expressed by either one of the following equations:

$$R = R_{Ox} = (k_B T/h) \cdot (N_S)^{n/\nu} \cdot \exp[-(W_S - \psi_S nF)/(\nu RT/n)] \quad (I-32)$$

$$\text{or } R = R_{Fe} = (k_B T/h) \cdot ({}_o N_{Fe})^{2/\nu} \cdot \exp\{[-2(W_M - W_o + \ell W_o) + nF(\Delta\psi_M + \Delta V)]/\nu RT\} \quad (I-33)$$

where N_S is the total number of surface sites on the oxide for OH^- adsorption and ${}_o N_{Fe}$ the number of iron ions per unit area of oxide at the metal surface, or as the combination of the above.

$$R = (R_{Ox} \cdot R_{Fe})^{1/2}$$

$$= (k_B T/h) (N_S)^{n/2\nu} \cdot ({}_o N_{Fe})^{1/2\nu} \cdot \exp\{-(W_S - \psi_S nF) \cdot n/2\nu RT\} \cdot \exp\{[-2(W_M - W_o + \ell W_o) + nF(\Delta\psi_M + \Delta V)]/2\nu RT\} \quad (I-34)$$

The current density of oxide film growth at steady state can be expressed as

$$i = 2 F \cdot R = K' \cdot \exp\{[n(\Delta\psi_M + \Delta V + \Delta\psi_S)F]/2\nu RT - (\ell W_o/\nu RT)\}$$

$$= K \cdot \exp[(nEF/2\nu RT) - (\ell W_o/\nu RT)] \quad (I-35)$$

with

$$K = (2Fk_B T/h) \cdot (N_S)^{n/\nu} \cdot ({}_o N_{Fe})^{2/\nu} \cdot \exp[(nE_o F/2\nu RT) - (W_M - W_o + 0.5nW_S)/\nu RT] \quad (I-36)$$

Substituting

$$\begin{aligned} \ell &= Q_T / (\text{no. of oxygen atoms/cm}^2\text{-lattice layer}) \cdot 2e \\ \ell &= (L^2 Q_T) / 4e \end{aligned} \quad (\text{I-37})$$

where e is the charge of the electron, L is the lattice distance of oxygen in the elemental face-centered cubic cell of oxygen in the lattice, and taking $\nu = n = 3$, obtained experimentally by Sato et al. (12), the rate of the overall reaction can be expressed as

$$i = K \cdot \exp[(0.5 FE/RT) - (L^2 W_o Q_T / (4neRT))] \quad (\text{I-38})$$

After integration the thickness can be expressed as

$$x = C + D \cdot \log t \quad (\text{I-39})$$

with

$$C = [(12eRT / (L^2 W_o))] \cdot \{\log[L^2 W_o K / (12eRT)] + [0.5FE / (RT)]\} \quad (\text{I-40})$$

and

$$D = 12eRT / (L^2 W_o) \quad (\text{I-41})$$

Their experimental results showed that the $\log i$ vs Q_T plots at constant E were linear indeed except at the very early times in a potential step. They further calculated the activation energy W_o (using the lattice distance of $\gamma\text{-Fe}_2\text{O}_3$) to be equal to 3.5 kcal/mole iron ion exchange at 25°C.

The two logarithmic growth laws (either inverse or direct) developed through two completely different mechanisms (high-field and place-exchange respectively) predict quite similar results: a linear relationship of $\log i$ vs $\log t$; a linear relationship of $\log i$ vs E ; and a linear relationship of Q_T and E . The main difference these two growth laws predicted are the dependence of the $\log i$ vs

charge density (or thickness) and thickness (or charge density) vs $\log t$ for a constant potential. In principle, the experimental measurements of the thickness during the oxide film formation should provide a means for distinguishing between these two mechanisms for logarithmic growth. Unfortunately, the growth rate under the conditions (steady-state or semi-steady-state) of these experiments were too small and the accuracy was insufficient to differentiate between the two growth laws.

Recently, Fehlner and Mott (23) in a quite extensive review of both the experimental evidence (17,24) and the various theories, suggested that modifications of the original Cabrera-Mott high-field theory were necessary. These modifications are: growth by both cation (17) and anion (24) migration; effects at the interfaces controlling the rate of formation of ions; replacement of the Cabrera-Mott constant voltage drop across the film by a constant field in case of anion migration because the anion may move away from surface before the full voltage drop ΔV is built up. Thus to explain logarithmic growth in this case it is proper to apply the activation barrier term as $(W_0 + \mu x - qa\Delta V)$, where μ is a constant related to the structure of the oxide (23). In an oxide which grows by cation migration, the oxygen ions, once incorporated, will not move any further. In oxide which grows by anion movement, they will move, but these workers suggest that this process required thermal activation before an ion can traverse the film. This is supported by the surface potential measurements on the growing films (25).

They further assumed that once the anion is freed from its surface position and enters the oxide, it travels relatively easily through the oxide to metal-oxide interface where full incorporation takes place. While traversing the oxide, the ion may be momentarily trapped again, but this possibility has been ignored, since it is difficult for an anion in the oxide to find a site to be even partially incorporated into the oxide network. If the ions do enter into a site in the oxide lattices, the ion would be trapped for appreciable times because the electron levels for such ions would be deep e.g., near the valence band. Such trapping could lead to much larger potential than those observed. Thus, they concluded that a large activation barrier for anion migration exists at the oxide-solution interface. This barrier is for ion movement from its partially incorporated position into the bulk oxide, but not for the process of ion formation nor for dissociation of the physical adsorbed oxygen species.

A model to account for a constant field across the film during growth is suggested by Fehlner and Mott (23). Anions sit in a partially incorporated position. An activation energy is necessary to move them into the oxide, after which they move quickly across the oxide layer. This activation energy is lowered by the field; the field builds up to the point where the ions can move easily into the oxide. The rate at which they move into the oxide balances the rate at which ions can be partially incorporated. Therefore the field remains constant during film growth, but the potential drop will vary. Un-

der these conditions, it is necessary to assume an Eley-Wilkinson (21) activation energy of the form $W_0 + \mu x$ to explain the logarithmic growth. It has been shown experimentally that surface potential and oxide thickness can increase with increasing oxygen pressure, but only surface potential decreases with decreasing pressure, i.e., the oxygen ions are incorporated, not desorbed. With the Cabrera-Mott model, very little dependence on oxygen pressure is to be expected.

Several mechanisms involving the effects of space charge on growth rate have been proposed (19,27,28). These include:

1. uniform or exponential distribution of non-diffusing (immobile), e.g., pinned defects without charge compensation, determine growth rate by limiting electron flow from the metal to the oxide (27);
2. a space charge field created by the incomplete electrical compensation of migration ions in the growing film affects growth by changing field (19);
3. the space charge causes the bulk concentration of the diffusing species (e.g., interstitial cation or anion vacancies, interstitial anions or cation vacancies) to vary exponentially with film thickness at the reaction interfaces and thus affects the growth rate (28).

The kinetic equations for oxide film growth including space charge effects have been treated both exactly and approximately by Fromhold and his coworkers (29,30) in a series of studies, including one very extensive review article (31). From an analysis of the effects of the space charge resulting from non-diffusing and/or diffusing species on rate of growth, the conclusion was reached

that the space charge affected the rate of growth by modifying the electric field, which in turn increases or decreases the ion migration currents.

Situations do exist for which charged particle transport is effected by a combination of electric fields and concentration gradients, in such a way that the current vs voltage is non-ohmic. In addition, whenever the electric field is particularly large the current no longer varies linearly with the field, even in the absence of a concentration gradient.

Concentration gradients of ions in the oxide are expected for anodic passive films for the case of bulk diffusion-limited currents with chemical reaction at the interfaces. Diffusional migration in these gradients become quite important relative to ion migration in the electric field in the range $10^4 - 10^6$ V/cm. Fields in excess of 10^6 V/cm are rather common, however, during anodic film formation (26). The current transients produced by sudden voltage changes in anodic oxidation should yield the time constant for modification of the ion concentration profile with changes in electric field for large fields ($>10^6$ V/cm). This time constant may be orders of magnitude longer than that for a system without an ionic space charge.

A diffusion equation which is valid in regions of varying carrier concentrations and very large space fields was developed by Fromhold (32). According to Schockley (125) in semiconductor barrier regions, charged particle transport takes place under conditions of large carrier concentration gradients and large position-

dependent space charge electric fields. Non-linear dependence of the diffusion current (17) on electric field is expected whenever the field exceeds values of the order of 10^5 V/cm.

Consider the usual microscopic picture of a discrete lattice in which charged particles with average thermal energy $k_B T$ hop from potential minimum to potential minimum with a phonon frequency ν and a Boltzmann probability of surmounting barrier of height W given by $\exp(-W/k_B T)$. The non-linear dependence of current on electric field will be derived from a simplified one-dimensional model of lattice periodicity. The net current through the k^{th} unit cell is given by

$$J_k = \nu \exp(W/k_B T) \cdot [n_{k-1} \exp(q\epsilon_k a/k_B T) - n_k \exp(-q\epsilon_k a/k_B T)] \quad (\text{I-42})$$

where $2a$ is the average spacing between potential minima, the index $k (= 0, 1, 2, \dots, N)$ labels the potential minima between two points, ϵ_k is the macroscopic electric field at the position of the k^{th} potential maximum, $q\epsilon_k a$ is the amount by which the barrier W is reduced relative to the preceding potential minimum for transport in the forward direction, $-q\epsilon_k a$ is the corresponding increasing amount for particles going in the reverse direction, q is the charge per particle of the mobile species, and n_k is the areal density (number/cm²) of charged particles in the k^{th} potential minimum. The electric field ϵ_k can be obtained from Poisson's equation, which in finite difference notation has the form

$$\Delta\epsilon_k = \epsilon_{k+1} - \epsilon_k = (4\pi/\epsilon)qn_k \quad (\text{I-43})$$

The corresponding electrostatic potential V_k is given by

$$\Delta V_k = V_{k+1} - V_k = -2a\epsilon_{k+1} \quad (I-44)$$

in the steady-state, for which

$$J_k - J_{k+1} = -\Delta J_k = 0 \quad (I-45)$$

The series of difference equations (i-43 to I-45) can be partially summed. The resulting expressions for the particle current J and concentration profile n_k are

$$J = (v/S_N) \cdot \exp(-W/k_B T) \cdot [n_0 - n_N \exp(qV_N/k_B T)] \quad (I-46)$$

$$n_j = [n_0 - (S_j J/v) \cdot \exp(W/k_B T)] \exp(-qV_j/k_B T) \quad (I-47)$$

with $j = 1, 2, \dots, N-1$

$$\text{where } S_j = \sum_{k=1}^j \exp[q(V_{k-1} + V_k)/2k_B T] \quad (I-48)$$

Even though this equation is derived utilizing the microscopic picture of a discrete lattice, it can for most practical purposes be considered to be a valid continuum equation over macroscopic regions since the lattice parameter is then small relative to the dimensions of the region. The bulk concentration $C(x)$ at position $x = 2ka$ is given in this limit simply by $n_k/2a$. The above equations, being exact, satisfy the basic criterion that in the limit of zero current, the Boltzmann distribution must prevail,

$$n_j^{\text{equil}} = n_0 \exp(-qV_j/k_B T) \quad (I-49)$$

This readily follows from above and is exactly equivalent to the requirement that the electrochemical potential $\bar{\mu}$,

$$\bar{\mu} = \mu^0 + k_B T \log C(x) + qV(x) \quad (I-50)$$

have the same value at all the potential minima in the solid, as can

be seen by differentiation of this expression with respect to position. All of the above results can be readily generalized to the case of several carriers by simply including the space charge due to the several species in equation I-42.

Numerical computations illustrate the effects of space charge and a concentration gradient on the steady-state mobile-defect concentration profile and the kinetics of anodic film formation. The position dependence of the concentration of mobile defects producing growth is shown to vary with current density and film thickness. Space charge is shown to have the capability of being a critical factor in retarding the growth rate of the anodic film.

In the case of equilibrium of a given species in an anodic film, the electrochemical potential for the species must be uniform in the film and there will be no particle current of that species through the film. In the absence of an electric field in the film, then the uniformity of the electrochemical potential may require that the concentration be uniform also, in which case there will be no concentration gradient in the film. On the other hand, the presence of a non-zero electric field in the film, the electrostatic potential within the film will be position-dependent. Since the electrochemical potential is made up of contributions due to electrostatic potential and defect concentration, the uniformity of the electrochemical potential then requires in general that the concentration be position dependent. That is, a concentration gradient is to be expected even in equilibrium when the electric field is

non-zero. In addition to illustrating that the equilibrium case involves concentration gradients, the conclusion is reached that concentration gradients and electric fields do not necessarily produce any net current (31).

In the case of changing the electric field in an existing film, the concentration of the diffusion species is constantly depleted at the reaction interface, so that the concentration profile cannot adjust itself arbitrarily to maintain a uniform electrochemical potential. The interfacial reaction plays an important role in determining the boundary concentrations, and these concentrations are more or less fixed independently of the electric field. Thus by changing the electric field, an accompanying change in the species current can be produced. This qualitative argument should not be misconstrued as a statement that the boundary concentrations are entirely independent of the electric field. Instead, it merely represents an argument that the concentration profiles are determined in accordance with conditions imposed by the interfacial reactions as well as by the electric field, and hence the profiles are not entirely free to adjust arbitrarily with the electric field. Thus we arrive at an idealized picture of the metal-oxide-solution system as an asymmetrical system with boundary concentrations of the defect species determined to a large extent by the interfacial reactions.

Under non-equilibrium conditions, the driving force promoting the ion migration is the electrochemical potential gradient ($\partial\bar{\mu}/\partial x$).

Such a gradient exists because of the asymmetry of the metal-oxide-electrolyte system even in the absence of an externally applied electric potential difference across the oxide layer.

The equations for a non-steady-state transient for a model system including concentration gradients and very large electric fields but excluding space charge effects was developed by Butter et al. (30). The fundamental equations are given by the current

$$J_k = \gamma(n_{k-1}\beta - n_k\beta^{-1}), \quad k = 1, 2, \dots, N \quad (\text{I-51})$$

and the continuity expressions are given by

$$\partial n_k / \partial t = J_k - J_{k+1}, \quad k = 1, 2, \dots, N-1 \quad (\text{I-52})$$

The n_k are the carrier concentrations (in terms of areal densities) and t is the time. The parameter $\gamma \equiv \nu \cdot \exp(-W/k_B T)$ is the product of a phonon (hopping) frequency ν and the Boltzmann statistical factor involving the barrier height W and the thermal energy $k_B T$. The parameter $\beta \equiv \exp(ze\epsilon_0 a/k_B T)$ is the corresponding modification produced by the electric field; the distance from the minimum to the maximum of the potential barrier is denoted by a , and ze is the charge of the carrier. For a series of N uniformly-spaced potential barriers, the thickness x of the medium in the diffusing direction would be given by $x = 2aN$. The assumption of fixed carrier concentrations n_0 and n_N in the potential minima located at the interfaces of the medium provides boundary conditions for the difference equations. The transformations $W_k = \beta^{-k} \cdot n_k$ convert the equations I-52 to the form

$$(1/\gamma) \cdot (\partial W_k / \partial t) = W_{k-1} - (\beta + \beta^{-1}) \cdot W_k + W_{k+1} \quad (\text{I-53})$$

This set of (N-1) equations can be Laplace transformed into a corresponding set of algebraic equations which can be solved simultaneously by matrix inversion. The inverse Laplace transform of the result then yields the $W_k(t)$ and thus the $n_k(t)$. The results obtained are as follows:

$$n_k(t) = (2\beta^k/N) \cdot \sum_{j=1}^{N-1} y_j \cdot \sin(jk\pi/N) \cdot \exp(-t/t_j) + (2\beta^k/N) \sum_{j=1}^{N-1} Z_j \cdot \sin(jk\pi/N) \cdot \gamma t_j [1 - \exp(-t/t_j)] \quad (I-54)$$

where

$$Y_j \equiv \sum_{m=1}^{N-1} \beta^m n_m(0) \cdot \sin(jm\pi/N) \quad (I-55)$$

$$Z_j \equiv n_0 \cdot \sin(j\pi/N) + \beta^{-N} \cdot n_N \cdot \sin[j(N-1)\pi/N] \quad (I-56)$$

and

$$t_j \equiv [\gamma(\beta + \beta^{-1} - 2 \cdot \cos(j\pi/N))]^{-1} \quad (I-57)$$

The non-steady-state currents are then given by equation I-54. These results reduce to the corresponding steady-state expressions in the limit $t \rightarrow \infty$, as expected. The first sum in Eq. I-54 can be interpreted as the exponential decay of various spatial Fourier components of an initial carrier profile; the second sum can be interpreted as the corresponding exponential rise toward the final steady-state profile.

The most important result is the time constant for the transient response of the system. The longest time constant is noted to be t_1 . In the limit of low fields, this agrees with the corresponding continuum result, assuming the usual expression $D = 4a^2 v_e^{-W/k_B T}$

for the diffusion coefficient and the Einstein relation $\mu = zeD/k_B T$ for the mobility. On the other hand, in the limit of very large fields (viz., $zeE_0 a/k_B T \gg 1$), the present analysis yields

$$t_1 = (\gamma \cdot \beta)^{-1} = v^{-1} \exp[(W - zeE_0 a/k_B T)] \quad (I-58)$$

In fact, Eq. I-58 shows that the time constants t_j for all relaxation modes become equal to this value in the large-field limit, with the consequence that the profile is forced to relax exponentially. For $W = 1$ eV, $T = 200^\circ\text{C}$, $z = 5$, $a = 3 \text{ \AA}$, and $v = 10^{13} \text{ s}^{-1}$, the value of t_1 is of the order of $6.3 \cdot 10^3$ s (= 2 hours) in zero field but only 20 s with a field of 10^6 V/cm. The corresponding times for $W = 0.25$ eV are $1.6 \cdot 10^{-9}$ s and $5 \cdot 10^{-12}$ s. It can also be noted that from Eq. I-58 there is a large temperature-dependence of the response time. The large span in response times, depending upon the values of the system parameters, is of immediate interest.

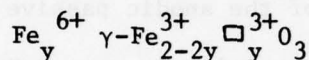
III. Characterization of Passive Film of Iron

A. Chemical Composition and Structure of the Passive Films on Iron

The chemical composition of the passive films on iron in borate buffer (pH 8.4) has been investigated intensively by various workers (33,37,1) using electrochemical and analytical chemical methods, the latter for the iron species in the electrolyte. Nagayama et al. (33) applied different values of constant cathodic current to study the reduction processes of passive films formed at different anodic potentials and found that there were two reduction waves in the charge vs voltage curves during the reduction of the

passive film back to bare iron. Based on these experimental results, they attributed these two reduction waves to two different layers within the passive film of different chemical compositions. Thus the two layer model (the inner layer next to the iron electrode composed of Fe_3O_4 and the outer layer next to the electrolyte composed of Fe_2O_3) or the "Sandwich Model" was proposed for the chemical composition of the passive film on iron. The relative thickness of these layers, which affects the chemical composition of the whole film, depends on the anodic formation potentials. From their extensive anodic oxidation and cathodic reduction studies, they further divided the passive region (Fig. I-1) into regions I and II. In region I, the inner and outer layers grew thicker with increasing anodic potentials, time and ferrous ion concentrations in the solution. In region II, the outer layer kept growing with a much slower rate than its growth rate in region I. It was proposed that excess O^- ions were introduced into the outer layer from the solution interface and further oxidized the trivalent iron to an higher valency state (Fe^{6+} as they proposed) in region II. Consequently, a redistribution of potential within the passive film occurred and caused the inner layer to resume its growth through the migration of iron into the Fe_2O_3 outer layer. These authors further assumed that the ferrous material produced during the first reduction process (assigned to be the reduction of the outer layer) dissolved into solution phase completely and the second reduction, corresponding to the reduction of the inner layer, went completely through the solid-state reduction (i.e.,

no iron loss). The chemical analysis of the ferrous ions in the solution showed that the expected amount of ferrous ions dissolved in the solution was far too low for the observed reduction of the outer layer of Fe_2O_3 . They attributed this discrepancy to the existence of excess of oxygen (or cation vacancies, \square) in the outer layer with charge compensation by Fe^{6+} ions, and the composition of the outer layer proposed to be expressed as



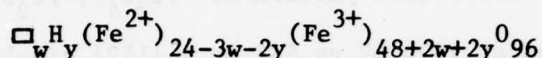
Various techniques, including in situ ellipsometric and radioactive tracer techniques have been combined with the electrochemical methods by Sato et al. (35-38) in a series of investigations. On the bases of the galvanostatic reduction charge vs voltage curves as well as the reduction in optical thickness of the oxide films formed at different anodic potentials, they propose that the reduction of the film takes place in two successive stages. The first stage of reduction involved the solid-state reduction of Fe_2O_3 to lower oxide as well as the reductive dissolution of the film into the solution, and the second stage reduction corresponded to the further reduction of the generated lower oxide during the first reduction stage to metallic iron. There is a significant difference in interpretation with that of Nagayama et al. (33) even though the data are substantially the same. Sato et al. (35,36) suggest that the passive film is a simple layer of Fe_2O_3 instead of the " $\text{Fe}/\text{Fe}_3\text{O}_4/\text{Fe}_2\text{O}_3/\text{solution}$ ". They further reported that the composition of the oxide film could

be represented as $\text{Fe}_2\text{O}_3 \cdot (\text{H}_2\text{O})_{0.39}$ or $\text{Fe}_2\text{O}_3 \cdot (\text{FeOOH})_{1.28}$ by assuming the film be stoichiometric and uniform through the whole film. However, in later publications (37,38) they further discussed the potential distribution of the film based on a non-uniform film model consisting of an inner layer of intrinsic anhydrous ferric oxide and an outer layer of hydrous, semiconducting ferric oxide.

The evidence for the association of protons predominantly with the outer layer of the anodic passive film has been reported by Yolken et al. (39) using tritiated water. Stepping the potential from a steady-state potential to a less anodic potential caused the overall hydrogen content to decrease. This suggested that the transition potential between region I and region II as observed by Nagayama et al. (1) is accompanied by a change in the hydrogen content of the layer. However, they did not make any further attempt to verify in which form the associated protons exist in the $\gamma\text{-Fe}_2\text{O}_3$ outer layer of the anodic passive film.

Bloom and Goldenburg (40) made an extensive review concerning the role water plays in the iron oxides and their transformations and indicated that the incorporated protons in the oxide lattice caused the main structural differences in Fe_2O_3 as the final oxides produced from the oxidation of Fe_3O_4 with or without the presence of water. The oxidation of Fe_3O_4 yielded $\alpha\text{-Fe}_2\text{O}_3$ in the absence of water and yielded $\gamma\text{-Fe}_2\text{O}_3$ in the presence of water. They attributed the transition from Fe_3O_4 to $\gamma\text{-Fe}_2\text{O}_3$ to the incorporation of protons into the lattice, with a minimum amount of about 0.5% water needed for this

transformation process. They further developed a generalized formula for the composition of iron oxides formed in the presence of water. The formula can be expressed as



where w is the number of vacancies, \square , and y is the number of protons. This formula takes into consideration three unit cells of magnetite under the transition process, where each unit contains eight units of Fe_3O_4 . Based on their extensive analysis of the existing literature data for crystallographic iron oxides Bloom et al. (40) concluded that the passive film of iron could not be a simple spinel structure containing vacancies but a modified spinel of the Fe_3O_4 structure in which some of the ferrous iron were replaced by protons and end up as $\gamma-Fe_2O_3$ when all the ferrous iron were completely replaced by protons.

A large number of investigations using different and very elaborate ex situ techniques have been carried out in an attempt to obtain the structural information and to determine the chemical composition of the passive films, e.g., electron diffraction (reflection and transmission) (41-43), soft X-ray spectroscopy (44), M \ddot{u} ssbauer spectroscopy (45,46), ESCA and LEED-Auger spectroscopy (47-49).

The electron diffraction (reflection or transmission) has been applied quite extensively by Cohen et al. (41,42) to study the thin iron oxide films formed in different environments. The pas-

sive film formed on a single crystal of iron exposed to a sufficient concentration of sodium nitrate (an oxidizing inhibitor) solution is epitaxial with the underlying metal and about 20-30 Å, with an electron diffraction pattern of " Fe_3O_4 - γ - Fe_2O_3 ". The anodic passive film formed at +190 mV vs SCE on a [112] single crystal in borate buffer indicated by reflection electron diffraction pattern with an average lattice parameter of $L = 8.37 \pm 0.04$ Å as reported by Nagayama et al. (1). These authors made an attempt to obtain a reflection diffraction pattern for the film of 30 Å obtained at higher passive potential but no clear information was obtained.

A transmission pattern showing the structure of cubic iron oxide was obtained for a film of similar thickness stripped from a polycrystalline specimen by the iodine-methanol method. Sewell et al. (50) have combined reflection high energy electron diffraction (RHEED) and X-ray emission techniques to examine the growth of oxide on (001) iron single crystal. The oxygen uptake, which provides kinetics and composition data, can be measured by the electron-excited X-ray emission from the surface oxygen of the O_k line. The diffraction patterns showed that the mean lattice parameter parallel to the surface varied from 8.18 ± 0.04 Å for low exposures to 8.34 ± 0.06 Å for long exposures. They concluded that the oxide starts out with a structure corresponding to an oxide containing even less iron than γ - Fe_2O_3 and as it thickens (and ages) gradually moves through γ - Fe_2O_3 to Fe_3O_4 . Cohen (42) interpreted the low lattice

parameter (cation vacancies in an essentially $\gamma\text{-Fe}_2\text{O}_3$ structure) is typical of conditions where oxygen incorporation into the oxide is more rapid than iron diffusion and all the oxides tend to "anneal" towards a $\gamma\text{-Fe}_2\text{O}_3 - \text{Fe}_3\text{O}_4$ composition at longer time.

The electron diffraction patterns of $\gamma\text{-Fe}_2\text{O}_3$ and Fe_3O_4 are almost identical except a few additional reflections existing in the diffraction pattern of $\gamma\text{-Fe}_2\text{O}_3$. Foley et al. (43) have attributed the additional reflections in their RHEED studies to the ordered vacancies or ordered incorporated protons for ferrous iron into the spinel-like lattice of Fe_3O_4 as suggested by Bloom et al. (40). From the transmission electron diffraction, Foley et al. (43) further investigated the electron diffraction patterns of the passive films formed at different crystal faces of iron, at different pH values, and at different anodic potentials. For all the crystal faces and all of the pH examined, the results showed that the film was $\gamma\text{-Fe}_2\text{O}_3$ in the passive potential region and Fe_3O_4 in the transpassive potential region. The dissolution rate of the film formed in the pre-passive region, however, was dependent on the pH and crystal face but the structure was also that of the Fe_3O_4 spinel based on the RHEED measurements.

Mössbauer spectroscopy has been applied to investigate the passive film on iron and its closely related bulk iron oxide by many researchers. Simmons et al. (45) reported that the passive film is $\gamma\text{-Fe}_2\text{O}_3$. O'Grady et al. (46), however, reported that the passive film did not resemble the spectra of any known bulk iron oxide, a conclusion reached by their in situ Mössbauer spectroscopic method. They

reported the spectrum was similar to those obtained from amorphous polymeric-type compounds and further suggested that the passive film consists of clusters of iron hydroxyl compounds with di-oxy or di-hydroxy bonding, where iron is octahedral coordinated only (thus eliminating $\gamma\text{-Fe}_2\text{O}_3$ for the passive film, which according to Armstrong et al. (51) has 61% of iron in the octahedral sites and 39% is tetrahedral coordinated). A structural representation of the passive film on iron is proposed by O'Grady et al. (46) as shown in Fig. I-6.

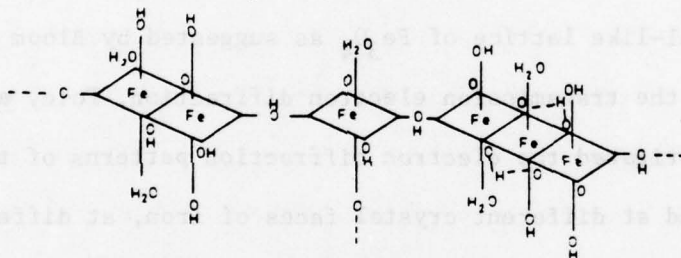


Fig. I-6 A structural representation proposed by O'Grady et al. (46) for the passive film on iron in borate buffer (pH = 6.8) at 300 mV vs NHE.

Recently, many researchers have made attempts to use Auger, LEED and Auger, and ESCA (electron spectroscopy for chemical analysis) to determine the chemical composition of the anodic passive films on iron and alloys. Seo et al. (47) concluded from their Auger with depth profiling techniques (by Argon ion sputtering) that the anodic passive films on iron consisted of two phases and the phases exist as two separate layers. The above conclusion reached by these authors may have been influenced by the artifactual consequences of the partial reduction of the film during argon ion bombardment (119-121).

A monitoring technique (e.g., SIMS) for the sputtering yield of the removed species coupled with these techniques is needed in order to obtain an unambiguous conclusion. Bockris et al. (48) also reported Auger spectra for the passive film formed in the same electrochemical environments with a much improved sample transferring technique from electrochemical system to Auger system. They concluded that the passive film consisted of chemically bonded hydroxyl (or water) species in the film and further supported the polymeric-type structure for the passive film on iron as reported by O'Grady et al. (46).

The discrepancy in the in situ Mössbauer and ex situ electron diffraction results may indicate that the film formed electrochemically undergoes structural changes after removal from the electrolyte. The vacuum environment and likely beam heating in the electron emission can produce substantial changes.

B. General Electronic Properties

Based on the observation that various solution phase redox couples (e.g., $\text{Fe}(\text{CN})_6^{3-}$, $\text{Fe}(\text{CN})_6^{4-}$) exhibited their reversible potentials at open circuit on passivated iron electrodes, Vetter (52) concluded that the passive film on iron is electronically conducting. Franck et al. (53) also measured the current-potential behavior of redox couples on passivated iron but were not able to interpret the experimental results quantitatively. Makrides (54,55) in overpotential measurements for the $\text{Fe}^{2+}/\text{Fe}^{3+}$ couple on passive films of Ni, Fe, and Ti formed in sulphate solution ($\text{Na}_2\text{SO}_4 + \text{H}_2\text{SO}_4$) found that

the Tafel plots were generally obtained with exchange currents between 10^{-7} and 10^{-5} A/cm² and cathodic transfer coefficients were less, particularly with Fe and Ti electrodes. The kinetic parameters of this redox couple on oxide-free platinum electrode are 1.5×10^{-2} A/cm² for the exchange current, 0.58 for the anodic transfer coefficient and 0.45 for the cathodic transfer coefficient.

Makrides suggested that these differences between passive and film-free electrodes are due to the electron transfer process through the superficial film. Makrides explained the small rectification effect on passive films in acid sulfate solutions with the model developed by Vetter (56) and further extended more recently by Nagayama et al. (33); i.e., the passive film on iron consists of an inner approaching Fe₃O₄ and an outer of "γ-Fe₂O₃" with a defect structure of the form Fe⁶⁺Fe_{2-2y}³⁺□_yO₃. Makrides (54,55), however, thought that a film of this sort could not possibly support a fully developed space-charge region similar to that which gives rise to the rectifying properties of semiconductor p-n junctions as postulated by van Geel (57). Thus Makrides concluded that the rectification of passive electrodes is probably caused by the distribution of the total potential drop from metal to solution between the film and the oxide-electrolyte interface. The potential drop across the passive film appears to be a constant fraction of the total applied potential. Therefore, the overpotential for oxidation of Fe²⁺ is $(1-\gamma)\eta$ and the apparent transfer coefficient for the anodic reaction is $(1-\gamma)\beta_r$.

where γ is the fraction of the total potential which is across the film and β_r is the apparent anodic charge transfer coefficient across the double layer. This result is consistent with a model suggested by Vetter (56) for the passive film in which a potential drop of about 0.6 V is across the passive film in the absence of a redox couple. A potential difference across the oxide with no current flowing presupposes a distribution of charge carriers similar to that suggested by Makrides' results. Makrides (54) further applied the concepts of electron transfer between an electrode and a redox couple to explain the exchange current of the $\text{Fe}^{2+}/\text{Fe}^{3+}$ on passive electrodes which is smaller than that on metals by orders of magnitude.

The original concepts of electron transfer between a metal and redox couple in solution developed by Gurney (58) were reformulated and extended to semiconductors by Gerischer (59). The basic postulate of the theory is that a weak electronic interaction occurs between the electrode and the ion (60, 126); electron tunnelling occurs between the metal and ion with the activation energy corresponding to that of a state in which the energy of the system is the same with the electron in the metal (at or near the Fermi level) or in the localized orbitals of the ion. Gerischer (59) used the concept of electron energy states in a redox couple in analogy to the notion of energy levels in a solid. For example, the energy of unoccupied states in the solution phase redox species is defined by the energy change accompanying the introduction of an electron from infinity to the lowest state of an oxidized ion without changing

its solvation structure. The equilibrium distribution of available energy levels can be shown to follow a Fermi distribution where the "Fermi" level of the electrolyte is directly related to the free energy change for the redox reaction.

The current flowing from electrode to electrolyte is given by Gerischer (61)

$$i_c = e \int_{-\infty}^{\infty} v_{el}(E) D_{el}(E) f(E_{F,ROX} - E) D_{ROX}(E) f(E - E_{F,ROX}) dE \quad (I-59)$$

where ROX stands for redox, e is the electronic charge, D_{el} and D_{ROX} the density of states functions for the electrode and electrolyte respectively, and $f(E - E_{F,el})$ and $f(E_{F,ROX} - E)$ the Fermi distribution functions for the two phases, $v_{el}(E)$ is a proportionality factor which contains the frequency with which electrons arrive at the electrode-electrolyte interface and the tunnelling probability through the potential barrier between the two phases.

Exchange current, i_c at $\eta = 0$, can be much smaller for semiconductors than for metal electrodes, since the actual density of states near the Fermi level (where most of the exchange takes place on metal electrodes) may be very small for a semiconductor. Thus a main result of the theory is that the exchange current on semiconductor electrodes may be smaller than that on metals by orders of magnitude.

Makrides (54) viewed the small exchange currents found for the Fe^{2+}/Fe^{3+} couple on passive film electrodes to be a consequence of a decrease of $v_{el}(E)$ due either to a substantial decrease in the tunneling probability or to the semiconducting character of the film.

He found the current to change by only a small factor (<10) when the film thickness changed by a factor of about 2. This rules out a rate limiting process involving electron tunneling through the oxide, but concluded that the small exchange currents found for the $\text{Fe}^{2+}/\text{Fe}^{3+}$ reaction on passive electrode are a consequence of the semiconducting character of the passive films.

Moshetev (62) studied pulse potentiostatically the electronic conduction of the passive film formed in a neutral borate buffer with 0.2 M in NaNO_3 (pH 7.4 adjusted by addition of NaOH) through the $\text{Fe}(\text{CN})_6^{3-}$ and $\text{Fe}(\text{CN})_6^{4-}$ couple reaction on the passive iron electrode. The experimental results showed that the Tafel slopes and reaction orders are similar to those observed on a platinum electrode but with a 10^5 smaller exchange current density. In this study, he further reported a value of about $10^{15} \Omega\text{-cm}$ of the electronic resistivity of the film in the absence of redox couple and 0.66 eV for the apparent activation energy of the electronic conduction processes. He also correlated the small exchange current density with the band gap energy of the passive films on different metals according to the theory of Kuznetsov and Dogonadze (63). Under some circumstances the theoretical treatment of these authors yielded the following expression for the exchange current density on a semiconductor electrode.

$$\log(i_{o,sc}/i_{o,m}) = -E_g/(2k_B T) \quad (\text{I-60})$$

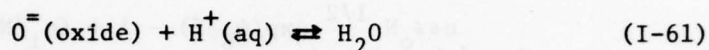
where $i_{o,m}$ is the exchange current density of the same redox couple reaction but on a metal electrode, and E_g is the band gap energy for

electronic conduction.

A tentative mechanism of the conduction process based on the semiconductor concepts of Gerischer is given by Moshetev (62). Similar to bulk $\gamma\text{-Fe}_2\text{O}_3$ the passive film on iron is an n-type semiconductor. In the passive potential region, where the film is subjected to a considerable anodic bias, the energy levels are strongly bent upwards and the electron concentration at the interface is extremely low. Under these circumstances the charge transfer from the conduction band will be negligible and the transfer of holes from the valence band seems more likely. For cathodic polarization with respect to the reversible potential of the redox couple the film is still anodic to its flat band potential; however, the potential barrier is evidently lowered. Consequently, the electrons from the conduction band may now be transferred to surface states created, e.g., by adsorption of $\text{Fe}(\text{CN})_6^{3-}$ acting as an electron acceptor. Whether such specific adsorption occurs on the passive layer is open to question.

A detailed discussion of electron transfer reaction on passive electrodes, especially that on passive iron electrode, has been given by Schultze (64) who used a band bending model to explain redox couple behavior on passive iron as well as the impedance characteristics of the passive film. In addition to the common variables involved in electron transfer on metal electrodes, Schultze considered the thickness (d), stoichiometry, and dielectric constant of the film, and the solution pH. The latter as well as electrode

potential strongly influence the band structure of the passive film, which increases linearly with the electrode potential if the potential drop in the Helmholtz layer is constant. This condition can be fulfilled if the following reaction



is in equilibrium. With increasing solution pH, the flat band potential E_{FB} of the film decreases by 60 mV/unit pH. Consequently, the band bending $E - E_{FB}$ increases correspondingly for a given electrode potential.

On the bases of theory with experiment Schultze (64) concluded that the electronic conduction process of passive iron electrode shifts from a conduction band participation mechanism at low anodic bias potential to a valence band participation mechanism at higher anodic potentials. A valence band participation should be possible if the band gap energy, E_g , of the passive film is relatively small. Under such circumstances large band bending, which can be achieved by high anodic bias and high pH values, results in the depletion of donors and creation of holes in the valence band.

The capacity of passivated iron electrode including the dependence on the oxide layer thickness and the electrode potential E in 1 N NaNO_3 solution (pH 8.4 adjusted by borate) was measured by Stimming et al. (65) using the potentiostatic pulse method. The experimental results showed three characteristic regions: with increasing potential, C decreases in the first region by a factor of 2; in the second region it stays constant; and in the third region

C increases again.

The authors discussed the capacity data according to Bohnenkamp and Engell (66), who expressed the capacity of an n-type semiconductor as

$$C = \left(\frac{e \epsilon \epsilon_0 N}{2f} \right)^{1/2} \left(\frac{\exp(\psi_B/f) - 1 + (n_i/N)^2 \cdot 2 \sinh(\psi_B/f)}{\{\exp(\psi_B/f) - 1 - (\psi_B/f) + (n_i/N)^2 [\cosh(\psi_B/f) - 1]\}^{1/2}} \right) \quad (I-62)$$

where e is the electron charge, ϵ and ϵ_0 the dielectric constant of the oxide layer and the vacuum respectively, N the donor concentration (cm^{-3}), $n_i = (Np_0)^{1/2}$, $f = k_B T/e$, and $\psi_B = \psi_x - \psi_i$ is the difference between the electric potential of the oxide surface and the inner (bulk) oxide. On the basis of this equation, Stimming and Schultze (65) explained the decrease of $C(E)$ of the passive iron in the first region as due to the exhaustion of donors. The second region with constant capacity is explained as due to an exhausted oxide of fixed thickness corresponding to the thickness of the anodic films minus the Fe II - Fe III layer immediately adjacent to the iron metal. The third region with increasing capacity is proposed to be due to the participation of the valence band. For low values of ψ_B in Eq. I-62, the terms involving $(n_i/N)^2$ can be neglected because $N \gg n_i$. The term $\exp(\psi_B/f)$ can also be neglected at sufficient high anodic potential, where band bending exceeds 0.1 V (i.e., $\psi_B/f < -4$), Eq. I-62 can be approximated as the Schottky-Mott equation (I-63)

$$1/C^2 = (2/e \epsilon \epsilon_0 N) (E - E_{FB} - f) \quad (I-63)$$

where ψ_B is replaced by the potential difference $E - E_{FB}$ which is justified for a constant potential drop ψ_H in the Helmholtz layer.

The application of Eq. I-63 includes the following assumptions:

1. the donor concentration must be constant within the whole space charge region;
2. the dielectric constant must be constant;
3. the space charge layer capacity C_{SC} must be small in comparison with the Helmholtz layer capacity C_H , which is about $20 \mu F/cm^2$.

As pointed out by Stimming and Schultze (65) for the passive layers on iron electrodes, donors (Fe^{2+} -ions) are mobile in the layer and therefore, N need not be constant if the continuous model of the donor profiles as suggested by Wagner (15) is operative. The second assumption might also not be valid because of the strong interdependence of the dielectric constant of the iron oxides on Fe II concentration as reported by Jantzen (62). He reported ϵ equal to 10 for $\gamma-Fe_2O_3$ and 250 for Fe_3O_4 . Assumption 3 does not influence the Schottky-Mott slope but the apparent value of E_{FB} only. When C_H is not large compared to the space charge capacitance, the potential intercept in Eq. I-63 has been shown by Gerischer et al. (67) and de Gryse et al. (68) to

$$E = e\epsilon \cdot N(8\pi C_H^2) + E_{FB} - f \quad (I-64)$$

provided that C_H is independent of E .

The Schottky-Mott plot in the potential region $0.0 V < E < 0.5 V$ showed good linear behavior. For $x = 27 \text{ \AA}$ the donor concentration N , calculated from the slope by using $\epsilon = 12$ as the dielectric con-

stant of the oxide layer is $1.5 \cdot 10^{20} \text{ cm}^{-3}$ which is equivalent to having a concentration of 0.75% Fe-ions (donors) in the layer (percentage with respect to the total concentration of iron ions). The corresponding Debye length calculated according to the following equation

$$d_{sc} = [f\epsilon / (2\pi dN)]^{1/2} \quad (\text{I-65})$$

is about 5 Å. Polarization-time dependence data showed that the slope of the $1/C^2$ vs E lines increases with increasing time of polarization (t_p), which indicated that the donor concentration N, decreased with polarization time. The authors explained this as due to crystallization and having less dislocations for the thicker and aged films.

The extrapolation of the Schottky-Mott lines to $1/C^2 = 0$ yields a potential E^0 which, in turn, can be used to calculate the flat band potential, E_{FB} , of the film based on the following equation

$$E^0 = E_{FB} + f - \epsilon Ne / (8\pi C_H^2) \quad (\text{I-66})$$

using $C_H = 20 \mu\text{F}/\text{cm}^2$ and the donor concentration, $N = 1.5 \cdot 10^{20} \text{ cm}^{-3}$ for 27 Å film, the flat band potential is located at -70 mV vs SHE for this specific film.

The constant capacity region between 0.5 V and 1.0 V can be interpreted similar to those of Engell and Ilschner (69) and Moshetev (70). With increasing E, the thickness of the space charge layer increases until all donors in the oxide layers are exhausted except possibly for the Fe II - Fe III layer immediately adjacent to the iron. The capacity then decreases to a limiting value which can

be calculated from a simple condenser model

$$1/C = 1/C_{\text{ox}} + 1/C_{\text{H}} = d/(\epsilon\epsilon_0) + d_{\text{H}}/(\epsilon_{\text{H}}\epsilon_0) \approx d/(\epsilon\epsilon_0) \quad (\text{I-67})$$

The final increase of C in the region $E > 1.0$ V can be explained by using Eq. I-62. The terms involving $(n_1/N)^2$ can exceed all the other terms because of an increasing hole concentration in the valence band yielding a dominating space charge concentration at the surface. Equation I-62 thus can be approximated as

$$C = (\epsilon\epsilon_0 \cdot n_1^2 / fN)^{1/2} \exp(-\psi_B / 2f) \quad (\text{I-68})$$

or

$$b \log C = a + E \quad (\text{I-69})$$

with $b = 120$ mV/decade.

At potentials where the upper valence band edge reaches the Fermi level, the degeneracy at the surface might occur. The capacity of a semiconductor electrode for the degeneracy case has been treated by Dewald (71) as

$$C_{\text{VB}} = [(10/3\pi)^{1/2} (\epsilon\epsilon_0 / f) \cdot (2m^*k_{\text{B}}T/h^2)^{3/2} [(E_{\text{V}}^0 - E_{\text{F}}) / k_{\text{B}}T]^{1/4}] \quad (\text{I-70})$$

where m^* is the effective mass of the electron and E_{V}^0 is the energy of the valence band of the surface. Using Eq. I-70, the experimental capacity data with Helmholtz capacity correction can be fitted well with the calculated capacity values for 27 Å film when $E \geq 1.1$ V, i.e., the valence band contribution starts around 1.1 V, which corresponds to a band bending of 1.2 eV.

At $E > 1.3$ V Stimming and Schultze (65) found the capacity to decrease again. Oxygen evolution occurs in this potential region

and holes may be exhausted by electrons from oxygen ions or the p carriers may fall into surface traps. Thus the capacity may decrease again to that of a simple condenser.

Stimming and Schultze (65) further constructed a band structure of the passive film on iron, combining results of their data analysis on thickness and potential-dependent capacity measurements, and known properties of bulk iron oxides. According to their construction, the Fermi potential of the passive film on iron corresponds to 50% octahedral sites occupied by Fe^{2+} -ions in bulk Fe_3O_4 structure, and the donors (Fe^{2+} -ions) terms of the oxide Fe_3O_4 must be at the height of the Fermi potential in the metal. Following Matejcek (62), they located the conduction band edge at about 0.37 eV above the Fermi potential. The valence band edge was located at 1.2 eV below the Fermi potential, as a result of the calculated values of C_{VB} relative to their experimental values of capacity measurements. A band gap energy E_g of 1.6 eV, which is higher than that for the bulk iron oxide ($E_g = 1.0$ eV for $\gamma\text{-Fe}_2\text{O}_3$) is thus obtained.

The band structure of passive films on iron under different anodic bias potential conditions is also given by these authors, as shown in Fig. I-7: (a) the passive film is under low anodic bias potential and the outer layer is charged partially (Schottky-Mott region). The electrode charge q_m equals the space charge density within the outer oxide layer $q_{\text{ox}, \text{Fe}_2\text{O}_3}$. (b) The passive film under moderate anodic bias, the outer layer is exhausted and $q_{\text{ox}, \text{Fe}_2\text{O}_3} =$

N_{ex} = constant. Further increase of potential causes a partial charge on the inner Fe_3O_4 layer, $q_{ox, Fe_3O_4} = q_m - N_{ex}$ and the outer $\gamma-Fe_2O_3$ layer behaves as an insulator. (c) The passive film is under very high anodic bias, e.g., $E = 1.3$ V. The band bending is strong enough to charge the valence band. The space charge in the oxide layer increases as $q_{ox, Fe_2O_3} = N_{ex} + q_{VB}$.

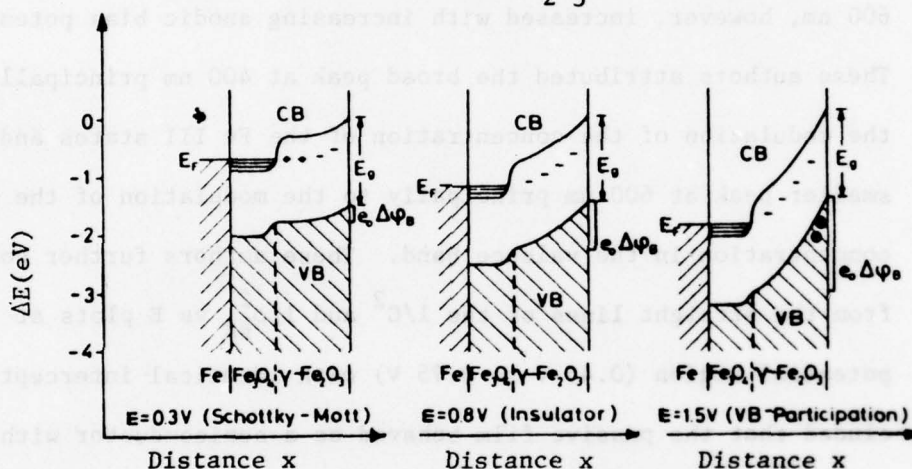


Fig. I-7. A band structure of passive films on iron under different anodic bias potentials proposed by Stimming et al. (65): (a) low anodic bias; (b) moderate anodic bias; (c) very high anodic bias.

Wheeler et al. (72) have reported on a wide frequency range (10 Hz to 1 kHz) ac impedance and ac electroreflectance studies using a lock-in amplifier technique. This technique measured both the in-phase and out-of-phase components of the reflected light and current. The corresponding components were also measured for the ac potential using special IR correction technique (fast-rise potentiostat specially designed by B.D. Cahan). The amplitude of the ac electroreflectance coefficient, $\rho_{ER} [= (1/R)(\partial R/\partial E)]$ at a modulation

frequency of 500 Hz for a film grown at 1.55 V for an hour in borate buffer solution (pH 9.6) indicated that a broad maximum occurred at 400 nm for a dc bias potential at 0.45 V and a comparatively much smaller peak occurred at about 600 nm for a dc bias potential at 1.15 V. The broad maximum at 400 nm decreased at more anodic bias potentials until at 1.15 V it was quite low. The small peak at 600 nm, however, increased with increasing anodic bias potential. These authors attributed the broad peak at 400 nm principally to the modulation of the concentration of the Fe III states and the smaller peak at 600 nm principally to the modulation of the hole concentration in the valence band. These authors further concluded from the straight lines of the $1/C^2$ and $1/\rho_{ER}^2$ vs E plots at lower potential region (0.45 V to 0.75 V) with identical intercept concluded that the passive film behaved as a semiconductor with flat band potential located at 0.39 - 0.35 V. The effective carrier concentration was $2.5 \times 10^{20} \text{ cm}^{-3}$ (using 12 for dielectric constant) for a 40 Å film as compared with the Stimming et al. (65) value of $1.5 \times 10^{20} \text{ cm}^{-3}$ for a 27 Å film. Such a high carrier concentration leads to substantial complications in the use of the Mott-Schottky treatment. The interpretation of the impedance characteristics in terms of simple n and p electronic carriers is a gross oversimplification for such highly defect structures (e.g., see Chapters III and IV).

C. In situ Ellipsometric Studies of Passive Films on Iron

In 1933, Tronstad introduced the method of Drude to examine thin invisible films on reflecting surfaces. After the further advancement in the theoretical background of this method utilizing the original equations of Drude by Winterbottom as well as others (73), a technique called in situ ellipsometry has been applied to study the anodic passive films on metals. This technique concerns the measurements of change in the state of polarization of light upon reflection from a surface. These measurements can be used to calculate the optical constants (n-ik), (here n is the index of refraction and k is the extinction coefficient of the simple reflecting surface. With additional measurements on that reflecting surface, the thickness as well as the refractive index for a thin film produced can be obtained.

For reflection, the incident monochromatic light at a metal surface can be resolved into two components; one along the plane of incidence and the other normal to the plane of incidence (i.e., the plane of the reflecting surface). The process of reflection introduces a phase difference Δ and an attenuation factor, $\tan \Psi$, of their amplitudes between these two components. Thus, the ratio of the reflection coefficient for light polarized in the plane of incidence to that for light polarized in the plane of the surface is given by

$$\hat{r}^P / \hat{r}^S = \tan \Psi \cdot e^{i\Delta} \quad (I-71)$$

where p and s denote the polarization of light parallel and perpen-

pendicular to the plane of incidence; Δ and Ψ are functions of the optical constants of the reflecting surface, the wavelength of light used, the angle of incidence, and, for a film covered surface, the thickness and refractive index of the film. The ellipsometric technique involving only these two parameters Δ , and Ψ corresponds to the conventional two-parameter (2-P) method. One of the principal problems associated with the use of the 2-P method is that only two parameters (Δ, Ψ) were measured but there are three unknowns (n , k , and thickness) to be determined. Thus the 2-P method is generally not sufficient to evaluate the complex refractive index and thickness of an absorbing film formed on an absorbing substrate. With the realization that the relative reflectivity R , upon reflection from a reflecting surface with and without the presence of a thin film is also a characteristic of the system, the corresponding three-parameter (3-P) ellipsometric technique including the measurements of the third additional parameter was developed (74-76).

Kruger and Calvert (22) studied the growth in the passive films by using a combination of the conventional 2-P in situ ellipsometric and a potentiostatic method at three different pH values (7.4, 8.4, and 9.1) in mixtures of $\text{Na}_2\text{B}_4\text{O}_7$ and H_3BO_3 solutions with monochromatic light of wavelength 5461 Å. The coulombic thickness was compared with the optical thickness calculated using a complex refractive index of $2.5 - 0.3 i$ (found for the oxide formed on iron in a gaseous oxidation study of Winterbottom) and $3.55 - 3.66 i$ for the refractive index of iron substrate at this wavelength. They

were able to identify three stages in the growth process:

1. first stage, growth limited by some anion species diffusing through the solution, a conclusion reached by the strong solution pH dependence of the growth rate, with the thickness proportional to the square root of time;
2. the second stage, the onset of the limitation of growth by the film but difficult to characterize by any rate law because it is a combination of two or more processes;
3. third stage, a growth described equally well by a direct logarithmic or inverse logarithmic rate law.

They further concluded that an inverse logarithmic rate of growth implied that the outer layer of the passive film was a poor electronic conductor in order that a high-field could be built up to assist the movements of cations through the film to the solution interface where they are oxidized. The pH dependence of the thickness of passive film grown potentiostatically showed that (dE/dx) is greater at the lowest pH (above $(E_a)_2$ of the i - E curve (Fig. I-1)) (1). These data were interpreted phenomenologically, i.e., that the barrier that ions must surmount for the film to grow at pH 7.4 is higher than that existing in film formed in the pH 9.1 solution.

Ord and DeSmet (77) applied a combination of conventional 2-P in situ ellipsometric and galvanostatic oxidation, coupled with an open-circuit transient technique to evaluate capacitance data, to study the passivation phenomena on iron in borate buffer (pH = 8.4) with monochromatic light of wavelength 5461 Å. The complex refractive index for a film of 2.6-0.4i on a substrate of index 3.50-3.66i could be used to fit their overall optical data. The ΔP (the change

during the oxide growth of the polarizer setting from film-free state), E_0 (the zero overpotential of the iron electrode), and $1/C$ (C is the capacitance of oxide film) vs the passivating potential (the potential on the galvanostatic oxidation transient at which the circuit is opened) plots indicated that a layer is still present optically by ΔP when the electrical limiting layer (characterized by E_0 and $1/C$ only) diminished. They further concluded that the electrically limiting layer is not the only layer present on the surface. A two-layer model in which the electrode surface is covered by a thin conducting layer of constant thickness (about 15 Å) and which is in turn covered by a electrically limiting layer of variable thickness up to 25 Å is proposed.

Ho and Ord (78) further investigated this system by either a combination of galvanostatic or potential sweep with the in situ 2-P ellipsometric technique at a monochromatic light of wavelength 6328 Å, (Helium-neon gas laser) to study the oxidation and reduction of the passive films. They concluded that the passive film on iron consists of two layers; inner layer of Fe_3O_4 and outer layer of Fe_2O_3 . They strongly emphasized that the outer layer of the passive film differed from $FeOOH$ (as determined in another study using $FeOOH$ films deposited anodically on iron electrode by the oxidation of ferrous ions contained in the electrolyte) (79). The simultaneous growth of the inner layer and outer layer requires that oxygen incorporated in the inner layer must be transported through the outer layer, and iron incorporated in the outer layer must be transported

through the inner layer. They concluded that the passive-state overpotential must appear across both the outer layer and the inner layer formed in the passive state with a major portion across the inner layer. The refractive index calculated for iron at 6328 Å is 3.44 - 3.97 i and 2.5 - 0.45i was chosen for the inner layer of Fe_3O_4 for purposes of calculation of the outer layer, but the outer layer index calculation was not overly sensitive to the value chosen for the inner layer.

Bockris and his coworkers (80-82) have used transient ellipsometry extensively, measuring light intensity during the transients in combination with other electrochemical methods to investigate the formation and reduction of the passive film on iron in borate buffer (pH 8.4) using 5461 Å light. They concluded from their studies that the oxide growth initially involved a phase oxide, probably $\text{Fe}(\text{OH})_2$, followed by a mechanism involving place-exchange of Fe and O. The phase oxide thickness at the current-potential peak is about 1 to 2 monolayers. At the current-potential peak, $\text{Fe}(\text{OH})_2$ is converted to $\gamma\text{-Fe}_2\text{O}_3$. The conversion continues without significant change in oxide thickness for 0.2-0.4 V more positive to the peak. The cause of the passivation is the sealing off of the Fe surface by the phase-oxide, $\text{Fe}(\text{OH})_2$. The "passive layer" which grows at higher anodic potentials is $\gamma\text{-Fe}_2\text{O}_3$. The galvanostatic transients during reduction for the oxide films formed at the passive region are in two sections which correspond to a charge of 1 to 2 ratio in the charge consumed in the reduction process. At slightly anodic to

the peak of the i - E curve (Fig. I-1) region coulometry allowed evaluation of the ratio $\text{Fe}^{2+}:\text{Fe}^{3+}$ in the film. Bockris et al. (82) further concluded that a transformation of a ferrous to a ferric oxide begins at the i - E peak and is complete at about 500 mV anodic to the peak. Such transformations are controlled by potential and not by field. Film thickness, index of refraction, and extinction coefficient showed indication that they were functions of electrode potential (82). Application of coulometric thickness measurements to allow solution of the ellipsometric equations shows a growth of ferrous oxide to the peak; a region during which the oxide is transformed to a ferric oxide and then linear growth with potential to about 40 Å.

Sato and his coworkers (36-38) in a series of studies on the passive film on iron by combining techniques of ellipsometry ($\lambda = 5461 \text{ Å}$), electrochemical methods, radiotracer analysis, and chemical analysis of the ferrous iron in solution concluded that the passive film can be demonstrated to be a single uniform layer of $\gamma\text{-Fe}_2\text{O}_3 \cdot (\text{H}_2\text{O})_{0.4}$ (36) or as two uniform layers with an outer hydrous ferric oxide layer and an inner anhydrous ferric oxide layer, over which the major potential drop (or overpotential) occurs (38). Their optical thickness (calculated from the change of Δ and Ψ during the cathodic reduction of the film using the experimentally determined values of refractive indexes: 1.335 for solution; 2.55-0.35i for the film and 3.18-3.85i for iron at 5451 Å) correlated linearly with the potential E in the potential range from -0.30 V to 0.90 V

vs SHE with an equation expressed by

$$x = 9 + 24(E - E_0) \text{ \AA} \quad (\text{I-72})$$

where E_0 is the equilibrium potential of $\gamma\text{-Fe}_2\text{O}_3$ oxide formation on iron. Iron in the film is all ferric and oxygen is in excess of stoichiometric ferric oxide; hence hydrogen may be associated with excess oxygen to form bound water. Bound water in the oxide may serve as a donor of electrons as well as protons. Protons will diffuse out of the space charge layer leaving excess oxygen ions, which pull iron ions from the metal. At very high anodic potentials, most of the space charge will consist of excess oxygen ions because of depletion of free electrons.

With the idea of using in situ ellipsometric technique as a spectroscopic tool to obtain the optical spectra of a thin film on a reflecting surface as done by Bartell and Churchill (83), McBee et al. (84) made the first attempt to make in situ ellipsometric measurements over a range of wavelengths (390-610 nm) on the anodic passive film on iron in borate buffer (pH 8.4). Although the scatter of their wavelength dependence data interfered with the effective use of the technique, they pointed out the danger associated with the optical constant of a film formed at a specific condition at only one single wavelength as a basis for reaching an important conclusion about the properties of a film.

CHAPTER II

EXPERIMENTAL

I. Electrode and Cell

The passivation of ultrapure iron^d and the reduction of the passive films in an equal volume mixture of 0.15 M H_3BO_3 and 0.075 M $Na_2B_4O_7$ buffer solution (pH 8.4)^e has been the primary subject of this study.

An iron electrode with an optical quality surface was made by cutting a disk 2.863 cm in diameter and 0.318 cm high from the sample. The back and sides of the disk were masked off with microshield stop-off lacquer (product of Michigan Chrome and Chemical Company) and then it was press-fitted into a Teflon sample holder as shown in Fig. II-1. The electrode was then mechanically polished with 6 μ and 1 μ diamond paste sequentially and finally with 0.05 μ alumina paste followed by ultrasonic cleaning in spectra pure methanol.

After microscopic examination for optical quality, the elec-

^dThe iron with 99.998% purity (see Table I) was obtained from Battelle Columbus Laboratories as a material grant through the courtesy of American Iron and Steel Institute. It was prepared from a spectrographic sponge, loosely pressed, hydrogen purified, and finally consolidated into an ingot by a floating-zone-melting technique.

^eThe borate buffer was prepared from equal volume mixture of 0.15 M H_3BO_3 (contains 9.276 g/liter solution) and 0.075 M $Na_2B_4O_7$ (contains 7.548 g/liter solution). Some confusion exists over the equivalent weight of H_3BO_3 which equals the molecular weight since $H_3BO_3 + H_2O \rightarrow B(OH)_4^- + H^+$.

TABLE I: Analysis of Pure Iron
(ppm by weight)

Metallic Impurities Often Detected
with the Mass Spectrometer

(Impurities not detected are denoted
N together with the estimated
detection limits)

Aluminum	2.00	Nickel	N<0.5
Arsenic	N<0.05	Phosphorus	0.05
Boron	0.005	Potassium	0.10
Calcium	0.3	Silicon	N<0.5
Chromium	1.0	Sodium	2.0
Cobalt	1.0	Tantalum	2.0
Columbium	0.05	Tin	0.1
Copper	10.0	Titanium	0.3
Germanium	N<0.3	Tungsten	0.1
Magnesium	0.1	Vanadium	N<0.03
Manganese	0.2	Zinc	N<0.2
Molybdenum	0.1	Zirconium	N<0.1

Total detected metallic impurities 21
(Includes values marked < except ger-
manium, and values underlined below
plus and arbitrary 2 ppm aluminum.)

Nonmetallic
Impurities

Oxygen	4.0
Nitrogen	1.0
Hydrogen	0.4
Carbon	
Combustion-	
Conductometric	5.0
Sulfur	1.0
Mass Spectrometer	
Total nonmetallic impurities	<u>11</u>

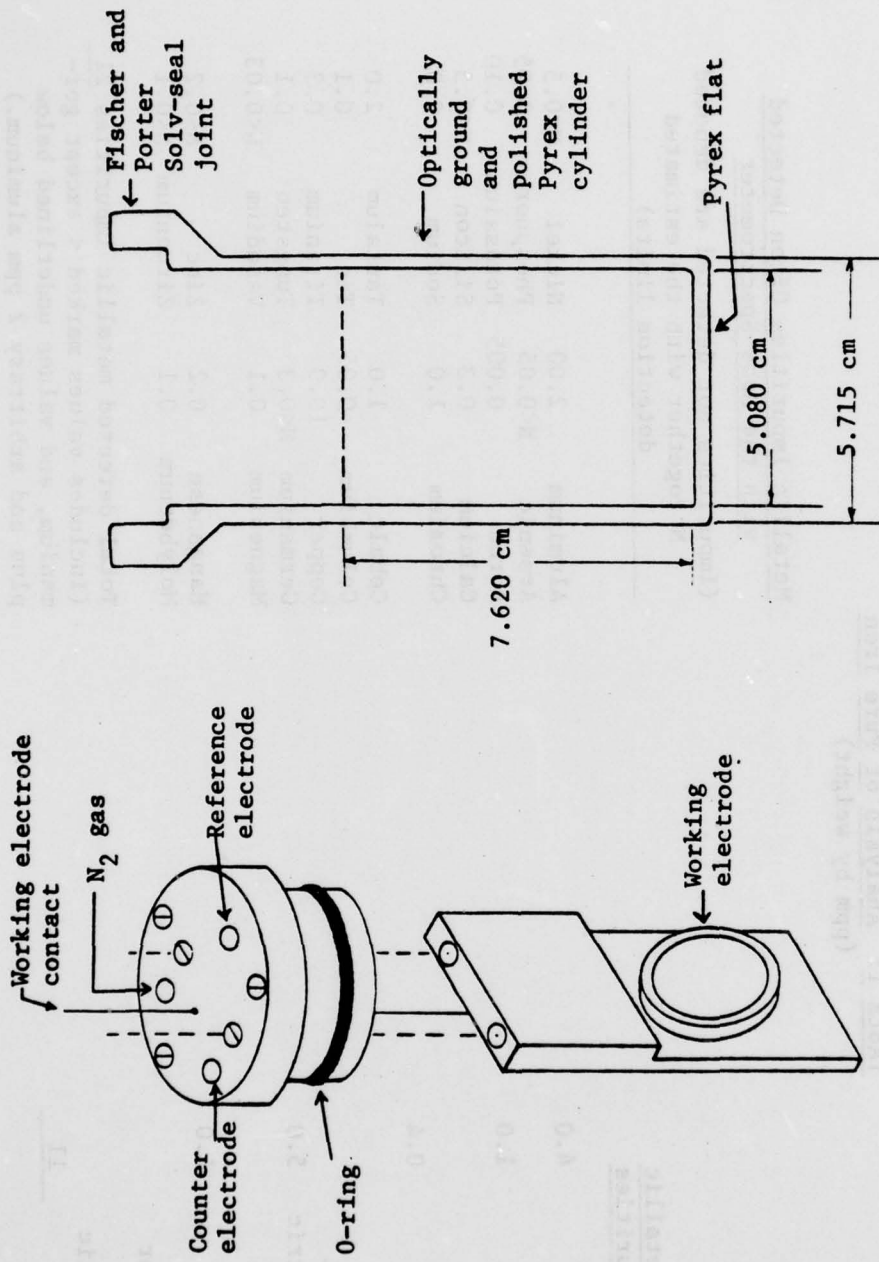


Fig. II-1. Teflon cell top and electrode.

Fig. II-2. Cylindrical optical cell (85).

trode was inserted into the optical cylindrical cell (see Fig. II-2) (85) with a α -Pd-H bead as reference electrode and Ag-Pd tubing supplied from the inside with H_2 as counter electrode. The reference electrode can be positioned within a few mm of the working electrode surface. The counter electrode was located behind the working electrode because of optical considerations (see Fig. II-3).

The solution was deaerated with purified nitrogen for more than 12 hours before transferring to the cell. The N_2 (derived from liquid N_2) was purified by passing through hot copper turnings followed by molecular sieves. The system was periodically regenerated with H_2 .

The electrode was cathodically reduced at -0.25 V vs RHE as soon as the electrode was transferred into the cell. Under these conditions we have shown that the electrode surface is film-free (see Chapter III).

II. Optical Alignment

The ellipsometric system used in this study was a Rudolph Automatic Ellipsometer with or without quarter-wave plate. The block diagram of the optical components, the electronics involved, the electrochemical system, and the PDP-11/45 minicomputer with its peripherals are shown in Fig. II-4.

A very reliable and efficient alignment procedure has been followed prior to all the experimental measurements. With the aid of a properly aligned autocollimator-telescope, located before the photomultiplier, the rest of the optical components including the

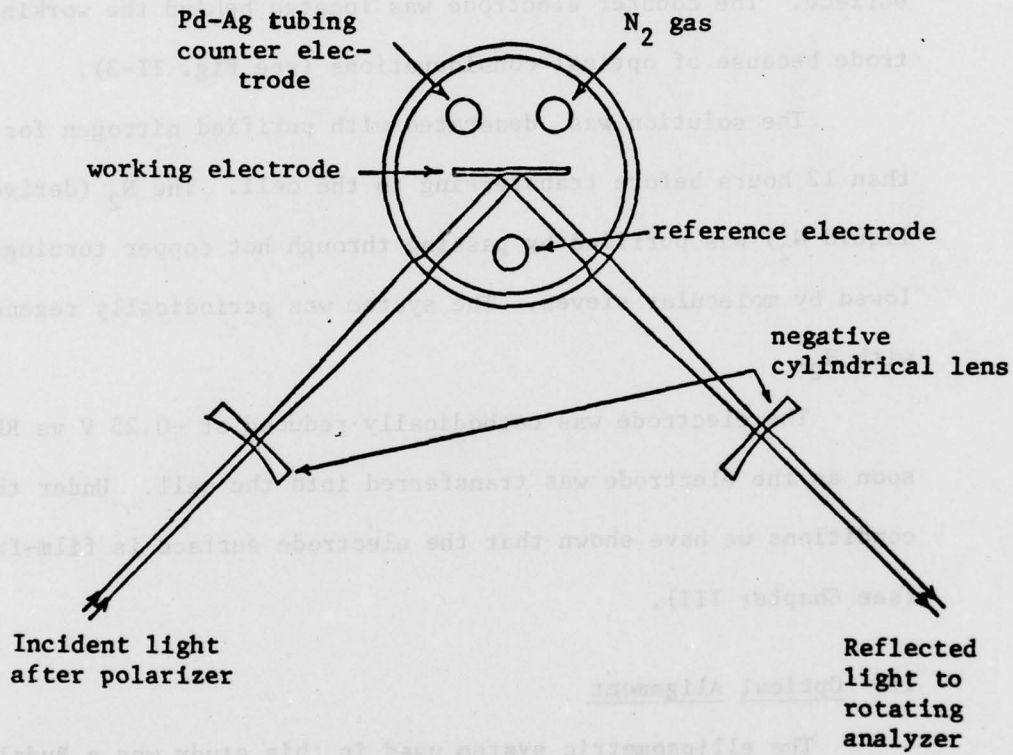


Fig. II-3. Configuration of cylindrical cell for optical and electrochemical studies. Top view (85).

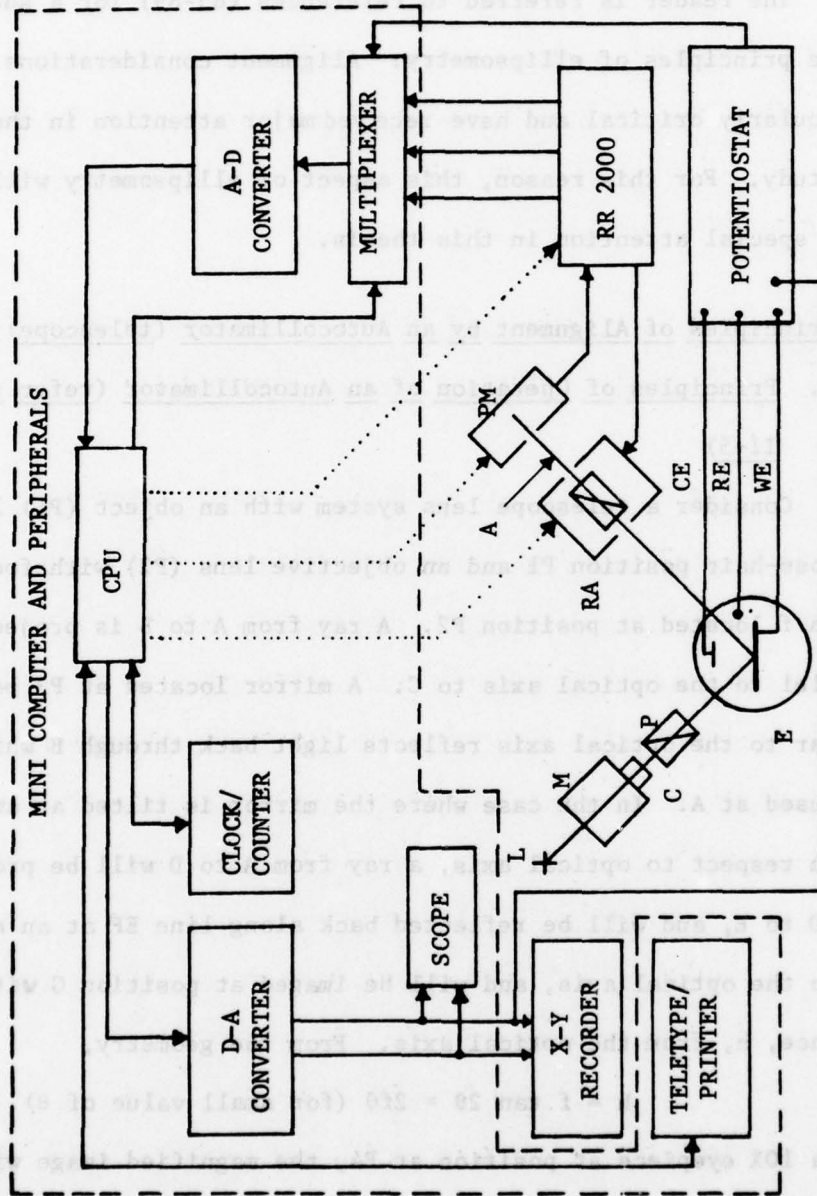


Fig. II-4. Block diagram of ellipsometer and electrochemical instrumentation. L - Tungston halogen or xenon lamp. M - J-Y (H10) monochromator with drive. P - Polarizer, RA - Rotating analyzer, PM - Photo-multiplier, Potentiostat - specially designed by B.D. Cahan, RR 2000 - Rudolph automatic ellipsometer electronics, Minicomputer - PDP-11/45, C - Collimator, E - Electrochemical cell, A - position of autocollimator-telescope during alignment.

cylindrical cell with two negative cylindrical compensating lenses (for minimizing spherical aberration) can be properly aligned.

The reader is referred to references (85-89) for a summary of the principles of ellipsometry. Alignment considerations are particularly critical and have received major attention in the present study. For this reason, this aspect of ellipsometry will receive special attention in this thesis.

A. Principles of Alignment by an Autocollimator (telescope)

1. Principles of Operation of an Autocollimator (refer to Fig. II-5)

Consider a telescope lens system with an object (P1) located at cross-hair position P1 and an objective lens (P2) with focal length f located at position P2. A ray from A to B is projected parallel to the optical axis to C. A mirror located at P3 perpendicular to the optical axis reflects light back through B which is refocused at A. In the case where the mirror is tilted at an angle θ with respect to optical axis, a ray from A to D will be projected from D to E, and will be reflected back along line EF at an angle 2θ to the optical axis, and will be imaged at position G with a distance, h , from the optical axis. From the geometry,

$$h = f \tan 2\theta \approx 2f\theta \text{ (for small value of } \theta \text{)} \quad (\text{II-1})$$

With a 10X eyepiece at position at P4, the magnified image will be located at h' ($= 10h$) from the optical axis. Thus θ is expressed as

$$\theta = (h'/20f) \cdot 180^\circ \quad (\text{II-2})$$

For a focal length $f = 190^f$ mm, a tilt angle $\theta = 0.01^\circ$ will give a deviation h' of about 0.7 mm from the optical axis. This value is independent of the distance of the mirror from the objective lens since a ray from A to H projected to I is reflected back along the same ray EF and is also imaged at G. If a separate illuminated graticle (see Fig. II-6) is used with a half-silvered beam splitter such that its distance d from the beam splitter is equal to that of the cross-hair, the same geometric considerations apply. The graticle shown in Fig. II-6 has two concentric circles of radii of 2.5 mm and 0.5 mm with a linewidth of 0.04 mm. These numbers correspond to angle deviations of 0.375° , 0.075° , and 0.006° respectively. Since it is relatively easy to align the system within one linewidth, an angular resolution better than 0.0001° is attainable. The accuracy of this system has been checked using the angle adjustment vernier of the sample mount (see following section). This vernier is calibrated at $0.02^\circ/0.001$ "of deflection by the micrometer which is readable to 0.0001".

If the objective lens is displaced to the left (see Fig. II-5), a near object on the optical axis can be focused at the cross-hair. Thus the autocollimator-telescope can be used to define a line in space and all angles relative to it.

^f
The actual value for the objective achromat used in our instrument.

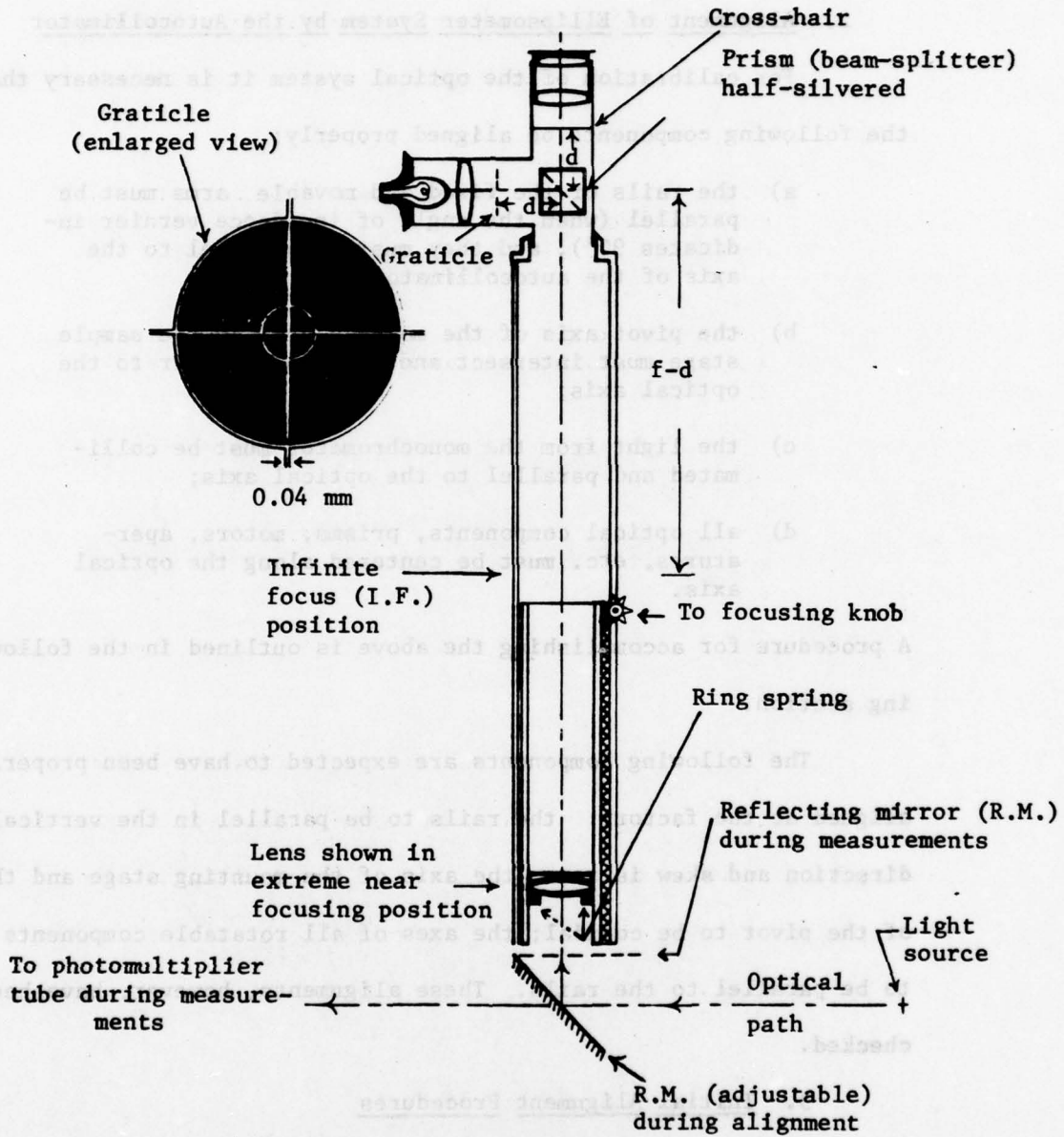


Fig. II-6. Cut-away view of telescope-autocollimator.

2. Alignment of Ellipsometer System by the Autocollimator

For calibration of the optical system it is necessary that the following components be aligned properly:

- a) the rails of the fixed and movable arms must be parallel (when the angle of incidence vernier indicates 90°), and they must be parallel to the axis of the autocollimator;
- b) the pivot axis of the movable arm and the sample stage must intersect and be perpendicular to the optical axis;
- c) the light from the monochromator must be collimated and parallel to the optical axis;
- d) all optical components, prisms, motors, apertures, etc. must be centered along the optical axis.

A procedure for accomplishing the above is outlined in the following section.

The following components are expected to have been properly aligned at the factory: the rails to be parallel in the vertical direction and skew is zero; the axis of the mounting stage and that of the pivot to be coaxial; the axes of all rotatable components to be parallel to the rails. These alignments, however, have been checked.

3. Initial Alignment Procedures

- a) The autocollimator is mounted on the system and roughly aligned.
- b) The superposition of the graticle and cross-hair is checked by putting a mirror in the light path and focusing at the mirror

surface. A near image of the graticle (which is independent of the angle θ) will be formed and should superimpose on the cross-hair if the autocollimator eyepiece is adjusted correctly.

c) An adjustable mirror with a three-point spring-loaded mount is inserted in one of the rotatable prism mounts (with prism removed) and placed on the movable arm. The mirror is rotated while observing the graticle image from the eyepiece. The mount is adjusted so that the image does not move as the mirror is rotated. The mirror is now perpendicular to its axis of rotation. This axis will be used as a master-reference for all the subsequent alignment steps.

d) Using the three screws under the mirror box, the image from step c is centered. The mirror is moved to the fixed arm and the image is centered laterally (ignoring vertical error at this time) by moving the arm. The angle vernier (located under the name plate) is zeroed.

e) A needle mounted in a cork is placed on the sample stage, where the cell E is subsequently mounted (see Fig. II-8a and b). The stage is rotated and the position of the needle adjusted to remain stationary with rotation.

f) The autocollimator and/or reflecting mirror (R.M.) (Fig. II-6) are adjusted maintaining parallelism to center the image of the needle.^g Repeat steps c through f as needed. Remove the needle.

^gTranslating the three set screws controlling the alignment of the 45° mirror in Fig. II-6 moves the image in the plane defined by the optic axis and the center line of the telescope. At present, movement in the other direction can only be accomplished by physical translation of the telescope body. Note that the telescope is mounted at

g) Mount the 1 mm pinhole on the rails near the center of rotation and check for lateral centering.

h) Mount a double-sided mirror on the sample stage roughly vertical. Adjust the mirror to center the collimating image. Rotate the stage 180° and note the vertical deflection of the image. Adjust the tilt of the mirror to take off $1/2$ of the deflection and adjust R.M. to take off the other $1/2$. Rotate 180° and repeat until zero deflection (this adjusts the optical axis of the telescope perpendicular to the pivot axis). Repeat steps e through h as needed. Remove mirror.

i) Mount the pinhole at several positions along both arms and check for centering. If not centered, this implies that the rotating mirror axis was not parallel to the rails. The mount must be adjusted with shims and the entire procedure repeated.

At this point, we have accomplished 2a and 2b.

4. Light Source Alignment

a) Mount the monochromator and light source. Set the wavelength drive at straight-through (0.00 reading). Insert a filter to reduce light intensity and use the telescope to the autocollimator to adjust the position of the monochromator so that the input and output slit images are centered.

an angle to the vertical and adjustment of either of the above results in a mixed motion in the true horizontal and vertical plane. It is planned to mount the telescope on an X-Y translation mount in the near future.

b) Install the collimating lens (C in Fig. II-4). With the telescope at infinity focus, set the distance of the collimating lens so that the exit slit is in focus.

c) Using the two pairs of centering screws of the collimating mount, center the image of the slit (using the narrow slit and fishtail).

d) Mount the rest of the optical components and check their centering.

The stage of the ellipsometer system is now aligned.

5. Alignment of Rotating Analyzer Prism

At least two types of errors (designated as 1F and 2F) are possible due to the alignment of a rotating prism. These are detected by using circularly polarized (or randomly depolarized) light and observing the output signal from the photomultiplier as the motor is rotated.

a) 1F error is a signal whose frequency is the same as that of the rotation speed of the motor (54 Hz). This error signal can be caused by: (i) improper centering of the prism; (ii) prismatic tilt of the prism; (iii) a wedge error (beam deviation) in the crystal due to manufacturing errors; (iv) spurious internal reflections and scattered light. It is possible to eliminate (i) and (ii) by proper centering of the prism and it is possible to minimize all four by intentional misalignment of the prism for a given prism-photomultiplier distance.

These misalignments lead to optical asymmetries in the prism.

Intrinsic and alignment errors are also induced by curvature, tilt, and inhomogeneities of the photodetecting surface. Thus, the beam does not pass through the same portion of the prism during its rotation or the beam moves over the surface of the photomultiplier to regions of dissimilar sensitivity. Both lead to an error signal. Empirically it has been found possible to adjust the centering and tilt of the prism to reduce this source of error below 0.01° in azimuth (α).

b) 2F error is a signal whose frequency is twice that of the rotation speed (108 Hz). Several factors can cause this type of error. Among them are: (i) stress polarization of the photomultiplier face plate; (ii) optical anisotropy caused by curvature of the photomultiplier surface; (iii) or by tilt of the photomultiplier surface plate caused by the orientation of photomultiplier tube; (iv) spurious internal reflections and scattered light.

The 2F noise is primarily evident when using a calcite prism and is caused by interaction of the polarizer output beam with a polarization-sensitive detector. This type of error can be minimized by using a pseudo-random depolarizer in the output beam. A Rochon prism is inherently depolarized and exhibits very little 2F error. However, the presence of the extra-ordinary beam creates considerable 1F error by scattering. In addition, the Rochon prism appears to have a residual polarization sensitivity (90) to the input beam. This may be due to misalignment of the two halves of the prisms during manufacture. This is detectable visually as a

double image when observed in the autocollimator-telescope. Further errors can occur by multiple reflection from the prism surfaces.

c) Rotating Prism (Analyzer) Alignment

The prism is mounted in its holder by two sets of four double opposed nylon screws, one set at each end. Initially the prism is centered visually in its barrel and mounted on the motor. A two-phase vector phase-lock meter (PAR 129A) is synchronized to the motor zero pulse.^h The polarizer and quarter-wave plate are set in the light beam and they are adjusted together with the wavelength for perfect circular light as shown by an oscilloscope and by the phase-lock amplifier to indicate the first harmonic (i.e., 2F). Setting the phase-lock at the fundamental (i.e., 1F), it is possible to adjust alternately the pairs of screws to minimize the 1F indication. Note that a small residue 2F component is ignored by the phase-lock. The polarizer is rotated 90°, circular light should once again be obtained but with opposite handedness. Experimentally, perfect adjustment is usually not obtainable probably due to errors in the Rochon or in the quarter-wave plate. This error is usually less than 0.05° in azimuth and the system should be set for the best compromise. Adjustment of the tilt and/or orientation of the photomultiplier tube can sometimes help to minimize the above errors.

^hIt may be necessary to stretch the zero pulse electronically for proper synchronization.

After this procedure is followed, the azimuthal reading error should be plotted vs the polarizer settings over the entire 360° at suitable intervals. Experiments have shown that the errors are typically $\pm 0.01^\circ$ when the above procedure has been followed carefully. The error curves can be resolved in terms of 1F and 2F (relative to polarizer angles) components.

No provision has been made for tilt alignment of the polarizer after the prism has been installed in the rotatable crystal mount. A redesign of the mount would be helpful.

6. Alignment of the Prisms (Polarizer and Rotating Analyzer)

a) Using the procedure outlined in the preceding section, check the alignment of the optical components (i.e., collimator, autocollimator, sample mounting stage, etc.).

b) Mount the polarizer and rotating analyzer on the optical bench and check the agreement between the vernier polarizer scale and azimuthal readout.

c) Remove the rotating analyzer and mount a mirror on the sample stage with the mirror surface facing front. Rotate the sample mount to face the autocollimator and set its angle with the tilt angle micrometer to be perpendicular to the optical axis. Rotate the sample mount back and center the front mirror surface with the translation micrometer. Recheck the angle.

d) Swing the movable arm to a convenient angle (i.e., 60° - 70°) and mount the rotatable mirror (as a master reference) on the fixed arm. Adjust the angle of the sample mount to center the

image of the graticle in the horizontal plane. This will set the surface for the correct angle of incidence, since the light beam is now reflected twice from the sample surface. The geometry of this reflection is shown in Fig. II-7a. The light beam from the autocollimator enters at 1. If the sample surface is correctly aligned with angle of incidence ϕ , the beam is reflected at 0 to 2. The rotatable mirror (MM') is perpendicular to the line $\vec{20}$ and the light will be reflected back to 0 and then to 1 with no deviation. If the sample surface has a tilt angle τ , the normal to the surface is described by the vector $\vec{0n}$. The reflected beam will be in the plane defined by the vector pairs $\vec{01}$ and $\vec{0n}$ along the vector $\vec{02'}$ in the great circle passing through the vertical axis (shown full view in Fig. II-7b. The reflection from the rotatable mirror MM' is to 3. Since only angles are considered, the vector $\vec{2'3}$ can be translated to $\vec{40}$. This beam returns to the sample surface and will be reflected in the plane $\vec{40n}$ along the vector $\vec{05}$ with a vertical deflection γ from the original beam (see Fig. II-7c. As the angle of incidence approaches zero, the deflection γ approaches 4τ , but for larger angles of incidence, the sensitivity decreases. Finally remove the rotatable mirror.

e) Mount the polarizer and rotating analyzer and set the polarizer at 90° . The azimuthal readout should be $90^\circ \pm 0.002^\circ$ at 100 times integration (averaged over 100 revolutions of the analyzer). If not, the prisms must be reoriented using procedure f below.

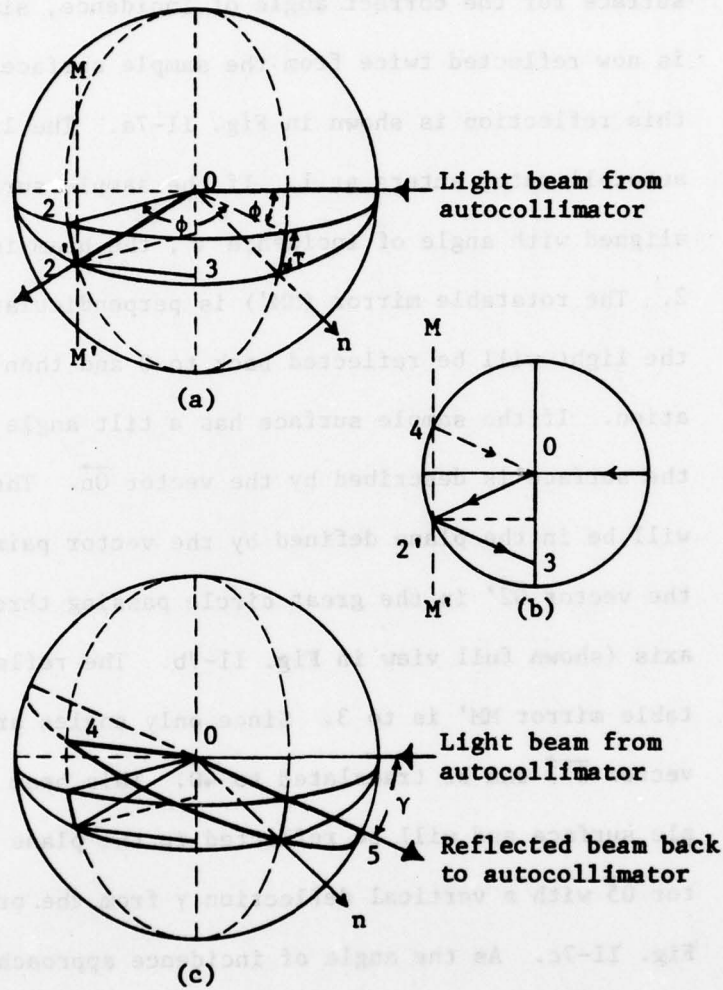


Fig. II-7. (a) The geometry to show the reflected light from a sample surface at an angle of incidence ϕ with a tilt angle τ from the rotation axis of the sample mount. (b) Full view of the great circle passing through the vertical axis, to show the geometry of the reflected light from a tilted sample surface. (c) The geometry to show the deflection γ of the final reflected light back to autocollimator and the original beam from autocollimator.

f) Record the azimuthal (α) readout and polarizer setting for a series (4-5 pairs) of polarizer positions around 90° (e.g., 80° - 100°) to obtain symmetric $\tan^2 \epsilon$ values. Set the polarizer at the midpoint of the corresponding polarizer values (i.e., at the minimum of $\tan^2 \epsilon$). Adjust the rotating analyzer for 90° with double-opposed set screws at the bottom of the motor mount. (If the error is greater than a few degrees, the prism must be reoriented in the motor shaft.) Remove the sample and swing the arm back to the straight-through position. Reset the polarizer prism to agree with the α -readouts. Repeat steps d through f as needed. [Note: asymmetric readings may indicate anisotropy of the sample surface.]

7. Alignment of the Cylindrical Optics for Electrochemical Studies

a) Description of Cell Mount (see Fig. II-8a and b)

The cell mount is designed with 4-degrees of freedom. These are: i) rotation (coaxial with the instrument axis) (A); ii) front to back translation (B); iii) vertical translation (coarse and fine) (C); iv) tilt (D).¹ The cell mounting platform has been designed with two V-blocks to mechanically center the cylindrical cell. Together with mechanical adjustment (B), the cell can be located co-

¹ The distance between the pivot and the center of the tilt micrometer is 2.865" (= 7.277 cm), so that 0.001" (= 0.0254 mm) on the micrometer corresponds to 0.02° . The resolution of the micrometer is 0.0001" (= 0.00254 mm) corresponding to 0.002° .

f) Record the azimuthal (α) readout and polarizer setting for a series (4-5 pairs) of polarizer positions around 90° (e.g., 80° - 100°) to obtain symmetric $\tan^2 \epsilon$ values. Set the polarizer at the midpoint of the corresponding polarizer values (i.e., at the minimum of $\tan^2 \epsilon$). Adjust the rotating analyzer for 90° with double-opposed set screws at the bottom of the motor mount. (If the error is greater than a few degrees, the prism must be reoriented in the motor shaft.) Remove the sample and swing the arm back to the straight-through position. Reset the polarizer prism to agree with the α -readouts. Repeat steps d through f as needed. [Note: asymmetric readings may indicate anisotropy of the sample surface.]

7. Alignment of the Cylindrical Optics for Electrochemical Studies

a) Description of Cell Mount (see Fig. II-8a and b)

The cell mount is designed with 4-degrees of freedom. These are: i) rotation (coaxial with the instrument axis) (A); ii) front to back translation (B); iii) vertical translation (coarse and fine) (C); iv) tilt (D).¹ The cell mounting platform has been designed with two V-blocks to mechanically center the cylindrical cell. Together with mechanical adjustment (B), the cell can be located co-

¹ The distance between the pivot and the center of the tilt micrometer is 2.865" (= 7.277 cm), so that 0.001" (= 0.0254 mm) on the micrometer corresponds to 0.02° . The resolution of the micrometer is 0.0001" (= 0.00254 mm) corresponding to 0.002° .

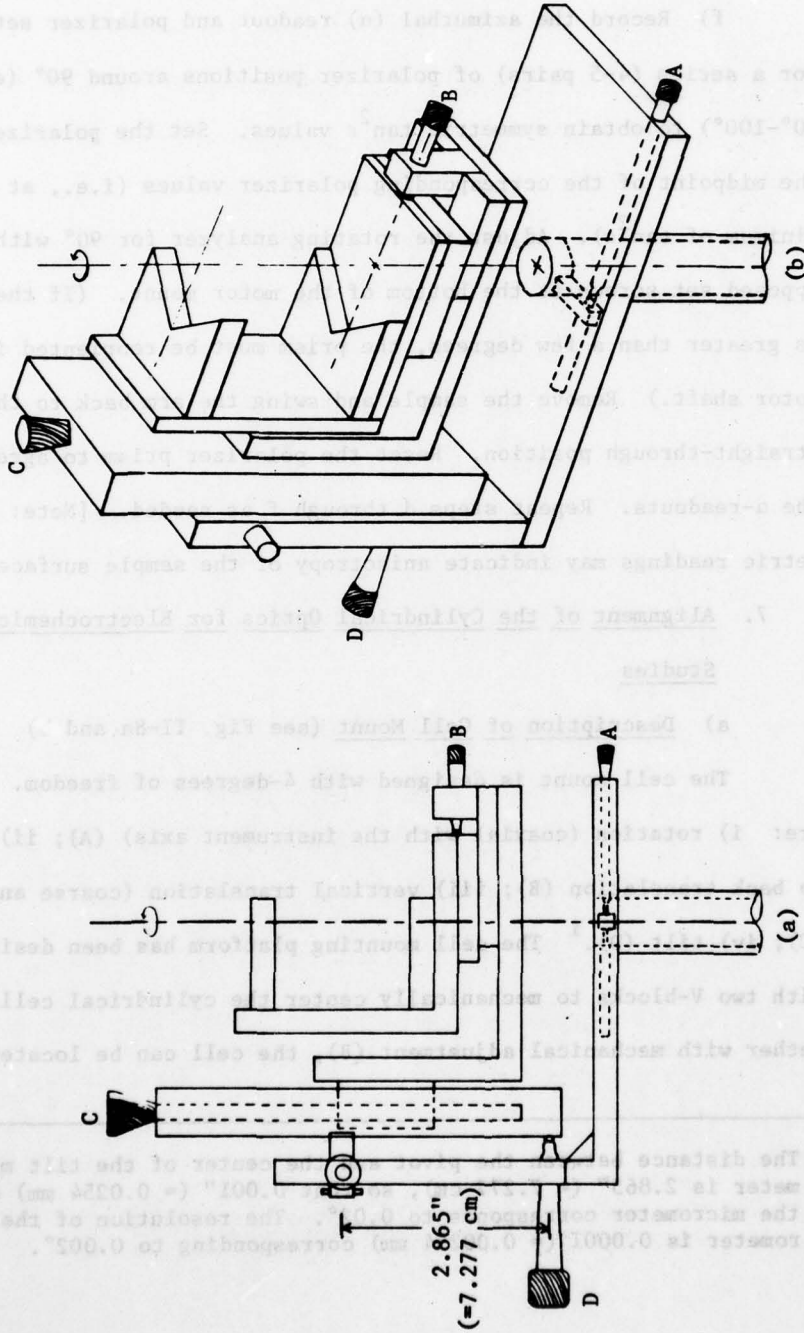


Fig. II-8. Schematic representation of cell mount on ellipsometer table. Representation is intended to show degrees of freedom. Track and details are not shown: (a) side view; (b) perspective view.

axial with the main axis.^j

b) Cylindrical Optics

The cylindrical cells have been constructed in pyrex and in fused quartz with an O.D. of 5.715 cm and I.D. of 5.080 cm. The focal length for the cell with water is 89.6 mm. Negative plano-concave cylindrical lenses with a focal length of $f = -1$ cm are used with the cell.^k These lenses are mounted on two X-Y manipulators. The lenses are adjustable front to back for focus and side to side for centering. In addition, they can be tilted to align their long axis with that of the cell to minimize astigmatism. With the cell centered on the optical axis and coaxial with the center of rotation, it can be shown (see Fig. II-9a and b) that two foci (measured from the outer surface of the cell) exist. The external (first) focal length of the cell (i.e., where rays which are parallel in the solution converge) is f_1 . The internal (second) focal length (where rays which are parallel outside the cell will converge) is f_2 . Two negative cylindrical lenses with focal length less than $-f_1$ with their focal points located at the two external foci of the cell will allow collimated light to be collimated in the solution. With

^j At the time of this writing, master cylinders are being constructed to allow precise alignment of the V-blocks. A precision cylinder with a 5.715 cm O.D. contains an adjustable mirror and needle which can be centered using procedures similar to section 3. If the V-blocks are properly aligned, any cylinder can be made coaxial by translation only.

^k New minicus lenses with radii of curvature of +70 mm and -22.9 mm have been constructed to minimize cylindrical aberration.

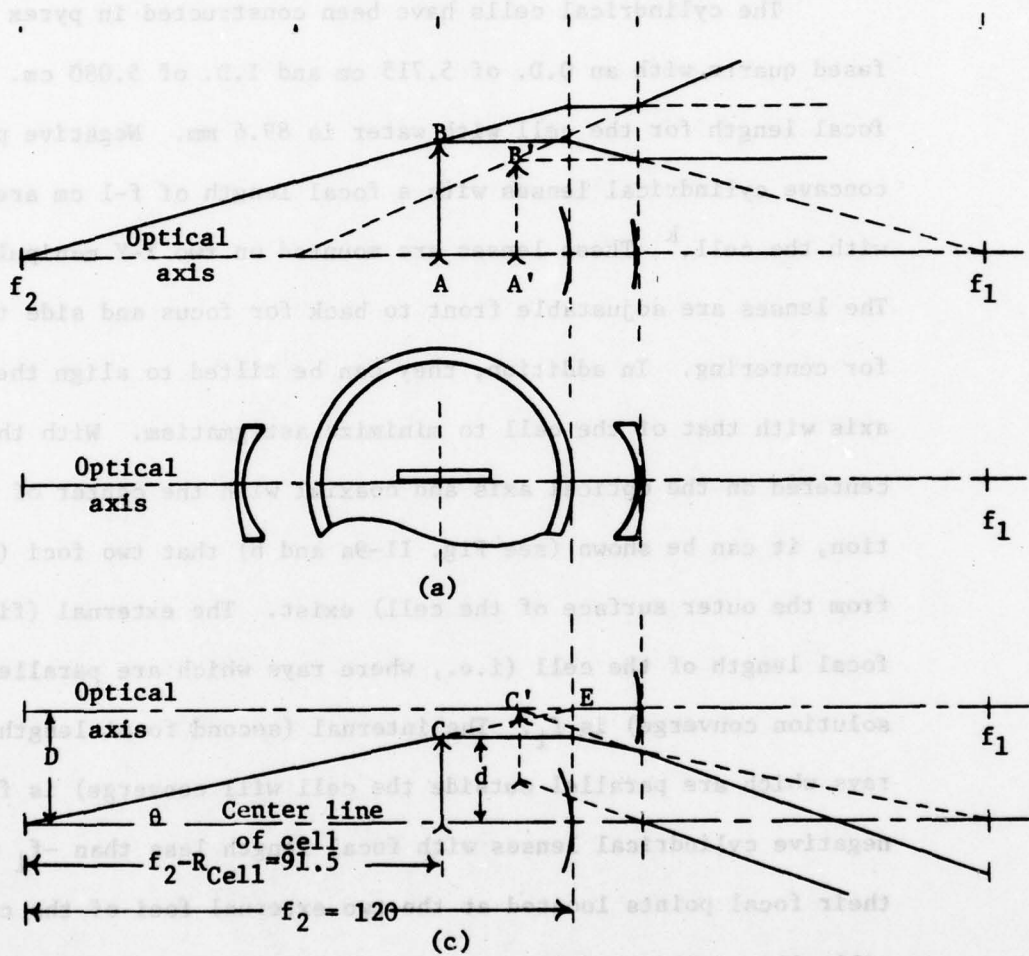


Fig. II-9. The optical geometry of the sample surface inside a cylindrical cell and lens system: (a) perfectly centered sample surface in a straight-through position; (b) displaced surface in a straight-through position; (c) displaced surface at an angle of incidence.

a reflecting surface at the center of the cell, the cylindrical lenses can be adjusted to give collimated light in and out for any desired angle of incidence. It will be shown later that a small displacement of the surface from the center can be corrected for by a suitable shift of the cell and lens positions.

c. Alignment of Cell and Lenses

With the V-blocks centered and tilt set to zero (using master cylinder), the cell filled with solution is mounted and the arms set for straight-through. The cell stage is oriented perpendicular to the optical axis. The telescope is focused for a line image of the small slit and the cell is translated to center the image. The exit negative lens is mounted and the new line image is centered with the X-translation at the approximately correct Y-position. A mirror is inserted in the cell and the mount and cell are rotated to face the telescope. The mirror surface is adjusted to zero tilt without tilting the cell as shown by the autocollimator. The Y-position of the lens is adjusted so that the image of the graticle is centered at infinity focus. Collinearity of the lens and cell axes is shown by the ability to focus the vertical and horizontal segments of the graticle simultaneously by adjusting lens #1 tilt. Rotate the cell and mount back to straight-through position. Mount the second lens and remove the first. Center the line image. Remount the first lens and focus the slit image at infinity and adjust the tilt of lens #2 for minimum astigmatism. Record the positions of the cell and lenses. The distances of lenses to the

cell should be equal. Mount the rotatable mirror and check for centering. Remove mirrors.

d) Sample Mounting and Alignment¹

Assemble the electrochemical system with the sample surface as close as possible to the center. Rotate the cell so that the sample surface faces the telescope. Adjust the tilt (e.g., using nylon screws on the Teflon cell top) with the autocollimator.^m Rotate the cell to the straight-through position and check the centering at a near focus. Translate (and rotate) as needed to center the image of the surface. Record the displacement D.

If we consider the cylindrical cell system (see Fig. II-9a) with a perfectly centered sample surface, the surface will be imaged with the telescope at the cross-hair (referring to Fig. II-9b, point A is imaged at A'). A displaced surface, point B (Fig. II-9b) is imaged at B' and is not centered. It is possible to re-center the image by displacement (and rotation) of the cell. The geometry is shown in Fig. II-9c. In order to re-center the image of a surface displaced by d, it is necessary to move the cell by D to image the surface C at C' (note that the surface must be rotated by an angle $\theta = \sin^{-1}[d/(f_2 - R_{\text{cell}})]$ to lie along the line

¹The following procedure must be modified depending on the type of sample.

^mIf the graticle cannot be focused at infinity or the image is astigmatic, the sample surface is curved and should be repolished.

CE. From the geometry

$$d = [(f_2 - R_{\text{cell}})/f_2] \cdot D = [(120-28.5)/120] \cdot D = 0.7625 \cdot D$$

With the system set for reflection at an angle of incidence ϕ , it is necessary to adjust the cell and lenses if D is not zero. Figures II-10a and II-10b show the geometry of this situation.

Figure II-10a shows a centered surface. The collimated input beam diverges laterally after the negative lens but is re-collimated in the cell. Similar considerations apply for the exit beam. If the surface is displaced by d, the cell and lenses must be moved with respect to the original positions (see Fig. II-10b). The displacements of the lenses are expressed as

$$L_x = [(f_2 - R_{\text{cell}}) \cdot f_{\text{neg}} / (f_1 f_2)] \cdot D \cdot \cos \phi$$

and

$$L_y = [(f_2 - R_{\text{cell}})/f_2] \cdot D \cdot \sin \phi$$

and the corresponding displacement for the cell in the direction normal to the surface is

$$\delta = (L_x^2 + L_y^2)^{1/2} = [(f_2 - R_{\text{cell}})/f_2] [(f_{\text{neg}}^2 \cos^2 \phi / f_1^2) + \sin^2 \phi]^{1/2}$$

Using the value of D, calculate and set the displacements.ⁿ

Check with the rotatable mirror and pinholes.

C. in situ Automatic Ellipsometric Measurements

A Rudolph Automatic Ellipsometer RR 2000 was interfaced with

ⁿMost early results were not done according to this rigorous procedure, thus uncertainty in true ϕ probably exists.

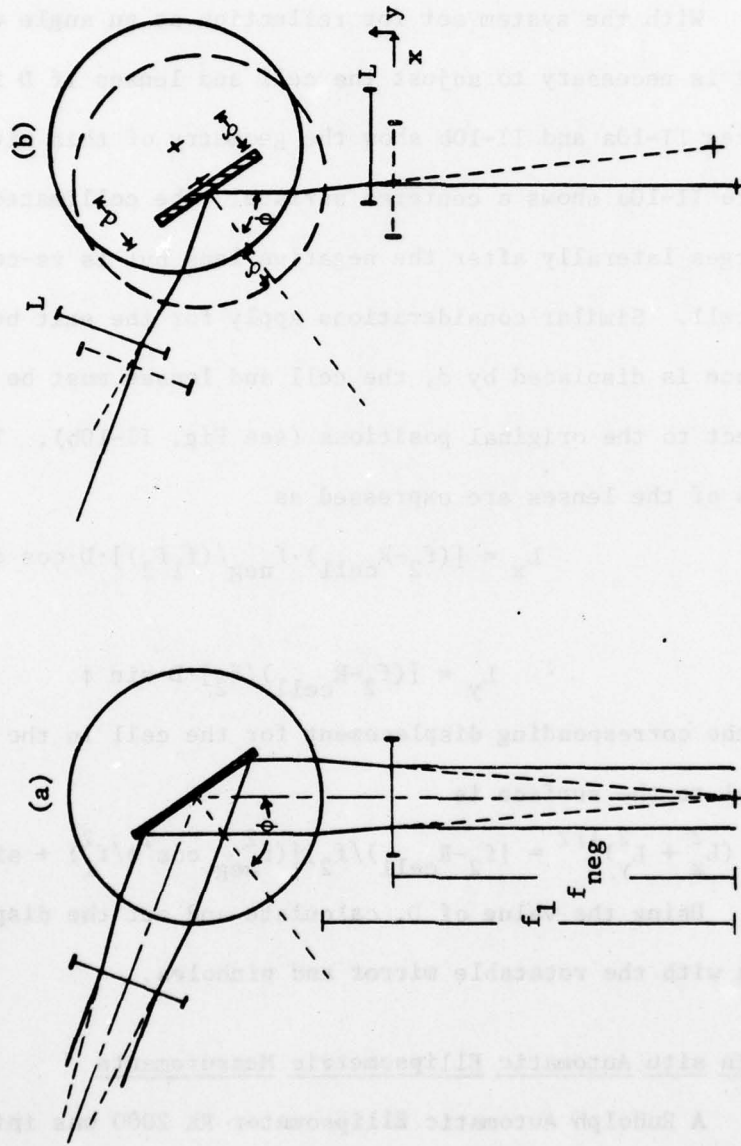


Fig. II-10. The optical geometry for a system set for reflection at an angle of incidence ϕ to show the necessary adjustment of the cell and lenses if the sample is displaced from center of the cell by a distance D ; (a) for a centered surface; (b) for a displaced surface.

a PDP-11/45 minicomputer. The computer was used to handle the following multiple tasks: (i) the control, initiation and synchronization of the experiments; (ii) generation of the reference potential signal for voltage sweep, voltage step, and other voltage waveforms; (iii) recording the optical (α , ϵ , R_T) and electrochemical (i , E) data; (iv) storage of the experimental data for further analysis; (v) data processing; (vi) plotting of data and results. A flow chart is presented in Fig. II-11.

In an attempt to find the best methods to unravel the complexity of the iron system, many types of experimental measurements with different potential waveforms have been tried.^o These included:

- i) potentiodynamic sweep over a wide range of potentials between the potentials of the onset of hydrogen evolution and oxygen evolution;
- ii) potentiostatic step oxide formation including single-step oxidation (the electrode potential was stepped from -0.25 V vs RHE to the desired anodic potential) and progressive-step oxidation (the potential of the electrode, which had been pre-polarized anodically for a given length of time, was stepped progressively towards higher anodic potentials);
- iii) spectroscopic ellipsometric measurements on semi-steady state films;
- iv) potentiostatic step reduction, including single-step reduction (the electrode potential was stepped from an anodic potential, at which the electrode was covered with a passive film, to -0.25 V)

^oone of the advantages of computer control is the flexibility in generation of voltage waveforms.

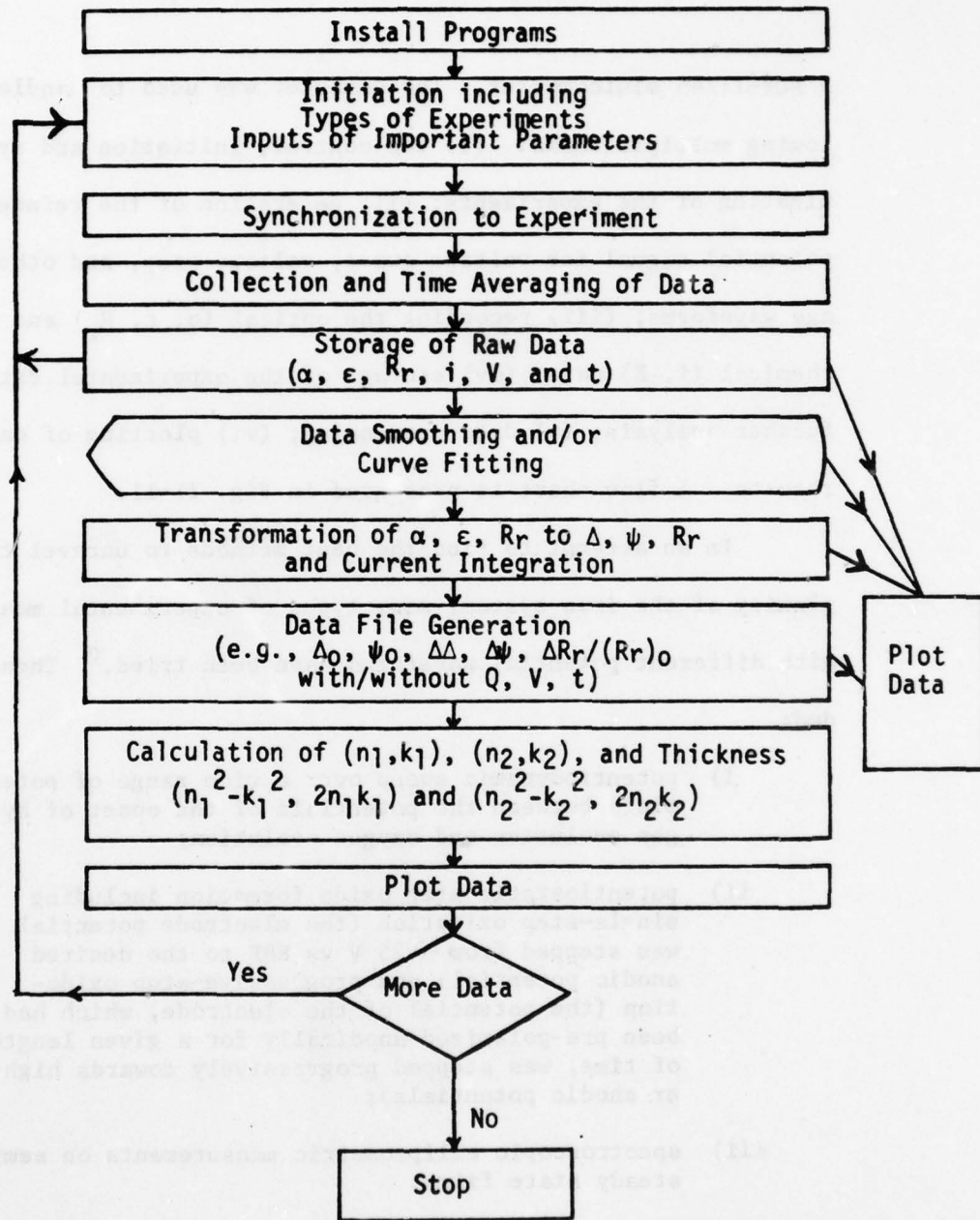
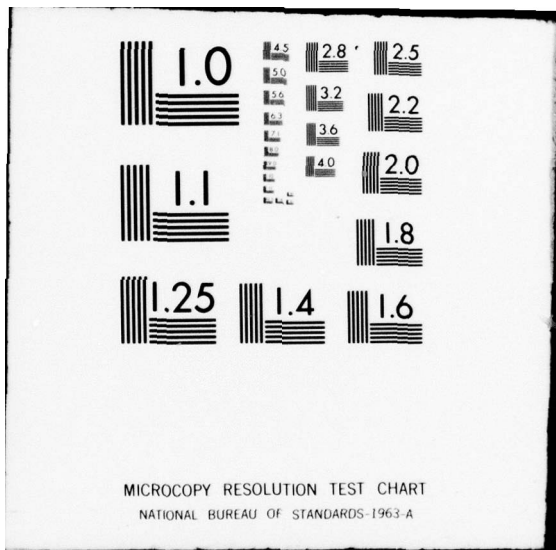


Fig. II-11. Flow chart of data gathering (real-time) and data processing.



MICROCOPY RESOLUTION TEST CHART
NATIONAL BUREAU OF STANDARDS-1963-A

and progressive-step reduction (the electrode potential was lowered progressively back to -0.25 V).

Potentiodynamic sweeps were run at a number of wavelengths. Four different types of voltage waveforms were used (Fig. II-12). (a) Shows a typical voltammetric sweep with anodic and cathodic sweep rates as independent variables. (b) Is same as (a) but maintaining the electrode potential for varying lengths of time at the highest anodic potential. (c) Is the same as (a) but the potential was stepped to a value at which further oxidation ceases but film reduction does not commence. The electrode is allowed to rest at this potential before cathodic sweep is resumed. (d) Is the same as (c) but with resuming the cathodic sweep immediately after the potential step. Using these different sweeps, some of the complexities associated with scan (a) can be elucidated. Scan (b) allows the oxide formation to reach a steady-state value at the highest anodic potential and minimizes the interference of film thickening with decreasing potential. This allows the separation of the film growth from aging effects. Scan (c) allows aging and dissolution to take place while eliminating complications arising from oxygen evolution. In addition any electromodulation of the oxide covered surface can be singled out. Scan (d) minimizes aging effects.

One-single oxidation and reduction were done as follows. The electrode potential was stepped from -0.25 V vs RHE, (at which the electrode surface has been shown to be film-free, see Chapter III), to different potentials in the passive region for various

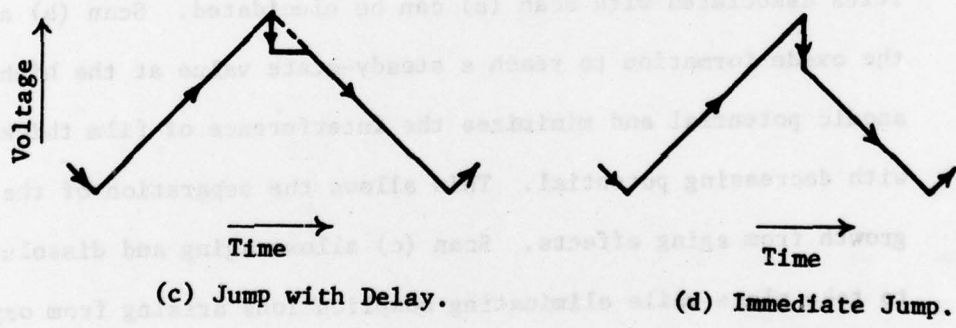
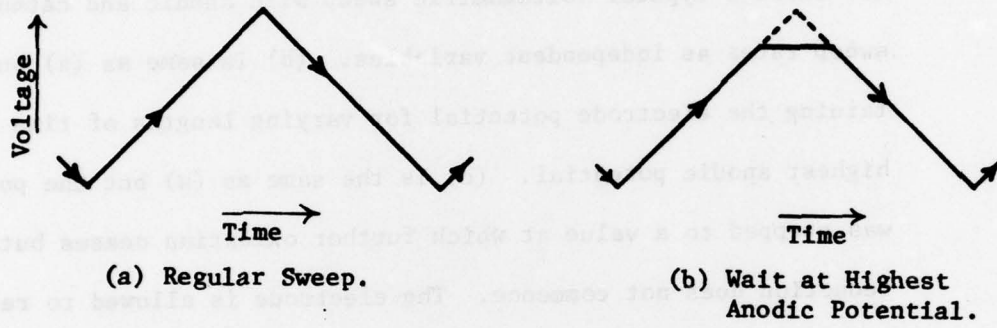


Fig. II-12. Schematic of various waveforms.

lengths of time. Since the changes are greatest at the early stages of growth and slow down appreciably, the data were collected with a modified logarithmic time scale. The first 100 data sets were collected individually (every 18 ms). The rest of the data sets were averaged during logarithmically spaced time intervals. The electrode potential was then potentiostatically stepped back to -0.25 V after each experiment. During these reduction steps, the data were also collected logarithmically. Separate runs were made over the wavelength range at intervals of 50 nm.

Progressive-step potentiostatic measurements for oxide formation and reduction were done similarly except the film-free electrode was stepped to an anodic potential in the passive range (e.g., 0.8 V vs RHE) for varying lengths of time. The electrode was further oxidized in small steps. Progressive-step reduction were done similarly except the electrode was reduced in small steps back to the film-free state.

Spectroscopic ellipsometric measurements of semi-steady state oxides were done as follows. First α_0 , ϵ_0 , and $(R_r)_0$ were determined over the range e.g., 350-800 nm at 10 nm intervals for the film-free state at -0.25 V vs RHE. The electrode potential was then stepped anodically (e.g., 1.2 V) for a given length of time (e.g., an hour). The electrode potential^P was lowered 100 mV for

^PThe electrode potential was referred to RHE.

an additional 30 minutes. No further changes were detectable during this time period. α , ϵ , and R_T were measured at the corresponding wavelengths. The electrode was then reduced to the film-free state and α_0 , ϵ_0 , and $(R_T)_0$ were used to check for reproducibility of the surface.

D. Spectroscopic Ellipsometry of Poly- and Single-Crystal α -Fe₂O₃

Pellets of α -Fe₂O₃ were pressed and sintered from powder and were mechanically polished to an optical quality surface. They were mounted on a 360°-rotatable mount with double sided Scotch tape so that its normal was perpendicular to the rotation axis of the main sample mount. α , ϵ , were measured over the wavelength range (e.g., 260-800 nm). Single crystals of hematite are optical active. The reflecting surfaces of single crystal hematite were cut to contain the C-axis (optic axis). Using the 360°-rotatable mount, the optic axis of the reflecting surface can be set at any inclination angle ω with respect to the plane of incidence. Since there are two complex refractive indices (one for the ordinary ray and one for the extra-ordinary ray) two sets of (α , ϵ) measured at two polarizer settings were required (91-93).

E. Ex situ ESCA Measurements

The electrode materials and their sources are listed in Table II. Cylindrical or foil specimens were mechanically polished, finishing with 4/0 emery paper. They were then degreased with isopropanol vapor followed by rinsing with triple-distilled water and

TABLE II: Electrode Materials for ESCA Measurements and Their Sources

Electrode Material	Its Source	Fabrication	Composition and major impurities
1) Fe	ROI*		99.999%
2) Ni	MRC**	Vacuum processed and cold worked	99.990%; 20 ppm C; 45 ppm Fe; 20 ppm O; 2.0 ppm Al
3) 20% Cr-Ni	MRC**	Vacuum melted and cold worked	20.16% Cr; 120 ppm O ₂ ; 30 ppm C; 25 ppm Si; 30 ppm S; 50 ppm Fe; 20 ppm Co; 10 ppm As; 15 ppm Sb
4) 30% Cr-Ni	MRC**	Vacuum melted and cold worked	VP grade 29.80% Cr
5) 50% Ni-Fe	Driver-Harris #152 Alloys	Hard, as rolled	50.5% Ni; 0.01% C; 0.3% Mn, 0.1% Si and balance Fe
6) Cr	MRC**	Vacuum melted and cold worked	VP grade, no details
7) 316 SS	ROI*	Annealed and cold rolled	16-18% Cr, 10-14% Ni, 2-3% Mo and balance Fe (no details)

*Research Organic/Inorganic Chemical Corporation.

**Material Research Corporation.

dried with lens tissue. A Varian IEE-15 system was used to obtain the spectra. The vacuum in most cases was in the range mid- 10^{-6} to high- 10^{-7} Torr in this instrument although the pressure was probably considerably higher in the vicinity of the sample.

The procedure for obtaining electrodes is described below: the pretreated samples were cathodically reduced (e.g., reduced at -0.4 V for Fe and Ni electrodes) for approximately 20 min. The electrode potential was then stepped to the potential to form an oxide film for 30 min. At the end of this time period, the change of current density was very small. Prior to transferring the sample from electrochemical system to the sample chamber of IEE-15 spectrometer, the electrolyte was drained and the sample was removed from the cell and rinsed with argon purged spectroscopic methanol as soon as possible after losing potential control (about one minute). Within another minute, the sample was transferred to the sample chamber (under an argon atmosphere) and then transferred to the energy analyzer chamber for taking spectra. This procedure can reduce the chances of drastic change during the transfer process but some change may be unavoidable. The analyzer energy used for obtaining spectra was 100 eV. Using this analyzer energy, we can obtain a good statistical curve in 10 min. Due to the poor vacuum, low temperature cooling techniques were not possible.

CHAPTER III

RESULTS AND DISCUSSION

I. Three-Parameter (3-P) Solutions: n_2 , k_2 , d (thickness of the film)

A. Model and Basic Equations

The model to be used for the present optical studies of the passive film is that of an isotropic layer with complex refractive index \hat{n}_2 imposed between two homogeneous bulk phases consisting of the metal (\hat{n}_3) and the electrolyte (n_1). This model requires three parameters to describe the film, $\hat{n}_2 = n_2 - ik_2$ and thickness d .

Two basic equations are involved in the three-parameter (3-P) solution of the ellipsometric equations (76,85). Following the Nebraska conventions, the ratio of the complex amplitude reflection coefficients is given by

$$\hat{r}^P/\hat{r}^S = \tan \psi \cdot e^{i\Delta} \quad (\text{III-1})$$

and the reflectivity by

$$R = (\hat{r}^P)^* \cdot \hat{r}^P \sin^2 P + (\hat{r}^S)^* \cdot \hat{r}^S \cos^2 P \quad (\text{III-2})$$

where P is the angle of the polarizer setting and the superscripts p , s refer to the polarization of light parallel and perpendicular to the plane of incidence; and $(r^P)^*$ denotes the complex conjugate.

The complex reflection coefficients are then

$$\hat{r}^V = (\hat{r}_{12}^V + \hat{r}_{23}^V \cdot X) / (1 + \hat{r}_{12}^V \cdot \hat{r}_{23}^V \cdot X) \quad (\text{III-3})$$

with $X = \exp(S) \quad (\text{III-4})$

where

$$S = -4i\pi\hat{n}_2 \cdot \cos\hat{\phi}_2 \cdot d/\lambda \quad (\text{III-5})$$

and $v = p$ or s , and λ is the wavelength, $\hat{\phi}_2$ is the complex angle of light propagation in the growing film. Equation III-3 is the general form of the reflection coefficients of three layer interfaces. The subscripts 1, 2, 3 refer to the electrolyte, the film, and the metal electrode with the subscripts 12, 23 refer to the interface between 1 and 2 and between 2 and 3, respectively.

The interfacial reflection coefficients r_{ij} are,

$$\hat{r}_{ij}^P = (\hat{n}_j \cos\hat{\phi}_i - \hat{n}_i \cos\hat{\phi}_j) / (\hat{n}_j \cos\hat{\phi}_i + \hat{n}_i \cos\hat{\phi}_j) \quad (\text{III-6})$$

and

$$\hat{r}_{ij}^S = (\hat{n}_i \cos\hat{\phi}_i - \hat{n}_j \cos\hat{\phi}_j) / (\hat{n}_i \cos\hat{\phi}_i + \hat{n}_j \cos\hat{\phi}_j) \quad (\text{III-7})$$

where $i, j = 1, 2, \text{ or } 3$.

The three values determined experimentally by the automatic ellipsometer are α , ϵ , and R_r where α is the azimuth and ϵ is the ellipticity of the reflected light. These can be transformed by

$$\Delta = \tan^{-1}(\tan 2\epsilon / \sin 2\alpha) \quad (\text{III-8a})$$

$$\Psi = \tan^{-1}\{\tan P \cdot \tan[1/2 \cos^{-1}(-\cos 2\alpha \cdot \cos 2\epsilon)]\} \quad (\text{III-8b})$$

for any polarizer setting P to provide the conventional ellipsometric parameters Δ , Ψ , and R_r when no quarter wave plate is used.

With the additional known values of n_1 and \hat{n}_3 , the quantities of Δ , Ψ , and $\Delta R/R\%$ can be used to calculate the optical constant of an absorbing film and its thickness. A direct analytical solution is not possible. Numerical solutions can be found using an exten-

sion of Newton's approximation in one-dimension to two- or three-dimensions if we define the following three functions:

$$f(n_2, k_2, d) = \delta\Delta = \Delta\Delta_c - \Delta\Delta_m \quad (\text{III-9})$$

$$g(n_2, k_2, d) = \delta\Psi = \Delta\Psi_c - \Delta\Delta_m \quad (\text{III-10})$$

$$h(n_2, k_2, d) = \delta(\Delta R/R\%) = (\Delta R/R\%)_c - (\Delta R/R\%)_m \quad (\text{III-11})$$

The subscripts c and m stand for calculated and experimentally measured values respectively.

Equations III-9, III-10, and III-11 mean that for each given set of n_2 , k_2 , and d values, we are able to find a corresponding set of $\delta\Delta$, $\delta\Psi$, and $\delta(\Delta R/R\%)$ values. Furthermore, they also indicate explicitly that by applying iteration methods, the true solution of n_2 , k_2 , and d can be obtained in a condition such that the corresponding values of $\delta\Delta$, $\delta\Psi$, and $\delta(\Delta R/R\%)$ are all equal to zero. Numerically this condition is equivalent to finding the minimum value of the function $F(n_2, k_2, d)$, defined as

$$F(n_2, k_2, d) = f^2(n_2, k_2, d) + g^2(n_2, k_2, d) + h^2(n_2, k_2, d) \quad (\text{III-12})$$

Newton's approximation in two- or three-dimensions can be expressed as

$$\Sigma dX_j = \Sigma [(X_j)_{m+1} - (X_j)_m] = -G(Y_1)/G'_{X_j}(Y_1) \quad (\text{III-13})$$

where $Y_1 = \Delta, \Psi, \Delta R/R\%$ and $X_j = n_2, k_2, \text{ and } d$. The term $(X_j)_m$ denotes a trial value and $(X_j)_{m+1}$ is the next approximation; $G(Y_1)$ and $G'_{X_j}(Y_1)$ are the function value at $(X_j)_m$ and its first derivative with respect to X_j at $(X_j)_m$ respectively; dX_j is the increment to be applied for the next trial value and $(X_j)_{m+1}$ then becomes the

new trial value and the iteration process continues until convergence is obtained. The set of n_2 , k_2 , and d at convergence will be a solution.

The partial derivatives involved in Eqs. III-13 are obtained from Eqs. III-1 and III-2 and their related equations. By differentiating Eq. III-1 with respect to n_2 and rearranging terms, one obtains

$$(1/\hat{r}^P)(\partial\hat{r}^P/\partial n_2) - (1/\hat{r}^S)(\partial\hat{r}^S/\partial n_2) = (2/\sin 2\psi)/(\partial\psi/\partial n_2) + i(\partial\Delta/\partial n_2) \quad \text{(III-14)}$$

Equating the real part and imaginary part of Eq. III-14 separately gives the following two equations:

$$\partial\psi/\partial n_2 = (\sin 2\psi/2) \cdot [(\partial\hat{r}^P/\partial n_2)/\hat{r}^P - (\partial\hat{r}^S/\partial n_2)/\hat{r}^S] \quad \text{(III-15)}$$

and

$$\partial\Delta/\partial n_2 = \text{Im}[(\partial\hat{r}^P/\partial n_2)/\hat{r}^P - (\partial\hat{r}^S/\partial n_2)/\hat{r}^S] \quad \text{(III-16)}$$

Similarly, we can obtain the following two equations by the same mathematical manipulation with respect to k_2 :

$$\partial\psi/\partial k_2 = (\sin 2\psi/2) \cdot \text{Re}[(1/\hat{r}^P)(\partial\hat{r}^P/\partial k_2) - (1/\hat{r}^S)(\partial\hat{r}^S/\partial k_2)] \quad \text{(III-17)}$$

and

$$\partial\Delta/\partial k_2 = \text{Im}[(1/\hat{r}^P)(\partial\hat{r}^P/\partial k_2) - (1/\hat{r}^S)(\partial\hat{r}^S/\partial k_2)] \quad \text{(III-18)}$$

Differentiation of Eq. III-2 with respect to n_2 gives

$$\partial(\Delta R/RZ)/\partial n_2 = \{2 \sin^2 P \cdot \tan 2\psi \cdot \text{Re}[(1/\hat{r}^P)/(\partial\hat{r}^P/\partial n_2)] + 2 \cos^2 P \cdot$$

$$\text{Re}[(1/\hat{r}^S)/(\partial\hat{r}^S/\partial n_2)]\} / (\sin^2 P \cdot \tan^2 \psi + \cos^2 P) \quad \text{(III-19)}$$

Differentiation with respect to k_2 gives

$$\begin{aligned} \partial(\Delta R/RX)/\partial k_2 &= \{2 \sin^2 P \tan^2 \psi \cdot \text{Re}[(1/\hat{r}^P)/(\partial \hat{r}^P/\partial k_2)] + 2 \cos^2 P \cdot \\ &\quad \text{Re}[(1/\hat{r}^S)/(\partial \hat{r}^S/\partial k_2)]\}/(\sin^2 P \cdot \tan^2 \psi + \cos^2 P) \quad (\text{III-20}) \end{aligned}$$

Differentiating Eq. III-3 with respect to n_2 , k_2 , and d , respectively, the following three equations can be obtained:

$$\begin{aligned} (1/\hat{r}^V)\partial \hat{r}^V/\partial n_2 &= \{(\partial \hat{r}_{12}^V/\partial n_2)[1-(\hat{r}_{23}^V X)^2] + [1-(\hat{r}_{23}^V)^2](\partial \hat{r}_{23}^V/\partial n_2)X + \\ &\quad \hat{r}_{23}^V(\partial X/\partial n_2)\}/(1+\hat{r}_{12}^V \hat{r}_{23}^V X) \cdot (\hat{r}_{12}^V + \hat{r}_{23}^V X) \quad (\text{III-21}) \end{aligned}$$

$$\begin{aligned} (1/\hat{r}^V)\partial \hat{r}^V/\partial k_2 &= \{(\partial \hat{r}_{12}^V/\partial k_2)[1-(\hat{r}_{23}^V X)^2] + [1-(\hat{r}_{23}^V)^2](\partial \hat{r}_{23}^V/\partial k_2)X + \\ &\quad \hat{r}_{23}^V(\partial X/\partial k_2)\}/(1+\hat{r}_{12}^V \hat{r}_{23}^V X) \cdot (\hat{r}_{12}^V + \hat{r}_{23}^V X) \quad (\text{III-22}) \end{aligned}$$

$$(1/\hat{r}^V)\partial \hat{r}^V/\partial d = X \cdot S \cdot \hat{r}_{23}^V [1-(\hat{r}_{12}^V)^2]/d(1+\hat{r}_{12}^V \hat{r}_{23}^V X) \cdot (\hat{r}_{12}^V + \hat{r}_{23}^V X) \quad (\text{III-23})$$

and also

$$\partial X/\partial d = X \cdot \left(\frac{\partial S}{\partial d}\right) = XS/d, \quad \partial X/\partial n_2 = XS/n_2 \cos^2 \hat{\phi}_2 \quad (\text{III-24})$$

From Eqs. III-6 and III-7

$$\partial \hat{r}_{12}^P/\partial n_2 = 2n_1 \cos \phi_1 \cos \hat{\phi}_2 (1 - \tan^2 \hat{\phi}_2) / (n_2 \cos \phi_1 + n_1 \cos \hat{\phi}_2)^2 \quad (\text{III-25})$$

$$\partial \hat{r}_{23}^P/\partial n_2 = 2\hat{n}_3 \cos \hat{\phi}_3 \cos \hat{\phi}_2 (1 - \tan^2 \hat{\phi}_2) / (\hat{n}_3 \cos \hat{\phi}_2 + \hat{n}_2 \cos \hat{\phi}_3)^2 \quad (\text{III-26})$$

$$\partial \hat{r}_{12}^S/\partial n_2 = -2n_1 \cos \phi_1 \cos \hat{\phi}_2 (1 + \tan^2 \hat{\phi}_2) / (n_1 \cos \phi_1 + n_2 \cos \hat{\phi}_2)^2 \quad (\text{III-27})$$

$$\partial \hat{r}_{23}^S/\partial n_2 = 2\hat{n}_3 \cos \hat{\phi}_3 \cos \hat{\phi}_2 (1 + \tan^2 \hat{\phi}_2) / (\hat{n}_3 \cos \hat{\phi}_3 + \hat{n}_2 \cos \hat{\phi}_2)^2 \quad (\text{III-28})$$

In general, if $\hat{A} = f(x-iy)$, this implies that $\partial \hat{A}/\partial y = -i \partial \hat{A}/\partial x$.

Thus

$$\partial \hat{A}/\partial k_2 = -i \partial \hat{A}/\partial n_2 \quad (\text{III-29})$$

B. Computer Iteration Procedure

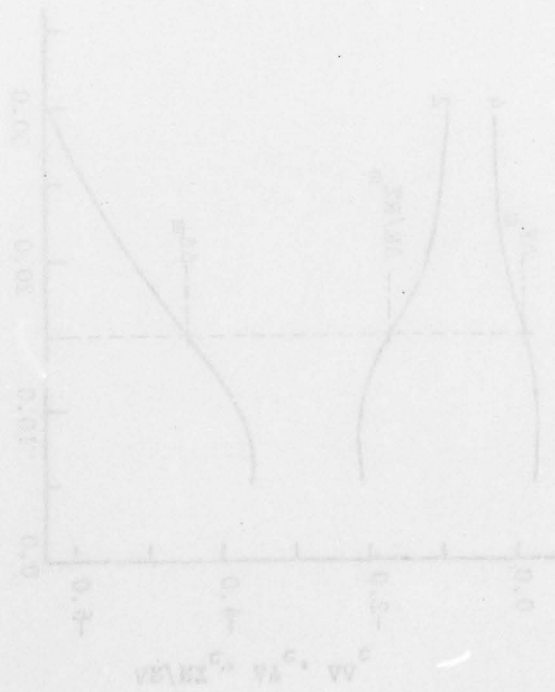
The computer programs for calculation of n_2 , k_2 , and d (thickness) consists of three program segments: NKT1, FUNCT1, and FNEWT. The main program NKT1 performs the initial calculation of the optical constant of the substrate ($n_3 - ik_3$) from the measured Δ_0 and Ψ_0 values and controls the iteration process. The subroutine FUNCT1 performs the calculation of $\Delta\Delta$, $\Delta\Psi$, and $\Delta R/R\%$ values for a given set of trial values of n_2 , k_2 , and d . The subroutine FNEWT involves Newton's approximation. Each set of experimentally measured $\Delta\Delta$, $\Delta\Psi$, and $\Delta R/R\%$ values are fed into this subroutine to generate a new set of n_2 , k_2 , and d values to recalculate the new $\Delta\Delta$, $\Delta\Psi$, and $\Delta R/R\%$ for further approximation until convergence is obtained. The computer program also contains the two-parameter (2-P) method as a subset. This subset has the capability of calculating the expected value of the third parameter by using any other two measured ellipsometric values for a given set of trial n_2 , k_2 , and d values. During the process of iteration, the expected third ellipsometric parameter values as well as the trial n_2 , k_2 , and d values are tabulated. From this tabulation, approximate roots of n_2 , k_2 , and d can be located.

It is always helpful to apply this 2-P method, especially for a new system, to locate approximate roots (n_2 , k_2 , and d) for a set of three measured values ($\Delta\Delta$, $\Delta\Psi$, $\Delta R/R\%$). These can be used as initial values for refinement by the 3-P method.

The solution of the equations for the 3-P method can be

illustrated graphically by the following three figures (Figs. III-1a, b, and c). Figure III-1a shows the variation of the expected parameter values as a function of assumed thickness for a given n_2 , k_2 . If a solution exists for a set of experimentally measured values of $\Delta\Delta$, $\Delta\Psi$, $\Delta R/R\%$, all three loci have to pass through each respected measured value at the same thickness. Figure III-1b shows the three different hypothetical n_2 curves corresponding to three different expected third parameter's values as functions of the assumed thickness. A root of n_2 , k_2 , d exists when they intersect at the same thickness for a set of experimentally measured values of $\Delta\Delta$, $\Delta\Psi$, and $\Delta R/R\%$. Similarly, Fig. III-1c shows the same type of plot as Fig. III-1b except the plot is for k_2 vs d .

By using this set of computer programs, the n_2 , k_2 , d solutions at a given set of $\Delta\Delta$, $\Delta\Psi$, and $\Delta R/R\%$ can be located rapidly.



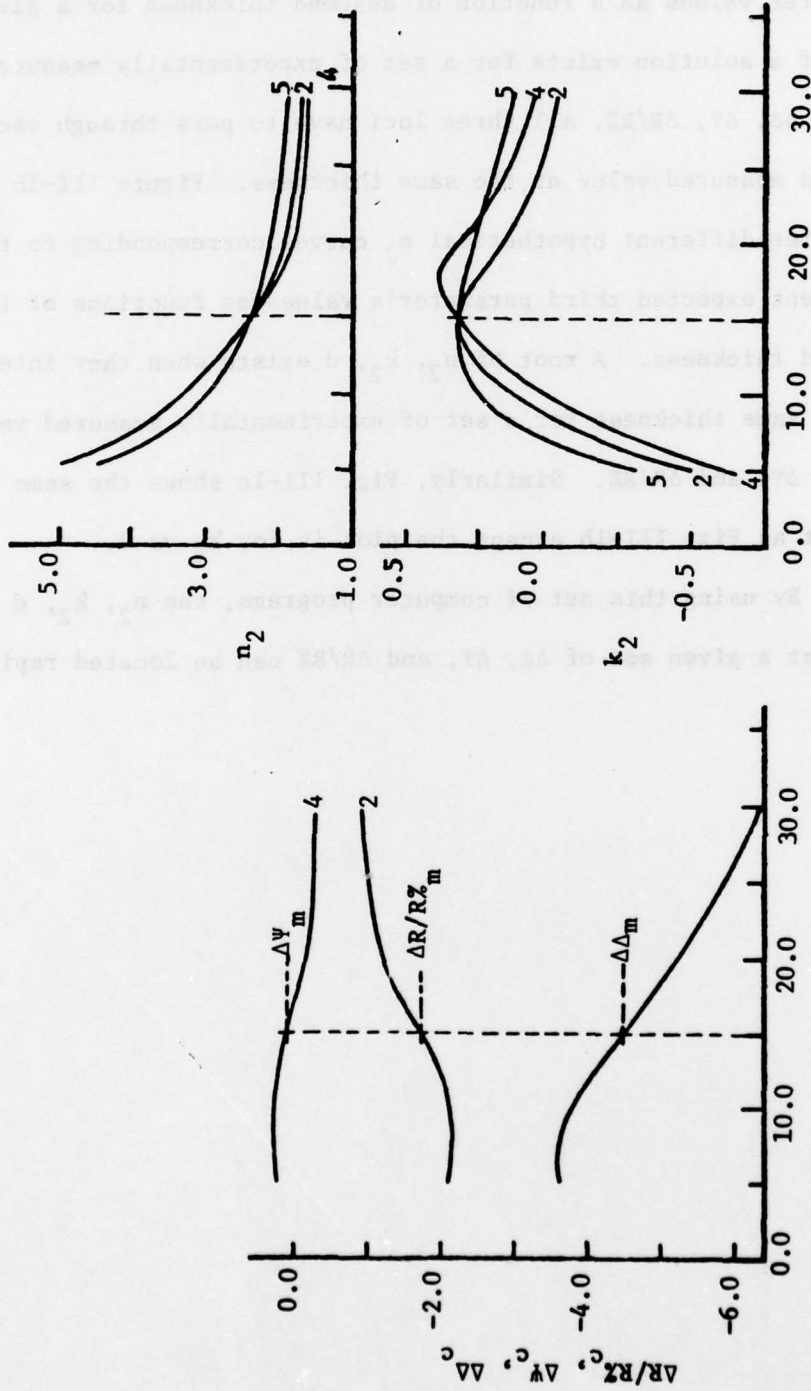


Fig. III-1a,b,c. Graphical representation of 3-P solution for a film of 15 Å thick with $\lambda = 350$ nm and $\phi = 68^\circ$. The curves marked 2, 4, 5 were generated by iteration processes by using $\Delta R/R\%$, $\Delta\psi$, and $\Delta\Delta$ as the third parameter respectively (see text for details).

II. Critique on Present Status of Ellipsometric Data

Before presentation of the data obtained ellipsometrically it is necessary to discuss the confidence level that can be placed on the interpretation of the data. This must include a treatment of the effects of small but finite errors residual in the measuring system, artifacts including those now known to have been present in early stages of the measurements and which have been corrected, and those still unavoidably present. In addition, a discussion of model non-ideality and breakdown of classical treatments in the domain of a few Angstroms must be included.

Experimentally, there are three major errors which may be involved in the ellipsometric measurements. First, the early measurements of the wavelength dependence data, which have been presented earlier (72) at the long wavelengths (above 550 nm) involved some errors caused by second order blue light leakage from the diffraction grating. This type of error has caused the apparent values of film thickness in this wavelength region to be much too high. Consequently, the complex refractive indices and complex dielectric constants were in error, especially in the real components (n_1 and ϵ_1) of these values. The errors caused by the blue light leakage have been avoided in the later sets of measurements by the use of a yellow filter inserted between the collimator (C) and polarizer (P) (see Fig. II-4).

A second type of error was caused by the early alignment pro-

cedure (see Chapter II). Rigorous alignment including corrections for translation displacement of the center of the electrochemical cell and compensating cylindrical lenses was not made properly even in the latest sets of measurements. Thus there exists an uncertainty in the actual angle of incidence ϕ which may have been as large as a few tenths of a degree. The residual inconsistency in the quantitative value of the data may well have been caused by this non-rigorous alignment procedure, since calculations invoking variation of ϕ produced changes of comparable magnitude (i.e., a few tenths of a degree in ϕ correspond to $\sim 10^{-2}$ change in k_2 and $\sim 10^{-1}$ in n_2).

The third type of error is caused by a combination of several residual non-linearities in the photomultiplier, pre-amplifier, and filter and in the logarithmic analog computer circuits. This non-linearity was not fully appreciated until the majority of the data was accumulated. To a first order, operation at the same effective response level (obtained by adjustment of the high voltage of the photomultiplier), will result in a constant non-linearity which will produce only a small absolute error which is usually negligible in measuring relative changes. In the single potentiostatic step and potential sweep experiments, the initial intensity was adjusted to a constant response level (in the regime of the best operating conditions of the measuring system). In some of the steady state measurements made over a range of wavelengths, this condition was not fulfilled.

In regions of low light level, noise is unavoidable. This

results in a greater uncertainty in all the measured values. Since most of the optical components were not of UV-grade material, appreciable quantitative errors exist in much of the data obtained below 400 nm. The calculated optical constant of the film are not highly sensitive to some errors in the optical constant of the substrate.

In general, the self consistency of the experimental results for n_2 , k_2 , and d were within a few per cent, but in some of the experiments, the results were outside of this range.

Theoretically the three-layer model is valid for a uniform, isotropic film on a smooth surface not interacting with the underlying substrate. With films of a few Angstrom, this ideal model may not approximate the actual system very well. With thicker film, however, the present study has provided substantial evidence that this optical model is reasonable (see Section V).

In the text we shall try to point out those areas of questionable validity and also those areas which we can consider well established.

III. Optical Spectrum of Bare Iron

The optical spectrum for bare iron for wavelengths from 350 nm to 760 nm is shown in Fig. III-2. This figure also shows the optical spectrum of iron substrate measured by Kruger et al. (84,94) in high vacuum ($<5 \times 10^{-10}$ Torr) and electrochemical studies (without explicit indication of the electrochemical reduction method) in the same electrolyte (pH 8.4 borate buffer solution) as used in the present study. The agreement of this work with that done in high vacuum by Kruger et al. (84) indicates that a bare iron surface without any appreciable oxide film can be produced in this electrolyte by the careful choice of cathodic potential.

The optical spectrum of the present work used a wider range of wavelength and showed less scatter than that reported by Kruger et al. (84) in a similar electrochemical environment. The small residual discrepancies are probably due to the differences in the choice of the cathodic potential to produce the film-free state and to differences in sample preparation (e.g., roughness).

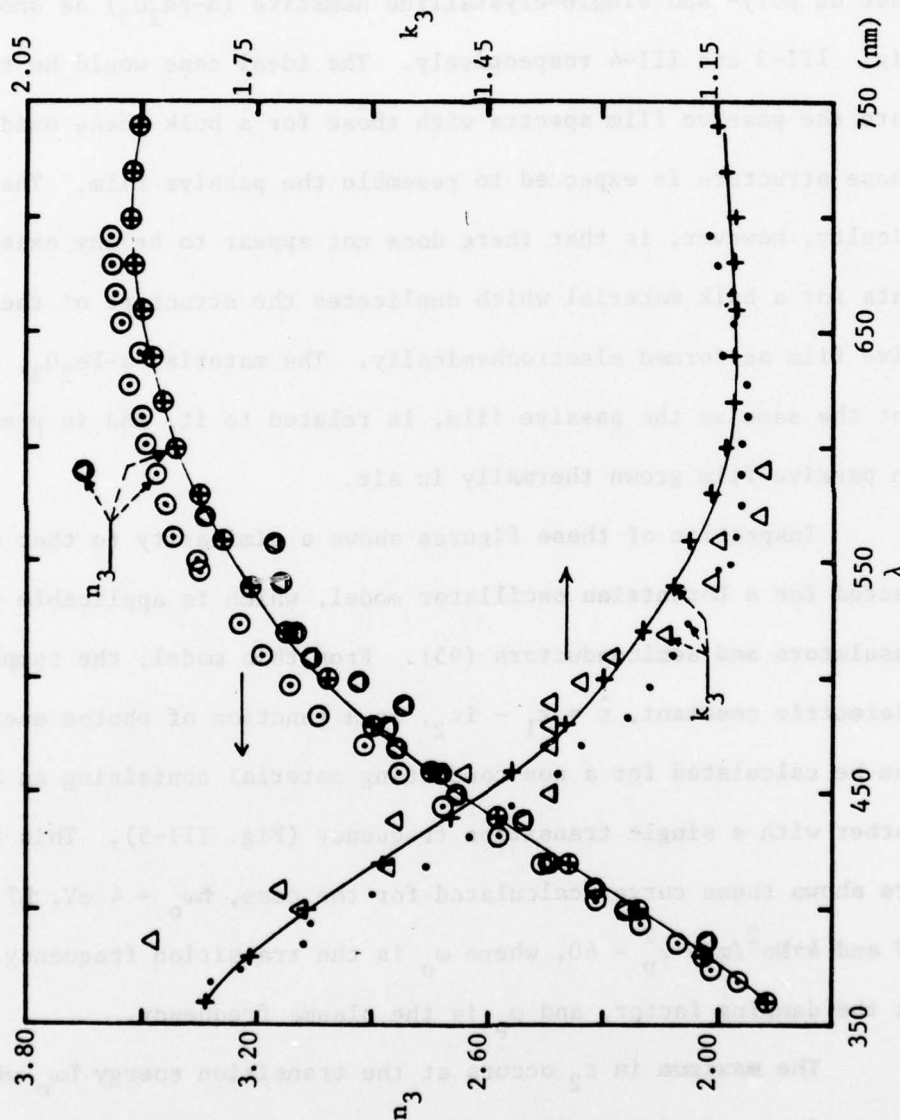


Figure III-2: Complex refractive index ($\hat{n}_3 = n_3 - ik_3$) of iron: + and \oplus are ellipsometric results of the present study for electrochemically reduced iron at -0.25 V vs RHE in borate buffer at pH 8.4, $\phi = 65^\circ$; Δ and \odot are results from Ref. 84 for electrochemically reduced iron in the same electrolyte; \cdot and \ominus are results from Ref. 94 for chemically reduced iron by H_2 in high vacuum ($<5 \cdot 10^{-10}$ Torr) condition.

IV. Optical Spectra of Poly- and Single-Crystalline Hematite

($\alpha\text{-Fe}_2\text{O}_3$)

For comparison purposes, parallel ellipsometric studies were made on poly- and single-crystalline hematite ($\alpha\text{-Fe}_2\text{O}_3$) as shown in Fig. III-3 and III-4 respectively. The ideal case would be to compare the passive film spectra with those for a bulk phase oxide whose structure is expected to resemble the passive film. The difficulty, however, is that there does not appear to be any existing data for a bulk material which duplicates the structure of the passive film as formed electrochemically. The material $\alpha\text{-Fe}_2\text{O}_3$, while not the same as the passive film, is related to it, and is present in passive film grown thermally in air.

Inspection of these figures shows a similarity to that expected for a Lorentzian oscillator model, which is applicable to insulators and semiconductors (95). From this model, the complex dielectric constant, $\hat{\epsilon} = \epsilon_1 - i\epsilon_2$, as a function of photon energy can be calculated for a non-conducting material containing an absorber with a single transition frequency (Fig. III-5). This figure shows these curves calculated for the case, $\hbar\omega_0 = 4$ eV, $\hbar\Gamma = 1$ eV and $4\pi Ne^2/m = \omega_p^2 = 60$, where ω_0 is the transition frequency, Γ is the damping factor, and ω_p is the plasma frequency.

The maximum in ϵ_2 occurs at the transition energy $\hbar\omega_0$ while the maximum and minimum in ϵ_1 are displaced from this energy by $\pm \hbar\Gamma/2$. The half-width of the ϵ_2 peak is Γ and the height of the maximum in ϵ_2 can be expressed as,

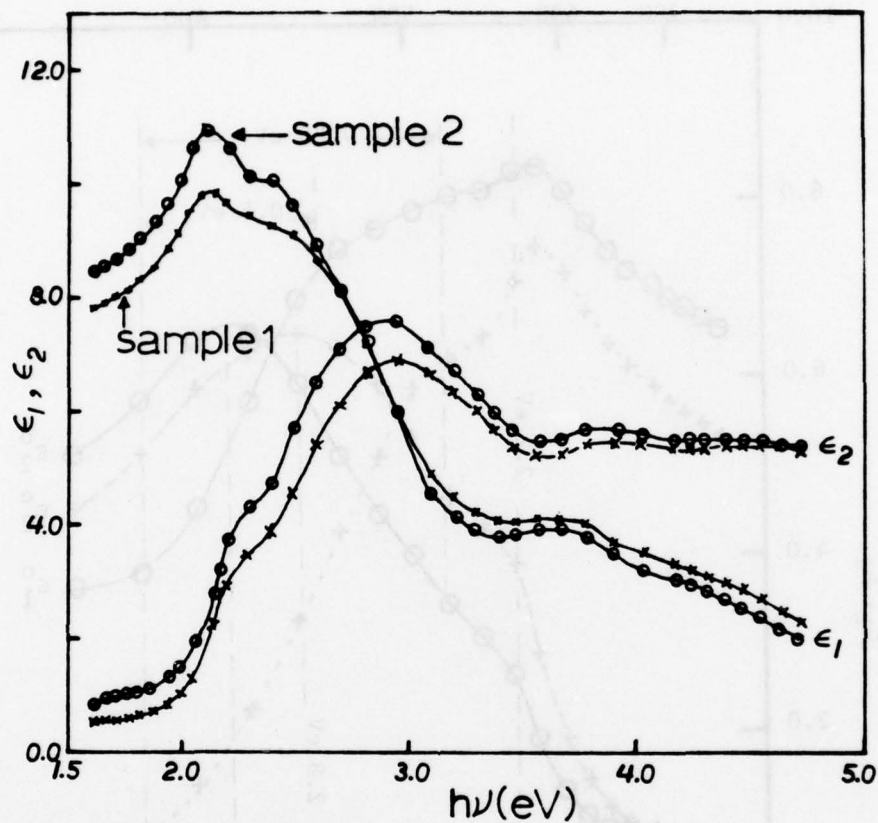


Figure III-3. Complex dielectric constant $\hat{\epsilon} = \epsilon_1 - i\epsilon_2$ of two polycrystalline specimens of $\alpha\text{-Fe}_2\text{O}_3$ powder-pressed pellet, followed by sintering at high temperature ($\sim 1100^\circ\text{C}$). (Sintering temperature of sample 2 is higher than that of sample 1).

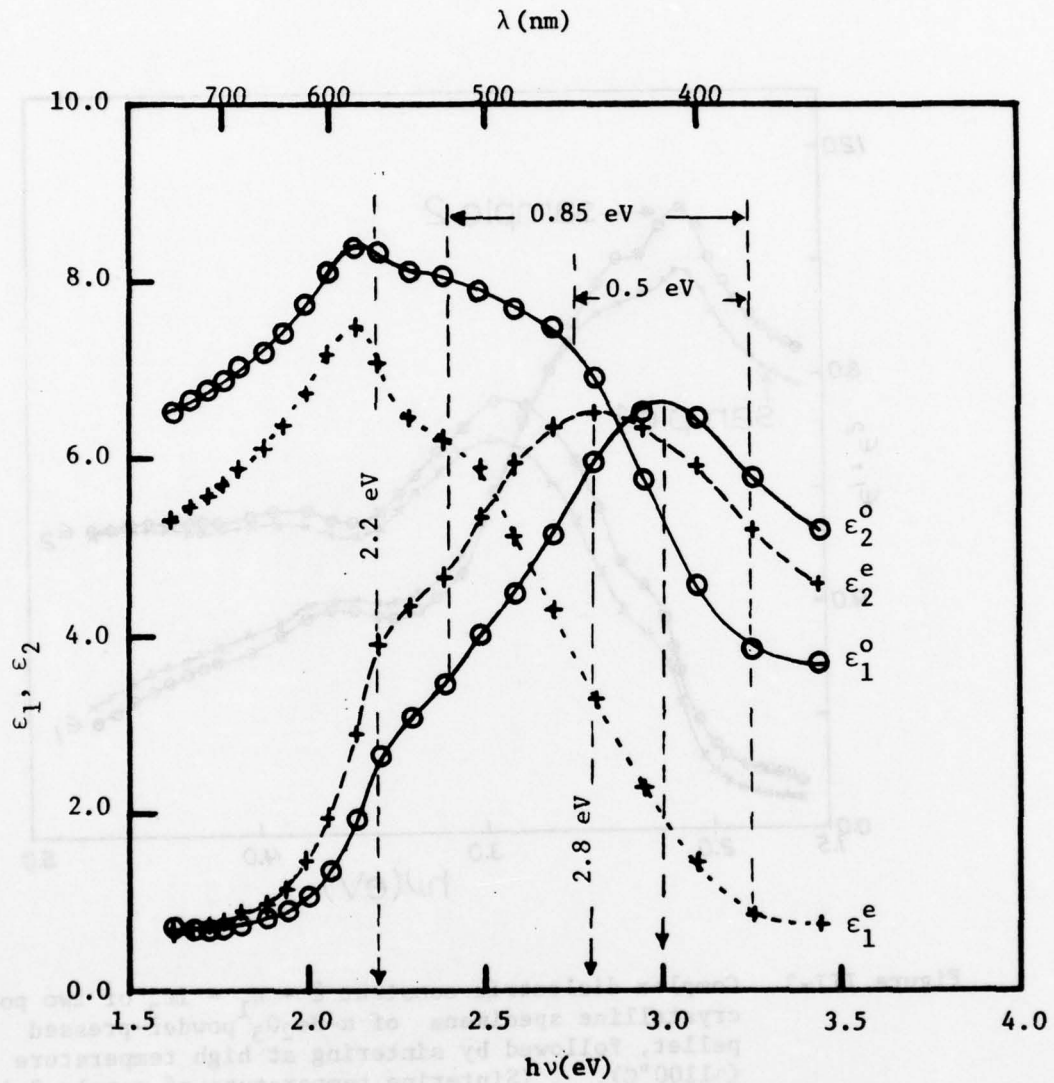


Figure III-4. Complex dielectric constants of single crystal α - Fe_2O_3 : solid lines for $\hat{\epsilon}^o (= \epsilon_1^o - i\epsilon_2^o)$, the complex dielectric constant for the ordinary ray; dashed lines for $\hat{\epsilon}^e (= \epsilon_1^e - i\epsilon_2^e)$ for the extraordinary ray.

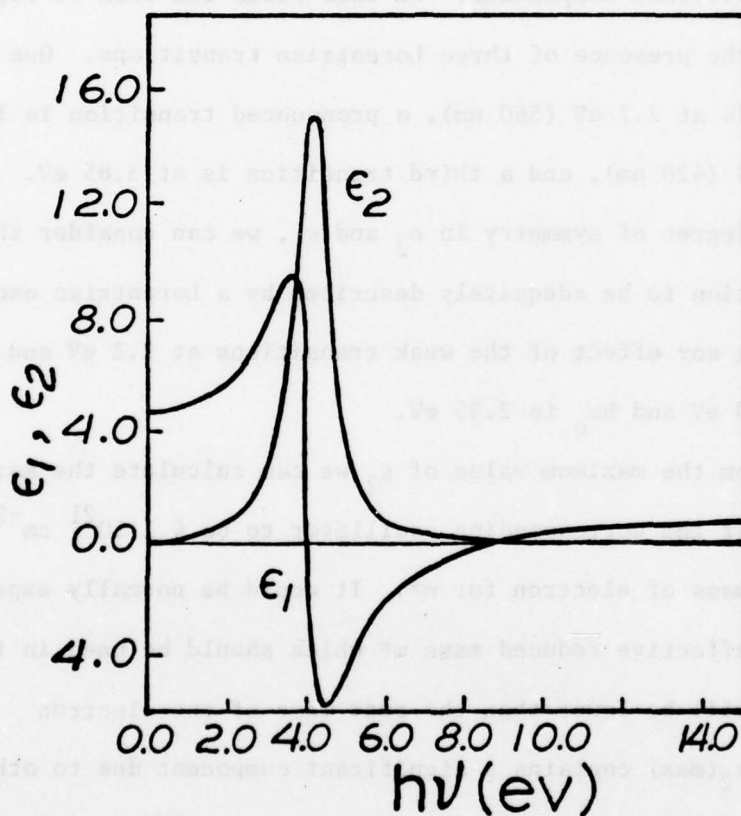


Figure III-5. Complex dielectric constant spectrum for the Lorentz oscillator model. Curves calculated for $\hbar\omega_0 = 4$ eV, $\hbar\Gamma = 1$ eV, and $4\pi Ne^2/m^* = 60$ (see text for details) (95).

$$\epsilon_2(\text{max}) = 4\pi N f e^2 / (m^* \Gamma \omega_0) \quad (\text{III-30})$$

Where N is the density of electrons bound with resonance frequency ω_0 and f the transition probability. To a first approximation the optical properties of materials containing more than one oscillator sufficiently separated in frequency can be represented by the sum of the individual components. On this basis the data of Fig. III-3 suggests the presence of three Lorentzian transitions. One weak absorber is at 2.2 eV (560 nm), a pronounced transition is located at 2.95 eV (420 nm), and a third transition is at 3.85 eV. From the high degree of symmetry in ϵ_2 and ϵ_1 , we can consider the 2.95 eV transition to be adequately described by a Lorentzian oscillator. Neglecting any effect of the weak transitions at 2.2 eV and 3.85 eV, $\hbar\Gamma$ is 0.80 eV and $\hbar\omega_0$ is 2.95 eV.

From the maximum value of ϵ_2 we can calculate the maximum value of Nf of the corresponding oscillator to be $4.1 \cdot 10^{21} \text{ cm}^{-3}$ using the rest mass of electron for m^* . It would be normally expected that the effective reduced mass m^* which should be used in this calculation will be lower than the rest mass of the electron and that $\epsilon_2(\text{max})$ contains a significant component due to other oscillators and background. These factors will significantly reduce the calculated value of Nf . Since the concentration of Fe in $\alpha\text{-Fe}_2\text{O}_3$ is $3.94 \cdot 10^{22} \text{ cm}^{-3}$, the product Nf is much less than 10%. At this point it is difficult to make any quantitative statement concerning the small peaks at 2.2 eV and 3.85 eV, but it is qualitatively clear

that these absorbers are much weaker than that at 2.95 eV. The absorber at 2.2 eV may be due to impurities or a forbidden transition made permissible by the distortion of the lattice. The absorber at 3.85 eV is difficult to identify as to origin at this stage.

Further, from the Kramers-Kronig relation:

$$\epsilon_1(0) = 1 + (2/\pi) \cdot \int_0^{\infty} [\epsilon_2(\omega')/\omega'] \cdot d\omega' \quad (\text{III-31})$$

where $\epsilon_1(0)$ is the real dielectric constant at frequencies well below the optical transition frequencies but above the frequencies corresponding to molecular rearrangements (microwave) and lattice vibrations (IR).

In order to account for the low frequency values of ϵ_1 in Fig. III-4, it is necessary to have the second term in Eq. III-31 equal to ~ 6 . This can be achieved only when there is a strong contribution to the integral from an absorption peak beyond the range of the measurements (3.5 eV) in Fig. III-4. Such absorption is evident in Fig. III-3 above 3.5 eV for the polycrystalline $\alpha\text{-Fe}_2\text{O}_3$. Even so, there must still be a very pronounced transition in ϵ_2 above the range of measurements in either figure to account for $\epsilon_1(0)$. Such is likely to occur because of the 2p-4s gap, which Goodenough (97) expects to occur at about 5.5 to 6.0 eV and has been observed by Gardner *et al.* (96) at 5.6 eV in thin film of $\alpha\text{-Fe}_2\text{O}_3$.

The 2.2 eV minor peak probably corresponds to a d-d transition and the more substantial peak at 2.95 eV to a charge transfer transition (O 2p \rightarrow Fe 3d). The additional absorber (up to the photon energy used in this study) at 3.85 eV is also tentatively assign-

ed to a charge transfer process from the 2p state to a different 3d state. Detailed identification cannot be done until the higher photon energy portion of the spectrum (above 5.5 eV at least) is completed. This would be expected to include the $0\ 2p \rightarrow Fe\ 4s$ transition.

The solid curves and dashed curves of single-crystal hematite (shown in Fig. III-4) are for the direction perpendicular to the optic axis (the "ordinary" axis) and parallel (the "extraordinary" axis) to it respectively. The shift in peak position is from 3.0 eV to 2.8 eV for the ϵ_2^o and ϵ_2^e with crystallographic direction. These experimental results indicate the applicability of ellipsometry to the identification of orientational splittings in optical active materials.

V. Optical Spectra of Passive Film on Iron

The wavelength dependence of the complex dielectric constant ($\hat{\epsilon} = \epsilon_1 - i\epsilon_2$) is shown in Fig. III-6 for a passive film grown in borate buffer (pH 8.4) at 1.35 V and measured at 1.25 V with an angle of incidence of 68° . Ellipsometric measurements at $P = 45^\circ$, and $P = -45^\circ$ were averaged to obtain (Δ_o, Ψ_o, R_o) for the film-free iron and to obtain (Δ, Ψ, R_r) for the film in the wavelength region between 350 nm and 760 nm. The thickness was evaluated from the ellipsometric data by 3-P calculations, independently for each wavelength (see Table III) and found to be $40 \text{ \AA} \pm 10\%$ for all wavelengths. The spectra were evaluated from 2-P calculations using a weighted average thickness from 3-P calculations.

A minor peak is evident in ϵ_2 at 2.2 eV and a more substantial peak at or above 3.6 eV. It is possible to gain some insight as to the shape of the curve above 3.6 eV in Fig. III-6 on the basis of the Lorentz oscillator model used to analyze the $\alpha\text{-Fe}_2\text{O}_3$ data. Applying this model, the data in Fig. III-6 have been projected to higher energies (dashed line). To complete the symmetry of the ϵ_2 curve expected for a Lorentzian oscillator, the lowest energy for the peak is at ~ 3.6 eV.

The 2.2 eV peak probably corresponds to a d-d transition and the 3.6 eV peak to a charge transfer transition ($O 2p \rightarrow Fe 3d$). We believe the d states in the passive layer should be narrow relative to that in crystalline $\alpha\text{-Fe}_2\text{O}_3$ because of less long range ordering and less orbital overlap. The apparent broadening of the peak at

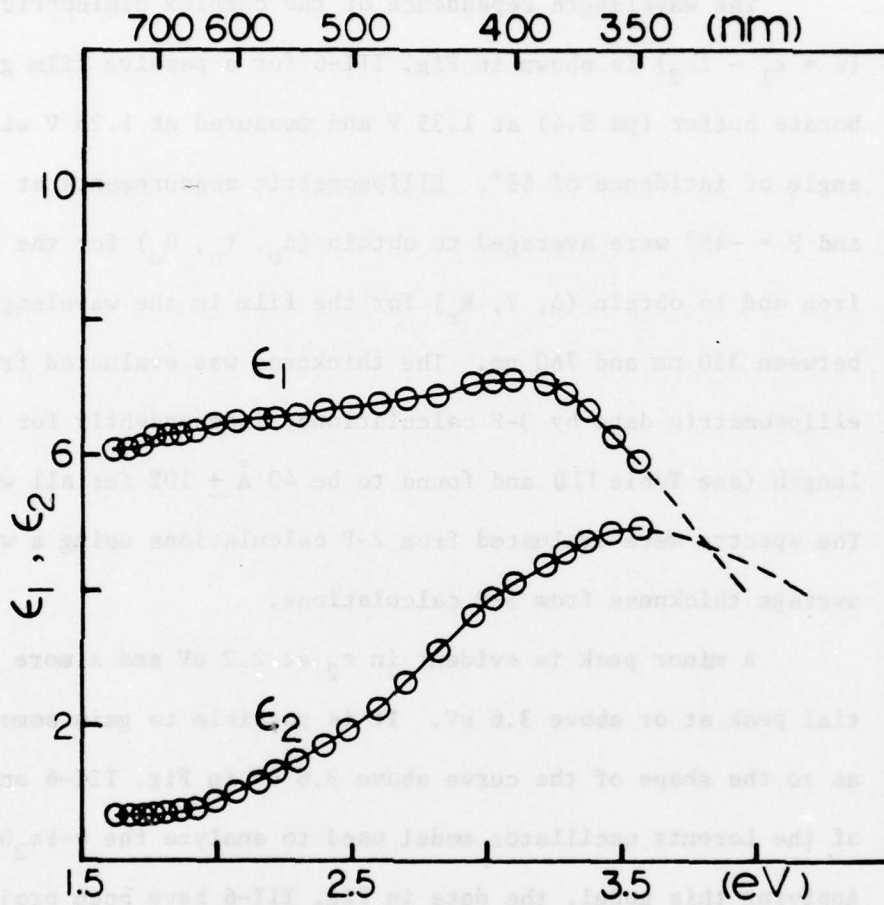


Figure III-6. Complex dielectric constant ($\epsilon_1 - i\epsilon_2$) of passive film on iron grown in borate buffer at pH 8.4 at 1.35 V and measured at 1.25 V. The dotted section is extrapolated using Lorentz model as a basis. Angle of incidence = 68° .

TABLE III: The n_2 , k_2 , and d (thickness) evaluated from ellipsometric data by 3-P method for passive film on iron grown in borate buffer at 1.35 V and measured at 1.25 V at $\phi = 68^\circ$

λ (nm)	n_2	k_2	d (Å)	λ (nm)	n_2	k_2	d (Å)
350	2.664	0.965	37.24	520	2.644	0.322	39.42
360	2.720	0.939	36.97	530	2.602	0.320	39.85
370	2.786	0.895	36.63	540	2.600	0.280	39.79
380	2.832	0.857	36.56	550	2.429	0.305	42.47
390	2.810	0.810	37.44	560	2.569	0.258	40.14
400	2.820	0.757	37.62	570	2.527	0.254	40.77
410	2.808	0.707	38.03	580	2.392	0.254	43.03
420	2.769	0.667	38.71	590	2.515	0.224	41.39
430	2.743	0.622	39.08	600	2.544	0.200	40.76
440	2.721	0.576	39.31	620	2.542	0.174	40.00
450	2.665	0.548	40.05	640	2.470	0.174	41.07
460	2.649	0.505	40.13	660	2.562	0.135	39.24
470	2.663	0.461	39.73	680	2.552	0.129	39.26
480	2.667	0.425	39.51	700	2.323	0.178	43.43
490	2.638	0.399	39.80	720	2.603	0.094	38.15
500	2.615	0.377	40.07	740	2.617	0.087	37.66
510	2.631	0.348	39.74	760	2.600	0.094	37.94

~ 3.6 eV in Fig. III-6 is believed to be the result of a distribution of defect states and the presence of protons rather than intrinsic width of the involved energy levels. The proton incorporation makes the charge transfer process ($O\ 2p \rightarrow Fe\ 3d$) have a higher transition energy because the proton interaction with the O lowers the O 2p energy. Mössbauer studies of O'Grady et al. (46) provide evidence for polymer-like structures for the passive film. Further evidence for the proton incorporation in the passive film by transient ellipsometric and ESCA techniques will be discussed in a later section. The transition corresponding to the gap between the predominately oxygen 2p band and the predominately iron 4s band probably occurs at much higher photon energies (>5.6 eV) than the 2p-3d transition.

Figures III-7 and III-8 show the complex dielectric constant ($\epsilon_1 - i\epsilon_2$) of a passive film grown at 1.15 V and measured at 1.05 V for two angles of incidence (65° for Fig. III-7 and 70° for Fig. III-8). The thickness was found to be $37 \text{ \AA} \pm 10\%$ for all wavelengths. Two spectra are practically identical in ϵ_1 and slightly different in ϵ_2 (less than 5%) for the different angles of incidence. This provides some evidence that the passive film are reasonably uniform and isotropic and that the surface roughness does not have a major effect. This conclusion, however, is based only on two different angles of incidence 5° apart. More experimental measurements over a much wider range of angle of incidence are needed for a definitive conclusion. The greater the anisotropy of the film, the larger the difference in the optical constants is expected to be as evaluated

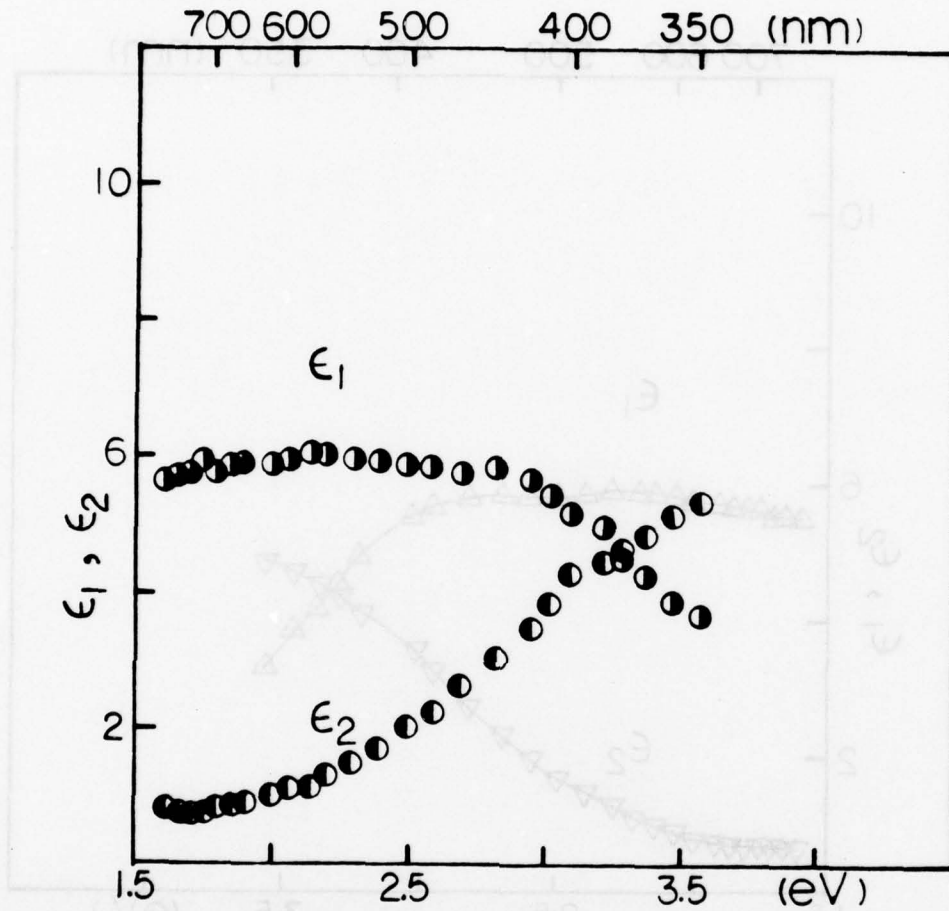


Figure III-7. Complex dielectric constant ($\epsilon_1 - i\epsilon_2$) of passive film on iron grown in borate buffer at pH 8.4 at 1.15 V and measured at 1.05 V. Angle of incidence = 65°.

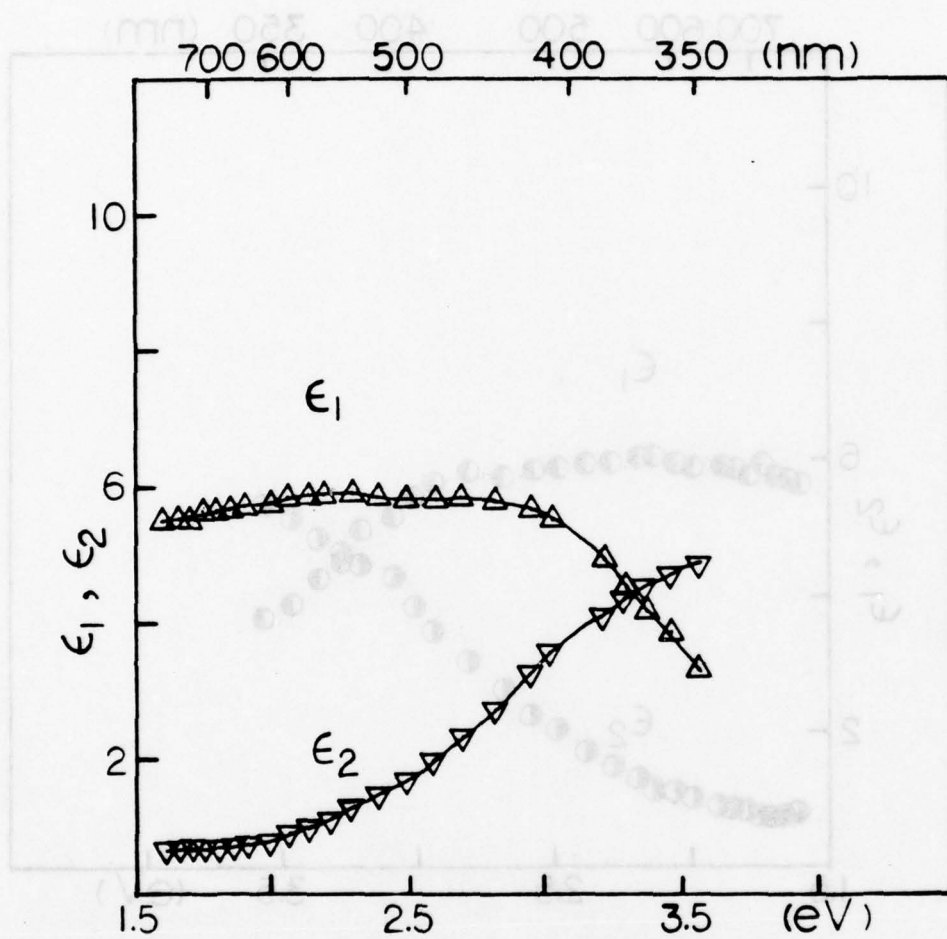


Figure III-8. Complex dielectric constant ($\epsilon_1 - i\epsilon_2$) of passive film on iron grown in borate buffer at pH 8.4 at 1.15 V and measured at 1.05 V. Angle of incidence = 70°.

at different angles of incidence (92).

A comparison of the spectra shown in Fig. III-6 and the spectra shown in Fig. III-8 for films grown at two different potentials revealed spectroscopic differences. The ϵ_1 for the passive film grown at 1.35 V and measured at 1.25 V with an angle of incidence $\phi = 68^\circ$ is greater than that for the film grown at 1.15 V and measured at 1.05 V with $\phi = 70^\circ$. The 2.2 eV minor peak for the former is greater than that for the latter film. Such is to be expected on the basis that the defect states (oxygen hole or Fe^{+4} ions) increase somewhat as the anodic potential increased from 1.05 V to 1.25 V (see Ref. 72). The broad peak in ϵ_2 at or above 3.6 eV is attributed to charge transfer ($2p \rightarrow 3d$) and the broadening is proposed to be caused by a combination of defect states and the presence of protons as proposed for Fig. III-6. This peak did not change appreciably for films grown at these two potentials, indicating that changes in the defect structure and proton concentration were not great enough to cause appreciable changes in the spectrum.

VI. Potentiostatic Anodic Oxidation

A. Single Potential Step Oxidation

The logarithmic current versus logarithmic time plots of an iron electrode stepped from -0.25 V to different anodic potentials 0.75 V, 0.95 V, and 1.15 V are shown in Fig. III-9a. The plots of $\log i$ vs $\log t$ are linear except at beginnings of the potential steps. The deviation from linearity can be explained on the basis that the current in the early stage of oxidation has two major contributions, e.g., from initial film formation and double-layer charging. Figure III-9b shows the charge Q (after the current integration) vs $\log t$ increases linearly except for the early stage (up to 2 seconds after the start of the step). The time duration before linearity behavior is achieved is the same for both Q vs $\log t$ and $\log i$ vs $\log t$.

Typical ellipsometric parameters (Δ , Ψ , and $\Delta R/R\%$) as well as Q vs $\log t$ plots are shown in Fig. III-10. This figure demonstrates that the time dependence of the ellipsometric parameters have corresponding features to that for charge Q . They are also linear logarithmic dependence on time at longer times. Figure III-11a shows the Ψ vs $\log t$ plots of an iron electrode stepped from -0.25 V to different anodic potentials 0.75 V, 0.95 V, 1.15 V, and 1.35 V at $\phi = 68^\circ$ and $\lambda = 450$ nm, which wavelength is in the neighborhood of maximum $\Delta\Delta$ and sign reversal in $\Delta\Psi$. The Ψ vs $\log t$ plots for anodic potentials of 0.95 V, 1.15 V, and 1.35 V show that the Ψ values increase rapidly at the very early state of the step (less than

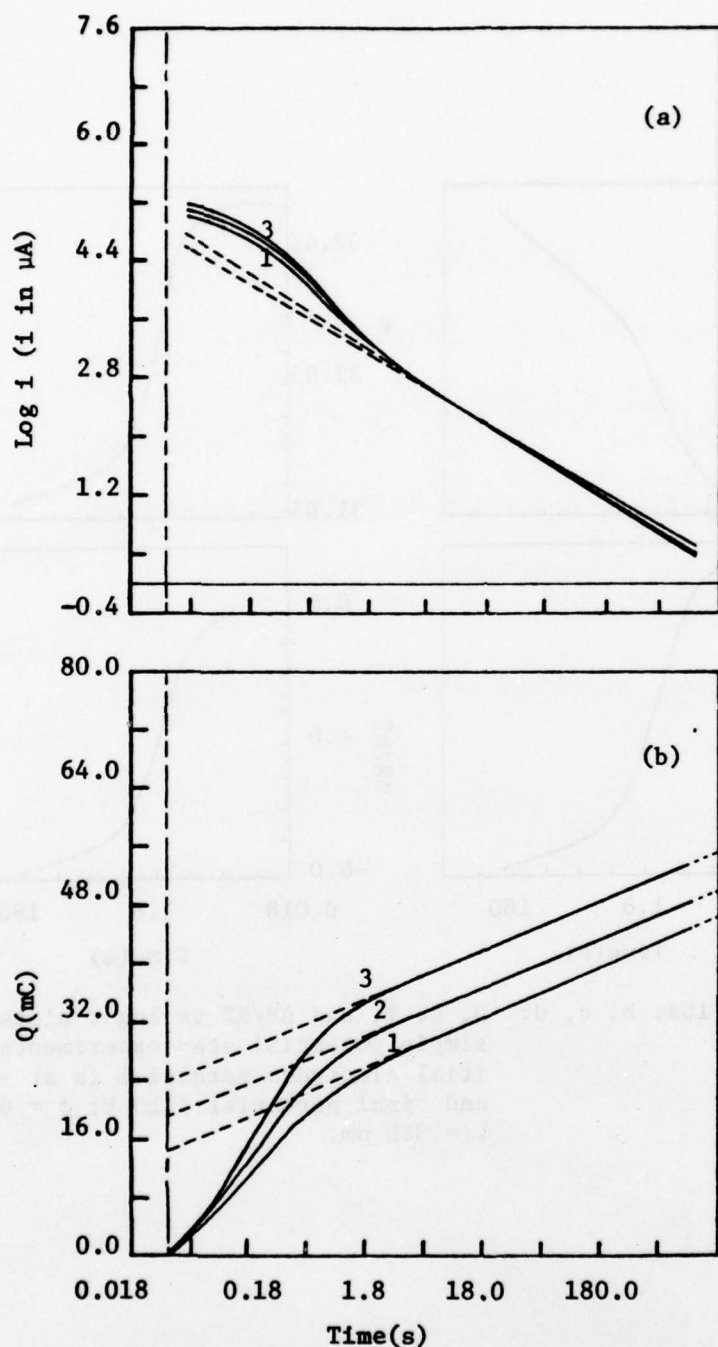


Figure III-9a, 9b: $\text{Log } i$ vs $\log t$ and Q (charge after current integration) vs $\log t$ plots during single potential steps experiments: the electrode potential initially is at -0.25 V; the final potentials are 0.75 V for curves 1, 0.95 V for curves 2, and 1.15 V for curves 3. Electrode area: 6.44 cm^2 .

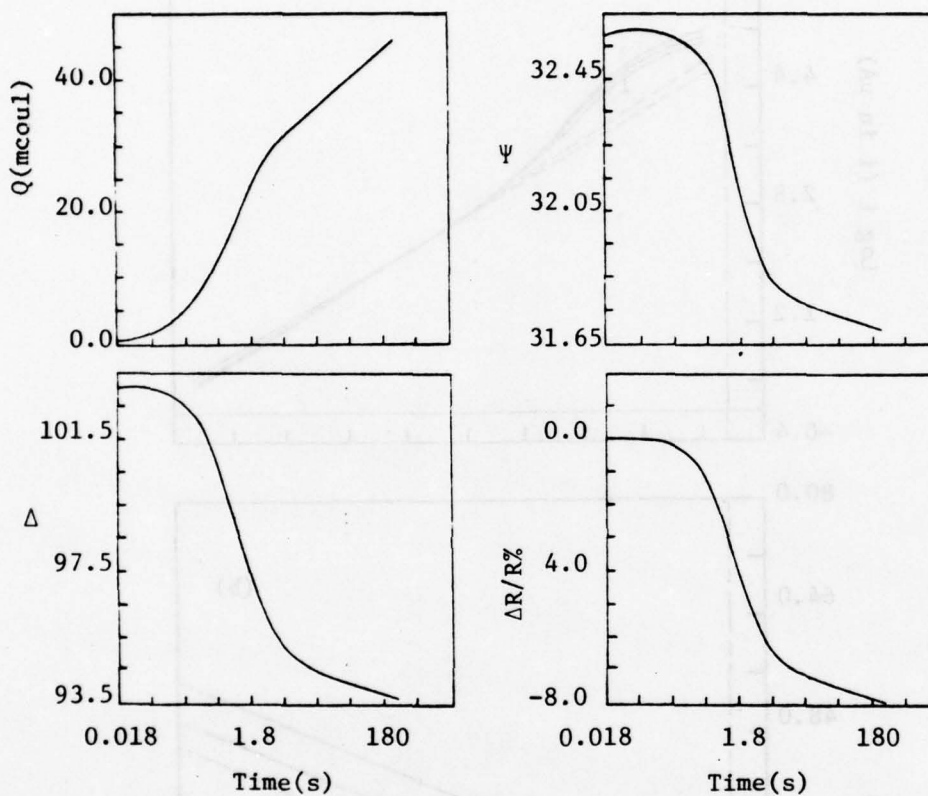


Figure III-10a, b, c, d: Q , Δ , Ψ , and $\Delta R/R\%$ vs $\log t$ plots for simple potential step experiments: initial electrode potential is at -0.25 V and final potential 1.15 V; $\phi = 68^\circ$ and $\lambda = 380$ nm.

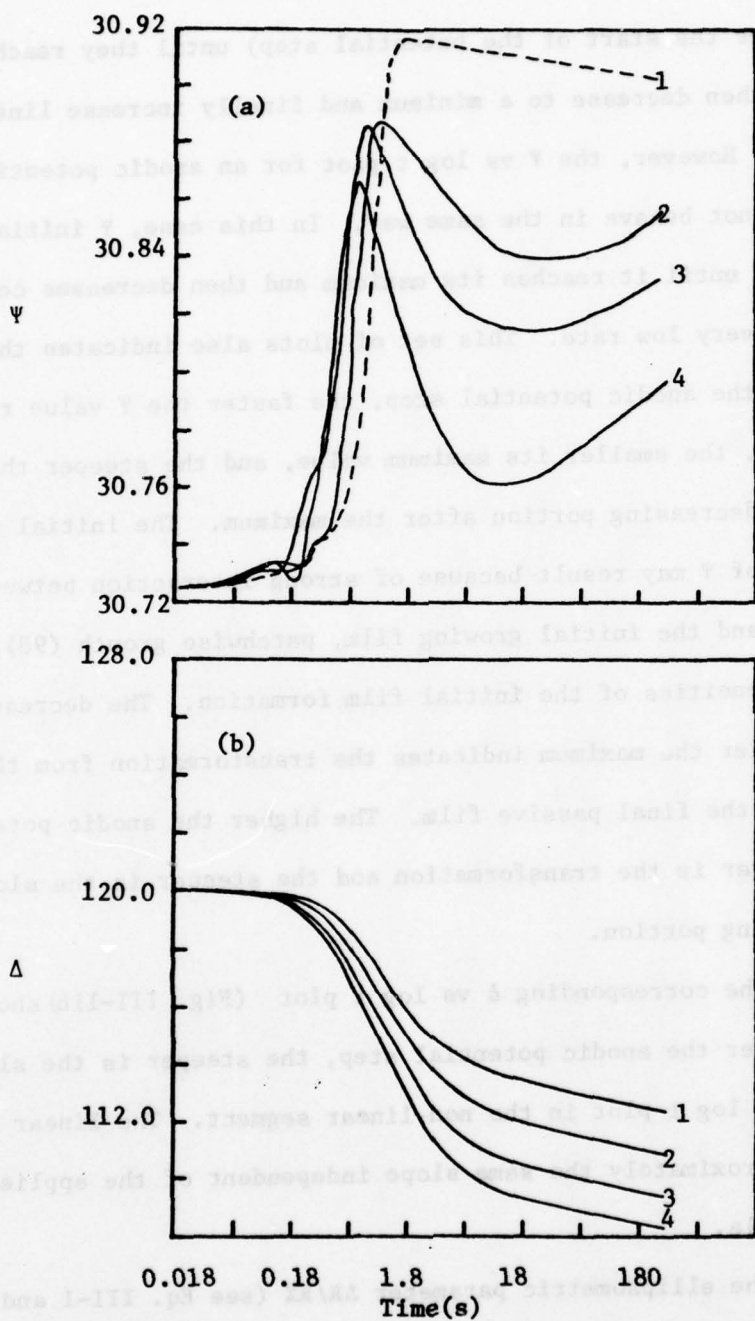


Figure III-11a, 11b: The ellipsometric parameters (Δ , Ψ) vs log t plots for single potential step experiments: the initial electrode potential was -0.25 V; the final potentials were 0.75 V for curves 1; 0.95 V for curves 2; 1.15 V for curves 3; and 1.35 V for curves 4. $\lambda = 450$ nm; $\phi = 68^\circ$.

2s after the start of the potential step) until they reach a maximum, then decrease to a minimum and finally increase linearly with $\log t$. However, the Ψ vs $\log t$ plot for an anodic potential of 0.75 V does not behave in the same way. In this case, Ψ initially changes rapidly until it reaches its maximum and then decreases continuously with a very low rate. This set of plots also indicates that the higher the anodic potential step, the faster the Ψ value reaches its maximum, the smaller its maximum value, and the steeper the slope of the decreasing portion after the maximum. The initial rapid increase of Ψ may result because of strong interaction between the substrate and the initial growing film, patchwise growth (98), or other inhomogeneities of the initial film formation. The decreasing portion after the maximum indicates the transformation from the initial film to the final passive film. The higher the anodic potential, the faster is the transformation and the steeper is the slope of the decreasing portion.

The corresponding Δ vs $\log t$ plot (Fig. III-11b) shows that the higher the anodic potential step, the steeper is the slope of the Δ vs $\log t$ plot in the non-linear segment. The linear portions show approximately the same slope independent of the applied anodic potentials.

The ellipsometric parameter $\Delta R/R\%$ (see Eq. III-1 and III-2) vs $\log t$ plots (Fig. III-12) show a much more complicated behavior. The film thickness, the absorbing properties of the growing film,

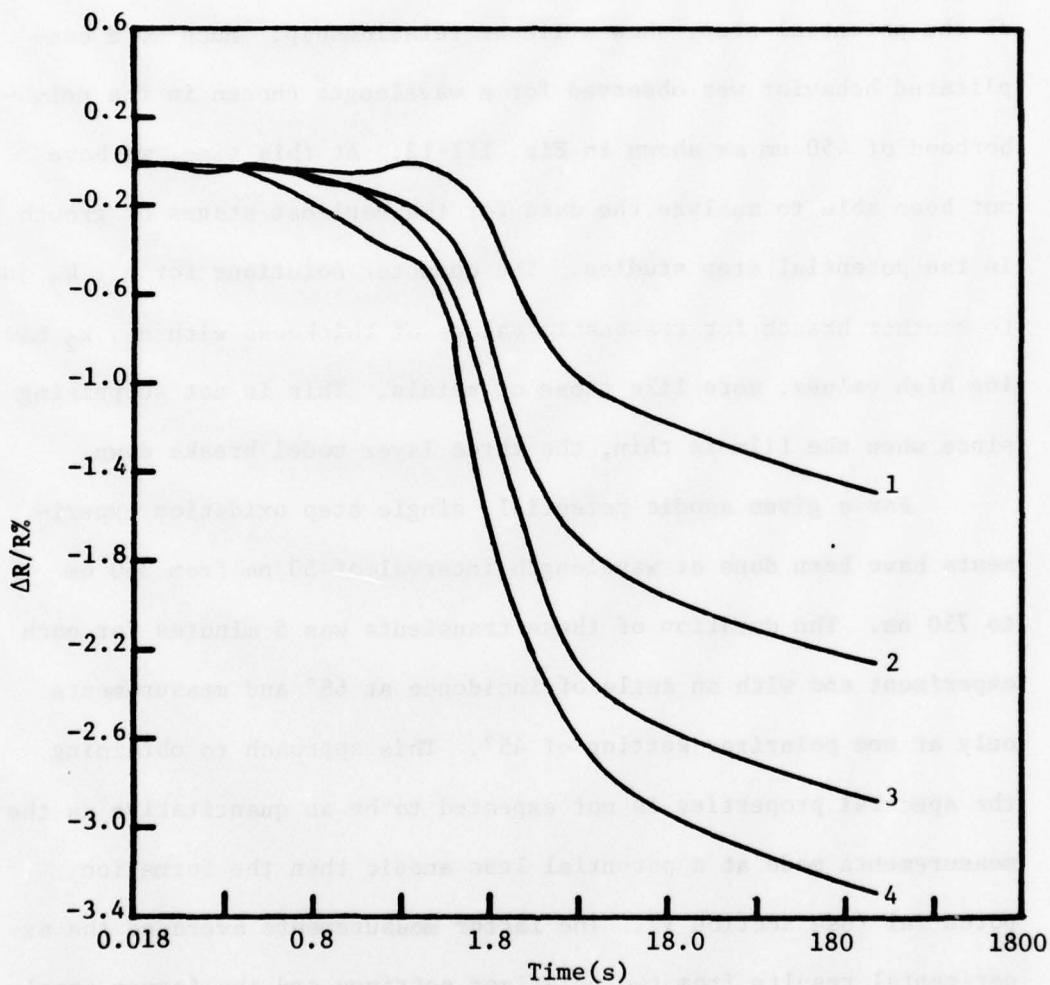


Fig. III-12: The ellipsometric parameter $\Delta R/R\%$ vs $\log t$ plots for single potential step experiments: the initial electrode potential was -0.25 V; the final potentials were 0.75 V for curve 1; 0.95 V for curve 2; 1.15 V for curve 3; and 1.35 V for curve 4; $\lambda = 450$ nm; $\phi = 68^\circ$.

anisotropy (98), and the state of the sample (e.g., roughness factor of the sample surface) (99,100) will contribute to the change of this parameter. The $\Delta R/R\%$ vs $\log t$ plots, after 2s from the start of the potential step, show a linear relationship. Much more complicated behavior was observed for a wavelength chosen in the neighborhood of 450 nm as shown in Fig. III-12. At this time, we have not been able to analyze the data for the earliest stages of growth in the potential step studies. The computer solutions for n_2 , k_2 jump to another branch for reasonable values of thickness with n_2 , k_2 having high values, more like those of metals. This is not surprising since when the film is thin, the three layer model breaks down.

For a given anodic potential, single step oxidation experiments have been done at wavelength intervals of 50 nm from 350 nm to 750 nm. The duration of these transients was 5 minutes for each experiment and with an angle of incidence at 68° and measurements only at one polarizer setting of 45° . This approach to obtaining the spectral properties is not expected to be as quantitative as the measurements made at a potential less anodic than the formation potential (see Section V). The latter measurements averaged the experimental results from two polarizer settings and the former involved only one polarizer setting. Qualitatively, both sets of experimental results are consistent with one another. Only k_2 and film thickness vs $\log t$ plots are shown in Fig. III-13 and III-14 respectively. The quantity n_2 shows relatively little detail, which is

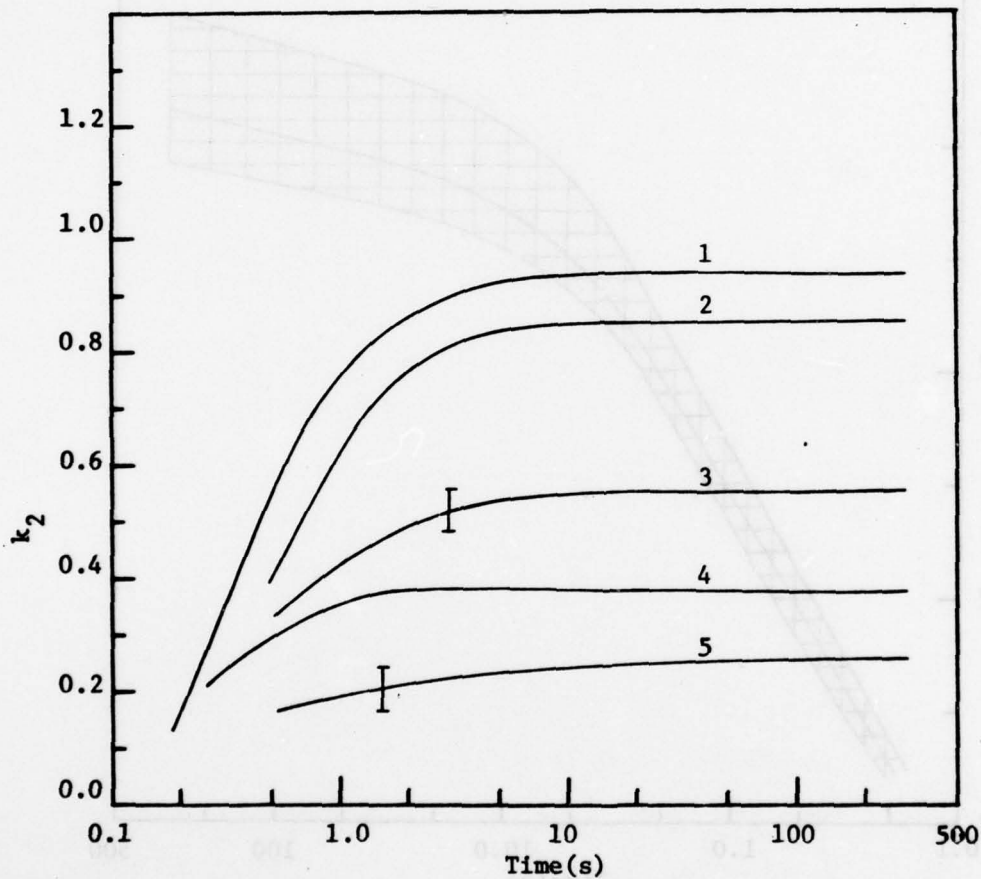


Figure III-13: The k_2 vs $\log t$ plots for a single potential step oxidation (-0.25 V to 1.15 V) at $\phi = 68^\circ$ and wavelengths at: 1. at 350 nm; 2. at 380 nm; 3. at 420 nm; 4. at 480 nm; 5. at 550 nm.

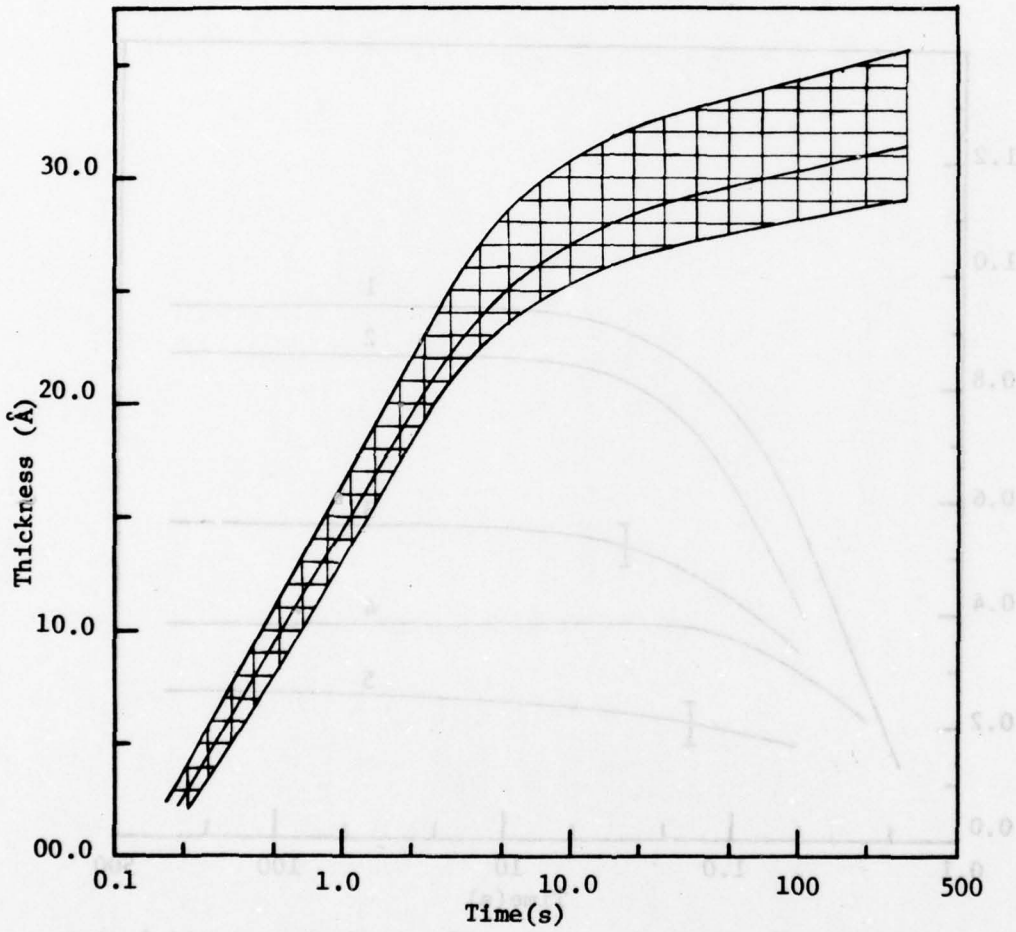


Figure III-14: The range of thickness (d) vs $\log t$ plots for the corresponding experiments shown in Fig. III-13. Cross sections correspond to scatter of data.

obscured by the scatter at short time. The k_2 vs log t plots show rather constant values except at the very beginning of the step. The d vs log t plots shown in Fig. III-14 indicate the range of values for thickness at all wavelengths studied. The d vs log t plot for each individual wavelength shows linear behavior after the corresponding k_2 values reaches constant values. The k_2 and thickness as well as n_2 shows much scattering at the early stage. We attribute this scatter to the noise in the data collecting process (see Chapter II).

Figures III-15 and III-16 show the corresponding k_2 vs Q and d vs Q plots. The k_2 values are reasonably constant after 3.7 mC/cm² of charge has been passed. This amount of charge is approximately equivalent to 20 Å of anhydrous ferric oxide formed on the electrode surface. The k_2 values at the early stage change substantially, indicating the growing oxide film changes its nature as the film grows thicker.

Single step oxidation experiments have been done at some wavelengths with anodic potentials of 0.75, 0.95, 1.35, and 1.65 V. Figures III-17a and b show the n_2 , k_2 vs log t and thickness vs log t plots for the experiments at 460 nm and an angle of incidence 68°. Figure III-17 b shows that the thickness was a logarithmic function of time a few seconds after the start of the potential step. The time to reach the logarithmic growth region is potential dependent. Furthermore, reciprocal thickness exhibits a similar range of linear dependence on log t. The thickness also reasonably well fits

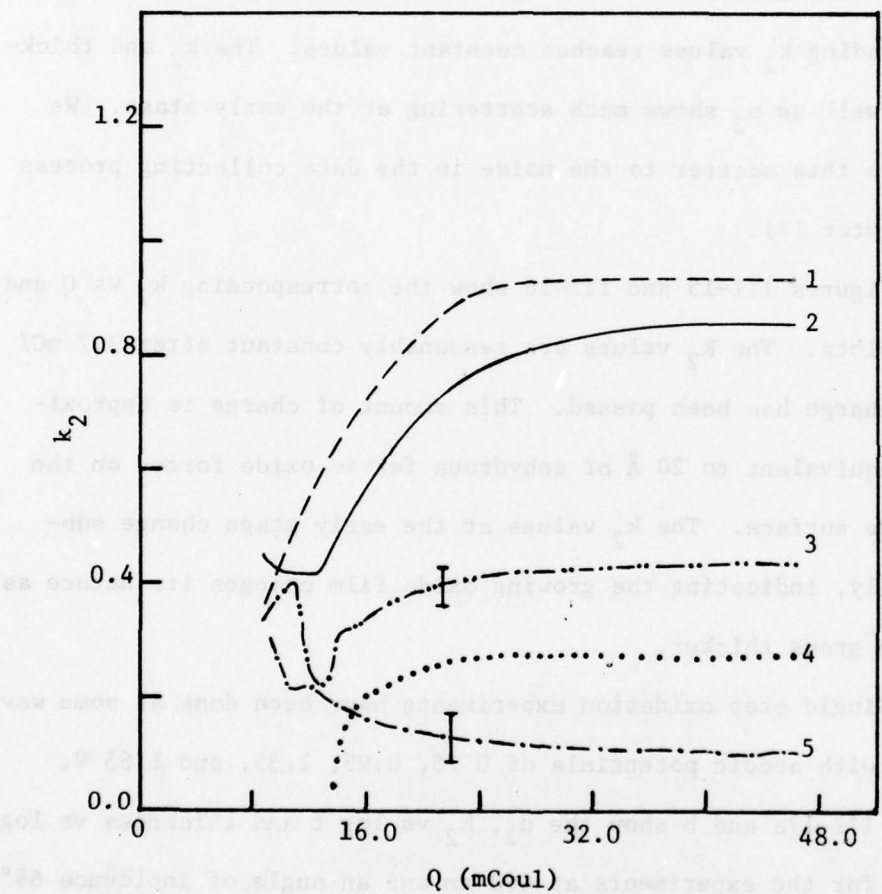


Figure III-15. The k_2 vs Q plots for the corresponding experiments shown in Fig. III-13: 1. 350 nm; 2. 380 nm; 3. 450 nm; 4. 550 nm; 5. 650 nm. Electrode area 6.44 cm^2 .

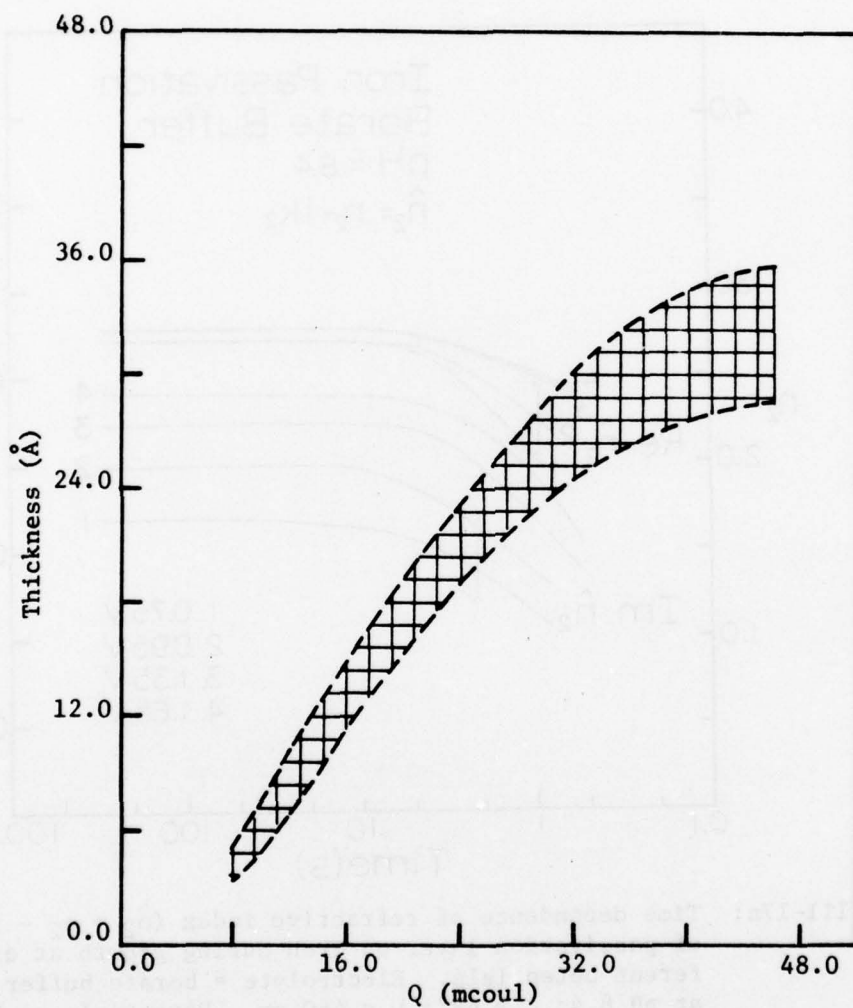


Figure III-16. The range of thickness (d) vs Q plots for the corresponding experiments shown in Fig. III-13. Electrode area 6.44 cm^2 .

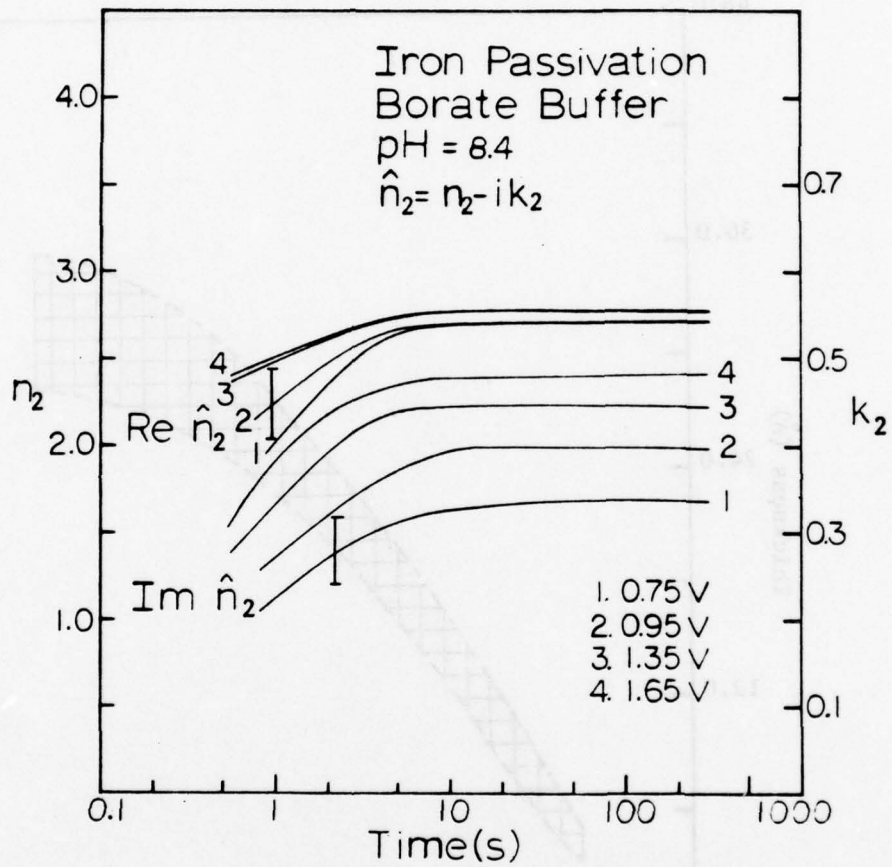


Figure III-17a: Time dependence of refractive index ($\hat{n}_2 = n_2 - ik_2$) of passivation layer on iron during growth at different potentials. Electrolyte = borate buffer at pH 8.4; $\phi = 68^\circ$; $\lambda = 460$ nm. Potentials vs RHE.

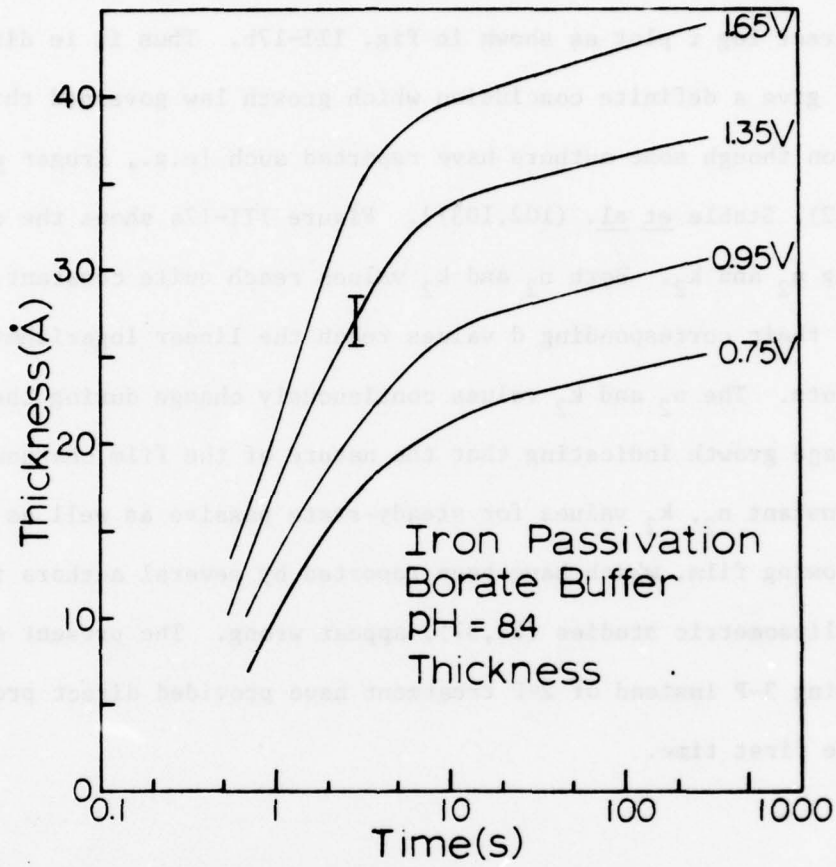


Figure III-17b: Time dependence of thickness of passivation layer on iron during growth at different potentials. Electrolyte: Borate buffer at pH 8.4; Temp. $\sim 25^{\circ}\text{C}$, $\phi = 68^{\circ}$; $\lambda = 460 \text{ nm}$. Potentials vs RHE.

the time dependence given by the equation of Ghez (101) besides the direct log t plot as shown in Fig. III-17b. Thus it is difficult to give a definite conclusion which growth law governed this system even though some authors have reported such [e.g., Kruger et al. (22), Stahle et al. (102,103)]. Figure III-17a shows the corresponding n_2 and k_2 . Both n_2 and k_2 values reach quite constant values as their corresponding d values reach the linear logarithmic segments. The n_2 and k_2 values continuously change during the early stage growth indicating that the nature of the film changes. The constant n_2 , k_2 values for steady-state passive as well as for the growing film, which have been reported by several authors in earlier ellipsometric studies (22,37), appear wrong. The present studies using 3-P instead of 2-P treatment have provided direct proof for the first time.

B. Progressive Step Oxidation

Figure III-18 shows the current vs log t plots for the progressive step oxidation from 0.95 V to 1.15 V and 0.95 V to 1.35 V respectively. Prior to these steps, the electrode surface has grown a stable oxide for 30 min by single step oxidation from -0.25 V to 0.95 V as mentioned in the previous section. The current vs log t plots show that a current increases rapidly to a maximum, then decreases to a plateau for more than a few tens of seconds and finally decreases to a very small value. The time and the current density during the current plateau region show an appreciable difference: 10 s and $11.2 \mu\text{A}/\text{cm}^2$ for the 0.95 V to 1.35 V step; and 60 s and $2 \mu\text{A}/\text{cm}^2$ for the 0.95 V to 1.15 V step. Both steps, however, show that the charge passed during the initial step to the end of the current plateau minus the charge passed during the initial step (due to double layer charging) to the very beginning of the current plateau is about $115 \mu\text{C}/\text{cm}^2$. This charge is about one monolayer electron per surface iron atom of the metal passed during the current plateau region.

The corresponding ellipsometric parameters Δ , Ψ , as well as i , Q vs log t plots $\lambda = 550 \text{ nm}$ (Fig. III-19) did not show the initial maximum and plateau regions. They did, however, show rapid change at the end of the plateau region indicating the film resuming its growth only after the end of the current plateau.

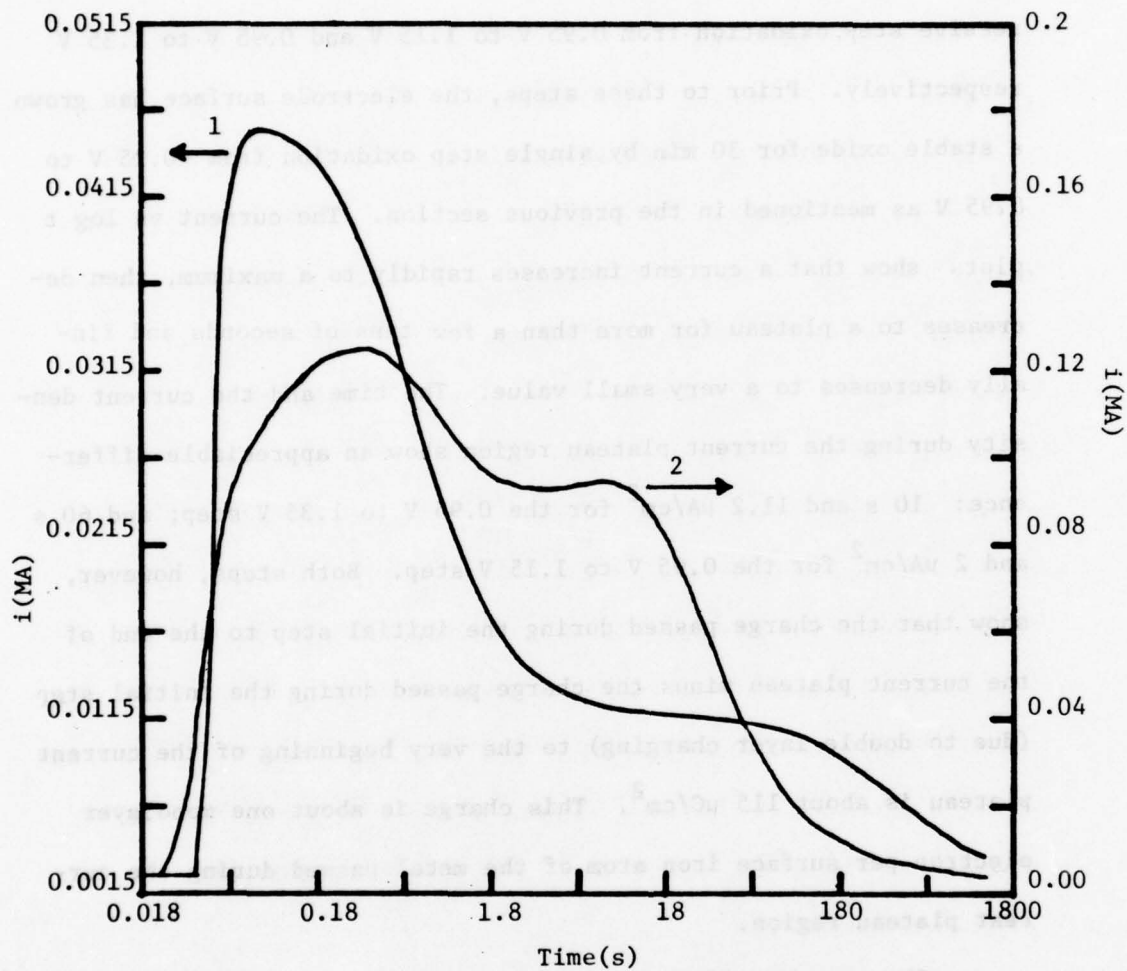


Fig. III-18: i vs $\log t$ plots for the progressive step oxidation. Curve 1 for 0.95 to 1.15 V and curve 2 for 0.95 to 1.35 V. Electrode area = 6.44 cm^2 . Electrode potential vs RHE.

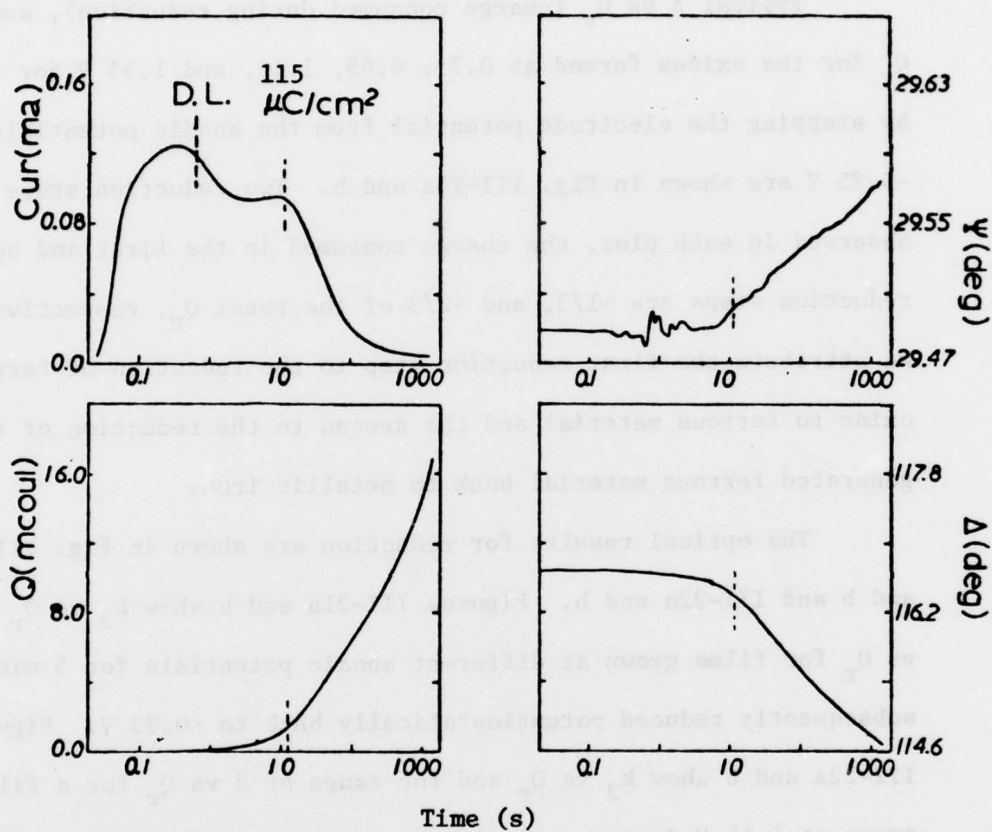


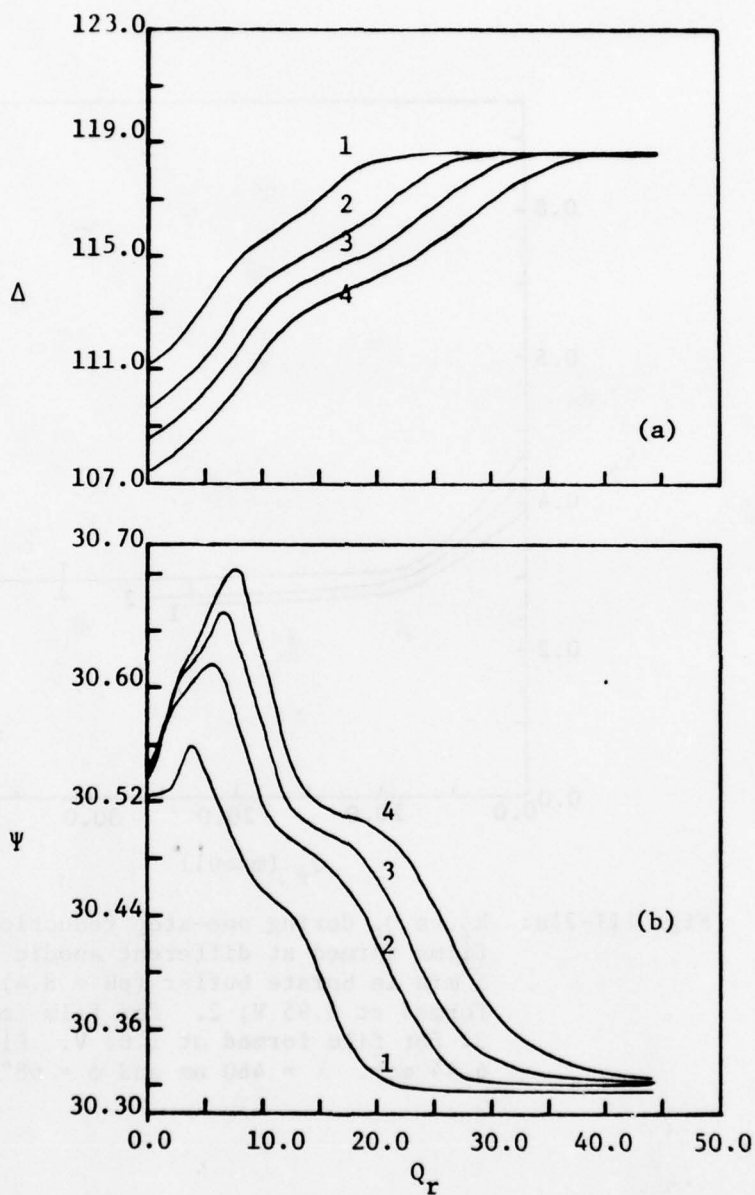
Fig. III-19: i , Q , Δ , Ψ vs $\log t$ for a progressive step oxidation: the electrode potential was raised from 0.95 V to 1.35 V; $\lambda = 550$ nm and $\phi = 68^\circ$ (see text for details).

VIII. Potentiostatic Oxide Reduction

A. Single Step Reduction

Typical Δ vs Q_r (charge consumed during reduction), and Ψ vs Q_r for the oxides formed at 0.75, 0.95, 1.15, and 1.35 V for 5 min by stepping the electrode potential from the anodic potentials to -0.25 V are shown in Fig. III-20a and b. Two reduction steps are observed in each plot, the charge consumed in the first and second reduction steps are $\sim 1/3$, and $\sim 2/3$ of the total Q_r , respectively. We attribute the first reduction step to the reduction of ferric oxide to ferrous material and the second to the reduction of the generated ferrous material back to metallic iron.

The optical results for reduction are shown in Fig. III-21a and b and III-22a and b. Figures III-21a and b show k_2 vs Q_r and d vs Q_r for films grown at different anodic potentials for 5 min and subsequently reduced potentiostatically back to -0.25 V. Figures III-22a and b show k_2 vs Q_r and the range of d vs Q_r for a film grown at 1.15 V during a single potentiostatic reduction process at different wavelengths, respectively. All these figures show a sharp break at the point where approximately one third of the Q_r is consumed. The values calculated for k_2 for the film are constant after $\sim 1/4$ to $\sim 1/3$ of Q_r has passed during the reduction process and are significantly different from those found for the initial passive films. This phenomenon is independent of the wavelength used and of the anodic formation potentials. This constancy indicates that a new single species has been generated. In addition, from the d vs



Figures III-20a, b: Typical Δ vs Q_r (charge consumed during reduction) and Ψ vs Q_r plots respectively for the oxides formed at different potentials for 5 min: 1. 0.75 V; 2. 0.95 V; 3. 1.15 V; 4. 1.35 V. The final reduction potential -0.25 V. $\lambda = 460$ nm and $\phi = 68^\circ$.

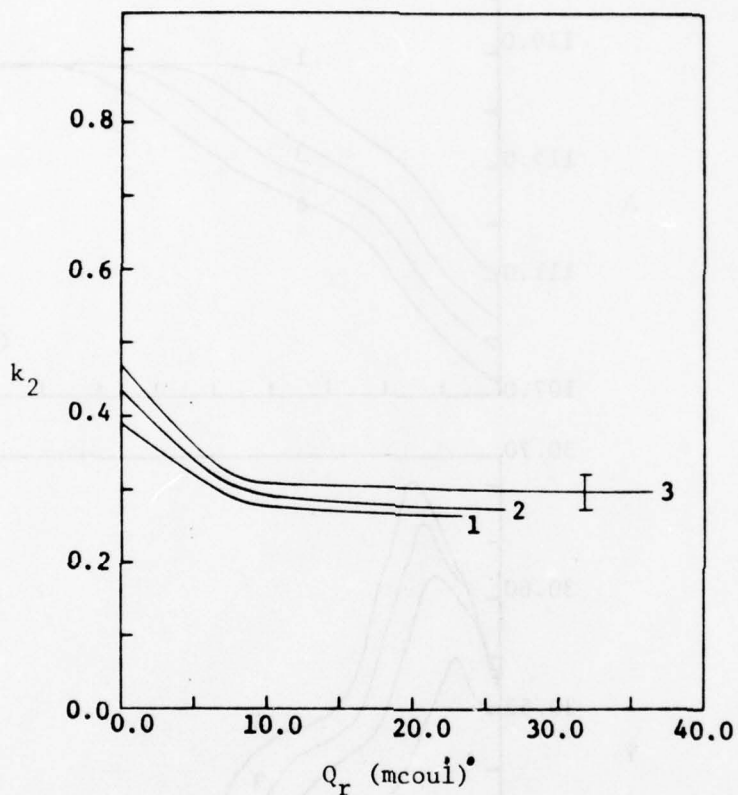


Fig. III-21a: k_2 vs Q_r during one-step reduction for passive films formed at different anodic potentials for 5 min in borate buffer (pH = 8.4): 1. for film formed at 0.95 V; 2. for film formed at 1.15 V; 3. for film formed at 1.65 V. Electrode area 6.44 cm². $\lambda = 460$ nm and $\phi = 68^\circ$.

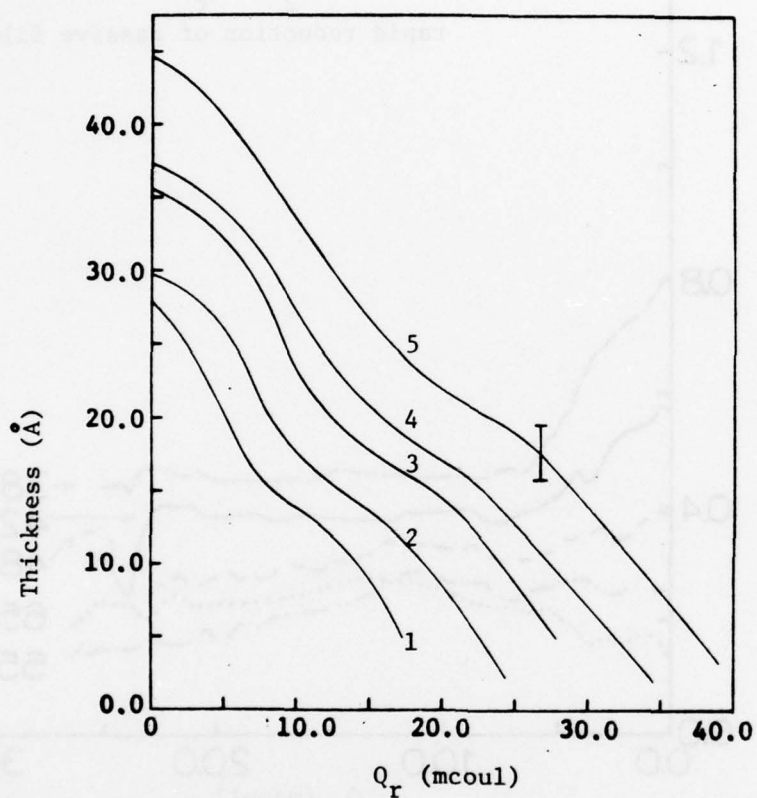


Fig. III-21b: d (thickness) vs Q_r during one-step reduction for passive films formed at different anodic potentials for 5 min in borate buffer solution (pH 8.4): 1. for film formed at 0.75 V; 2. for film formed at 0.95 V; 3. for film formed at 1.15 V; 4. for film formed at 1.35 V; 5. for film formed at 1.65 V. Electrode area 6.44 cm^2 . $\lambda = 460 \text{ nm}$ and $\phi = 68^\circ$.

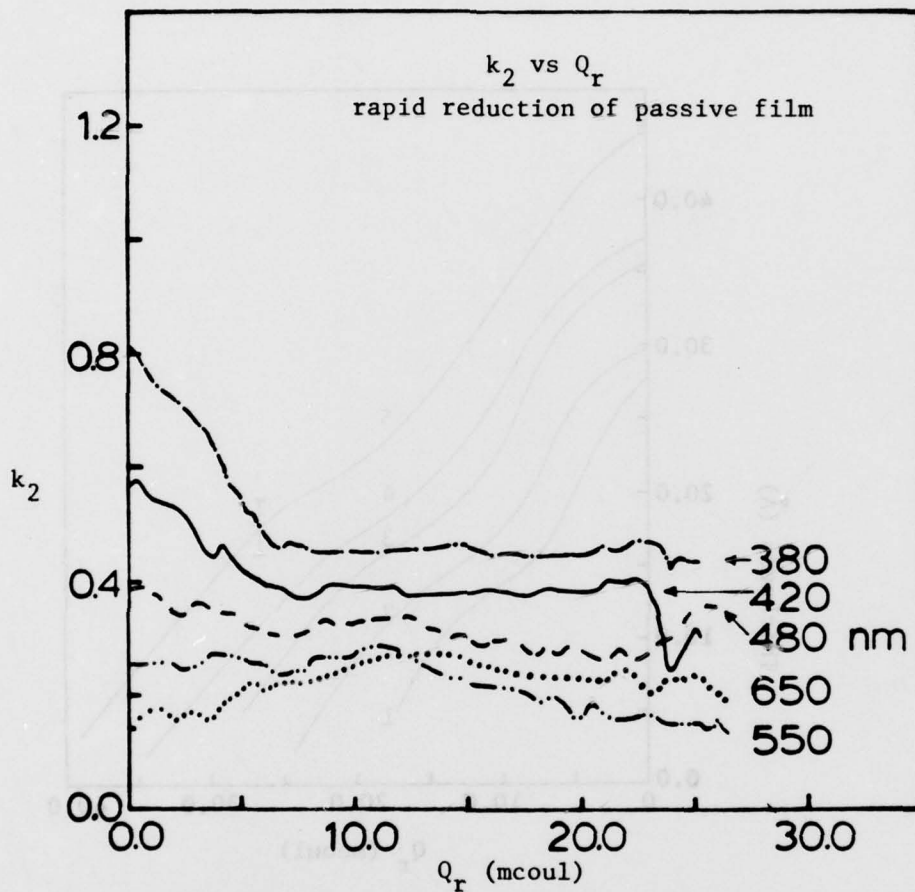


Figure III-22a: The k_2 spectrum vs Q_r for a film grown at 1.15 V for 5 min and subsequently reduced potentiostatically back to -0.25 V at each wavelength. Electrolyte = borate buffer at pH 8.4; Temp. ~ 25 C, $\phi = 68^\circ$. Electrode area 6.44 cm^2 and potentials vs RHE.

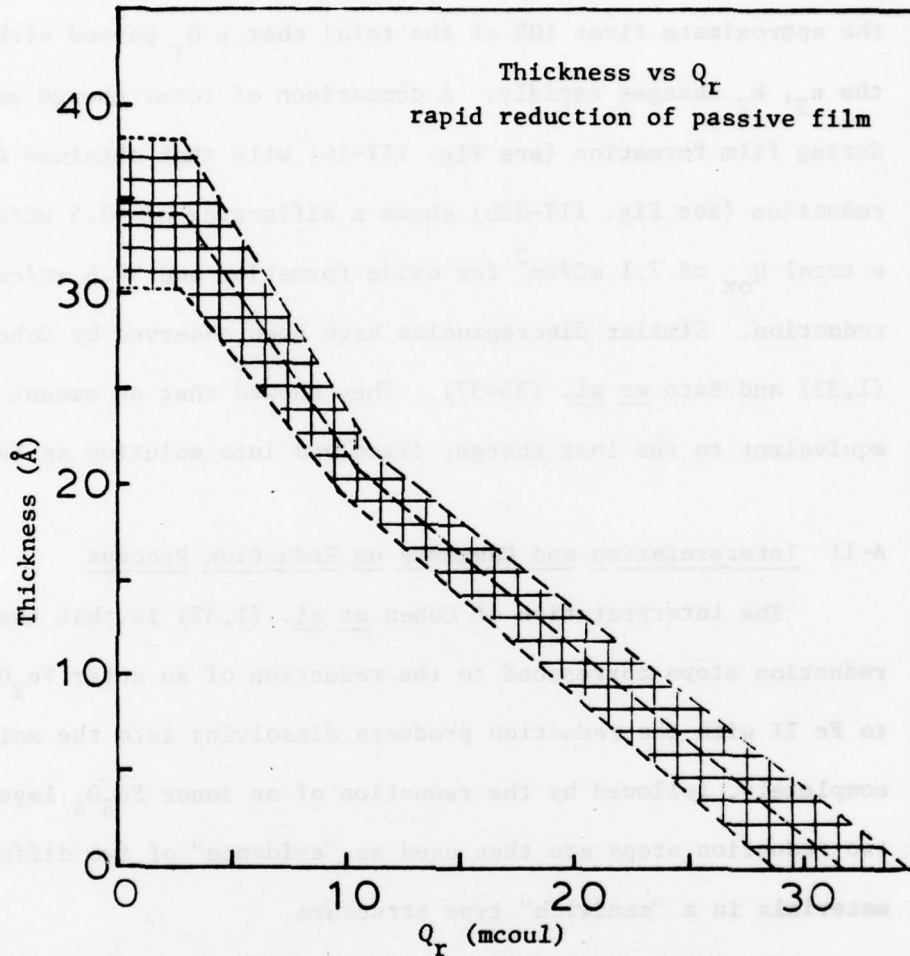


Figure III-22b: The range of d (thickness) vs Q_r for a film grown at 1.15 V for 5 min and subsequently reduced potentiostatically back to -0.25 V at each wavelength (350 nm to 750 nm). Electrolyte = borate at pH 8.4; temp. ~ 25 C, $\phi = 68^\circ$. Electrode area 6.44 cm² and potentials vs RHE.

Q_r plots, it appears that no significant change in d occurs during the approximate first 10% of the total charge Q_r passed although the n_2 , k_2 changes rapidly. A comparison of total charge passed during film formation (see Fig. III-16) with that obtained during reduction (see Fig. III-22b) shows a difference of $\sim 2.5 \text{ mC/cm}^2$ with a total Q_{ox} of 7.1 mC/cm^2 for oxide formation and $\sim 4.6 \text{ mC/cm}^2$ for reduction. Similar discrepancies have been observed by Cohen et al. (1,33) and Sato et al. (35-37). They showed that an amount of iron, equivalent to the lost charge, dissolved into solution as Fe^{2+} ions.

A-1) Interpretation and Comments on Reduction Process

The interpretation of Cohen et al. (1,33) is that these two reduction steps correspond to the reduction of an outer Fe_2O_3 layer to Fe II with the reduction products dissolving into the solution completely, followed by the reduction of an inner Fe_3O_4 layer. The two reduction steps are then used as "evidence" of two different materials in a "sandwich" type structure.

The above interpretation appears to be in contradiction to that which is expected from the reduction of a material which is capable of existing in more than one valency state. Many materials common in battery technology exhibit more than one reduction plateau even though the original starting material is known to be one single phase. For example, PbO_2 in acid medium shows two equal length plateaus for $\text{Pb}^{4+} \rightarrow \text{Pb}^{2+}$ and $\text{Pb}^{2+} \rightarrow \text{Pb}^0$ (104). MnO_2 (105) in alkaline solution shows two clear steps for $\text{Mn}^{4+} \rightarrow \text{Mn}^{3+}$ and Mn^{3+}

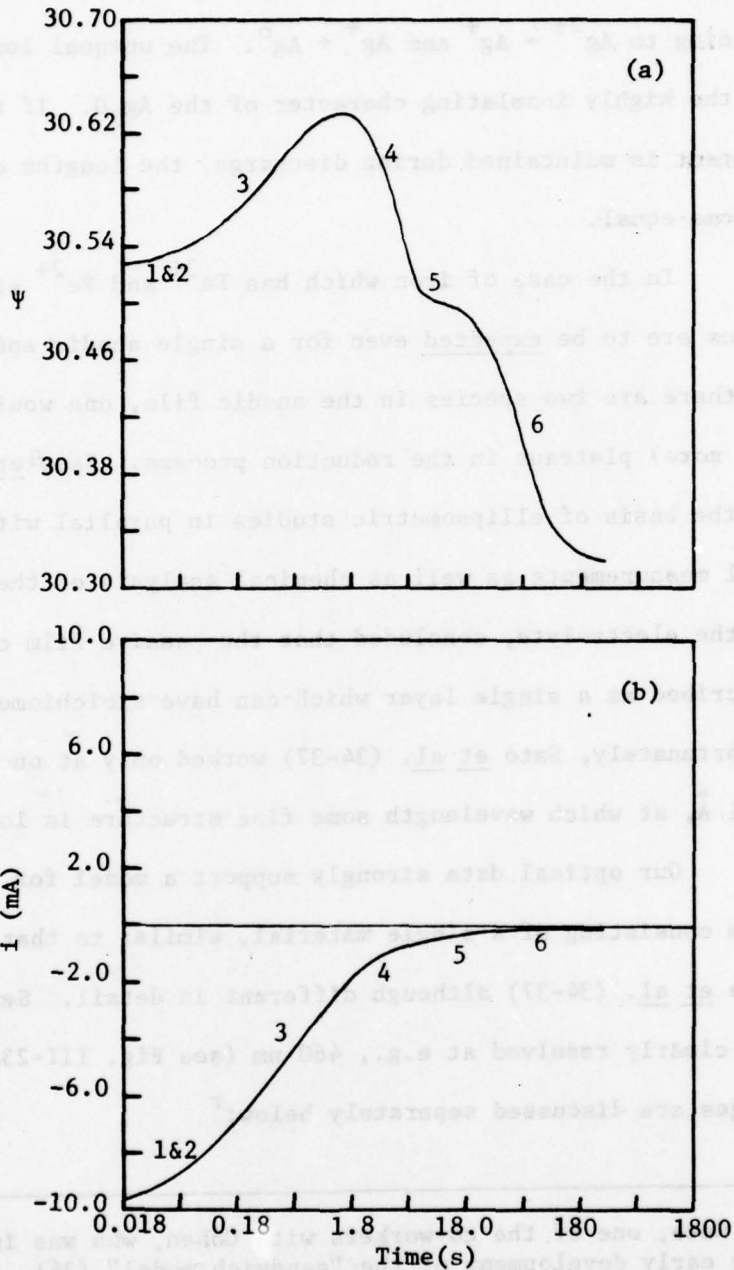
$\rightarrow \text{Mn}^{2+}$. AgO (106) shows two plateaus with unequal lengths corresponding to $\text{Ag}^{2+} \rightarrow \text{Ag}^+$ and $\text{Ag}^+ \rightarrow \text{Ag}^0$. The unequal lengths are caused by the highly insulating character of the Ag_2O . If the intimate contact is maintained during discharge, the lengths of the plateaus become equal.

In the case of iron which has Fe^{3+} and Fe^{2+} states, two plateaus are to be expected even for a single anodic species. Indeed if there are two species in the anodic film, one would expect three (or more) plateaus in the reduction process. Sato^q et al. (34-37) on the basis of ellipsometric studies in parallel with electrochemical measurements as well as chemical analysis of the iron species in the electrolyte, concluded that the passive film can be best described as a single layer which can have stoichiometric gradients. Unfortunately, Sato et al. (34-37) worked only at one wavelength, 5461 Å, at which wavelength some fine structure is lost (vide infra).

Our optical data strongly support a model for the passive film consisting of a single material, similar to that presented by Sato et al. (34-37) although different in detail. Several segments are clearly resolved at e.g., 460 nm (see Fig. III-23a). These stages are discussed separately below:^r

^qN. Sato, one of the co-workers with Cohen, who was involved in the early development of the "sandwich model" (34).

^rIn stages 1 and 2, the electrode is not fully potentiostatic controlled because of the ohmic losses and relatively high currents.



Figures III-23a, b: The Ψ vs $\log t$ and i vs $\log t$ plots during a single potential step reduction (1.15 V to -0.25 V) for a film grown in borate buffer solution (pH 8.4) at 1.15 V for 5 min. Electrode area 6.44 cm^2 , $\phi = 68^\circ$, $\lambda = 460 \text{ nm}$.

Stage 1: This portion occurs in good part before the earliest time (0.018 s) shown in Figs. III-23a and b and involves 5 to 10% of the total charge. On the basis of the discussion in chapter 1, this charge is assigned to the reduction of the iron in a valency state +4. During this period the optical constants of the film change markedly as is to be expected on the basis of a valency and compositional change of the film (i.e., reduction of +4 to +3 attended by incorporation of protons or loss of oxygen. The latter may occur through loss of water.

Stage 2: When the surface concentration of the Fe IV states has been reduced to a sufficiently low value, the reduction to Fe II will occur with further introduction of protons or loss of oxygen. The Fe II states can dissolve into the solution until local saturation is reached. An estimate of the charge which must be passed to achieve this saturation can be made by calculating the time required for the concentration of Fe^{2+} to reach the saturation value in the solution taking into account the time dependent diffusion of Fe^{2+} into the solution, using a saturation concentration of $C(\text{Fe}^{2+}) = 2.5 \times 10^{-6}$ moles/cm³ evaluated from the solubility product at pH = 8.4 for $\text{Fe}(\text{OH})_2$ (127) and a diffusion coefficient of 10^{-5} cm²/s. Assuming that the current density is essentially constant in this stage, the time is 0.1 s.

Stage 3: In this stage, the interface between the ferrous outer layer and ferric inner layer progressively moves towards the metal while simultaneous dissolution of Fe^{2+} occurs from the outer surface. This formation of the Fe^{2+} outer layer, however, is expected to occur in patches because of lateral inhomogeneities in the passive layer. The growth of patches can occur at the edges and extend into the passive film. This growth of the Fe II regions in the overall film is not believed to involve a solution precipitation mechanism. At the conclusion of this stage, the passive layer is covered with a layer of ferrous hydroxide which probably has low electronic conductivity. During this stage, the optical constants continue to change and the effective thickness to decrease.

Stage 4: Reduction of Fe II to the metal starts in this stage. This process is probably highly non-uniform and iron dendrite-like growth may occur on a microscopic scale with the iron dendrites extending out into partially reduced film. Even though some of the film is still in the Fe III state.

Stage 5: The microscopic regions of metal growth have now reached the stage when they make direct contact with the solution phase. The local concentration of Fe^{2+} in solution at the interface is drastically reduced as redeposition of some of the Fe^{2+} which entered the solution earlier.

Stage 6: This is a continuation of stage 5 with simultaneous reduction of the Fe II in the film and electrolyte to metallic iron. Film reduction, however, predominates and the effective thickness decreases until the film is entirely reduced.

Stage 7: A small but finite current continues to pass, this is attributed to the co-deposition of H_2 and $Fe^{2+} \rightarrow Fe$ from the bulk of the electrolyte.

According to the model⁸ used to interpret the reduction, the film is highly inhomogeneous both laterally and perpendicular to the surface during the reduction process. The change of the optical parameters Δ , and Ψ are quite sensitive to the changes in the film and have diagnostic value but cannot be used to calculate quantitative values of the optical constants and thickness since the three layer model is no longer quantitative.

B. Potential Dependence of the Film Properties Grown at More Anodic Potentials

The following experiment was carried out to establish how the potential affected the optical properties of a film grown at a relatively high anodic potential and then subjected to less anodic potentials still well above the range where reduction of Fe III states occurs (see Fig. III-24). The film was grown at 0.75 V for 30 min and then in 200 mV steps the potential raised to 1.55 V with 20 min for each step. The optical measurements were then made at decreasing

⁸Efforts to quantify this model for the reduction of the passive film, especially the stages 4 and 5, are being undertaken by Dr. B. D. Cahen but requires work beyond the scope of this thesis.

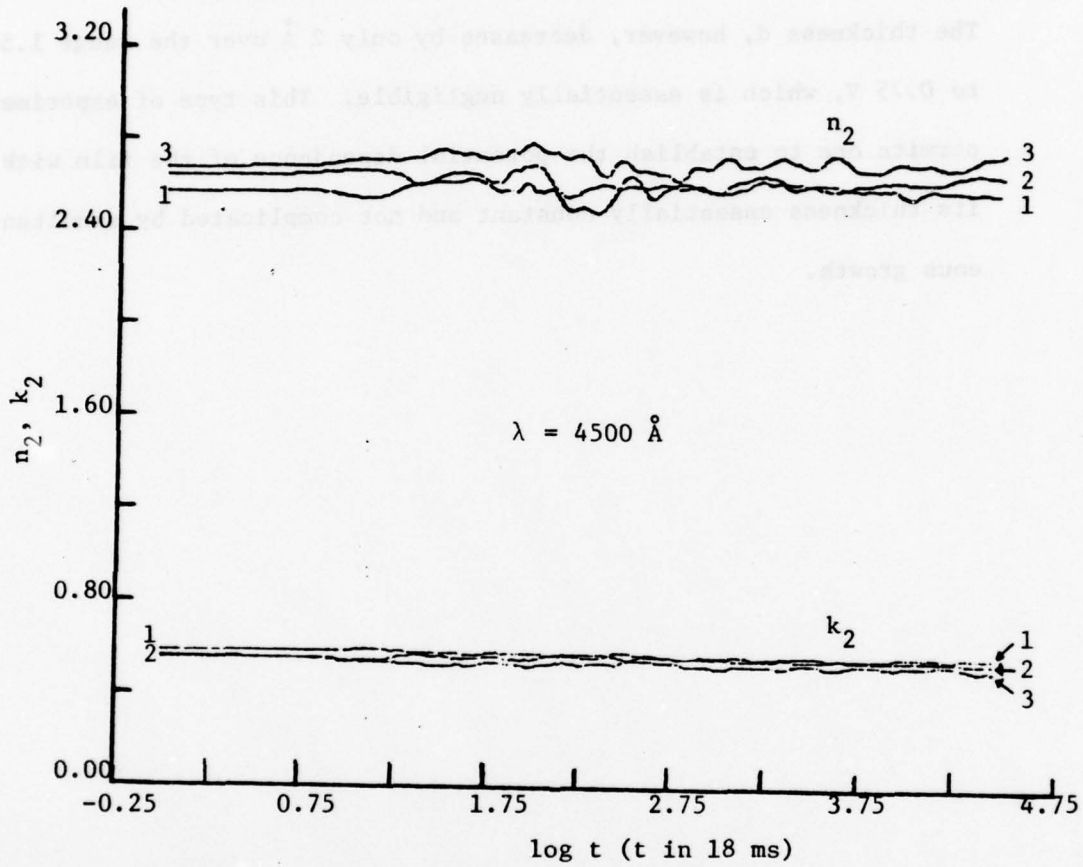


Fig. III-24: n_2 , k_2 vs $\log t$ for progressive reduction of a film on iron grown in borate buffer: curves 1 for 1.35 V; curves 2 for 1.15 V; and curves 3 for 0.75 V (see text for details).

potentials in the range 1.55 to 0.75 V in a stepwise fashion with the potential steps separated by 200 mV and 20 min in each step. The thickness d , however, decreases by only 2 Å over the range 1.55 to 0.75 V, which is essentially negligible. This type of experiment permits one to establish the potential dependence of the film with its thickness essentially constant and not complicated by simultaneous growth.

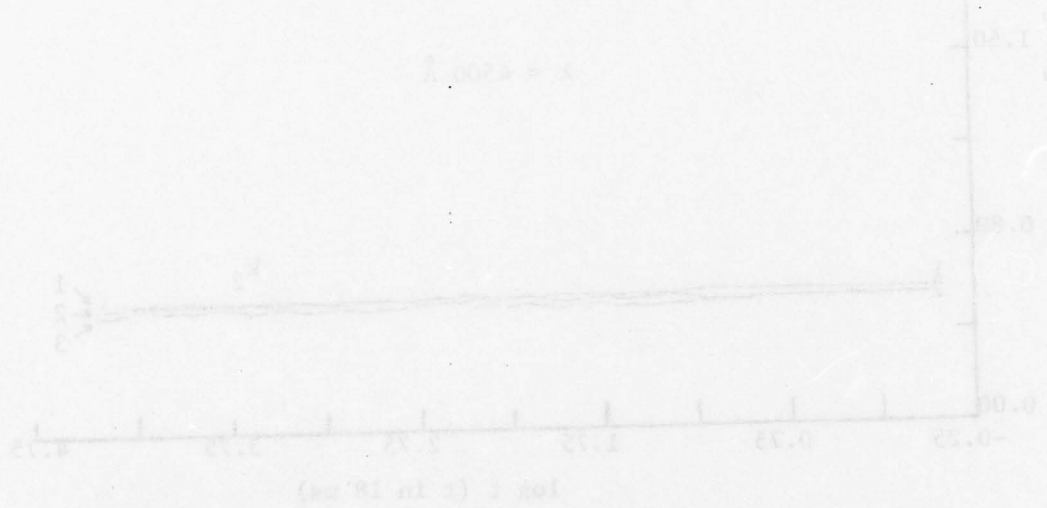


Fig. 11-14c. $\log i$ vs $\log t$ for progressive reduction of a film on iron grown in porous holder; curves 1 for 1.55 V; curves 2 for 1.35 V; and curves 3 for 0.75 V (see text for details).

VIII. Cyclic Sweep Experimental Results

Data for a typical experiment is shown in Fig. III-25a-d.

These experiments were done with sweep rate of 60 mV/s, sweeping between -0.6 and 1.4 V with $\phi = 68^\circ$, $\lambda = 380$ nm. With such a moderately high sweep rate, the system does not approach steady state condition in the film formation region and the current-potential curves are quite different from the usual passivation curves. The i - E curve (Fig. III-25a) shows that the active dissolution starts at -0.25 V (point 1)^t and reaches its maximum at about 0.05 V (point 2). There is a dip at 0.35 V (point 3) and a broad hump with its maximum located at about 0.78 V (point 4) along with the anodic sweep. In the cathodic (point 5) small anodic currents continue to pass until the current becomes cathodic when the electrode potential reaches 0.55 V (point 6). There is a broad reduction peak with its maximum at -0.05 V (point 7). A much sharper reduction peak occurs at about -0.55 V (point 10) before hydrogen evolution takes place. The first anodic peak (point 2) located at 0.05 V is due to the initial film formation of ferrous material on the electrode surface. This initially formed ferrous material (which dissolved into the solution under the steady state condition) covers the electrode surface and inhibits further active dissolution.

Figures III-25b-d show the corresponding Δ vs E , Ψ vs E , and

^tCorresponding points on the four curves are labelled with the same numbers.

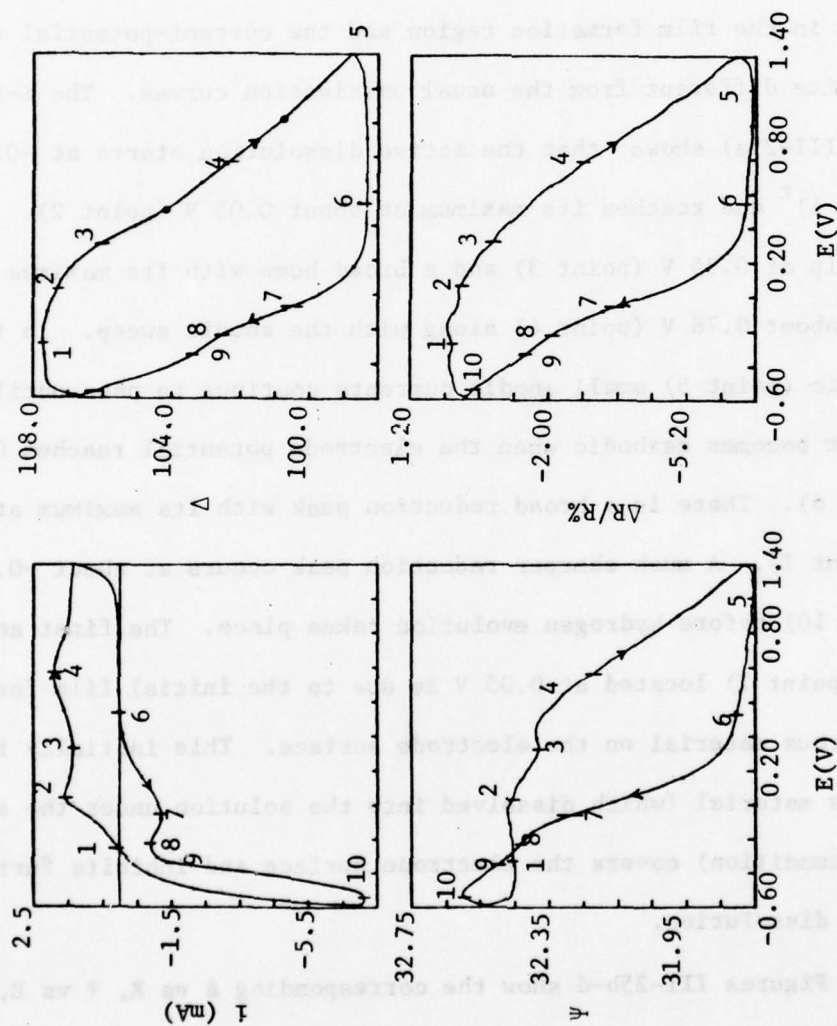


Figure III-25: Typical sweep experimental data: (a) the i - E curve; (b), (c), (d) are the corresponding Δ - E , ψ - E , and $\Delta R/R\%$ - E curves respectively at $\lambda = 380$ nm, $\phi = 68^\circ$. Electrolyte = borate buffer at pH 8.4; sweep rate = 60 mV/s; electrode area 6.44 cm² and electrode potentials vs RHE.

$\Delta R/R\%$ vs E plots, respectively. Initial film formation starts at point 1 with a very slow decrease of Δ , $\Delta R/R\%$, and a barely noticeable Ψ change towards point 2. This is followed by a much steeper decrease of Δ , $\Delta R/R\%$ and markedly decrease in Ψ towards point 3 (indicating faster film formation on the electrode surface and possibly with a combination of conversion to higher valency state iron oxide). With further sweeping of the electrode potential more anodic, there are three separable segments with different decreasing rates in Δ indicating that there are three separable film formation processes. The potential regions which categorize these three film formation processes are: region 1 (point 3 to point 4) represented by the potential region from 0.25 V to 0.5 V; region 2 represented by the potential region from 0.5 V to 1.05 V; and the last region as the potential increases towards the direction for oxygen evolution. There is a peak in Ψ corresponding to the first region of Δ -E plot for growth. The second and third regions of growth Ψ and $\Delta R/R\%$ could not be well-separated as in the Δ -E plot. On the basis of the steepest decreasing rate in Δ , the film growth in region 1 is the fastest. This, combining with the strong wavelength dependence in Ψ (for details see Fig. III-26a and b) and the drastic decrease in $\Delta R/R\%$, indicates that the growth in this region is a combination of initial film formation and conversion to the final passive film. The rates of Δ changes in the subsequent segments were smaller than that of the first region. This, combining with rather linear $\Delta R/R\%$ and non-separable Ψ changes, implicitly indicates that the absorbing property of

the passive film during the last two growth regions changes slightly, probably caused by partially losing its protons and consequently retards further oxide growth.

In the cathodic sweep, the Δ usually kept decreasing, indicating that the film growth continued during the very beginning of the cathodic sweep. This was followed by a region of constant Δ values until the potential sweep to point 6, at which the Δ values increased slightly until point 7 was reached, followed by a very significant linear increase in Δ towards point 8. A clear change over from one electrode process ($\text{Fe}^{3+} \rightarrow \text{Fe}^{2+}$) to another ($\text{Fe}^{2+} \rightarrow \text{Fe}^0$) occurred between 8 and 9 and continued through the rest of the cathodic sweep and the very beginning of the anodic sweep between point 10 and the flat portion of Δ before reaching point 1. The Ψ values kept changing in the same direction as that of the film growth during the final anodic sweep; then, within the first 100 mV, it reversed its direction when Δ values reached a constant value. This indicates that the film started changing its nature, possibly caused by the introduction of protons into the film without significantly affecting its corresponding Δ values. Significant Ψ changes started as soon as the current became cathodic (at point 6) indicating drastic changes in the absorbing property of the passive film at this early stage of the cathodic reduction. This drastic change in Ψ almost ended when the cathodic sweep to point 7, at which the first cathodic current maximum occurred. The change over as seen in Δ -E plot at point 8 is not clear in Ψ at this wavelength.

Similar experiments were run at wavelengths from 380 to 750 nm in an attempt to identify the individual electrode process elliptically during the potentiodynamic sweep. Very similar results were obtained for Δ vs E at all wavelengths. Ψ vs E, however, showed marked systematic differences.

Figures III-26a and b showed Ψ vs E plots for shorter wavelengths (380, 425, 450, and 480 nm) and for longer wavelengths (550, 600, 650, 700 and 750 nm) respectively.^u In the anodic sweep, the small peak and the dip corresponding to segment (points 1 to 3) varies only slightly with variation in wavelength. Drastic changes with wavelength appear in segment (points 3 and 4). The Ψ values at potential more anodic to point 3 for short wavelengths (shorter than or equal to 450 nm) increase to a maximum (corresponding to segment from points 3 to 4), then decreased at more anodic potentials. For longer wavelengths (above 450 nm), the Ψ values after the dip increased as the potential become more anodic and the peak after the dip (observable at shorter wavelengths) appeared as a shoulder, at which point the Ψ vs E curves change slope. The slope increased slightly as the wavelength increased. In the cathodic sweep, there is a very significant change of Ψ shape in the potential region corresponding to segments (points 6 to 8) and (points 8 to 10). The first cathodic reduction which corresponds to the electrode ($\text{Fe}^{3+} \rightarrow \text{Fe}^{2+}$) as well

^uThe individual curves have been drawn with displaced ordinates and with scale factors chosen to illustrate the general shape of changes rather than absolute magnitude.

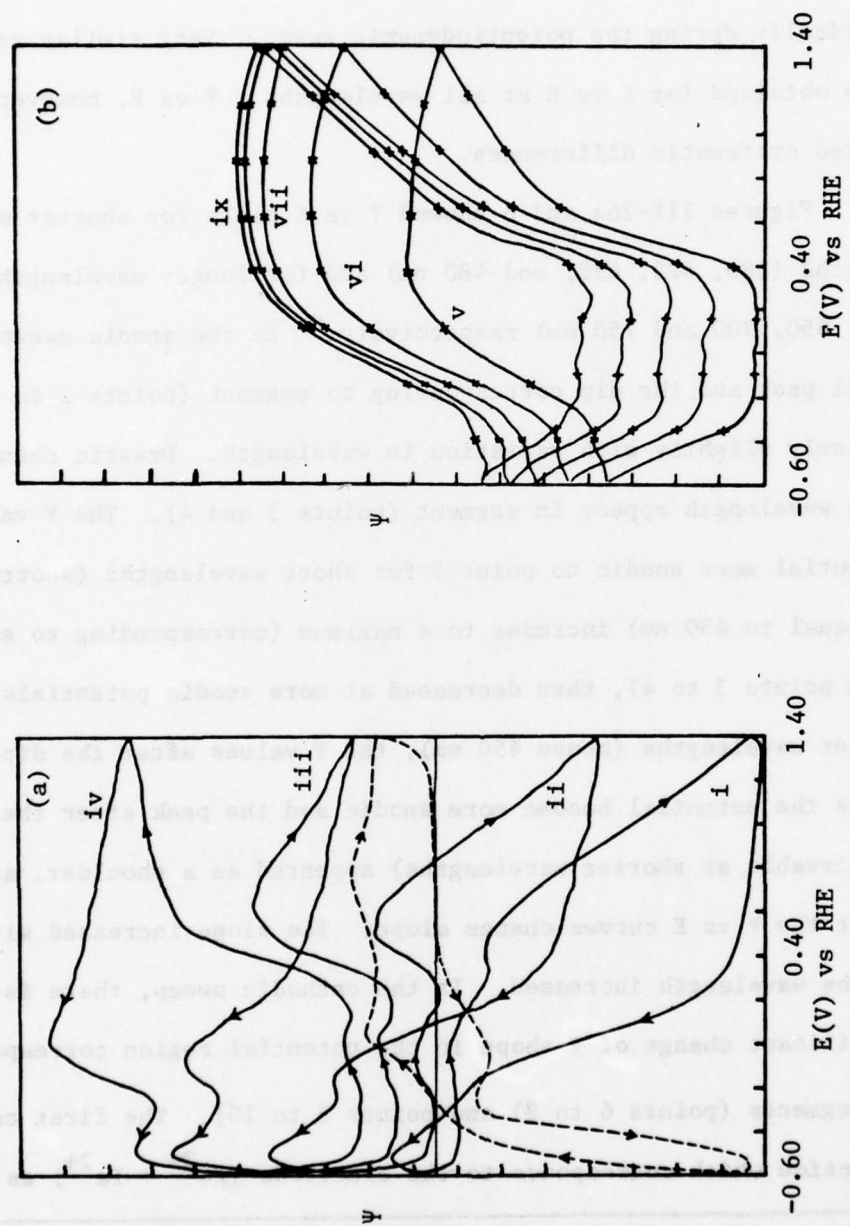


Figure III-26: The Ψ -E curves: (a) for lower wavelengths (i. 380 nm; ii. 425 nm; iii. 450 nm; iv. 480 nm); (b) for longer wavelengths (v. 550 nm; vi. 600 nm; vii. 650 nm; viii. 700 nm; ix. 750 nm). The dashed line in (a) is i-E curve. The Ψ values were displaced and scale factors chosen to illustrate the general shape of changes rather than absolute magnitude. $\phi = 68^\circ$; Electrolyte = borate buffer at pH 8.4, sweep rate = 60 mV/s.

as the sharper reduction corresponding to the $\text{Fe}^{2+} \rightarrow \text{Fe}^0$ process could be easily identified and resolved by the Ψ -E plot at $\lambda = 450$ nm. At other wavelengths, these two electrode processes showed up by Ψ would gradually be buried as the wavelength moving away from this specific wavelength.^v

Further detailed information on the individual electrode processes were obtained by the use of voltage waveforms other than conventional triangular sweeps. Figures III-27a and b show two examples of this sort (see Fig. II-12 of Chapter II). Through the use of these specialized waveforms, it is possible to separate various effects such as dissolution, roughening, electromodulation, and "aging".

Quantitative evaluation of most of these curves was not attempted. They served principally as a qualitative guide for subsequent selection of optimum experimental conditions and data analysis.

^vAn implication of these results is that the choice of proper wavelength to unravel electrode processes ellipsometrically is essential.

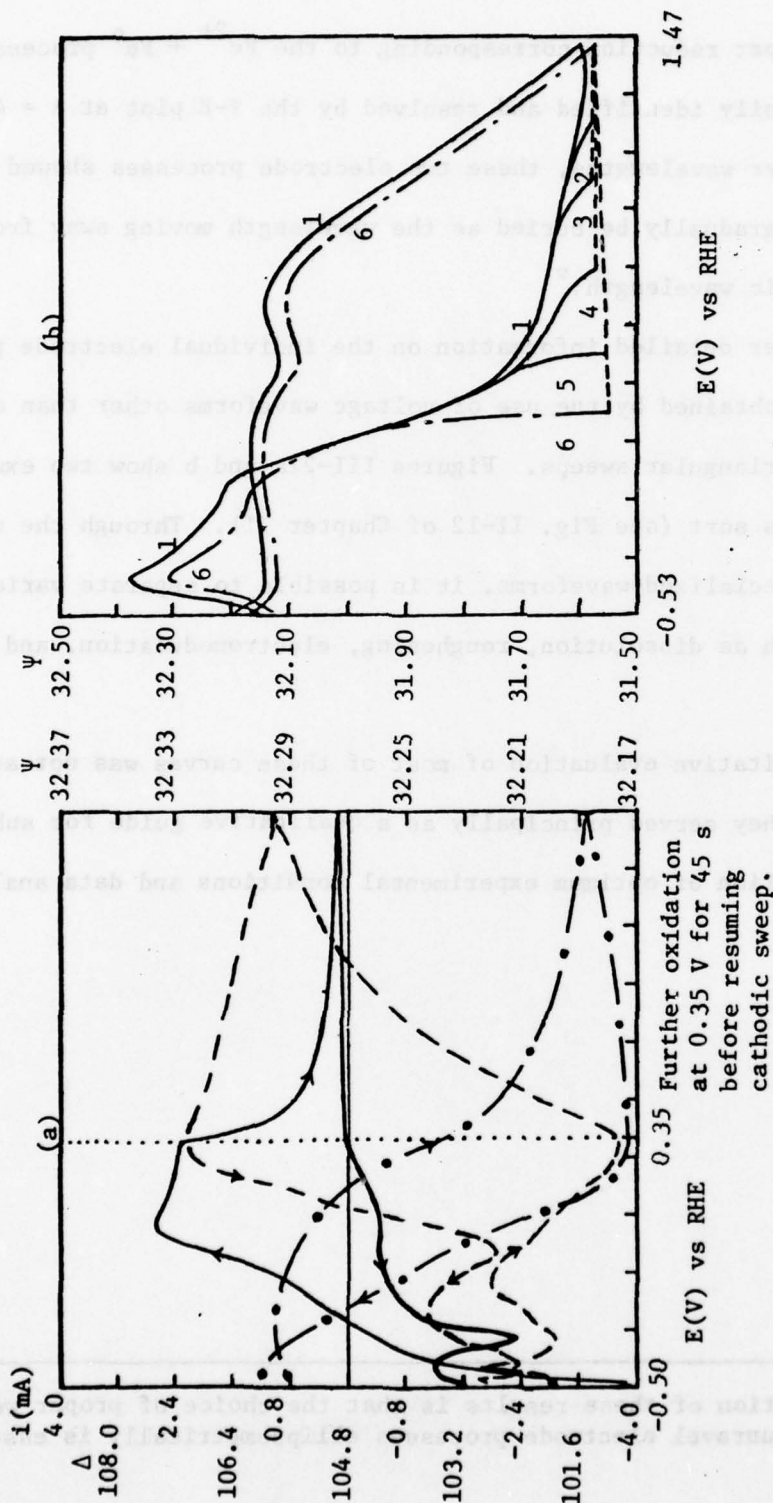


Figure III-27: Two typical sweep experimental results obtained by combinations of various voltage waveforms with the regular sweep: (a) wait at highest anodic potential (0.35 V in this case), followed by resuming cathodic sweep accompanied with changing sweep rate from 100 mV/s to 40 mV/s; solid line for i - E curve; dashed-dotted line for Δ - E curve; and dashed line for ψ - E curve; the curves above 0.35 V are data collected during waiting at 0.35 V for 45 s; (b) a regular sweep to highest anodic potential followed by an immediate jump to lower potentials and resuming cathodic sweep; experiments done according to ascending numerical order.

IX. Ex situ ESCA Studies on Passive Films

Ex situ ESCA has been used as a technique complementary to the optical studies in an attempt to determine the chemical composition, valency states of cations, and proton involvement in passive films on iron, nickel, and their alloys produced by electrochemical techniques (e.g., potentiostatic oxidation). These techniques permit one to grow a film to a limiting thickness, depending on the electrode potential, starting from a film-free electrode produced by cathodic reduction of mechanically polished electrodes. In order to minimize the interference of further oxidation (e.g., by air during the transfer process between electrochemical and ESCA systems), the electrodes examined in most cases had been potentiostated at the passive or transpassive region for 30 min. Most of the electrodes after this treatment appeared to be rather free from further interference by oxygen. This has been justified by the O 1s and cation 2p spectra, which indicated a rather reasonable film growth, consistent with that expected from raising anodic potential sequentially. The electrode materials are shown in Table II. Most of ESCA results and the related discussions of these electrodes, except those of iron, are assembled in Appendix A and will not be discussed further since the main emphasis of this thesis has been on the passivation of ultrapure iron and the reduction of their passive films. The findings presented in Appendix A are important and may lead to a new understanding of passivation films in general, with films on Cr-steels in particular.

A. Pure Iron and its Electrochemical Treated Specimens

a) Fe Spectra

The ESCA spectra were examined for a pure iron electrode which had been passivated at 0.35, 0.65, 1.35, and 1.55 V in the borate buffer (pH = 8.4) and after subsequent treatment (described in Chapter II) were transferred to the ESCA.

In general, the iron $2P_{3/2}$ peak (see Fig. III-28) is very broad (full width at half maximum, FWHM, is about 4.0 eV or more) and centered at 710.2 ± 0.5 eV. The $2P_{3/2}$ peak of pure iron after polishing without electrochemical treatment and also after treatment in the low anodic potential region, e.g., 0.35 V and 0.65 V, show the shoulder at 706.6 eV characteristic of bare iron $2P_{3/2}$. This indicates that the films in both types of specimens are thinner than the escape depth of electrons without loss of energy (about 20 Å) (107).

With treatment at more anodic potentials, e.g., 0.95 V, 1.35 V, the bare iron peak disappears, indicating that the film thickness is greater than the electron escape depth. The $2P_{3/2}$ iron peak is still very broad and does not show evidence of becoming a sharper peak. In addition to interference of the Mg $K\alpha_{3,4}$ of the X-ray source with the Fe $2P_{1/2}$, the iron broadening may be due to multiple splitting, shake-up satellites, or unresolved peaks from different valency states. Comparison of the present results with those reported in the literature (108,109) for the iron oxides

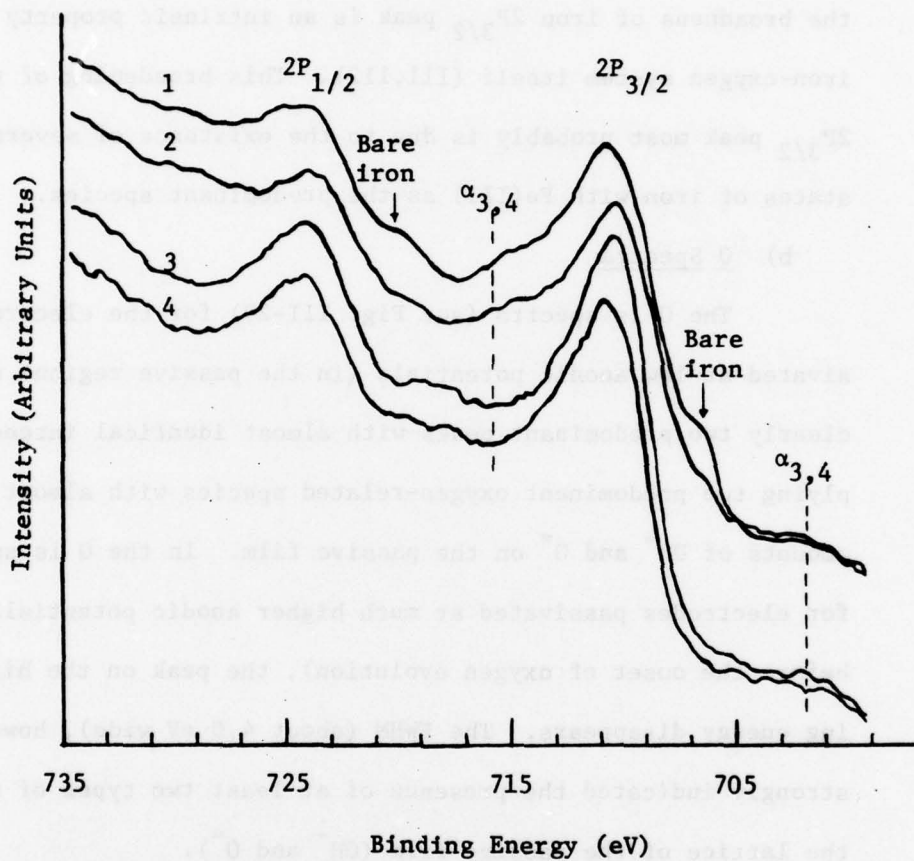


Figure III-28: Fe 2P photo-electron spectra for passive films on iron grown in borate buffer (pH 8.4) at different potentials: 1) 0.35 V; 2) 0.65 V; 3) 1.35 V; 4) 1.55 V vs RHE.

formed in electrolyte, air, or vacuum with controllable oxygen doses, using a monochromatized X-ray source (49,110) revealed that the broadness of iron $2P_{3/2}$ peak is an intrinsic property of the iron-oxygen system itself (111,112). This broadening of the iron $2P_{3/2}$ peak most probably is due to the existence of several valency states of iron with Fe(III) as the predominant species.

b) O Spectra

The O 1s spectra (see Fig. III-29) for the electrodes passivated at low anodic potentials (in the passive region) showed clearly two predominant peaks with almost identical intensity, implying two predominant oxygen-related species with almost equal amounts of OH^- and O^{2-} on the passive film. In the O 1s spectra for electrodes passivated at much higher anodic potentials (just before the onset of oxygen evolution), the peak on the higher binding energy disappears. The FWHM (about 4.0 eV wide), however, strongly indicated the presence of at least two types of oxygen in the lattice of the passive film (OH^- and O^{2-}).

c) Na and B Spectra

The spectra show that the amount of Na and B depends strongly on rinsing or not rinsing the electrochemical treated samples prior to transferring to the ESCA instrument. The intensities of B 1s and Na 1s peaks of an electrode subjected to rinsing, disappeared after only 2 min of Ar^+ ion bombardment^w (2 kV, 5 mA of emission

^wThis technique has been coupled with ESCA or Auger to investigate composition profiles of thin films on metal surfaces (114-118). The application of this technique without monitoring the sputtering yields of the removed species can lead to wrong conclusions (118-121).

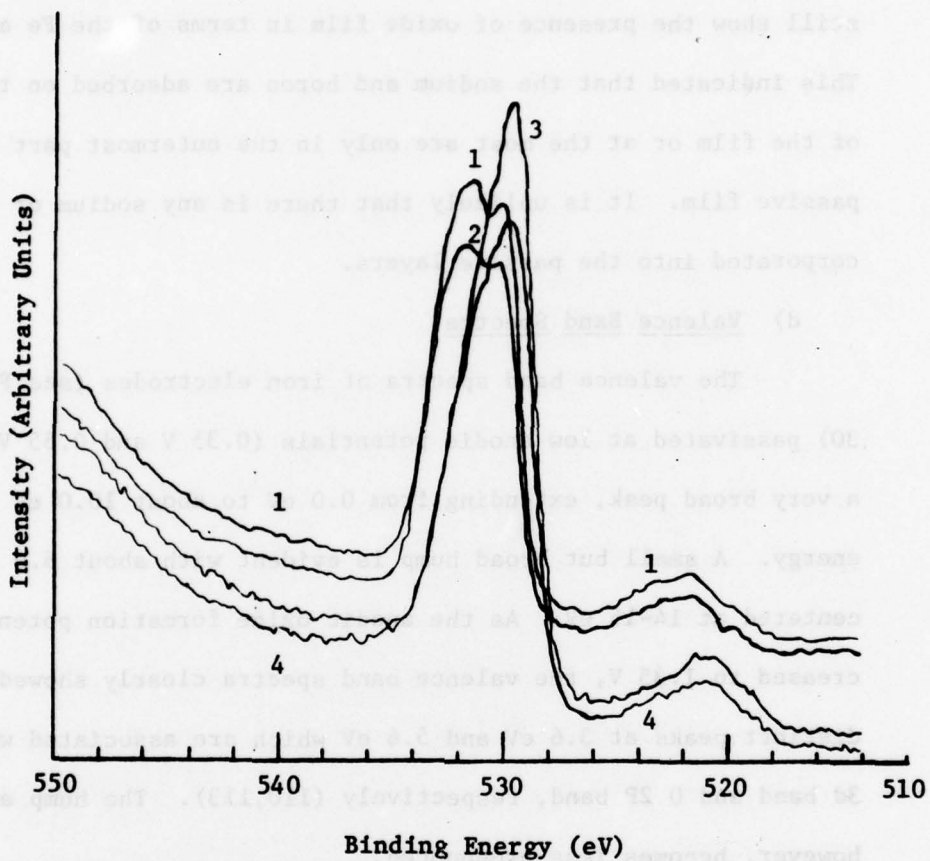


Figure III-29: 0 ls photo-electron spectra for passive films on iron grown in borate buffer (pH 8.4) at different potentials: 1) 0.35 V; 2) 0.65 V; 3) 1.35 V; 4) 1.55 V vs RHE.

current of the filament). The electrode surface after this treatment still show the presence of oxide film in terms of the Fe and O spectra. This indicated that the sodium and boron are adsorbed on the surface of the film or at the most are only in the outermost part of the passive film. It is unlikely that there is any sodium or boron incorporated into the passive layers.

d) Valence Band Spectra

The valence band spectra of iron electrodes (see Fig. III-30) passivated at low anodic potentials (0.35 V and 0.65 V) showed a very broad peak, extending from 0.0 eV to about 10.0 eV binding energy. A small but broad hump is evident with about 6.0 eV width centered at 14-15 eV. As the anodic oxide formation potential increased to 1.35 V, the valence band spectra clearly showed two distinct peaks at 3.6 eV and 5.6 eV which are associated with Fe 3d band and O 2P band, respectively (110,113). The hump at 15 eV, however, becomes less pronounced.

The O 1s and Fe 2P spectra of the passive film grown in borate buffer (pH 8.4) at different potentials (Fig. III-28 and 29) support the view that the passive film has a high concentration of protons over the entire potential region.

The ESCA spectra carry quantitative information concerning the Fe to O ratio. To evaluate such, however, requires reliable values for the X-ray photo-electron efficiencies for these elements. Unfortunately the literature (122-124) has a considerable scatter-

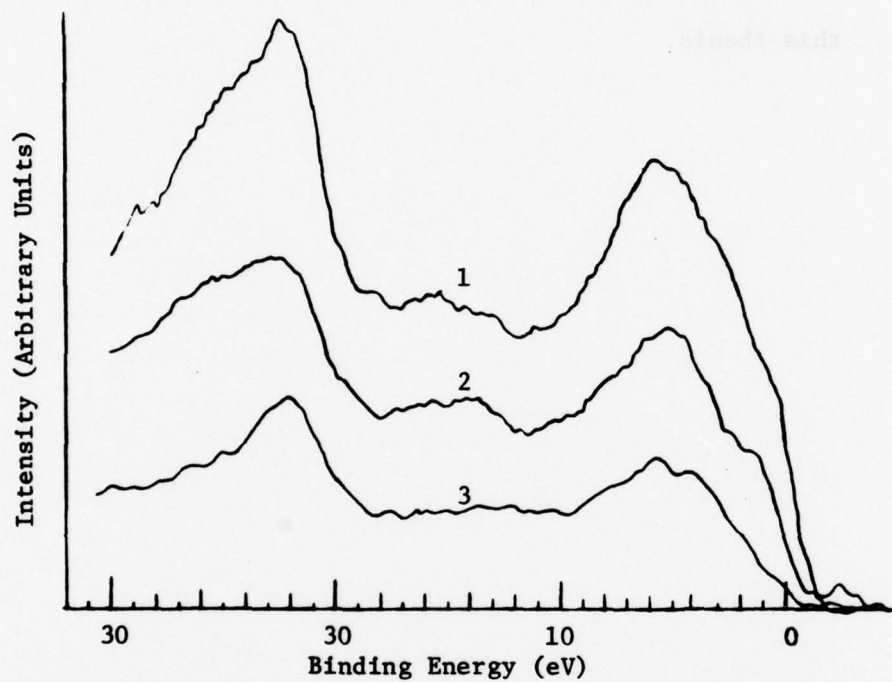


Figure III-30: X-ray photo-electron spectra of valence band of passive films on iron grown in borate buffer (pH 8.4) at different potentials: 1) 0.35 V; 2) 0.65 V; 3) 1.35 V vs RHE.

ing of values particularly for Fe, probably because of the dependence on the instrument (108,109) and the nature of reference sample. Consequent quantitative evaluation has not been included in this thesis.

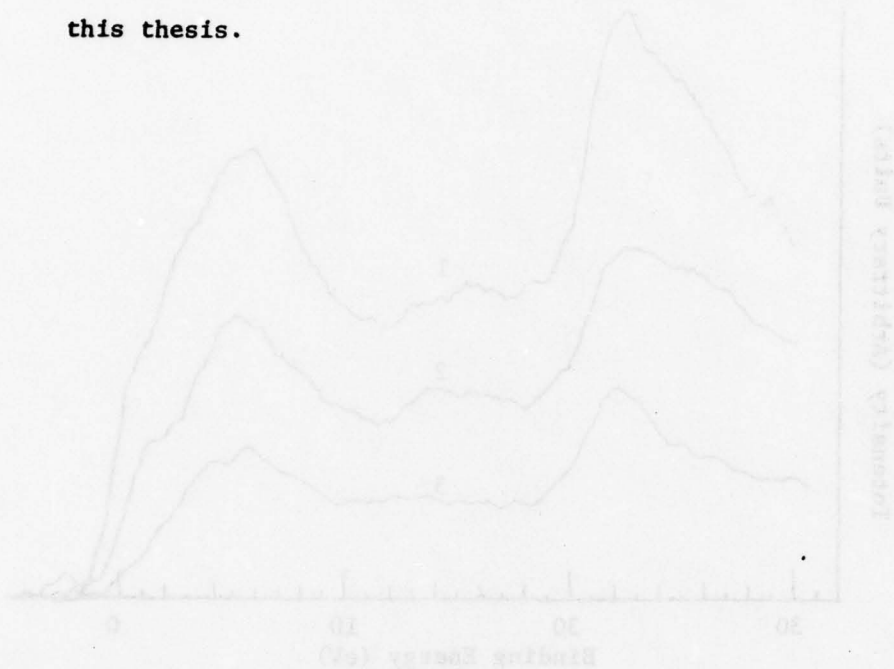


Figure 111-30: X-ray photoelectron spectra of valence band of positive films on iron grown in borate buffer (pH 8.4) at different potentials: 1) 0.32 V; 2) 0.42 V; 3) 1.32 V vs NHE.

CHAPTER IV

CONCLUSIONS AND REMARKS

I. Applicability of Automatic Ellipsometry to Passivation Studies

In situ automatic ellipsometry using the three-parameter method has been shown for the first time to be capable of obtaining the optical spectra of passive film on iron as well as following optical changes and thickness during its growth and reduction in borate buffer solution (pH = 8.4). With the use of three parameters instead of two parameters, ellipsometry has become an independent and non-destructive in situ technique to study the passivation film on iron and other metals without any additional assumptions beyond three layer models.

The wavelength-scanning capability has been coupled with electrochemical potentiostatic techniques to obtain the optical spectrum of the steady-state (or semi-steady-state) oxide film grown in electrolytic environment. The optical spectrum is of critical importance in the determination of the electronic properties (e.g., band gap and defect concentrations) of the passive film.

The specificity of the wavelength has been useful in helping resolve several steps in the passivation process. For example, measurements made during voltage sweep at 425 nm (at which $\Delta\Delta$ is a maximum and $\Delta\Psi$ is zero for the passive film with respect to the film-free iron electrode) at an angle of incidence at 68° clearly show two steps or processes at -0.05 and -0.55 V. Away from this

wavelength, the prevailing Ψ changes contributing from the ferric species mask the much smaller Ψ contribution from the intermediate species occurring along the voltage sweep. Only by a detailed analysis of the wavelength dependence data is it possible to decide on the best condition to be used for investigation of specific electrode process. The use of this wavelength specificity may extend and broaden the applicability of ellipsometry as a technique for studies of intermediate states in an electrode process.

The analysis of ellipsometric data obtained by large potential steps was easier to interpret than that obtained in slow sweep experiments. The latter experimental results were further complicated by artifacts such as dissolution, anodic redeposition of the Fe^{2+} (which had dissolved into the solution during the earlier stages of the oxidation) back onto the oxide film, and roughening caused by the slow sweeps. With careful choice of potentials used, a suitable combination of voltage waveforms, and sweep rate even for slow sweep experimental measurements one can minimize these artifacts as well as provide a means to study the potential dependence of the oxide at a constant thickness.

II. The Growth of Passive Film on Iron

There appears to be a critical minimum thickness (d_{crit})^x which is a function of the applied potential and not less than $\sim 10-15 \text{ \AA}$. Above this thickness the optical constants remain almost invariant for a given potential within experimental error. Continued oxidation proceeds with a much slower rate, which can be expressed either as a direct or inverse logarithmic function of time. The growth rate can also be plotted in accord with the Ghez (101) formulation (Eq. I-11a) derived exactly from the original equation derived by Cabrera and Mott (16) without any approximation, yielding two straight segments with opposite signs of slope separated by a bending over transition region. For $d > d_{crit}$, a small variation of calculated d with λ (e.g., $\pm 3 \text{ \AA}$ for $d = 30 \text{ \AA}$) is also obtained, as well as a dependence of k_2 on potential of formation at some wavelengths. The earlier stages ($t < 2 \text{ s}$) show a linear variation of thickness (d) with charge (Q). The variation of apparent n_2 and k_2 over the initial region where $d < d_{crit}$ indicates that the initial film is continually changing its nature.

Convergent solutions of the three-parameter equations have been obtained for apparent d as low as a few Angstroms. The wavelength dependence of the optical constants for $d < d_{crit}$ show sig-

^xThis d_{crit} may be an artifact of the model used for solution of the equations. Consistent convergent solutions are often obtained with films of only a few Angstrom thick. This dilemma has not yet been resolved.

nificant structure.

Further oxide growth of a semi-steady state oxide, caused by raising the electrode potential towards a more anodic value occurs only after an amount of charge roughly equal to one electron per surface iron atom of the metal has passed, during a time which can be as long as a few tens of seconds depending on the electrode potential and the size of the potential step. The time can be clearly determined by the ellipsometric methods as well as the current-time curve of the potentiostatic transient.

III. The Reduction of the Passive Film on Iron

Three regions are apparent in the reduction process. During the first 5 to 10% of the charge consumed in the reduction, the effective thickness (d) as well as the n_2 and k_2 show a small but significant wavelength dependence ($\sim 10\%$), d at all values of λ converging towards a single value with increasing reduction. Further reduction up to 1/3 of the total charge causes a drastic change of the film parameters. During the final 2/3 of the reduction process (convergences are obtained down to a few Angstroms) the d decreases linearly with charge, and the optical constants remain invariant. The optical spectrum of this material is grossly different from that of the passive film.

The reduction process is believed to proceed through the following stages: 1) reduction of the iron from valency state +4 to +3 with introduction of protons into the lattice and/or loss of oxygen, indicated by a rather constant d but noticeable n_2 and k_2 changes; 2) continued introduction of protons or loss of oxygen with reduction of Fe III states to Fe II states in the film, accompanied by the dissolution of the Fe II states into solution until local saturation with $\text{Fe}(\text{OH})_2$ is reached; 3) reduction by continued growth laterally and vertically of a patch-like $\text{Fe}(\text{OH})_2$ outer layer with simultaneous dissolution of Fe II states into the solution until the passive layer is completely covered with a layer of ferrous hydroxide, indicated by continued changes of the optical constants and decrease of effective thickness; 4) further reduction involved

highly non-uniform reduction of Fe II to metallic iron and local dendritic growth extending out into the partially reduced film; 5) further metal growth extending to the solution phase, followed by redeposition of some of the Fe^{2+} in solution back onto the electrode; 6) a continuation of 5) with simultaneous reduction of the rest of the film and some of the Fe^{2+} in solution to metallic iron with film reduction as the predominant process. The ellipsometric parameters (Δ, Ψ), particularly Ψ , have been used to determine these transition times, which fit reasonably well with the calculated values for the reduction stages. This mechanistic model for the reduction also explains the discrepancy between the charge for film formation and reduction.

IV. Applicability of Ellipsometry to Study Transition Metal Oxides

The poly- and single-crystalline $\alpha\text{-Fe}_2\text{O}_3$ (hematite) work in this study shows that automatic ellipsometry can be used effectively to determine the optical properties of the single- or poly-crystalline transition metal oxide. Measurements of the complex dielectric constant have, in the past, usually been made indirectly by e.g., normal incidence reflectivity over an extended wavelength region (1-40 eV or more) and numerical integration using the Kramers-Kronig transformation. This process is difficult at best, and many sources of error and uncertainty are inherent. The values at any one wavelength are influenced by errors at all others. Because of the high angular resolution of our automatic ellipsometer, its capability of covering wide spectral range and the fact that each measurement is independent and does not involve any other, we are able to obtain a resolution and precision previously unattainable. The clear identification of the shift in peak position from 3.0 eV to 2.8 eV for the ϵ_2^o and ϵ_2^e with the crystallographic direction of the single crystal hematite may extend to studies of many other optical active materials, e.g., single crystal of transition metal oxides. The peak height differences in ϵ_2 of two polycrystalline $\alpha\text{-Fe}_2\text{O}_3$ at the lower photon energy (2.2 eV) are probably due to the defect concentration difference caused by the differences in the sintering process, e.g., temperature difference, doping concentration difference, and the variation in partial oxygen pressures

during the sample preparation.

The optical properties of some materials, studied by using ellipsometry can be very useful to such diverse areas as photoelectrolysis (128-130) and photo energy conversion devices. Recent research in this area has been concentrating on how to modify the electrode material in order to utilize energy from the majority of sunlight, e.g., modifying $\alpha\text{-Fe}_2\text{O}_3$ by doping foreign ions (e.g., Ti^{4+}) (131-134) or simply by anodization of iron foil at high temperature. The energy gap of these materials will be varied due to the defect or doping impurities in the modified materials. With the help of the ellipsometric determination of the optical spectrum, especially the absorption coefficient, related to the extinction coefficient, the effectiveness of the modification can be found.

V. Applicability of ESCA to Passivation Studies

With the restriction of being an ex situ technique for characterization of electrode surfaces, ESCA has the disadvantage of losing potential control on the sample during the processes of taking spectra and transfer from electrolyte to high vacuum system. The applicability of ESCA to passivation studies has become controversial to electrochemists in general. Consequently, there are relatively few reports in the literature regarding the use of ESCA technique to study the anodic passivation films, especially those on iron. The ESCA results of passive films on iron in this research, however, appear highly reasonable in terms of the models proposed for the film in this thesis and complement with the in situ ellipsometric results.

In the complementary ESCA study of alloys, the ESCA results on high chromium content nickel alloys electrodes at transpassive potential region show that the enriched outer chromium oxide layer are completely oxidized to chromium (VI) state. Consequently, the presence of water-soluble chromate (well-known for its strong passivating ability) will passivate the prevailing nickel underlayer. These ESCA results further indicated that the depletion depth of chromium from the electrode surface is deeper than the ejected electron depth (20 \AA). This approach to passivation studies can be extended to the investigation of diverse materials with Cr as one of their constituents and should help to unravel the fundamentals on the corrosion resistant behavior of Cr alloys and steels.

VI. Optical Properties of the Passive Film Grown in Borate Buffer

The complex dielectric constant of the passive film grown in borate buffer have been determined by in situ ellipsometry at different oxide formation potentials (1.35, 1.15 V), at different angles of incidence (65°, 68°, and 70°) for wavelengths from 350 to 760 nm. The spectra obtained have yielded some important information about the passive film on iron.

The wavelength dependence of the complex dielectric constant ($\hat{\epsilon} = \epsilon_1 - i\epsilon_2$) showed a minor peak in ϵ_2 at 2.2 eV and a more substantial peak at or above 3.6 eV. These spectra have been interpreted on the basis of the Lorentz oscillator model used to analyze the $\alpha\text{-Fe}_2\text{O}_3$ data. Furthermore, from the Kramers-Kronig relationship, there must still be a very pronounced transition in ϵ_2 above the range of measurements in order to account for the low frequency value of $\epsilon_1(0)$. Such is likely to occur because of the transition across the 2p-4s gap, which Goodenough (97) expects to occur at ~ 5.5 eV to 6.0 eV and has been observed by Gardner et al. (96) at 5.6 eV in thin film of $\alpha\text{-Fe}_2\text{O}_3$. We further assign the 2.2 eV peak to a d-d transition and the ~ 3.6 eV peak to a charge transfer transition ($0\ 2p + \text{Fe}\ 3d$). We believed the d states in the passive film should be narrow relative to that in crystalline $\alpha\text{-Fe}_2\text{O}_3$ because of less long range ordering and less orbital overlap. The apparent broadening of the ~ 3.6 eV peak is believed to be the result of a distribution of defect states and the presence of protons. The proton incorporation makes the charge transfer process ($0\ 2p + \text{Fe}$

3d) have a high transition energy.

The complex dielectric constant spectra for a film grown at 1.15 V and measured at 1.05 V with 5° difference in ϕ (65° and 70°) are practically the same. This provides some evidence that passive film are reasonably uniform and isotropic and that the surface roughness does not have a major effect.

The ϵ_1 for a passive film grown at 1.35 V and measured at 1.25 V is greater than that for a film grown at 1.15 V and measured at 1.05 V. The 2.2 eV minor peak in ϵ_2 for the former is greater than that for the latter film. Such is to be expected on the basis that the defect states (oxygen hole or Fe^{4+} ions) increase somewhat as the anodic potential increased from 1.05 V to 1.25 V (see Ref. 72). The broad peak in ϵ_2 at or above 3.6 eV did not change appreciably for films grown at these two potentials, indicating that changes in the defect structure and proton concentration were not great enough to cause appreciable changes in the spectrum.

VII. The Nature of the Passive Film Grown in Borate Buffer

The passive film on iron grown in borate buffer is believed to be a ferric oxyhydroxide with a variable concentration of incorporated protons. The material can exist over a moderate range of stoichiometry with variation of Fe^{2+} , Fe^{4+} , O^- , and H^+ , and by vacancies of any of these species. The overall concentrations and local distributions of these species is determined by the external potential and solution composition (particularly pH).

At the metal-film interface, the concentration of Fe^{2+} species is determined principally by the thermodynamic equilibrium of the reaction $\text{Fe}^0 + 2 \text{Fe}^{3+} \rightleftharpoons 3 \text{Fe}^{2+}$, and is relatively invariant over a wide electrode potential range. This excess Fe^{2+} must be balanced by a local excess of H^+ or a deficiency of O^- . At the film-solution interface, the concentration of Fe^{2+} or Fe^{4+} is determined by the applied potential and solution composition. The equilibrium local concentrations of the various charged species are then set by the requirement that their electrochemical potentials $\bar{\mu}_i$ be constant throughout the film. In view of the potential gradients in the film, at equilibrium there must be gradients in the chemical potentials and hence concentration gradients of these species to fulfill this thermodynamic requirement.

At intermediate potentials (~ 0.8 to 1.1 V) the major (outer) portion of the film is an insulator. In the region immediately adjacent to the metal, a finite concentration gradient of Fe^{2+} extends into the film. At lower potentials, this region extends further

into the oxide, accompanied by a redistribution of protons. The local conductivities in this region are higher than in the outer portion. With increasing potential the thickness of the outer insulating region increases and that for the Fe^{2+} region decreases but always remains finite. For potentials above ~ 1.1 V, a small concentration of Fe^{4+} is produced at the outer surface accompanied by a removal of protons or possibly introduction of excess oxygen as a consequence of electrochemical oxidation. As the potential increases further, the Fe^{4+} concentration increases, a concentration gradient extends into the film and this outer region is made conductive. At sufficiently high potentials (>1.5 V) the insulating middle region is made sufficiently thin that conduction through it occurs and O_2 evolution commences. This conduction may be electronic or ionic, and may involve electron tunnelling.

Over the passive potential range, the film probably always contains an insulating region essential void of Fe^{2+} or Fe^{4+} states. At the lowest accessible potentials (i.e., close to or at the Flade potential) a sufficient concentration of Fe^{2+} has reached the surface for film dissolution to start. At potentials above this value a substantial electrostatic potential drop exists across the insulating region. If the film is sufficiently thin, this potential gradient will reach the critical value required to induce field-assisted growth, thus lowering the potential gradient.

The two conductive regions are analogous to an n-type semiconductor (Fe^{2+}) region and a p-type (Fe^{4+} or hole) region as dis-

cussed briefly in Chapter I. The treatment as a classical n- or p-type semiconductor is probably greatly oversimplified since the passive film is such a highly defect system.

VIII. Remarks

This research reveals new insights into the nature and fundamentals of the passive film on iron grown in borate buffer (pH 8.4) solution. These new insights, however, raise more questions which have to be solved in order to understand the passivation phenomena as a whole. At the present time, we dare not say we have solved all the fundamental problems concerning the nature of the passive film on iron because we have not yet obtained some important information, e.g., 1) sufficient spectroscopies, especially at shorter wavelengths to establish the energy level diagram of the passive film; 2) electrode potential dependence of the optical spectra of the passive film (formed both at lower passivation potentials and at very high anodic potentials); 3) the concentration and chemical involvement of the protons in the film; 4) the time dependence of the optical and electrochemical properties by potential perturbation to determine the mobility of protons in the film.

-911-

REFERENCES

1. Masa-ichi Nagayama and M. Cohen, J. Electrochem. Soc., 109, 781 (1962).
2. J. O'M. Bockris, D. Drazic and A. R. Despic, Electrochim. Acta, 4, 325 (1961).
3. A. A. El Miligy, D. Geana and W. J. Lorenz, Electrochim. Acta, 20, 273 (1975).
4. J. Bessone, L. Karkaya, P. Lorbeer and W. J. Lorenz, Electrochim. Acta, 22, 1147 (1977).
5. G. Bech-Nielsen, Electrochim. Acta, 21, 627 (1976).
6. H. J. Engell, Electrochim. Acta, 22, 987 (1977).
7. F. K. Bonhoeffer, Z. Metellkde, 44, 77 (1953).
8. K. G. Weil and F. K. Bonhoeffer, Z. Phys. Chem. N. F., 4, 175 (1955).
9. H. H. Uhlig and P. King, J. Electrochem. Soc., 106, 1 (1959).
10. H. Göhr and E. Lange, Naturwissenschaften, 43, 12 (1956).
11. K. J. Vetter, Z. Elektrochem., 62, 642 (1958).
12. N. Sato and M. Cohen, J. Electrochem. Soc., 111, 512 (1964).
13. R. V. Moshtev, Ber. Bunsenges. Physik. Chem., 71, 1079 (1967).
14. R. Frankenthal, Electrochim. Acta, 16, 1845 (1971).
15. C. Wagner, Ber. Bunsenges. Physik. Chem., 77, 1090 (1973).
16. N. Cabrera and N. F. Mott, Rpts. Prog. Phys., 12, 163 (1948-49).
17. L. Young, "Anodic Oxide Films," Academic Press, New York 1961.
18. E. J. W. Verwey, Physica, 2, 1059 (1935).
19. J. F. Dewald, J. Electrochem. Soc., 102, 1 (1955).
20. M. A. H. Lanyon and B. M. W. Trapnell, Proc. Roy. Soc. Lond., A227, 387 (1955).

AD-A067 364

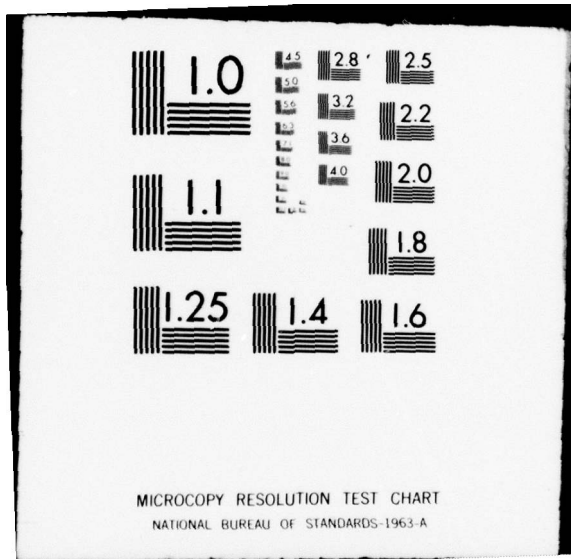
CASE WESTERN RESERVE UNIV CLEVELAND OHIO DEPT OF CHEMISTRY F/G 11/6
PASSIVATION STUDIES OF IRON, NICKEL AND THEIR ALLOYS BY 'IN SIT--ETC(U)
FEB 79 C T CHEN, B D CAHAN, E YEAGER N00014-75-C-0953
TR-48 NL

UNCLASSIFIED

3 OF 3
AD
A057364



END
DATE
FILMED
6 -79
DDC



MICROCOPY RESOLUTION TEST CHART
NATIONAL BUREAU OF STANDARDS-1963-A

21. D. D. Eley and P. R. Wilkinson, Proc. Roy. Soc. Lond., A254, 327 (1960).
22. J. Kruger and J. P. Calvert, J. Electrochem. Soc., 114, 43 (1967).
23. F. P. Fehlner and N. F. Mott, Oxidation of Metals, 2, 59 (1970).
24. J. A. Davies, B. Domeij, J. P. Pringle and F. Brown, J. Electrochem. Soc., 112, 675 (1965).
25. C. M. Quinn and M. W. Roberts, Trans. Faraday Soc., 60, 1865 (1964).
26. K. J. Vetter, "Electrochemical Kinetics," Academic Press, 1967.
27. H. H. Uhlig, Acta Met., 4, 541 (1956).
28. O. H. Hamilton and H. A. Miley, Trans. Electrochem. Soc., 81, 413 (1942).
29. A. T. Fromhold, Jr., and E. L. Cook. J. Appl. Phys., 38, 1546 (1967).
30. W. H. Butter, E. T. Kinzer, Jr., and A. T. Fromhold, Jr., Phys. Letters, 40A, 57 (1972).
31. A. T. Fromhold, Jr., and J. Kruger, J. Electrochem. Soc., 120, 722 (1973).
32. A. T. Fromhold, Jr., in "Oxides and Oxide Films," eds. J. W. Diggle and A. K. Vijh, Volume 3, Chap. 1, Marcel Dekker, Inc., New York, 1976.
33. Masa-ichi Nagayama and M. Cohen, J. Electrochem. Soc., 110, 670 (1963).
34. N. Sato and M. Cohen, J. Electrochem. Soc., 111, 519 (1964).
35. K. Kudo, T. Shibata, G. Okamoto and N. Sato, Corrosion Sci., 8, 809 (1968).
36. N. Sato, K. Kudo and T. Noda, Corrosion Sci., 10, 785 (1970).
37. N. Sato and K. Kudo, Electrochim. Acta, 16, 447 (1971).
38. N. Sato, K. Kudo and T. Noda, Electrochim. Acta, 16, 1909 (1971).

39. H. T. Yolken, J. Kruger and J. P. Calvert, *Corrosion Sci.*, 8, 103 (1968).
40. M. C. Bloom and L. Goldenberg, *Corrosion Sci.*, 5, 623 (1965).
41. M. Cohen, *J. Phys. Chem.*, 56, 451 (1952).
42. M. Cohen, *J. Electrochem. Soc.*, 121, 191c (1974).
43. G. L. Foley, J. Kruger and C. J. Bechtold, *J. Electrochem. Soc.*, 114, 936 (1967).
44. J. E. Holliday and R. P. Frankenthal, *J. Electrochem. Soc.*, 119, 1190 (1972).
45. G. W. Simmons, E. Kellerman and H. Leidheiser, *Corrosion Sci.*, 69, 227 (1973).
46. W. E. O'Grady and J. O'M. Bockris, *Surface Sci.*, 38, 249 (1973).
47. M. Seo, J. B. Lumsden and R. W. Staehle, *Surface Sci.*, 42, 337 (1974).
48. R. W. Revie, B. G. Baker, and J. O'M. Bockris, *J. Electrochem. Soc.*, 122, 1460 (1975).
49. C. R. Brundle, *Surface Sci.*, 66, 581 (1977).
50. P. B. Sewell, D. F. Mitchell and M. Cohen, *Surface Sci.*, 33, 535 (1972).
51. R. J. Armstrong, A. H. Morrish and G. A. Sawatzky, *Phys. Lett.*, 23, 414 (1966).
52. K. J. Vetter, *Z. Physik. Chem.*, 202, 1 (1953).
53. U. F. Franck and K. Weil, *Z. Elektrochem.*, 56, 814 (1952).
54. A. C. Makrides, *J. Electrochem. Soc.*, 111, 392 (1964).
55. A. C. Makrides, *J. Electrochem. Soc.*, 113, 1158 (1966).
56. K. J. Vetter, *Z. Elektrochem.*, 62, 642 (1958).
57. W. Ch. van Geel and J. W. A. Scholte, *Philips Res. Repts.*, 6, 54 (1951).
58. R. W. Gurney, *Proc. Roy. Soc. Lond.*, A134 137 (1931).

59. H. Gerischer, *Z. Phys. Chem. N. F.*, 26, 223, 325 (1960); 27, 48 (1961).
60. R. A. Marcus, *J. Chem. Phys.*, 24, 966 (1956).
61. H. Gerischer, in "Advances in Electrochemistry and Electrochemical Engineering," No. 1, p. 139, eds. P. Delahay, Interscience Publishers, New York, 1963.
62. R. V. Moshtev, *Electrochim. Acta*, 16, 2039 (1971).
63. A. M. Kuznetsov and R. R. Dogonadze, *Izv. Akad. Nauk SSSR, Ser. Kim.*, 12, 2140 (1964).
64. J. W. Schultze, "Electron Transfer Reactions on Passive Films," in Proceedings of the 4th International Symposium on Passivity, The Electrochemical Society, Princeton, New Jersey, in press.
65. U. Stimming and J. W. Schultze, *Ber. Bunsenges. Physik. Chem.*, 80, 1297 (1976).
66. K. Bohnenkamp and H. J. Engell, *Z. Elektrochem.*, 61, 1184 (1957).
67. B. Pettinger, H. -R. Schoppel and H. Gerischer, *Ber. Bunsenges. Physik. Chem.*, 78, 452 (1974).
68. R. DeGryse, W. P. Gomes, F. Cardon and J. Vennik, *J. Electrochem. Soc.*, 122, 711 (1975).
69. H. -J. Engell and B. Ilshner, *Z. Elektrochem.*, 59, 716 (1955).
70. R. V. Moshtev, *Ber. Bunsenges. Physik. Chem.*, 72, 452 (1968).
71. J. F. Dewald, *Bell System Techn. J.*, 39, 615 (1960).
72. D. Wheeler, B. D. Cahan, C. T. Chen and E. Yeager, in "Optical Studies of the Passivation of Iron," in Proceedings of the 4th International Symposium on Passivity, The Electrochemical Society, Princeton, New Jersey, in press.
73. A. B. Winterbottom, *Trans. Faraday Soc.*, 42, 487 (1946).
74. W. -K. Paik and J. O'M. Bockris, *Surface Sci.*, 28, 61 (1971).
75. B. D. Cahan, J. Horkans and E. Yeager, *Surface Sci.*, 37, 559 (1973).
76. B. D. Cahan, *Surface Sci.*, 56, 354 (1976).

77. J. L. Ord and D. J. De Smet, *J. Electrochem. Soc.*, 113, 1258 (1966).
78. F. C. Ho and J. L. Ord, *J. Electrochem. Soc.*, 119, 139 (1972).
79. J. L. Ord and D. J. DeSmet, *J. Electrochem. Soc.*, 118, 206 (1971).
80. J. O'M. Bockris, M. Genshaw and V. Brusich, *Sym. Faraday Soc.*, 4, 177 (1970).
81. H. Wroblowa, V. Brusich and J. O'M. Bockris, *J. Phys. Chem.*, 75, 2823 (1971).
82. J. O'M. Bockris, M. A. Genshaw, V. Brusich and H. Wroblowa, *Electrochim. Acta*, 16, 1859 (1971).
83. L. S. Bartell and D. Churchill, *J. Opt. Soc. Am.*, 65, 2242 (1961).
84. C. L. McBee and J. Kruger, *Surface Sci.*, 16, 340 (1969).
85. J. Horkans, Ph.D. Thesis, Case Western Reserve University, 1973.
86. F. L. McCrackin, E. Passaglia, R. R. Stromberg and H. L. Steinberg, *J. Res. Natl. Std.*, 67A, 363 (1963).
87. "Ellipsometry in the Measurement of Surfaces and Thin Films," eds. E. Passaglia, R. R. Stromberg and J. Kruger, *Natl. Bur. Std. Misc. Publ. 256* (U. S. Gort. Printing Office, Washington, D.C., 1964).
88. *Proceedings of the Symposium on Recent Developments in Ellipsometry*, eds. N. M. Bashara, A. B. Buckman and A. C. Hall (North-Holland, Amsterdam, 1969), published in *Surface Sci.*, 16 (1969).
89. *Surface Sci.*, 56 (1976).
90. D. E. Aspnes, *J. Opt. Soc. Am.*, 64, 812 (1974).
91. R. M. A. Azzam and N. M. Bashara, *J. Opt. Soc. Am.*, 62, 222 (1972).
92. M. Elshazly-Zaghloul, R. M. A. Azzam and N. M. Bashara, *Surface Sci.*, 56, 281 (1976).
93. R. M. A. Azzam and N. M. Bashara, *J. Opt. Soc. Am.*, 65, 462 (1975).

94. H. T. Yolken and J. Kruger, *J. Opt. Soc. Am.*, 55, 842 (1965).
95. F. Wooton, in "Optical Properties of Solids," Academic Press, 1972.
96. R. F. G. Gardner, F. Sweet and D. W. Tanner, *J. Phys. Chem. Solids*, 24, 1183 (1963).
97. J. B. Goodenough, in "Progress in Solid State Chemistry," ed. H. Reiss, p. 300, Pergamon Press, 1971.
98. M. J. Dignam and M. Moskovits, *J. C. S. Faraday II*, 69, 56 (1973).
99. M. J. Dignam and M. Moskovits, *J. C. S. Faraday II*, 69, 65 (1973).
100. I. Ohlidal and F. Lukes, *Optical Acta*, 19, 817 (1972).
101. R. Ghez, *J. Chem. Phys.*, 58, 1838 (1973).
102. K. W. Goswami and R. W. Staehle, *Electrochim. Acta*, 16, 1895 (1971).
103. C. Lukac, J. B. Lumsden, S. Smialowska, and R. W. Staehle, *J. Electrochem. Soc.*, 122, 157 (1975).
104. B. D. Cahan and P. Rùletschi, *J. Electrochem. Soc.*, 106, 543 (1959).
105. A. Kozawa and J. F. Yeager, *J. Electrochem. Soc.*, 112, 959 (1965).
106. B. D. Cahan, J. B. Ockerman, R. F. Amlie and P. Rùletschi, *J. Electrochem. Soc.*, 107, 725 (1960).
107. M. Klasson, J. Hedman, A. Berndtsson, R. Nilsson, C. Nordling, and P. Melnik, *Physica Scripta*, 5, 93 (1972).
108. I. Olefjord, *Corrosion Sci.*, 15, 687 (1975).
109. K. Asami and K. Hashimoto, *Corrosion Sci.*, 17, 559 (1977).
110. C. F. Brucker and T. N. Rhodin, *Surface Sci.*, 57, 523 (1976).
111. A. Muan, *Am. J. of Sci.*, 256, 171 (1958).
112. F. A. Krüger, *J. Phys. Chem. Solids*, 29, 1889 (1968).

113. K. Y. Yu, W. E. Spicer, J. Lindau, P. Pianetta, S. F. Lin, *Surface Sci.*, 57, 157 (1976).
114. I. Olefjord and H. Fischmeister, *Corrosion Sci.*, 15, 697 (1975).
115. M. Seo and N. Sato, *Corrosion Sci.*, 18, 577 (1978).
116. M. Seo, N. Sato, J. B. Lumsden and R. W. Staehle, *Corrosion Sci.*, 17, 209 (1977).
117. M. Seo, J. B. Lumsden and R. W. Staehle, *Surface Sci.*, 42, 337 (1974).
118. H. W. Pickering, in "Passivity and Its Breakdown on Iron and Iron Base Alloys," (1975) Honolulu, eds. R. W. Staehle and H. Okada, p. 79, N.A.C.E., Houston, Texas (1976).
119. Lo I. Yin, S. Ghose, and I. Adler, *Appl. Spectrosc.*, 26, 355 (1972).
120. S. Hulfner, R. L. Cohen and G. K. Wertheim, *Physica Scripta*, 5, 91 (1972).
121. K. S. Kim and N. Winograd, *Surface Sci.*, 43, 625 (1974).
122. C. D. Wagner, *Anal. Chem.*, 44, 1050 (1972).
123. W. Carter, Jr., Ph.D. Thesis, University of Tennessee, 1973.
124. H. Berthou and C. K. Jørgensen, *Anal. Chem.*, 47, 482 (1975).
125. W. Schockley, *Electrons and Holes in Semiconductors*, D. Van Nostrand, Princeton, N.J., 1966.
126. V. G. Levich, in "Advances in Electrochemistry and Electrochemical Engineering", No. 4, Chap. 5. ed. P. Delahay, Academic, New York, 1966.
127. R. Weast, in "Handbook of Chemistry and Physics," 57th edition CRC Press, Cleveland, Ohio, 1976.
128. K. L. Hardee and A. J. Bard, *J. Electrochem. Soc.*, 123, 1024 (1976).
129. L. -S. R. Yeh and N. Hackerman, *J. Electrochem. Soc.*, 124, 833 (1977).
130. J. H. Kennedy and K. W. Frese, Jr., *J. Electrochem. Soc.*, 125, 709 (1978).

131. E. J. W. Verwey, P. W. Haaïjman, F. C. Romeijn, and C. W. van Oosterhout, *Philips Res. Rep.*, 5, 173 (1950).
132. F. J. Morin, *Phys. Rev.*, 83, 1005 (1951).
133. J. H. Kennedy and K. W. Frese, Jr., *J. Electrochem. Soc.*, 125, 723 (1978).
134. J. S. Curran and W. Gissler, *J. Electrochem. Soc.*, 126, 56 (1979).

-187-

APPENDIX A

Ex situ ESCA Studies on Passive Films

The ex situ ESCA results and discussions assembled here include those of passive films on pure nickel, pure chromium, 20 and 30% Cr-Ni alloys, 50% Ni-Fe alloys, and 316 stainless steel grown in borate buffer (pH = 8.4).

The ESCA spectra were examined for the electrodes which had been passivated at 0.35, 0.65, 0.95, 1.35 and 1.55 V for 30 minutes in the borate buffer and after subsequent treatment described in Chapter II were transferred to the ESCA.

The results and discussions presented are primarily qualitative and comparative because of the same reasoning as pointed out in Section IX of Chapter III.

I. Passive Films on Pure Nickel Electrodes

A. Ni Spectra

Nickel electrode appears to be harder to be oxidized or contaminated by the residue gases in the vacuum system of a Varian IEE-15. It is easier to observe the bare Ni $2P_{3/2}$ peak at 852.0 eV (Fig. A-1). Ni $2P_{3/2}$ showed the bare nickel peak as a shoulder along with Ni(II) peak even after nickel passivated at 0.95 V for 30 minutes. As the anodic oxide formation potential increased from 0.35 V to 1.15 V, the bare Ni peak decreased continuously and eventually disappeared. By calibration, this will permit one to evaluate the film thickness of the passive film on nickel. It also

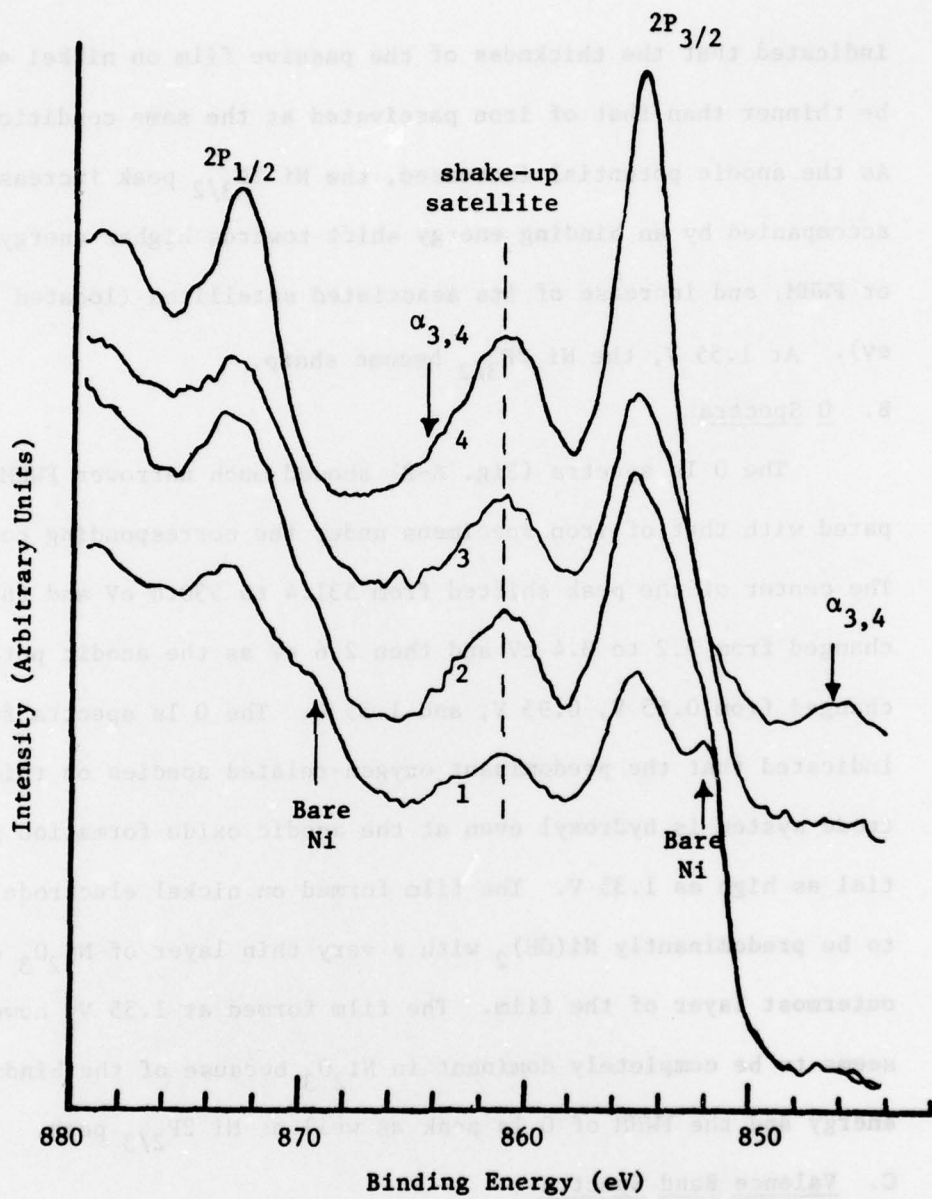


Figure A-1: Ni 2P photo-electron spectra for passive films on nickel grown in borate buffer (pH 8.4) at different potentials: 1) 0.65 V; 2) 0.95 V; 3) 1.35 V; 4) 1.55 V vs RHE.

indicated that the thickness of the passive film on nickel should be thinner than that of iron passivated at the same conditions. As the anodic potential increased, the Ni $2P_{3/2}$ peak increased, accompanied by an binding energy shift towards higher energy, broader FWHM, and increase of its associated satellites (located at 861.0 eV). At 1.55 V, the Ni $2P_{3/2}$ become sharp.

B. O Spectra

The O 1s spectra (Fig. A-2) showed much narrower FWHM compared with that of iron specimens under the corresponding conditions. The center of the peak shifted from 531.4 to 530.6 eV and the FWHM changed from 3.2 to 3.4 eV and then 2.6 eV as the anodic potential changed from 0.65 V, 0.95 V, and 1.55 V. The O 1s spectra further indicated that the predominant oxygen-related species on this electrode system is hydroxyl even at the anodic oxide formation potential as high as 1.35 V. The film formed on nickel electrode appears to be predominantly $Ni(OH)_2$ with a very thin layer of Ni_2O_3 on the outermost layer of the film. The film formed at 1.55 V, however, seems to be completely dominant in Ni_2O_3 because of the binding energy and the FWHM of O 1s peak as well as Ni $2P_{2/3}$ peak.

C. Valence Band Spectra

The valence band spectra (Fig. A-3) of nickel electrode passivated at 0.65, 0.95, 1.35, and 1.55 V indicated a large contribution of bare nickel, due to the much thinner films relative to those on iron formed at the corresponding conditions. As the anodic oxide formation potential increased from 0.65 V to 1.55 V

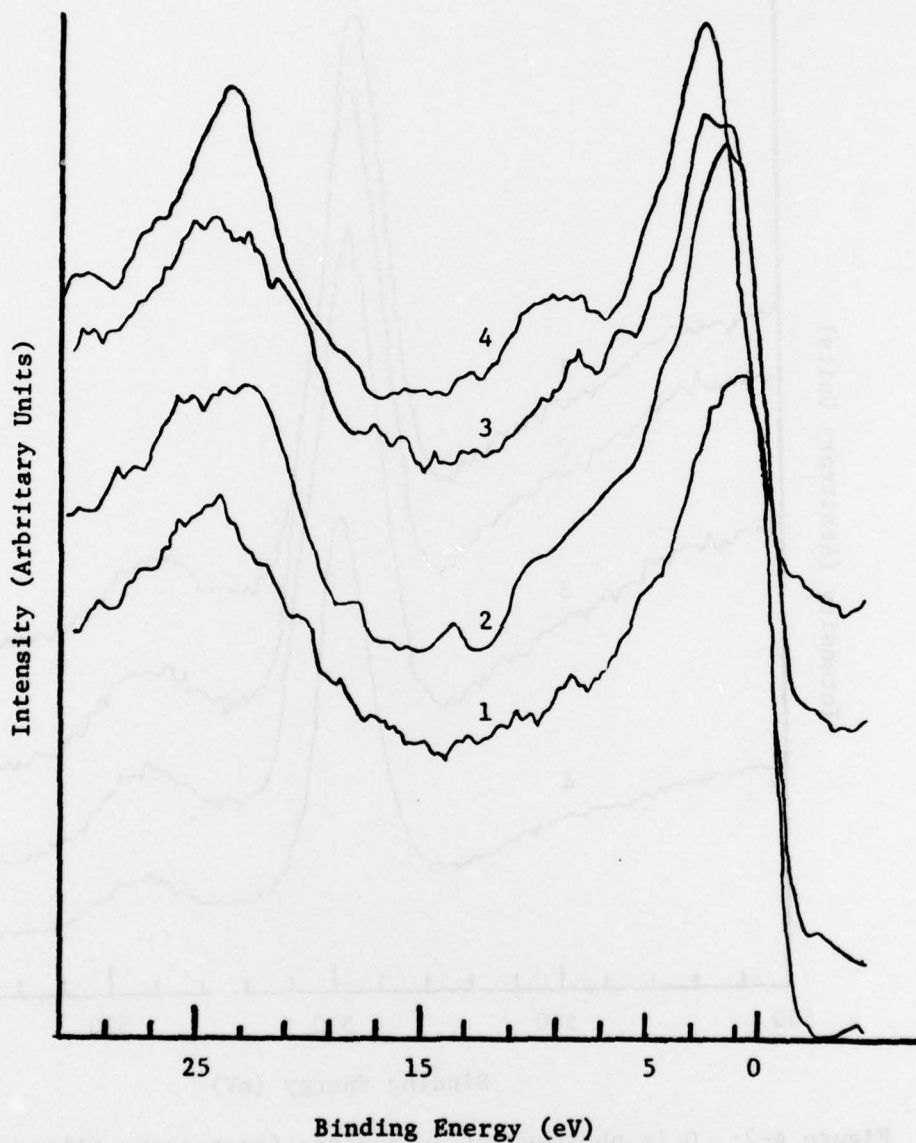


Figure A-3: X-ray photo-electron spectra of valence band of passive films on nickel grown in borate buffer (pH 8.4) at different potentials: 1) 0.65 V; 2) 0.95 V; 3) 1.35 V; 4) 1.55 V vs RHE.

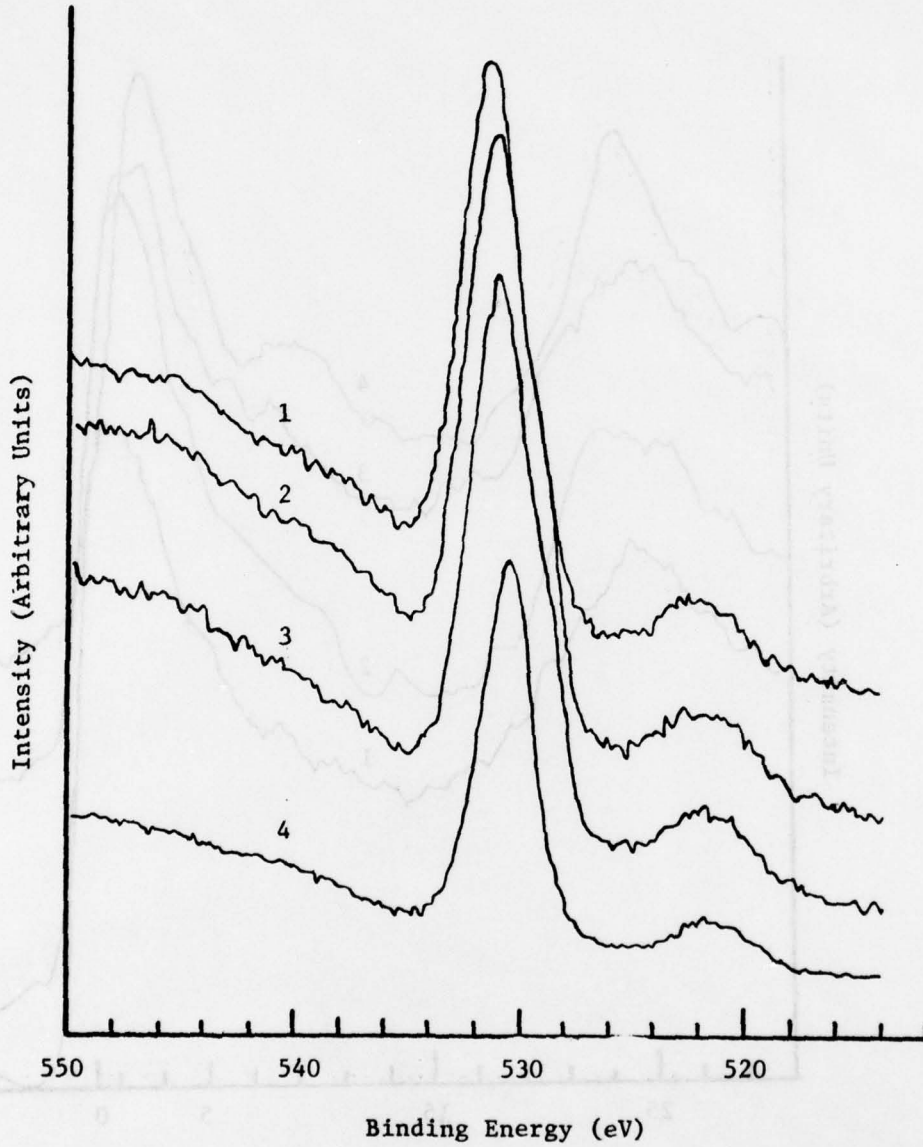


Figure A-2: 0 1s photo-electron spectra for passive films on nickel grown in borate buffer (pH 8.4) at different potentials: 1) 0.65 V; 2) 0.95 V; 3) 1.35 V; 4) 1.55 V vs RHE.

the peak position of Ni 3d band shifted from 1.6 eV to 2.6 eV. This can be explained in terms of the oxide formation on nickel metal reducing the free electronic density of states of the metal surface. The corresponding broadness of the peak narrower and its shoulder on high binding energy increased correspondingly. The valence band spectrum for the passive film formed at 1.55 V showed a broad and clear peak of 5.4 eV wide, located between 6.8 eV and 12.2 eV indicating satellites of nickel oxide, most probable in the form of Ni_2O_3 as has been suggested by Kim *et al.* (121) for the outermost surface layer oxides covered on the NiO or on the electrode surfaces (121).

II. Passive Films on Pure Chromium Electrodes

Electrochemically the chromium electrode did not exhibit an active dissolution region in this electrolyte. This might have resulted from the spontaneous oxide formation on the Cr surface in this electrolyte or the residue surface film, which is not reducible cathodically, on the Cr surface after 4/0 emery paper polishing. Consequently, the residue films inhibited anodic dissolution.

A. Cr Spectra

The spectra (Fig. A-4) taken on the electrodes passivated at 0.35 V and up to 1.32 V all showed the presence of bare Cr peak along the low energy shoulder of Cr 2P spectra. This indicated the thickness of the anodic oxide films on chromium grown at all potentials was thinner than the ejected electron escape depth (about 20 Å). As the anodic potential increased to 1.15 V, the solution in

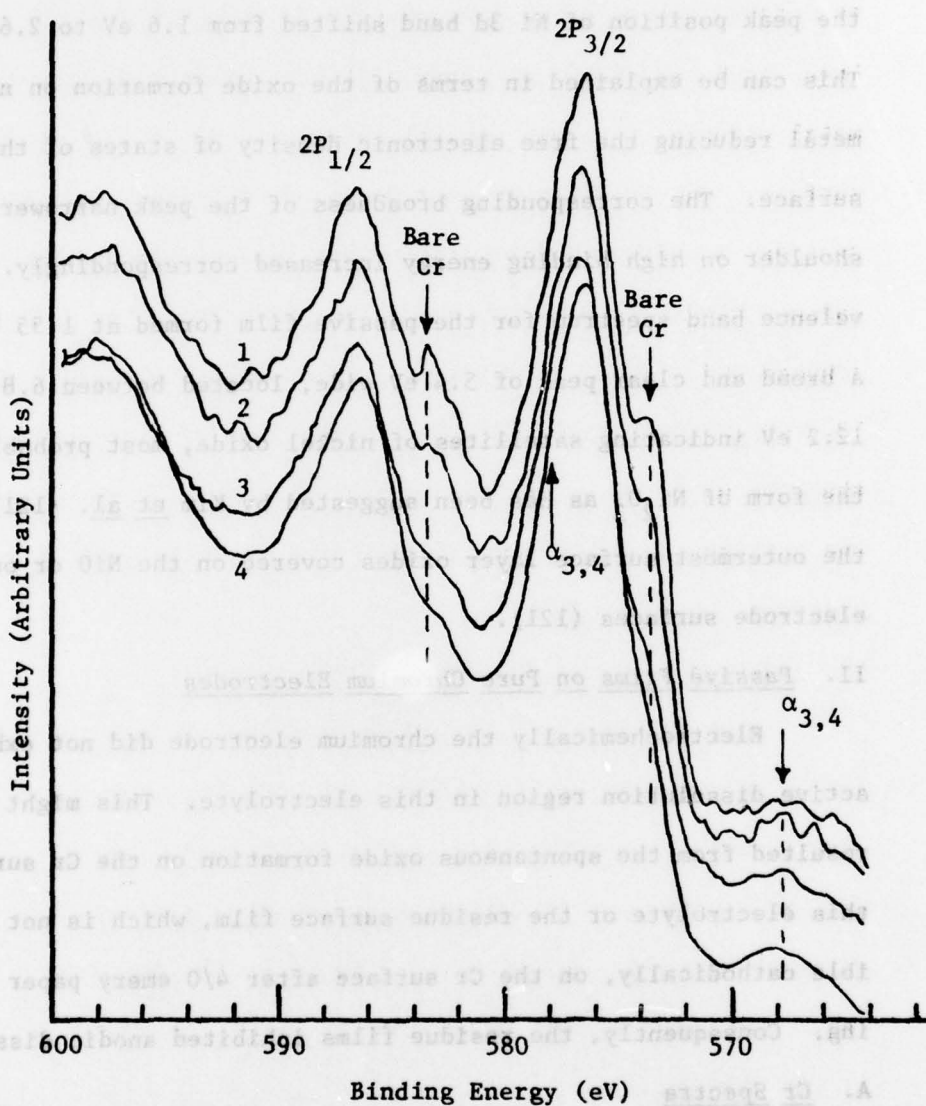


Figure A-4: Cr 2P photo-electron spectra for passive films on Cr grown in borate buffer (pH 8.4) at different potentials: 1) 0.35 V; 2) 0.65 V; 3) 0.95 V; 4) 1.15 V vs RHE.

the vicinity of the chromium electrode surface had a yellowish color, which diffused into the solution. This phenomenon is a confirmative result to explain why chromium, in the case of high chromium content nickel electrodes, is preferentially dissolved into solution in the transpassive region. Furthermore, the species remaining on the electrode surface appears to be undissolved Cr(III) species as formed in the low anodic potential region because of the resemblance of the O 1s and Cr 2P_{3/2} and 2P_{1/2} spectra.

B. O Spectra

The center position (531.4 eV) and broadness (about 4.0 eV) of the O 1s spectra (Fig. A-5) were invariant with the oxide formation potential from 0.35 to 1.15 V. (At this potential, the solution adjacent to the electrode starts to become yellowish.) The ESCA results indicate that the environment of the oxygen in this electrode system does not undergo any drastic changes. The broadness (about 4.0 eV wide) and the high symmetry of the O 1s spectra indicated that there were at least two oxygen species with almost equal amounts.

III. Passive Films on 50% Ni-Fe Electrodes

A. Fe Spectra

The Fe 2P spectra (Fig. A-6) showed significant differences from those obtained for the passive films on pure iron electrodes grown at the corresponding conditions. The Fe 2P_{3/2} peak was even wider than that for pure iron electrodes passivated at the corresponding conditions. The slope at the higher binding energy side

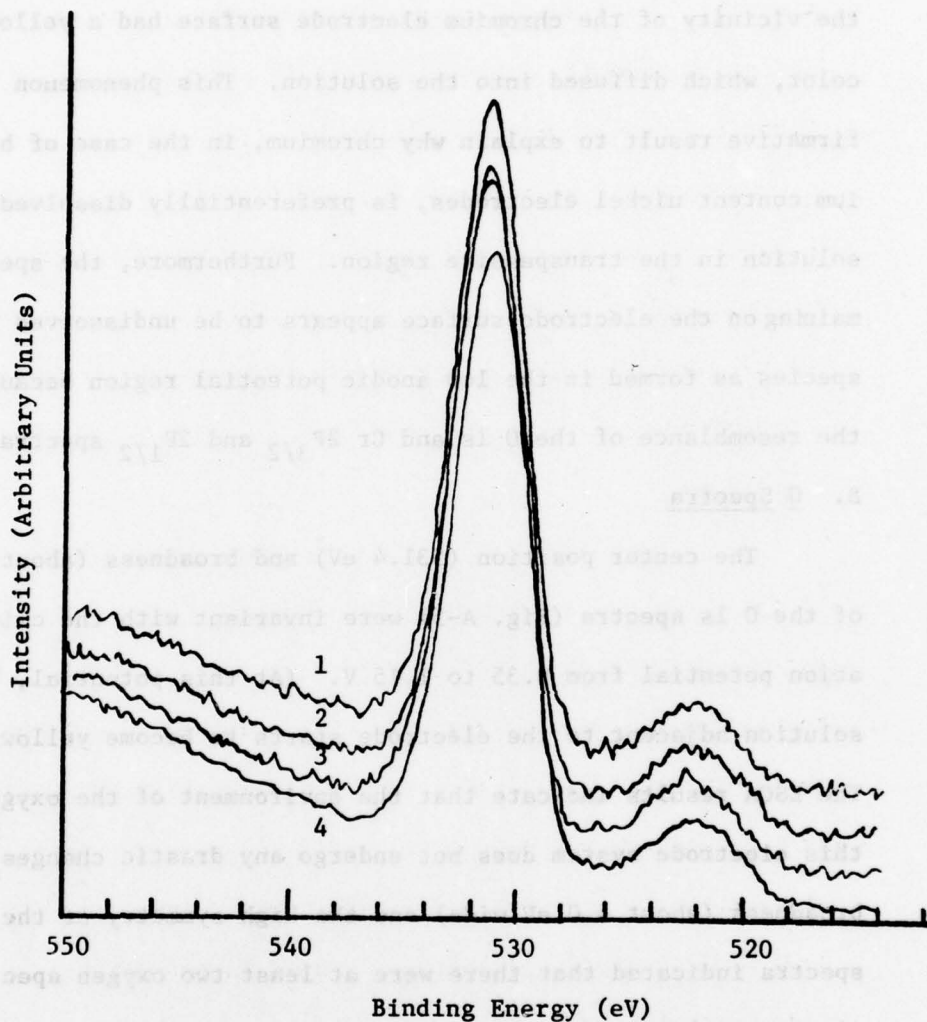


Figure A-5: Cr 2p photo-electron spectra for passive films on Cr grown in borate buffer (pH 8.4) at different potentials: 1) 0.35 V; 2) 0.65 V; 3) 0.95 V; 4) 1.15 V vs RHE.

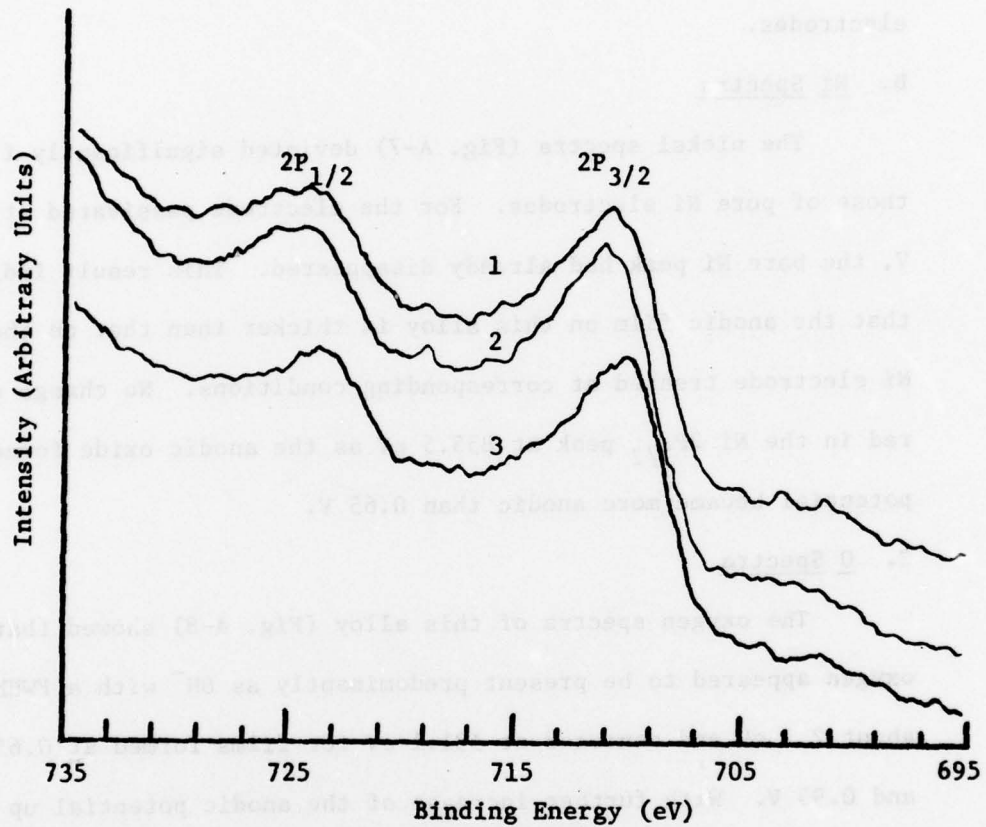


Figure A-6. Fe 2P photo-electron spectra for passive films on 50% Ni-Fe grown in borate buffer (pH 8.4) at different potentials: 1) 0.65 V; 2) 0.95 V; 3) 1.55 V vs RHE.

of $2P_{1/2}$ spectra of iron passivated at low anodic potentials (e.g., 0.65 V and 0.95 V) was not as steep as those obtained from iron electrodes.

B. Ni Spectra

The nickel spectra (Fig. A-7) deviated significantly from those of pure Ni electrodes. For the electrode passivated at 0.65 V, the bare Ni peak had already disappeared. This result indicated that the anodic film on this alloy is thicker than that on the pure Ni electrode treated at corresponding conditions. No change occurred in the Ni $2P_{3/2}$ peak at 855.5 eV as the anodic oxide formation potential became more anodic than 0.65 V.

C. O Spectra

The oxygen spectra of this alloy (Fig. A-8) showed that the oxygen appeared to be present predominantly as OH^- with a FWHM of about 2.7 eV and centered at 531.1 eV for films formed at 0.65 V and 0.95 V. With further increase of the anodic potential up to 1.55 V, the oxide (O^{2-}) content increased with an increase in FWHM (about 3.3 eV) indicated the presence of oxyhydroxide in the passive films.

IV. Passive Films on 20% Cr-Ni and 30% Cr-Ni Alloys

A. Ni Spectra

The nickel 2P spectra of the passive films on these two alloys (Fig. A-9) look almost the same as those on the pure nickel electrode grown at the corresponding conditions. From these experimental results, we could make a conclusion that the thickness

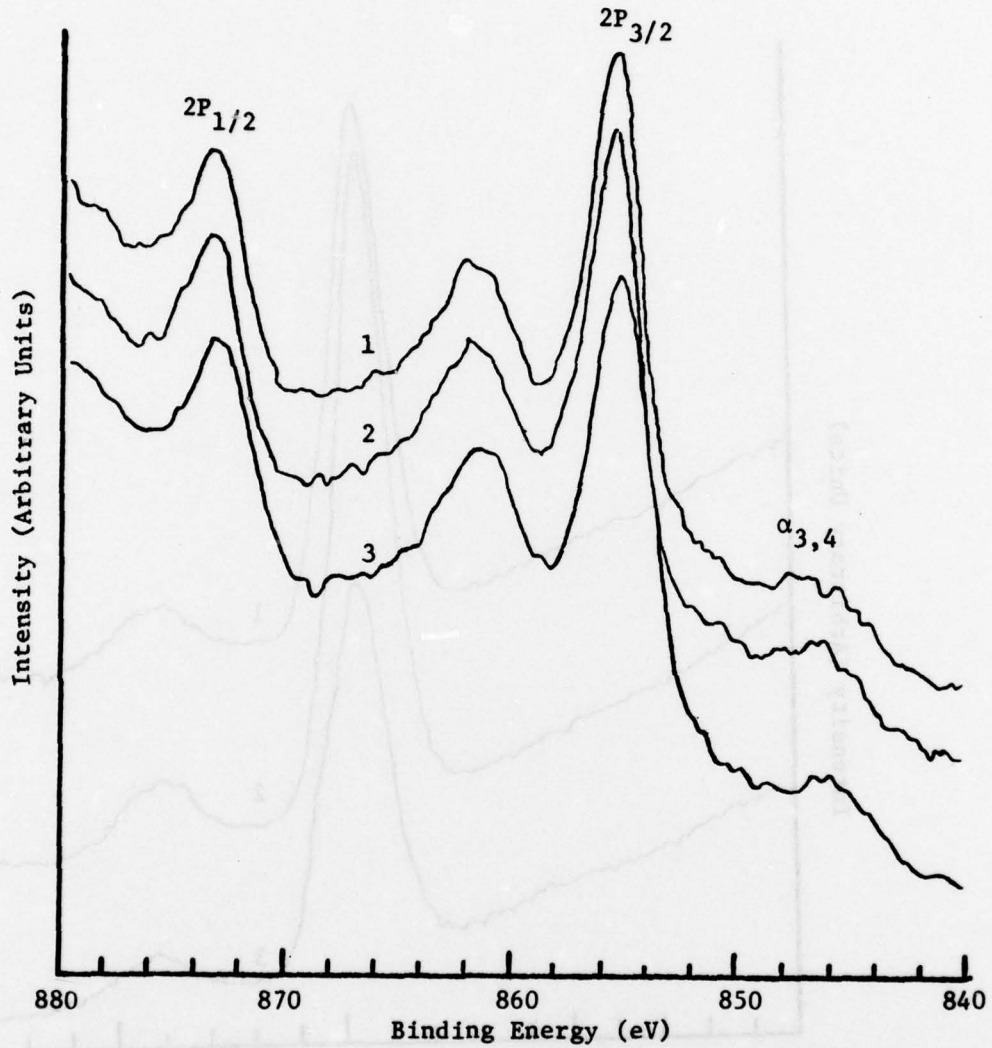


Figure A-7: Ni 2P photo-electron spectra for passive films on 50% Ni-Fe grown in borate buffer (pH 8.4) at different potentials: 1) 0.65 V; 2) 0.95 V; 3) 1.55 V vs RHE.

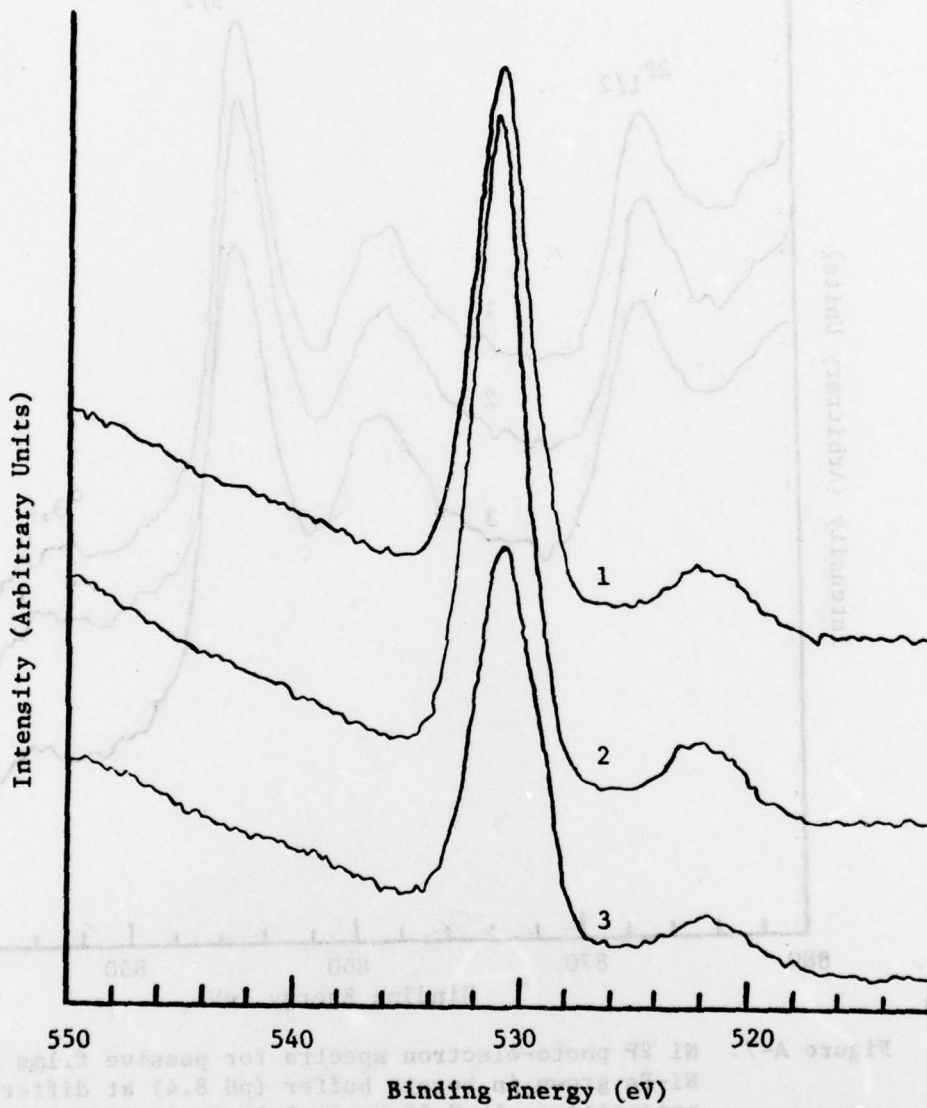


Figure A-8: Ni 2p photo-electron spectra for passive films on 50% Ni-Fe grown in borate buffer (pH 8.4) at different potentials: 1) 0.65 V; 2) 0.95 V; 3) 1.55 V vs RHE.

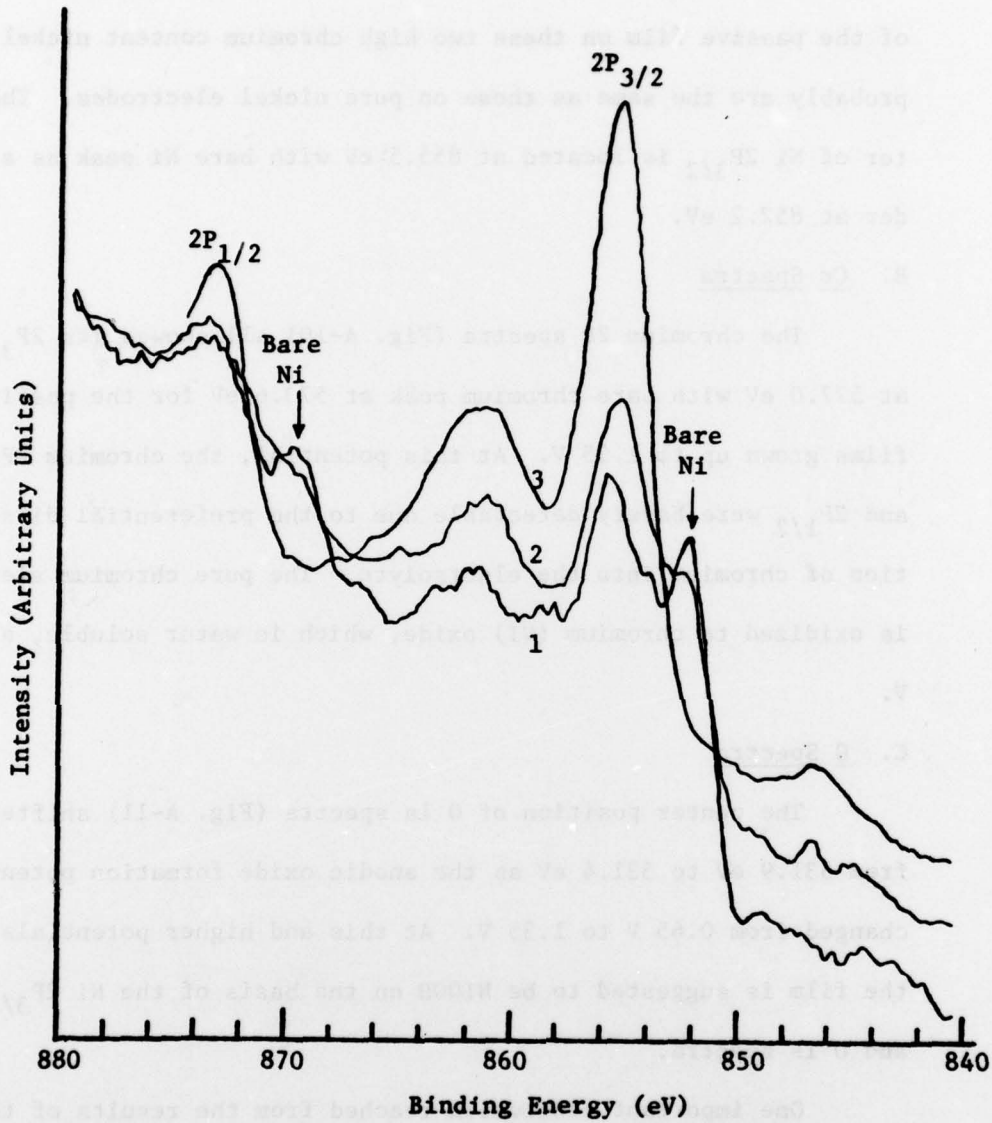


Figure A-9: Ni 2P photo-electron spectra for passive films on 30% Cr-Ni grown in borate buffer (pH 8.4) at different potentials: 1) 0.65 V; 2) 0.95 V; 3) 1.35 V vs RHE.

of the passive film on these two high chromium content nickel alloys probably are the same as those on pure nickel electrodes. The center of Ni $2P_{3/2}$ is located at 855.5 eV with bare Ni peak as a shoulder at 852.2 eV.

B. Cr Spectra

The chromium 2P spectra (Fig. A-10) all showed its $2P_{3/2}$ peak at 577.0 eV with bare chromium peak at 573.6 eV for the passive films grown up to 1.35 V. At this potential, the chromium $2P_{3/2}$ and $2P_{1/2}$ were barely detectable due to the preferential dissolution of chromium into the electrolyte. The pure chromium electrode is oxidized to chromium (VI) oxide, which is water soluble, at 1.15 V.

C. O Spectra

The center position of O 1s spectra (Fig. A-11) shifted from 531.9 eV to 531.4 eV as the anodic oxide formation potential changed from 0.65 V to 1.35 V. At this and higher potentials, the film is suggested to be NiOOH on the basis of the Ni $2P_{3/2}$ and O 1s spectra.

One important conclusion reached from the results of these two alloys was that when these two alloys electrochemically treated at the transpassive region (above 1.25 V), the chromium was preferentially dissolved into the solution and the electrode surfaces became black indicating either formation of NiOOH or Ni_2O_3 . These experimental evidence, combined with the FWHM of O 1s (about 3.5 eV)

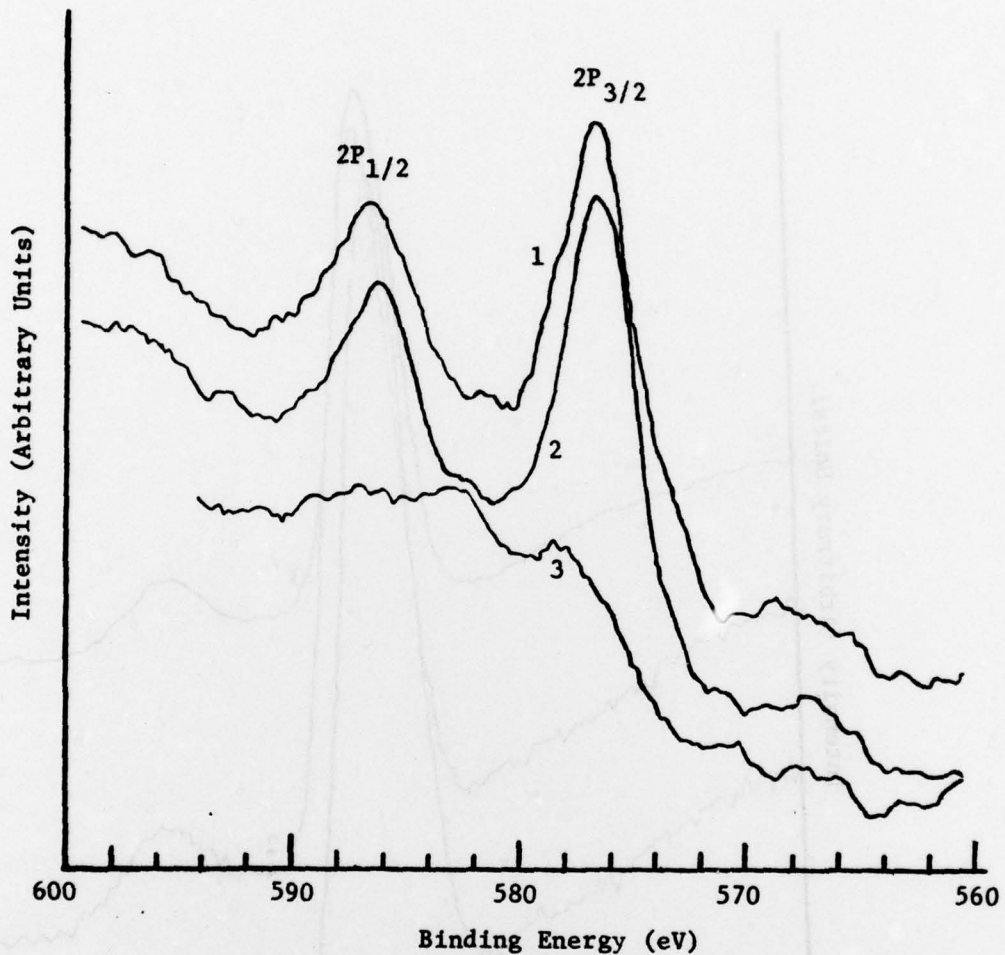


Figure A-10: Cr 2P photo-electron spectra for passive films on 30% Cr-Ni grown in borate buffer (pH 8.4) at different potentials: 1) 0.65 V; 2) 0.95 V; 3) 1.35 V vs RHE.

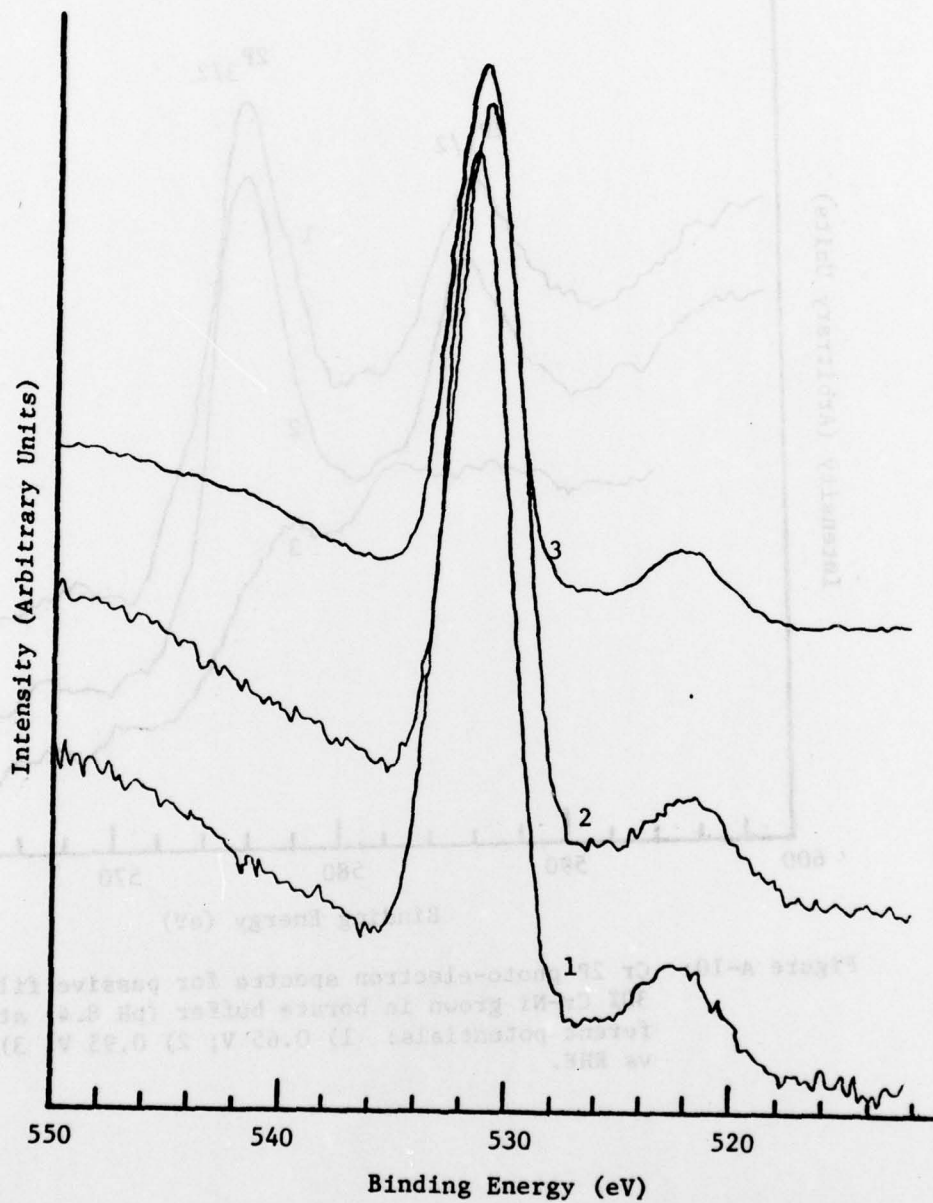


Figure A-11: 0 1s photo-electron spectra for passive films on 30% Cr-Ni grown in borate buffer (pH 8.4) at different potentials: 1) 0.65 V; 2) 0.95 V; 3) 1.35 V vs RHE.

indicate the film is most probable in the form of NiOOH. The spectra showed that on these two alloy surfaces mainly contained Ni, the chromium peak was barely detectable. These results further indicated that the surface layer were at least about 20 Å thick (ejected electron escape depth) oxide film of nickel completely.

V. Passive Films on 316 Stainless Steel

A. Fe Spectra

Experimental results (Fig. A-12) showed that the Fe $2P_{3/2}$ peak position shifted from 710.7 to 710.0 eV and the peak became sharper as the potential increased from 0.35 to 1.55 V.

B. Ni Spectra

The position of Ni $2P_{3/2}$ (Fig. A-13) located at 855.0 eV at potential between 0.35 V and 0.95 V. The peak position, however, shifted to 854.4 eV as the potential increased to 1.55 V and the peak became sharper.

C. Cr Spectra

The Cr $2P_{3/2}$ peak (Fig. A-14) became very broad as the anodic oxide formation potential increased from 0.35 to 1.55 V. The high energy side of the peak distorted to the extent that the Cr $2P_{1/2}$ peak almost disappeared indicating either the contribution of high valency chromium (VI) increase or the chromium content on the surface oxide layer decrease or both. An additional peak appeared at 578.1 eV for the oxide formed at 1.55 V, which indicated the presence of chromium (VI) ions.

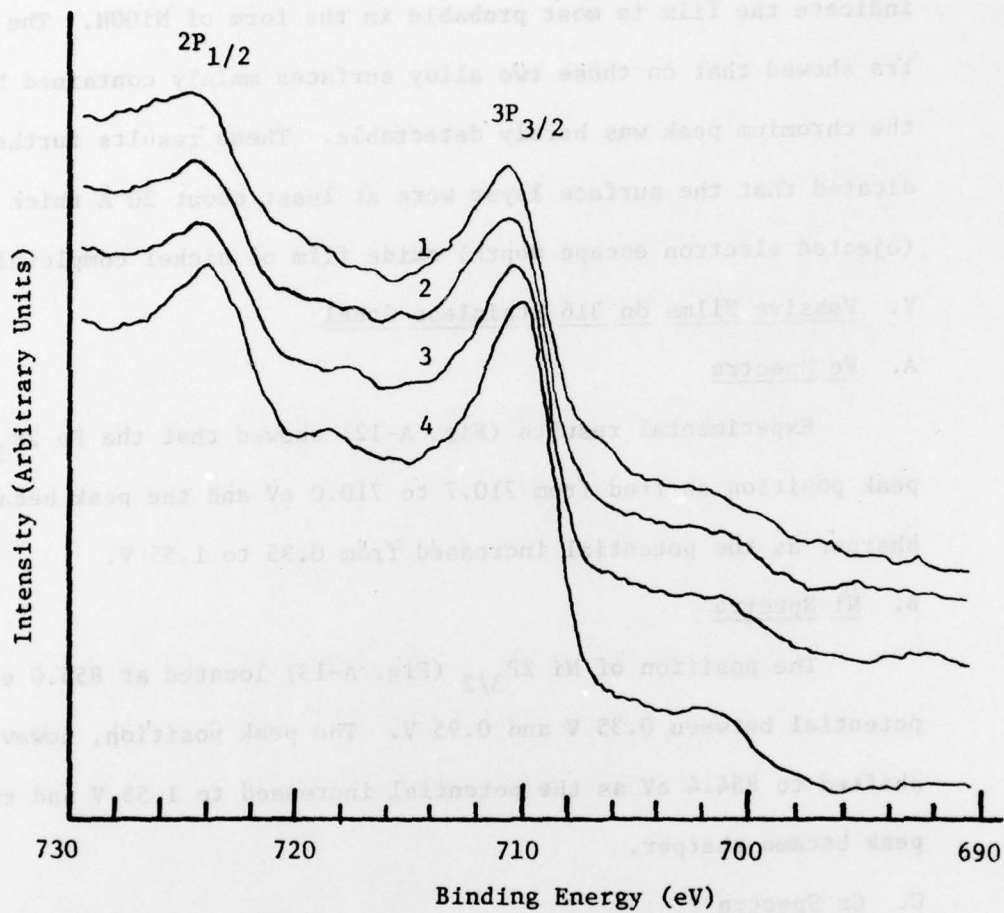


Figure A-12: Fe 2P photo-electron spectra for passive films on 316 stainless steel grown in borate buffer (pH 8.4) at different potentials: 1) 0.35 V; 2) 0.65 V; 3) 1.35 V; 4) 1.55 V vs RHE.

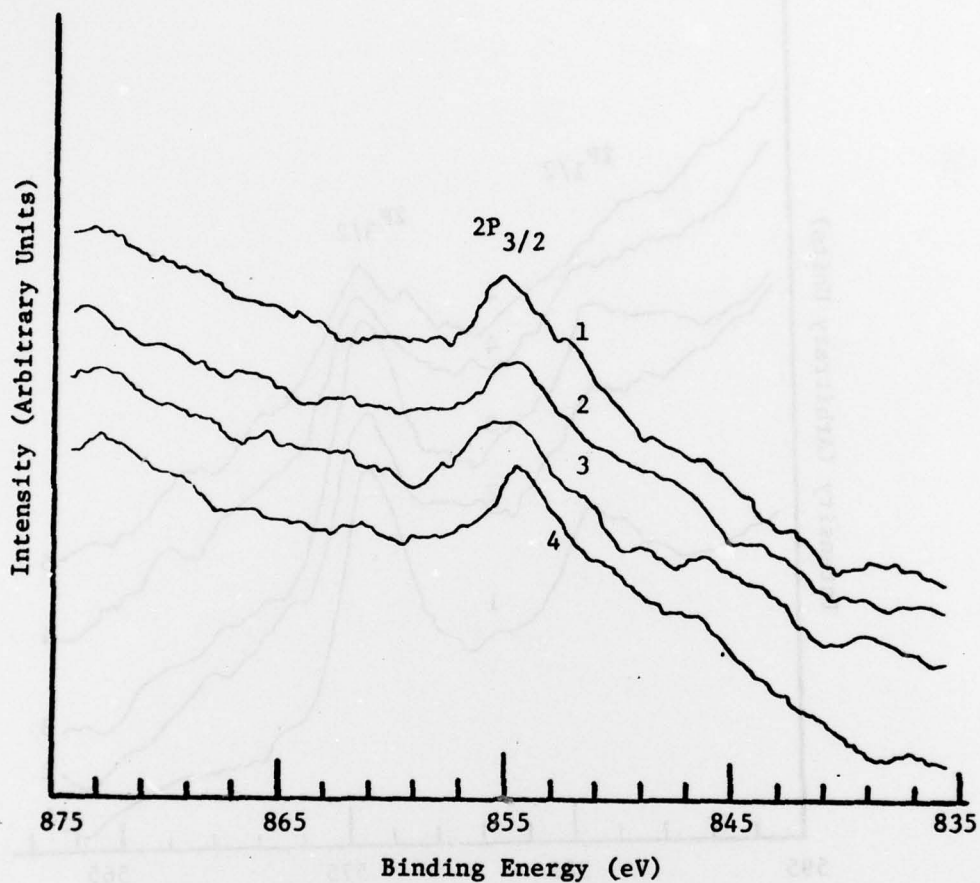


Figure A-13: Ni 2P photo-electron spectra for passive films on 316 stainless steel grown in borate buffer (pH 8.4) at different potentials: 1) 0.35 V; 2) 0.65 V; 3) 0.95 V; 4) 1.55 V vs RHE.

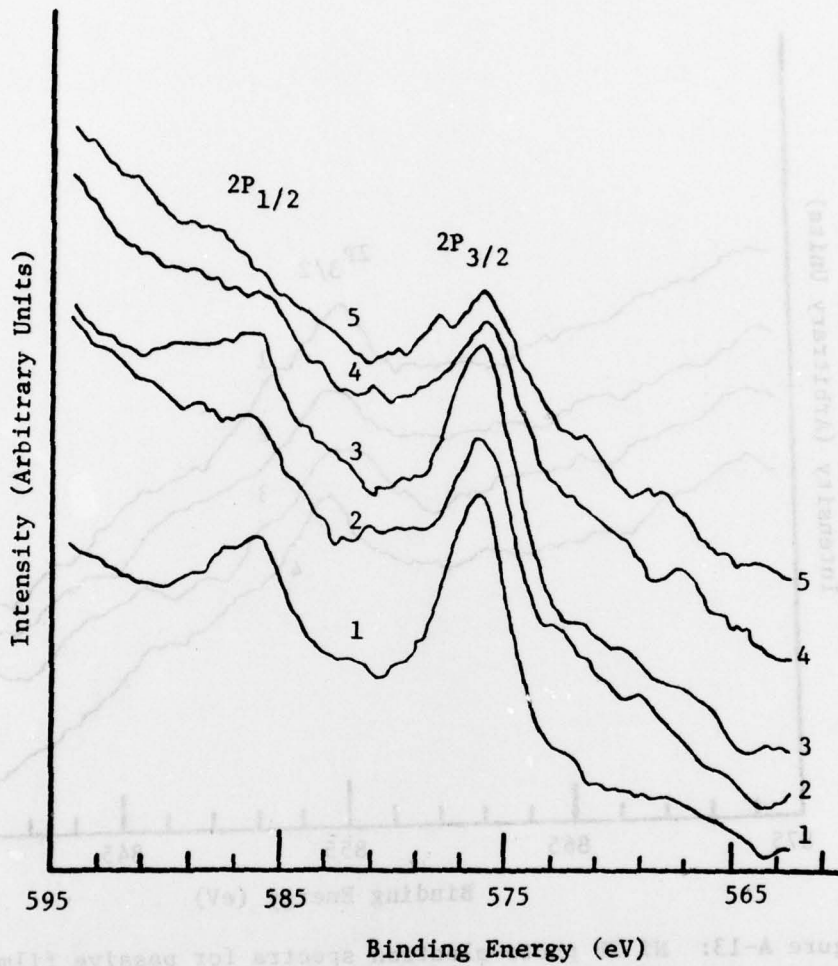


Figure A-14: Cr 2P photo-electron spectra for passive films on 316 stainless steel grown in borate buffer (pH 8.4) at different potentials: 1) 0.35 V; 2) 0.65 V; 3) 0.95 V; 4) 1.35 V; 5) 1.55 V vs RHE.

D. O Spectra

The position of the O 1s peak (Fig. A-15) showed a large shift from 530.8 eV (at 0.35 V) to 529.2 eV (at 1.55 V) indicating that the oxygen species is involved in a changing environment driven by the anodic oxide formation potentials.

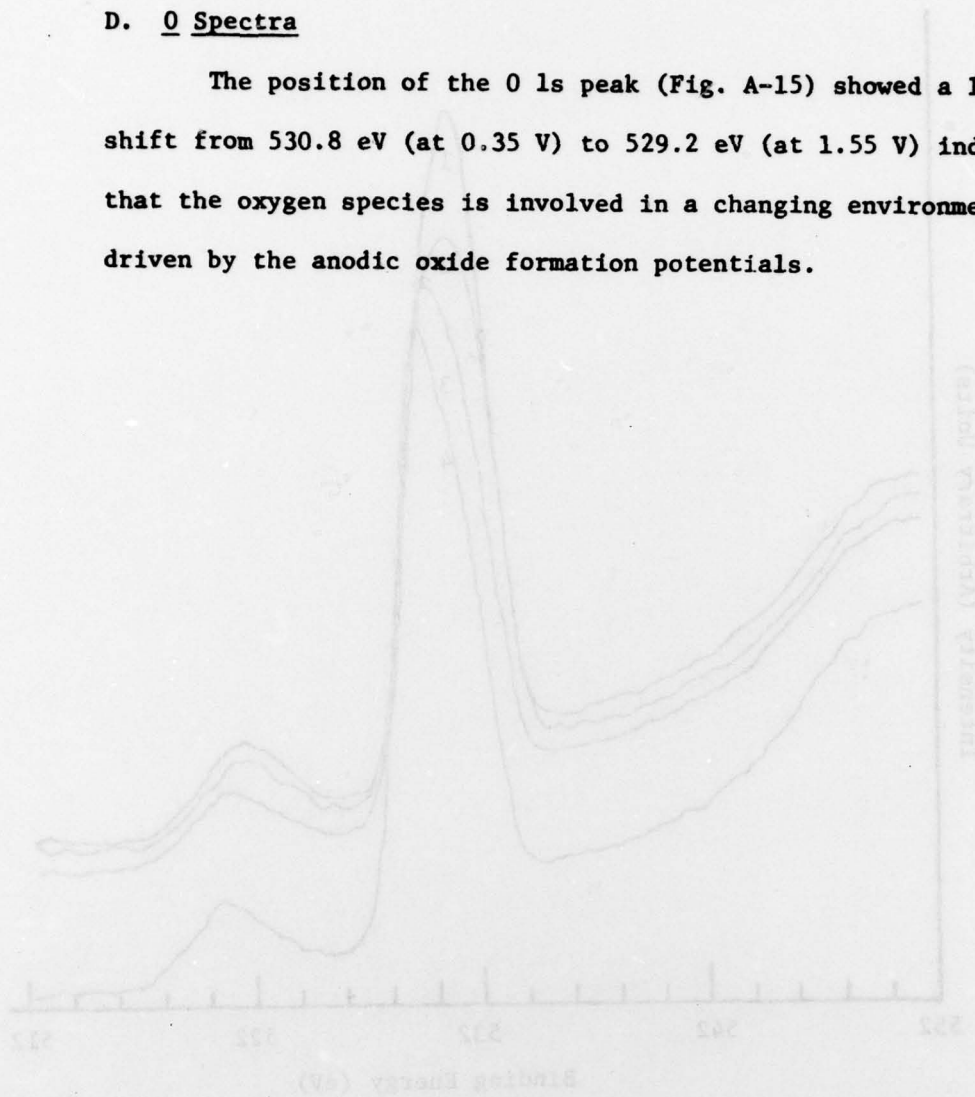


Figure A-15: O 1s photoelectron spectra for passive films on 316 stainless steel grown in borate buffer (pH 8.4) at different potentials: (1) 0.35 V; (2) 0.65 V; (3) 1.35 V; (4) 1.55 V vs RHE.

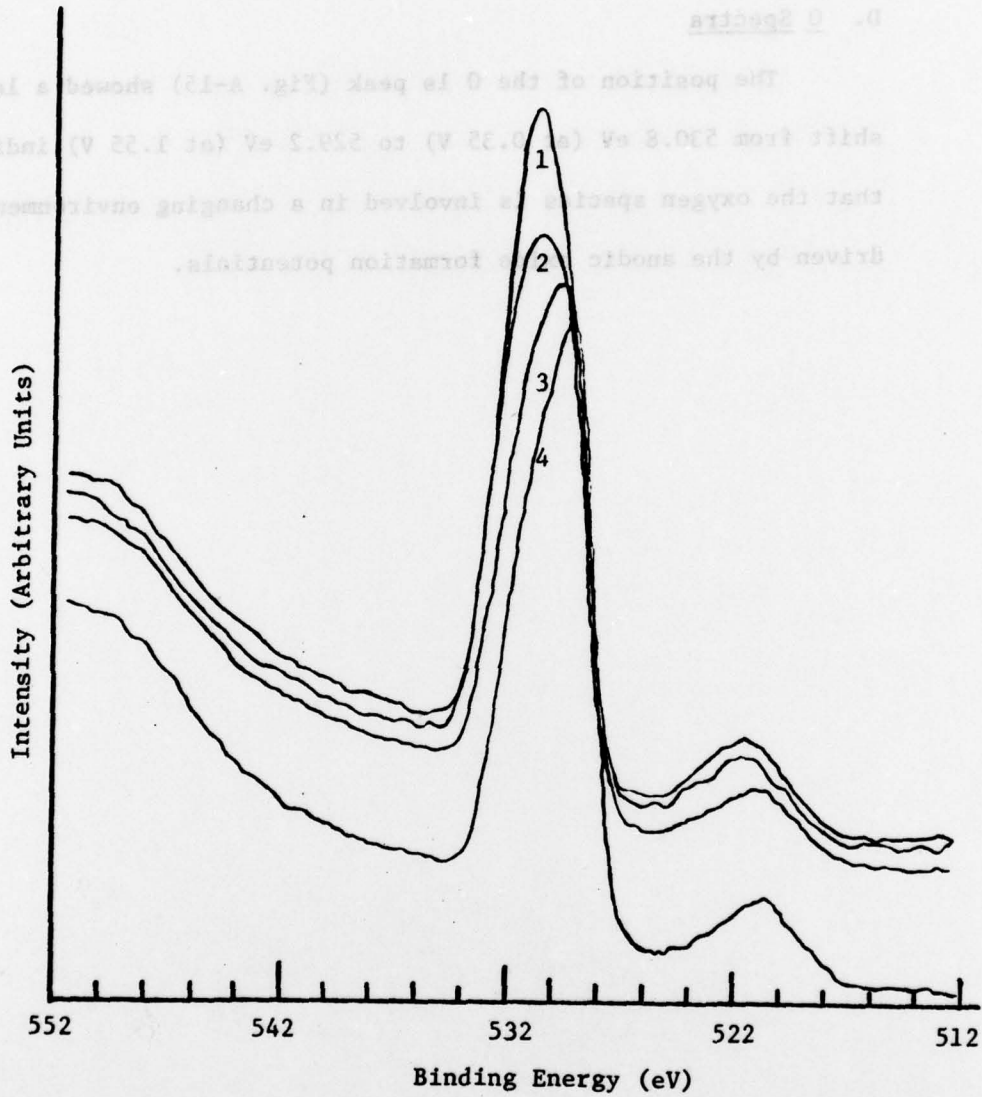


Figure A-15: O 1s photo-electron spectra for passive films on 316 stainless steel grown in borate buffer (pH 8.4) at different potentials: 1) 0.35 V; 2) 0.65 V; 3) 1.35 V; 4) 1.55 V vs RHE.

TECHNICAL REPORT DISTRIBUTION LIST, GEN

	<u>No.</u> <u>Copies</u>		<u>No.</u> <u>Copies</u>
Office of Naval Research 800 North Quincy Street Arlington, Virginia 22217 Attn: Code 472	2	Defense Documentation Center Building 5, Cameron Station Alexandria, Virginia	12
ONR Branch Office 536 S. Clark Street Chicago, Illinois 60605 Attn: Dr. George Sandoz	1	U.S. Army Research Office P. O. Box 1211 Research Triangle Park, NC 27709 Attn: CRD-AA-IP	1
ONR Branch Office 715 Broadway New York, New York 10003 Attn: Scientific Dept.	1	Naval Ocean Systems Center San Diego, California 92152 Attn: Mr. Joe McCartney	1
ONR Branch Office 1030 East Green Street Pasadena, California 91106 Attn: Dr. R.J. Marcus	1	Naval Weapons Center China Lake, California 93555 Attn: Dr. A. B. Amster Chemistry Division	1
ONR Area Office One Hallidie Plaza, Suite 601 San Francisco, California 94102 Attn: Dr. P.A. Miller	1	Naval Civil Engineering Laboratory Port Hueneme, California 93401 Attn: Dr. R.W. Drisko	1
ONR Branch Office Building 114, Section D 666 Summer Street Boston, Massachusetts 02210 Attn: Dr. L.H. Peebles	1	Professor K.E. Woehler Department of Physics & Chemistry Naval Postgraduate School Monterey, California 93940	1
Director, Naval Research Laboratory Washington, D.C. 20390 Attn: Code 6100	1	Dr. A. L. Slafkosky Scientific Advisor Commandant of the Marine Corps (Code RD-1) Washington, D.C. 20380	1
The Assistant Secretary of the Navy (R,E&S) Department of the Navy Room 4E736, Pentagon Washington, D.C. 20350	1	Office of Naval Research 800 N. Quincy Street Arlington, Virginia 22217 Attn: Dr. Richard S. Miller	1
Commander, Naval Air Systems Command Department of the Navy Washington, D.C. 20360 Attn: Code 310C	1	Naval Ship Research and Development Center Annapolis, Maryland 21401 Attn: Dr. G. Bosmajian Applied Chemistry Division	1
		Naval Ocean Systems Center San Diego, California 91232 Attn: Dr. S. Yamamoto, Marine Sciences Division	1

TECHNICAL REPORT DISTRIBUTION LIST, 359

	<u>No.</u> <u>Copies</u>		<u>No.</u> <u>Copies</u>
Dr. Paul Delahay New York University Department of Chemistry New York, New York 10003	1	Library P.R. Mallory and Co., Inc. Northwest Industrial Park Burlington, Massachusetts 01803	1
Dr. R. A. Osteryoung Colorado State University Department of Chemistry Fort Collins, Colorado 80521	1	Dr. P. J. Hendra University of Southampton Dept. of Chemistry Southampton SO9 5NH United Kingdom	1
Dr. D.N. Bennion University of California Chemical Engineering Dept. Los Angeles, California 90024	1	Dr. Sam Perone Purdue University Department of Chemistry West Lafayette, Indiana 47907	1
Dr. R. A. Marcus California Institute of Tech. Department of Chemistry Pasadena, California 91125	1	Dr. Royce W. Murray University of North Carolina Department of Chemistry Chapel Hill, North Carolina 27514	1
Dr. J. J. Auburn Bell Laboratories Murray Hill, New Jersey 07974	1	Naval Ocean Systems Center San Diego, California 92152 Attn: Technical Library	1
Dr. Adam Heller Bell Telephone Laboratories Murray Hill, New Jersey 07974	1	Dr. J. H. Ambrus The Electrochemistry Branch Materials Division, Research & Technology Department Naval Surface Weapons Center White Oak Laboratory Silver Spring, Maryland 20910	1
Dr. T. Katan Lockheed Missiles & Space Co., Inc. P. O. Box 504 Sunnyvale, California 94088	1	Dr. G. Goodman Globe-Union Incorporated 5757 North Green Bay Avenue Milwaukee, Wisconsin 53201	1
Dr. Joseph Singer, Code 302-1 NASA-Lewis 21000 Brookpark Road Cleveland, Ohio 44135	1	Dr. J. Boechler Electrochimica Corporation Attention: Technical Library 2485 Charleston Road Mountain View, California 94040	1
Dr. B. Brummer EIC Incorporated Five Lee Street Cambridge, Massachusetts 02139	1	Dr. P. P. Schmidt Oakland University Department of Chemistry Rochester, Michigan 48063	1

TECHNICAL REPORT DISTRIBUTION LIST, 359

	<u>No.</u> <u>Copies</u>		<u>No.</u> <u>Copies</u>
Dr. H. Richtol Chemistry Department Rensselaer Polytechnic Institute Troy, New York 12181	1	Dr. M. G. Sceats University of Rochester Department of Chemistry Rochester, New York 14627	1
Dr. A. B. Ellis Chemistry Department University of Wisconsin Madison, Wisconsin 53706	1		
Dr. M. Wrighton Chemistry Department Massachusetts Institute of Tech. Cambridge, Massachusetts 02139	1		
Larry E. Plew Naval Weapons Support Center Code 3073, Building 2906 Crane, Indiana 47522	1		
S. Ruby DOE (STOR) 600 E Street Washington, D.C. 20545	1		
Dr. Aaron Wold Brown University Department of Chemistry Providence, Rhode Island 02192	1		
Dr. R. C. Chudacek McGraw-Edison Company Edison Battery Division Post Office Box 28 Bloomfield, New Jersey 07003	1		
Dr. A. J. Bard University of Texas Department of Chemistry Austin, Texas 78712	1		
Dr. M. M. Nicholson Electronics Research Center Rockwell International 3370 Miraloma Avenue Anaheim, California 92803	1		